

Advances in Civil Engineering

Advances in the Failure Mechanisms of Asphalt Pavements

Lead Guest Editor: Jiaolong Ren

Guest Editors: Yingjun Jiang, Zhirong Jia, Ruixia Li, and Di Wang





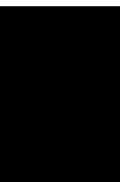
Advances in the Failure Mechanisms of Asphalt Pavements

Advances in Civil Engineering

Advances in the Failure Mechanisms of Asphalt Pavements

Lead Guest Editor: Jiaolong Ren

Guest Editors: Yingjun Jiang, Zhirong Jia, Ruixia Li,
and Di Wang



Copyright © 2021 Hindawi Limited. All rights reserved.

This is a special issue published in "Advances in Civil Engineering." All articles are open access articles distributed under the Creative Commons Attribution License, which permits unrestricted use, distribution, and reproduction in any medium, provided the original work is properly cited.





Chief Editor

Cumaraswamy Vipulanandan, USA














Associate Editors

Chiara Bedon , Italy
Constantin Chaliotis , Greece
Ghassan Chehab , Lebanon
Ottavia Corbi, Italy
Mohamed ElGawady , USA
Husnain Haider , Saudi Arabia
Jian Ji , China
Jiang Jin , China
Shazim A. Memon , Kazakhstan
Hossein Moayedi , Vietnam
Sanjay Nimbalkar, Australia
Giuseppe Oliveto , Italy
Alessandro Palmeri , United Kingdom
Arnaud Perrot , France
Hugo Rodrigues , Portugal
Victor Yepes , Spain
Xianbo Zhao , Australia

Academic Editors

José A.F.O. Correia, Portugal
Glenda Abate, Italy
Khalid Abdel-Rahman , Germany
Ali Mardani Aghabaglou, Turkey
José Aguiar , Portugal
Afaq Ahmad , Pakistan
Muhammad Riaz Ahmad , Hong Kong
Hashim M.N. Al-Madani , Bahrain
Luigi Aldieri , Italy
Angelo Aloisio , Italy
Maria Cruz Alonso, Spain
Filipe Amarante dos Santos , Portugal
Serji N. Amirkhania, USA
Eleftherios K. Anastasiou , Greece
Panagiotis Ch. Anastasopoulos , USA
Mohamed Moafak Arbili , Iraq
Farhad Aslani , Australia
Siva Avudaiappan , Chile
Ozgur BASKAN , Turkey
Adewumi Babafemi, Nigeria
Morteza Bagherpour, Turkey
Qingsheng Bai , Germany
Nicola Baldo , Italy
Daniele Baraldi , Italy

Eva Barreira , Portugal
Emilio Bastidas-Arteaga , France
Rita Bento, Portugal
Rafael Bergillos , Spain
Han-bing Bian , China
Xia Bian , China
Huseyin Bilgin , Albania
Giovanni Biondi , Italy
Hugo C. Biscaia , Portugal
Rahul Biswas , India
Edén Bojórquez , Mexico
Giosuè Boscato , Italy
Melina Bosco , Italy
Jorge Branco , Portugal
Bruno Briseghella , China
Brian M. Broderick, Ireland
Emanuele Brunesi , Italy
Quoc-Bao Bui , Vietnam
Tan-Trung Bui , France
Nicola Buratti, Italy
Gaochuang Cai, France
Gladis Camarini , Brazil
Alberto Campisano , Italy
Qi Cao, China
Qixin Cao, China
Iacopo Carnacina , Italy
Alessio Cascardi, Italy
Paolo Castaldo , Italy
Nicola Cavalagli , Italy
Liborio Cavaleri , Italy
Anush Chandrappa , United Kingdom
Wen-Shao Chang , United Kingdom
Muhammad Tariq Amin Chaudhary, Kuwait
Po-Han Chen , Taiwan
Qian Chen , China
Wei Tong Chen , Taiwan
Qixiu Cheng, Hong Kong
Zhanbo Cheng, United Kingdom
Nicholas Chileshe, Australia
Prinya Chindaprasirt , Thailand
Corrado Chisari , United Kingdom
Se Jin Choi , Republic of Korea
Heap-Yih Chong , Australia
S.H. Chu , USA
Ting-Xiang Chu , China




Zhaofei Chu , China
Wonseok Chung , Republic of Korea
Donato Ciampa , Italy
Gian Paolo Cimellaro, Italy
Francesco Colangelo, Italy
Romulus Costache , Romania
Liviu-Adrian Cotfas , Romania
Antonio Maria D'Altri, Italy
Bruno Dal Lago , Italy
Amos Darko , Hong Kong
Arka Jyoti Das , India
Dario De Domenico , Italy
Gianmarco De Felice , Italy
Stefano De Miranda , Italy
Maria T. De Risi , Italy
Tayfun Dede, Turkey
Sadik O. Degertekin , Turkey
Camelia Delcea , Romania
Cristoforo Demartino, China
Giuseppe Di Filippo , Italy
Luigi Di Sarno, Italy
Fabio Di Trapani , Italy
Aboelkasim Diab , Egypt
Thi My Dung Do, Vietnam
Giulio Dondi , Italy
Jiangfeng Dong , China
Chao Dou , China
Mario D'Aniello , Italy
Jingtao Du , China
Ahmed Elghazouli, United Kingdom
Francesco Fabbrocino , Italy
Flora Faleschini , Italy
Dingqiang Fan, Hong Kong
Xueping Fan, China
Qian Fang , China
Salar Farahmand-Tabar , Iran
Ilenia Farina, Italy
Roberto Fedele, Italy
Guang-Liang Feng , China
Luigi Fenu , Italy
Tiago Ferreira , Portugal
Marco Filippo Ferrotto, Italy
Antonio Formisano , Italy
Guoyang Fu, Australia
Stefano Galassi , Italy

Junfeng Gao , China
Meng Gao , China
Giovanni Garcea , Italy
Enrique García-Macías, Spain
Emilio García-Taengua , United Kingdom
DongDong Ge , USA
Khaled Ghaedi, Malaysia
Khaled Ghaedi , Malaysia
Gian Felice Giaccu, Italy
Agathoklis Giaralis , United Kingdom
Ravindran Gobinath, India
Rodrigo Gonçalves, Portugal
Peilin Gong , China
Belén González-Fonteboa , Spain
Salvatore Grasso , Italy
Fan Gu, USA
Erhan Güneyisi , Turkey
Esra Mete Güneyisi, Turkey
Pingye Guo , China
Ankit Gupta , India
Federico Gusella , Italy
Kemal Hacıefendioğlu, Turkey
Jianyong Han , China
Song Han , China
Asad Hanif , Macau
Hadi Hasanzadehshooiili , Canada
Mostafa Fahmi Hassanein, Egypt
Amir Ahmad Hedayat , Iran
Khandaker Hossain , Canada
Zahid Hossain , USA
Chao Hou, China
Biao Hu, China
Jiang Hu , China
Xiaodong Hu, China
Lei Huang , China
Cun Hui , China
Bon-Gang Hwang, Singapore
Jijo James , India
Abbas Fadhil Jasim , Iraq
Ahad Javanmardi , China
Krishnan Prabhakan Jaya, India
Dong-Sheng Jeng , Australia
Han-Yong Jeon, Republic of Korea
Pengjiao Jia, China
Shaohua Jiang , China

MOUSTAFA KASSEM , Malaysia
Mosbeh Kaloop , Egypt
Shankar Karuppannan , Ethiopia
John Kechagias , Greece
Mohammad Khajehzadeh , Iran
Afzal Husain Khan , Saudi Arabia
Mehran Khan , Hong Kong
Manoj Khandelwal, Australia
Jin Kook Kim , Republic of Korea
Woosuk Kim , Republic of Korea
Vaclav Koci , Czech Republic
Loke Kok Foong, Vietnam
Hailing Kong , China
Leonidas Alexandros Kouris , Greece
Kyriakos Kourousis , Ireland
Moacir Kripka , Brazil
Anupam Kumar, The Netherlands
Emma La Malfa Ribolla, Czech Republic
Ali Lakirouhani , Iran
Angus C. C. Lam, China
Thanh Quang Khai Lam , Vietnam
Luciano Lamberti, Italy
Andreas Lampropoulos , United Kingdom
Raffaele Landolfo, Italy
Massimo Latour , Italy
Bang Yeon Lee , Republic of Korea
Eul-Bum Lee , Republic of Korea
Zhen Lei , Canada
Leonardo Leonetti , Italy
Chun-Qing Li , Australia
Dongsheng Li , China
Gen Li, China
Jiale Li , China
Minghui Li, China
Qingchao Li , China
Shuang Yang Li , China
Sunwei Li , Hong Kong
Yajun Li , China
Shun Liang , China
Francesco Liguori , Italy
Jae-Han Lim , Republic of Korea
Jia-Rui Lin , China
Kun Lin , China
Shibin Lin, China

Tzu-Kang Lin , Taiwan
Yu-Cheng Lin , Taiwan
Hexu Liu, USA
Jian Lin Liu , China
Xiaoli Liu , China
Xuemei Liu , Australia
Zaobao Liu , China
Zhuang-Zhuang Liu, China
Diego Lopez-Garcia , Chile
Cristiano Loss , Canada
Lyan-Ywan Lu , Taiwan
Jin Luo , USA
Yanbin Luo , China
Jianjun Ma , China
Junwei Ma , China
Tian-Shou Ma, China
Zhongguo John Ma , USA
Maria Macchiaroli, Italy
Domenico Magisano, Italy
Reza Mahinroosta, Australia
Yann Malecot , France
Prabhat Kumar Mandal , India
John Mander, USA
Iman Mansouri, Iran
André Dias Martins, Portugal
Domagoj Matesan , Croatia
Jose Matos, Portugal
Vasant Matsagar , India
Claudio Mazzotti , Italy
Ahmed Mebarki , France
Gang Mei , China
Kasim Mermerdas, Turkey
Giovanni Minafò , Italy
Masoomah Mirrashid , Iran
Abbas Mohajerani , Australia
Fadzli Mohamed Nazri , Malaysia
Fabrizio Mollaioli , Italy
Rosario Montuori , Italy
H. Naderpour , Iran
Hassan Nasir , Pakistan
Hossein Nassiraei , Iran
Satheeskumar Navaratnam , Australia
Ignacio J. Navarro , Spain
Ashish Kumar Nayak , India
Behzad Nematollahi , Australia

Chayut Ngamkhanong , Thailand
Trung Ngo, Australia
Tengfei Nian, China
Mehdi Nikoo , Canada
Youjun Ning , China
Olugbenga Timo Oladinrin , United Kingdom
Oladimeji Benedict Olalusi, South Africa
Timothy O. Olawumi , Hong Kong
Alejandro Orfila , Spain
Maurizio Orlando , Italy
Siti Aminah Osman, Malaysia
Walid Oueslati , Tunisia
SUVASH PAUL , Bangladesh
John-Paris Pantouvakis , Greece
Fabrizio Paolacci , Italy
Giuseppina Pappalardo , Italy
Fulvio Parisi , Italy
Dimitrios G. Pavlou , Norway
Daniele Pellegrini , Italy
Gatheeshgar Perampalam , United Kingdom
Daniele Perrone , Italy
Giuseppe Piccardo , Italy
Vagelis Plevris , Qatar
Andrea Pranno , Italy
Adolfo Preciado , Mexico
Chongchong Qi , China
Yu Qian, USA
Ying Qin , China
Giuseppe Quaranta , Italy
Krishanu ROY , New Zealand
Vlastimir Radonjanin, Serbia
Carlo Rainieri , Italy
Rahul V. Ralegaonkar, India
Raizal Saifulnaz Muhammad Rashid, Malaysia
Alessandro Rasulo , Italy
Chonghong Ren , China
Qing-Xin Ren, China
Dimitris Rizos , USA
Geoffrey W. Rodgers , New Zealand
Pier Paolo Rossi, Italy
Nicola Ruggieri , Italy
JUNLONG SHANG, Singapore


Nikhil Saboo, India
Anna Saetta, Italy
Juan Sagaseta , United Kingdom
Timo Saksala, Finland
Mostafa Salari, Canada
Ginevra Salerno , Italy
Evangelos J. Sapountzakis , Greece
Vassilis Sarhosis , United Kingdom
Navaratnarajah Sathiparan , Sri Lanka
Fabrizio Scozzese , Italy
Halil Sezen , USA
Payam Shafigh , Malaysia
M. Shahria Alam, Canada
Yi Shan, China
Hussein Sharaf, Iraq
Mostafa Sharifzadeh, Australia
Sanjay Kumar Shukla, Australia
Amir Si Larbi , France
Okan Sirin , Qatar
Piotr Smarzewski , Poland
Francesca Sollecito , Italy
Rui Song , China
Tian-Yi Song, Australia
Flavio Stochino , Italy
Mayank Sukhija , USA
Piti Sukontasukkul , Thailand
Jianping Sun, Singapore
Xiao Sun , China
T. Tafsirojjaman , Australia
Fujiao Tang , China
Patrick W.C. Tang , Australia
Zhi Cheng Tang , China
Weerachart Tangchirapat , Thailand
Xiixin Tao, China
Piergiorgio Tataranni , Italy
Elisabete Teixeira , Portugal
Jorge Iván Tobón , Colombia
Jing-Zhong Tong, China
Francesco Trentadue , Italy
Antonello Troncone, Italy
Majbah Uddin , USA
Tariq Umar , United Kingdom
Muahmmad Usman, United Kingdom
Muhammad Usman , Pakistan
Mucteba Uysal , Turkey

Ilaria Venanzi , Italy
Castorina S. Vieira , Portugal
Valeria Vignali , Italy
Claudia Vitone , Italy
Liwei WEN , China
Chunfeng Wan , China
Hua-Ping Wan, China
Roman Wan-Wendner , Austria
Chaohui Wang , China
Hao Wang , USA
Shiming Wang , China
Wayne Yu Wang , United Kingdom
Wen-Da Wang, China
Xing Wang , China
Xiuling Wang , China
Zhenjun Wang , China
Xin-Jiang Wei , China
Tao Wen , China
Weiping Wen , China
Lei Weng , China
Chao Wu , United Kingdom
Jiangyu Wu, China
Wangjie Wu , China
Wenbing Wu , China
Zhixing Xiao, China
Gang Xu, China
Jian Xu , China
Panpan , China
Rongchao Xu , China
HE YONGLIANG, China
Michael Yam, Hong Kong
Hailu Yang , China
Xu-Xu Yang , China
Hui Yao , China
Xinyu Ye , China
Zhoujing Ye, China
Gürol Yildirim , Turkey
Dawei Yin , China
Doo-Yeol Yoo , Republic of Korea
Zhanping You , USA
Afshar A. Yousefi , Iran
Xinbao Yu , USA
Dongdong Yuan , China
Geun Y. Yun , Republic of Korea

Hyun-Do Yun , Republic of Korea
Cemal YİĞİT , Turkey
Paolo Zampieri, Italy
Giulio Zani , Italy
Mariano Angelo Zanini , Italy
Zhixiong Zeng , Hong Kong
Mustafa Zeybek, Turkey
Henglong Zhang , China
Jiupeng Zhang, China
Tingting Zhang , China
Zengping Zhang, China
Zetian Zhang , China
Zhigang Zhang , China
Zhipeng Zhao , Japan
Jun Zhao , China
Annan Zhou , Australia
Jia-wen Zhou , China
Hai-Tao Zhu , China
Peng Zhu , China
QuanJie Zhu , China
Wenjun Zhu , China
Marco Zucca, Italy
Haoran Zuo, Australia
Junqing Zuo , China
Robert Černý , Czech Republic
Süleyman İpek , Turkey

Contents

Mechanical Response and Structure Optimization of Nanomodified Asphalt Pavement

Wenjun Gu , Yao Tian, and Xuanyu Zhang


Research Article (13 pages), Article ID 6286704, Volume 2021 (2021)

Environment Effect on the Rutting Resistance of Nano-SiO₂-Modified Asphalt Concrete: Temperature and Water

Luchuan Chen, Wenjun Gu , and Xuanyu Zhang

Research Article (9 pages), Article ID 7439006, Volume 2021 (2021)

Coupled Dynamics of Vehicle-Bridge Interaction System Using High Efficiency Method

Lu Sun  and Xingzhuang Zhao 


Research Article (22 pages), Article ID 1964200, Volume 2021 (2021)

Using Continuum-Discontinuum Element Method to Model the Foliation-Affected Fracturing in Rock Brazilian Test

Qunlei Zhang, Zihan Zhi, Chun Feng, Ruixia Li, Jinchao Yue , and Junyu Cong


Research Article (9 pages), Article ID 1404568, Volume 2021 (2021)

Decision Method of Bridge Deck Pavement Maintenance Based on the Decision Maker's Objective

Xiaofei Liang , Jun Shi , and Zhongmei Li





Research Article (8 pages), Article ID 5593722, Volume 2021 (2021)

Analysis and Research on Energy-Saving Reconstruction of Building Heating System

Yongqiang Liu  and Zhanfang Huang




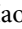
Research Article (6 pages), Article ID 5599479, Volume 2021 (2021)

Research on Fatigue Model of Semi-Rigid Base Asphalt Pavement before and after Polymer Grouting

Bei Zhang , Xu Zhang, Yanhui Zhong , Xiaolong Li , Meimei Hao , Xianwei Sang, Xiaoliang Wang, and Jianyang Liu

Research Article (16 pages), Article ID 6658943, Volume 2021 (2021)

Temperature Correction for FWD Deflection in Cement Pavement Void Detection

Bei Zhang , Xiaoliang Wang, Yanhui Zhong , Xiaolong Li , Meimei Hao , Yuanhao Ding, Jianyang Liu, and Xu Zhang





Research Article (14 pages), Article ID 6668003, Volume 2021 (2021)

Influence of the Activator Concentration and Solid/Liquid Ratio on the Strength and Shrinkage Characteristics of Alkali-Activated Slag Geopolymer Pastes

Zikai Xu, Jinchao Yue, Guanhong Pang , Ruixia Li, Peng Zhang, and Shengtang Xu 



Research Article (11 pages), Article ID 6631316, Volume 2021 (2021)

A BP Neural Network Method for Grade Classification of Loose Damage in Semirigid Pavement Bases







Bei Zhang , Jianyang Liu, Yanhui Zhong , Xiaolong Li , Meimei Hao , Xiao Li, Xu Zhang, and Xiaoliang Wang

Research Article (11 pages), Article ID 6658235, Volume 2021 (2021)

Finite Element (FE) Modeling of Indirect Tension to Cylindrical (IT-CY) Specimen Test for Damping Asphalt Mixtures (DAMs)

Jiandong Huang, Tianhong Duan , Yuantian Sun , Lin Wang, and Yawei Lei
Research Article (11 pages), Article ID 6694180, Volume 2020 (2020)

Prediction Model of Asphalt Content of Asphalt Mixture Based on Dielectric Properties

Yanhui Zhong , Yilong Wang, Bei Zhang , Xiaolong Li , Songtao Li , Yanmei Zhong , Meimei Hao , and Yanlong Gao
Research Article (10 pages), Article ID 6661593, Volume 2020 (2020)

Research Article

Mechanical Response and Structure Optimization of Nanomodified Asphalt Pavement

Wenjun Gu ¹, Yao Tian,² and Xuanyu Zhang³

¹Institute for Advanced Study, 7835 Muirfield Court, Potomac, MD 20854, USA

²Shandong Hi-Speed Group, Jinan, Shandong 250098, China

³Shandong Hi-Speed Infrastructure Construction Co. Ltd., Jinan, Shandong 250098, China

Correspondence should be addressed to Wenjun Gu; gu_wenjun@hotmail.com

Received 6 May 2021; Revised 5 July 2021; Accepted 16 August 2021; Published 26 August 2021

Academic Editor: Jiaolong Ren

Copyright © 2021 Wenjun Gu et al. This is an open access article distributed under the Creative Commons Attribution License, which permits unrestricted use, distribution, and reproduction in any medium, provided the original work is properly cited.

Nanomaterials are widely used in the preparation of modified asphalt because they can improve the high-temperature performance of matrix asphalt and have achieved good engineering results. However, the existing research mainly focuses on the material analysis and formula development of nanomodified asphalt and has not yet been involved in the mechanical response of the nanomodified asphalt pavement structure. The mechanical response contains the horizontal tensile stress and the vertical compressive stress of SiO₂ modified asphalt pavement. It is unable to propose the matching pavement structure combination for the unique material characteristics of nanomodified asphalt, which leads to the increase of the possibility of pavement diseases and material waste. Hence, considering that semirigid base is the most widely used base type in China, two different structural models of nanomodified asphalt pavement are established according to the current specifications. The effects of pavement thickness, material type, and pavement design parameters on the mechanical response of nanomodified asphalt pavement are analyzed, and then the principle of optimal mechanical performance is taken and the optimal combination of nanomodified asphalt pavement structure is proposed.

1. Introduction

In recent years, nanotechnology has been widely used in asphalt modification, which has obvious effect on improving the high-temperature performance of asphalt [1–5]. Caputo et al. introduced the properties of nanoparticles in an easy to review their use in bitumen and asphalt preparation and Silica, ceramic, clay, other oxides, and inorganic nanoparticles and discussed the framework of their use in bitumen and asphalt preparation for various scopes [6]. Li et al. found that the addition of nanomaterials could dramatically enhance the properties of an asphalt material such as viscoelasticity, high-temperature properties, and the resistances to aging, fatigue, and moisture [7]. Sun et al. studied improving base asphalt performance at both high temperature and low temperature in nanomaterials and polymers as composite modifiers to address the low-temperature performance of base asphalt binder [8]. Ma et al. dived TiO₂ nanoparticles application into the pavement and present an experimental investigation of performances and

automobile exhaust purification of asphalt and its mixture modified by nano-TiO₂ [9]. Hu et al. formulated thermo-chromic hot-mixing asphalt (HMA) mixture by doping thermo-chromic powder and/or nano-TiO₂ scatters at different concentrations into traditional asphalt mixture [10]. Hu et al. investigated the feasibility of TiO₂ waterborne epoxy resin as fog seal and exhaust degradation material in the asphalt pavement by adding a commercial anatase/rutile mixed-phase nano-TiO₂ [11]. Li et al. investigated the effects of surface-modified inorganic nanoparticle nano-ZnO on the physical and ultraviolet aging resistance of bitumen as well as the microstructures of the binders [12]. Karahancer et al. investigated a novel bitumen modification by aluminum oxide (Al₂O₃) nanoparticle, mixed with the bitumen in three percentages, to enhance the performance of bitumen and hot mix asphalt (HMA) [13]. Sarkar et al. improved the physical and mechanical properties of open-graded friction courses (OGFCs) by adding the combination of nanosilica (NS) material and alkali resistant (AR) glass fiber [14]. Li et al. used two nanometer microwave absorbers named

as carbon nanotubes (CNTs) and grapheme to improve the microwave heating and healing properties of bitumen under microwave irradiation [15]. Patchai Murugan et al. studied the proper blending methods to enhance the bitumen properties using both conventional and microwave heating methods by using NFC as bitumen modifier and the blending of NFC with bitumen [16]. Jeffry et al. produced nanocarbon from coconut shell ash (NCA) as bitumen modifier [17]. Akbari et al. investigated the fatigue response of hot mix asphalt (HMA) containing nanoclay and nanoalumina modified bitumen and its relationship with surface free energy (SFE) parameters [18]. Hussein et al. found good dispersion of the NCP within the bitumen matrix by XRD pattern and Scanning Electron Microscopy (SEM) of the NCP-modified bitumen (NCPMB) [19]. Shi et al. analyzed the rheological properties of sixteen asphalts with different contents of nanosilica and Qingchuan rock asphalt by univariate analysis and variance analysis [20]. Ren et al. evaluated the influences of asphalt properties, temperature, and moisture damage on the Ad/Co of the asphalt, mastic, and mortar and investigated the relationships between the durability and indirect tensile strength (ITS) of the mixture and the Ad/Co of binder by indirect tensile tests and Cantabro loss tests [21]. Jiang et al. proposed a novel method to characterize distribution of mortar film thickness in asphalt mixture through image processing techniques [22].

However, the existing research mainly focuses on the material analysis and formula development of nanomodified asphalt and has not been involved in the structural mechanics of nanomodified asphalt pavement [22–27]. In fact, because of the unique material characteristics of nanomodified asphalt, its mechanical role in pavement structure is bound to be quite different from that of traditional asphalt mixture [28–31]. It is necessary to carry out systematic mechanical analysis of pavement structure for nanomodified asphalt pavement and analyze the influence of material design parameters and pavement structure parameters on the mechanical response of nanomodified asphalt pavement. Thus, the pavement structure combination matching with nanomodified asphalt pavement is proposed, so as to prevent pavement diseases and material waste and improve the service quality of nanomodified asphalt pavement. Hence, considering that the semirigid base is the most widely used base type in China, two different structural models of nanomodified asphalt pavement are established according to the current specifications. The effects of pavement thickness, material type, and pavement design parameters on the mechanical response of nanomodified asphalt pavement are analyzed, and then the principle of optimal mechanical performance is taken and the optimal combination of nanomodified asphalt pavement structure is proposed.

2. Calculation Model

2.1. Pavement Structure and Calculation Index Selection

2.1.1. Selection of Loads and Calculation Points. “Specifications for Design of Highway Asphalt Pavement (JTG D50-2017)” in China stipulates that the pavement structure design adopts a double-circle uniformly distributed vertical load as the effective load for calculation. The

load circle radius is 10.65 cm, and the tire pressure is 0.707 MPa. The distribution of stress calculation points is shown in Figure 1. In the *XOY* horizontal plane of Figure 1, the coordinates of point *A* are (0, −15.975), the coordinates of point *B* are (0, −5.325), the coordinates of point *C* are (0, 0), and the coordinates of point *D* are (0, −2.6625). Take the maximum value of point *A*, point *B*, point *C*, and point *D* for mechanical response analysis. Direction *X* is the driving direction.

2.1.2. Design Index and Mechanical Response Position. According to 6.2.1 of the “Specifications for Design of Highway Asphalt Pavement (JTG D50-2017),” the design index of pavements with different structures is shown in Table 1. At the same time, according to 6.2.2, the mechanical response and vertical position corresponding to each design index are shown in Table 2.

2.2. Calculation of Nanomodified Asphalt Pavement Structure. To scientifically analyze the calculation results and reduce the amount of testing, this project uses the orthogonal test method to calculate and analyze the nanomodified asphalt pavement structure.

According to the actual use of the arterial highways in China, two different working conditions are set: working condition I (surface layer of nanoasphalt mixture + bottom layer of SBS modified asphalt + semirigid base layer + semirigid subbase layer), and working condition II (surface layer of nanoasphalt mixture + bottom layer of SBS modified asphalt + semirigid base layer + the subbase layer of granules). By changing the thickness and modulus of different layers, the influences of pavement structure parameters on pavement mechanics response (see Table 1) are used to provide a basis for pavement structure design and propose the recommended pavement structure combination form based on the principle of optimal mechanical response. The orthogonal tests of working conditions I and II are shown in Tables 3 and 4, respectively.

According to the Chinese standard “Specifications for Design of Highway Asphalt Pavement (JTG D50-2017),” the modulus of the SiO₂-modified asphalt concrete with the nominal maximum particle size of 13.2 mm is 7310 MPa and that with the nominal maximum particle size of 16 mm is 10,750 MPa. Hence, the modulus of the surfer layer is selected as 7310 MPa, 9030 MPa (average value), and 10,750 MPa.

3. Data and Discussion

The range histogram of working condition I is shown in Figure 2. According to the structural combination of the semirigid base and the semirigid subbase, two control indicators, namely, the bottom layer tensile stress of the inorganic binder stabilizing layer and the permanent deformation of the asphalt concrete layer, are selected.

Owing to the nano-SiO₂ modified asphalt concrete, of which the modulus is tested via laboratory tests, being adopted in the surface layer, the modulus of the surface layer

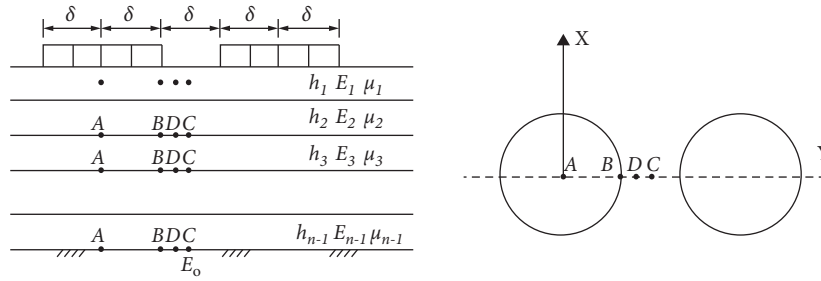


FIGURE 1: Compute point distribution.

TABLE 1: Design index of pavements with different structures.

Base type	Subbase type	Design index
Inorganic binder stabilizing type	Inorganic binder stabilizing type Granule type	Bottom layer tensile stress of inorganic binder stabilizing layer, permanent deformation of asphalt concrete layer

TABLE 2: The mechanical response corresponding to each design index and its vertical position.

Design index	Mechanical response	Vertical position
Bottom layer tensile stress of inorganic binder stabilizing layer	Horizontal tensile stress along the driving direction	The bottom of inorganic binder stabilizing layer
Permanent deformation of asphalt concrete layer	Vertical compressive stress	Top surface of each layer of asphalt concrete layer

TABLE 3: Working condition I the orthogonal test design.

No.	Surface layer		Bottom layer		Base layer		Subbase layer		Soil foundation
	Thickness (cm)	Modulus (MPa)	Thickness (cm)	Modulus (MPa)	Thickness (cm)	Modulus (MPa)	Thickness (cm)	Modulus (MPa)	Modulus (MPa)
1-1	3	7310	5	19,264	30	9000	15	7000	50
1-2	3	9030	7	19,264	36	11,500	18	8500	50
1-3	3	10,750	9	19,264	40	14,000	20	10,000	50
1-4	4	7310	5	19,264	36	11,500	20	10,000	50
1-5	4	9030	7	19,264	40	14,000	15	7000	50
1-6	4	10,750	9	19,264	30	9000	18	8500	50
1-7	5	9030	5	19,264	30	14,000	18	10,000	50
1-8	5	10,750	7	19,264	36	9000	20	7000	50
1-9	5	7310	9	19,264	40	11,500	15	8500	50
1-10	3	10,750	5	19,264	40	11,500	18	7000	50
1-11	3	7310	7	19,264	30	14,000	20	8500	50
1-12	3	9030	9	19,264	36	9000	15	10,000	50
1-13	4	9030	5	19,264	40	9000	20	8500	50
1-14	4	10,750	7	19,264	30	11,500	15	10,000	50
1-15	4	7310	9	19,264	36	14,000	18	7000	50
1-16	5	10,750	5	19,264	36	14,000	15	8500	50
1-17	5	7310	7	19,264	40	9000	18	10,000	50
1-18	5	9030	9	19,264	30	11,500	20	7000	50

TABLE 4: Working condition II the orthogonal test design.

No.	Surface layer		Bottom layer		Base layer		Subbase layer		Soil foundation
	Thickness (cm)	Modulus (MPa)	Thickness (cm)	Modulus (MPa)	Thickness (cm)	Modulus (MPa)	Thickness (cm)	Modulus (MPa)	Modulus (MPa)
2-1	3	7310	5	19,264	30	9000	15	200	50
2-2	3	9030	7	19,264	36	11,500	18	320	50
2-3	3	10,750	9	19,264	40	14,000	20	440	50
2-4	4	7310	5	19,264	36	11,500	20	440	50
2-5	4	9030	7	19,264	40	14,000	15	200	50
2-6	4	10,750	9	19,264	30	9000	18	320	50
2-7	5	9030	5	19,264	30	14,000	18	440	50
2-8	5	10,750	7	19,264	36	9000	20	200	50
2-9	5	7310	9	19,264	40	11,500	15	320	50
2-10	3	10,750	5	19,264	40	11,500	18	200	50
2-11	3	7310	7	19,264	30	14,000	20	320	50
2-12	3	9030	9	19,264	36	9000	15	440	50
2-13	4	9030	5	19,264	40	9000	20	320	50
2-14	4	10,750	7	19,264	30	11,500	15	440	50
2-15	4	7310	9	19,264	36	14,000	18	200	50
2-16	5	10,750	5	19,264	36	14,000	15	320	50
2-17	5	7310	7	19,264	40	9000	18	440	50
2-18	5	9030	9	19,264	30	11,500	20	200	50

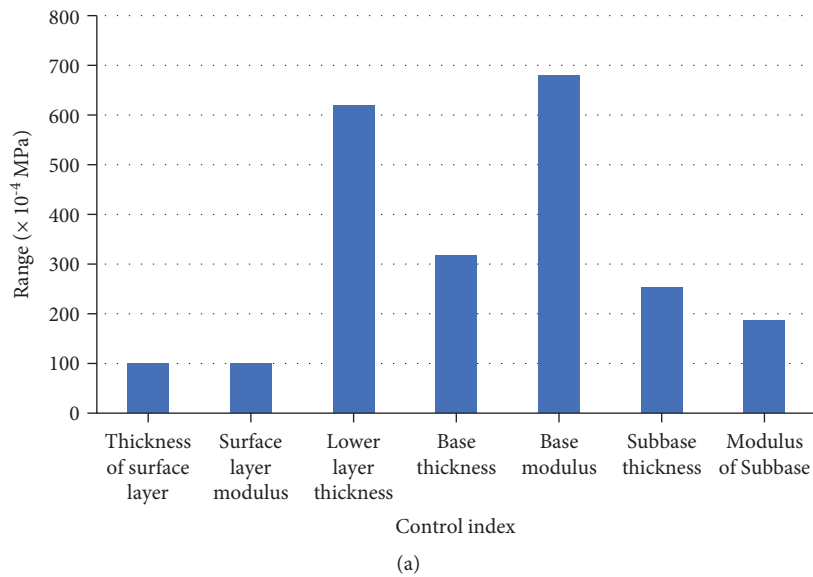
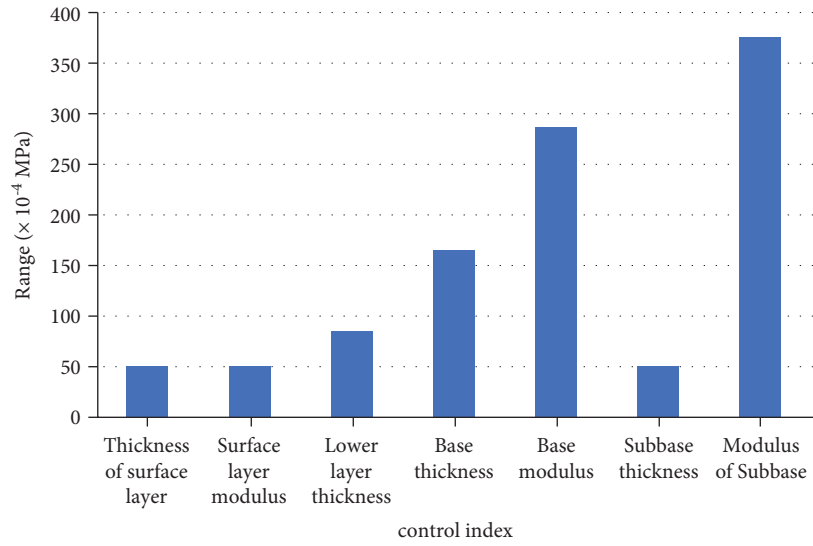
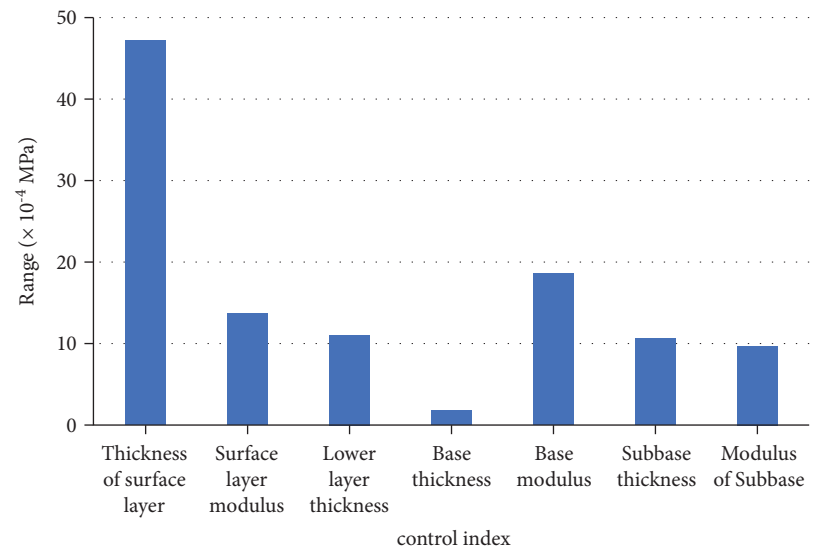


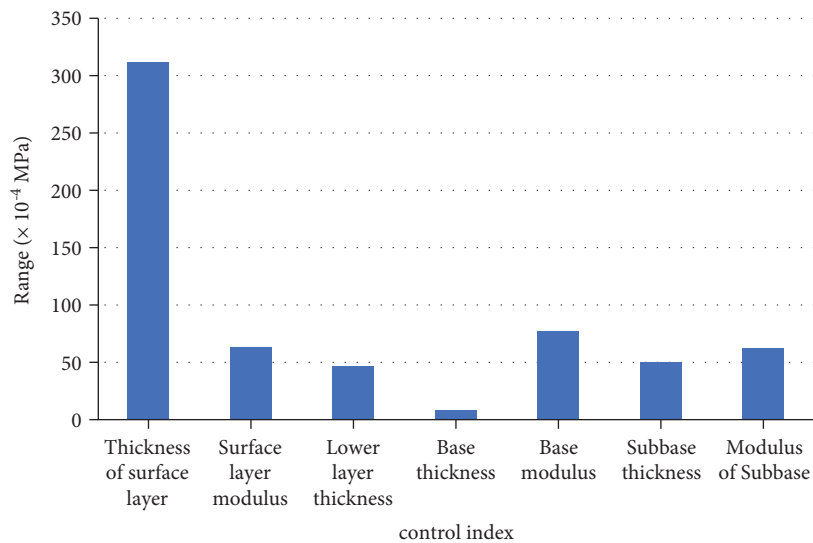
FIGURE 2: Continued.



(b)



(c)



(d)

FIGURE 2: Range diagram of working condition I. (a) Tensile stress at the bottom of inorganic binder base course. (b) Tensile stress of inorganic binder subbase. (c) Permanent deformation of asphalt concrete surface layer. (d) Permanent deformation of the lower layer of asphalt concrete layer.

is not considered in this study. The modulus of other layers is selected in accordance with the Chinese standard “Specifications for Design of Highway Asphalt Pavement.”

As shown in Figure 2(a), the thickness of the lower layer and the modulus of the base layer have a significant effect on the bottom layer tensile stress of the inorganic binder stabilizing layer, followed by the thickness of the base layer. As shown in Figure 2(b), the modulus of the base layer and the modulus of the subbase layer have a greater influence on the bottom layer tensile stress of the inorganic binder stabilizing subbase layer, followed by the thickness of the base layer. As shown in Figure 2(c), the thickness of the surface layer has a significant effect on the permanent deformation of the asphalt concrete surface layer. As shown in Figure 2(d), the thickness of the surface layer has a significant effect on the permanent deformation of the underlying layer of asphalt concrete.

Figure 3(a) shows that, with the increase of the thickness of the underlying layer, the thickness of the base layer, and the modulus of the base layer, the bottom layer tensile stress of the inorganic binder stabilizing base layer decreases. The increase in the thickness of the underlying layer from 5 cm to 7 cm has a more significant effect on the bottom layer tensile stress of the inorganic binder stabilizing base layer than the increase in the thickness of the underlying layer from 7 cm to 9 cm. When the thickness of the base layer increases from 30 cm to 36 cm, the bottom layer tensile stress of the inorganic binder stabilizing base layer decreases slowly, and when the thickness of the base layer increases from 36 cm to 40 cm, the bottom layer tensile stress of the inorganic binder stabilizing base layer decreases relatively quickly. The modulus of the base layer has a more uniform effect on the bottom layer tensile stress of the inorganic binder stabilizing the base layer. As shown in Figure 3(b), as the modulus of the base layer increases, the bottom layer tensile stress of the inorganic binder stabilizing subbase layer first decreases and then increases. As the modulus of the base layer and the thickness of the base layer increase, the bottom layer tensile stress of the inorganic binder stabilizing subbase layer decreases accordingly. When the modulus of the base layer increases from 9000 to 11,500 MPa, the decrease in the bottom layer tensile stress of the inorganic binder stabilizing base layer is smaller than the increase in the bottom layer tensile stress of the inorganic binder stabilizing subbase layer when the modulus of the base layer increases from 9000 to 14,000 MPa. The modulus of the subbase layer increased from 7000 MPa to 8500 MPa, and the bottom layer tensile stress of the stabilizing subbase layer changed slowly. The thickness of the base layer has a more uniform effect on the bottom layer tensile stress of the inorganic binder stabilizing subbase layer. Figure 3(c) shows that, as the thickness of the surface layer increases, the permanent deformation of the surface layer of the asphalt concrete layer first decreases and then increases. Figure 3(d) shows that, as the thickness of the surface layer increases, the permanent deformation of the underlying layer of the asphalt concrete layer decreases uniformly.

In conclusion, combined with economic efficiency, the recommended pavement structure is as follows: surface layer

thickness 4 cm + underlying layer thickness 7 cm + base layer thickness 36 cm + subbase layer thickness 15 cm. For the modulus of the base layer, the value should be medium to high, and for the modulus of the subbase layer, the value should be as high as possible, and for the modulus of the surface layer, the value should be as high as possible. The modulus of the surface layer can be flexibly selected according to the actual situation of the project. The range diagram of condition 2 is shown in Figure 4.

As shown in Figure 4(a), the thickness of the base course has the greatest influence on the bottom tensile stress of the inorganic binder layer, the thickness of the lower layer and the modulus of the base course also have a significant influence on the bottom tensile stress of inorganic binder layer, and the other four control indexes have little influence on the bottom tensile stress of inorganic binder layer. As shown in Figure 4(b), there is little difference in the influence level of the three control indexes on the permanent deformation of the surface layer of the asphalt mixture layer. As shown in Figure 4(c), among the seven control indexes, the influence of surface layer thickness, lower layer thickness, and base modulus on the permanent deformation of the lower layer of asphalt mixture is more obvious.

It can be seen from Figure 5(a) that, with the increase of the thickness of the base course and the thickness of the lower layer, the tensile stress at the bottom of the inorganic binder stable layer decreases, but the influence of the thickness of the base course on the decreasing trend of the tensile stress at the bottom of the inorganic binder stable layer is more uniform, while the influence of the thickness of the lower layer on the decreasing trend of the tensile stress at the bottom of the inorganic binder stable layer is not uniform, when the thickness of the lower layer increases from 5 cm to 7 cm, the reduction rate of the tensile stress at the bottom of the stabilized layer of the inorganic binder is 1.843 times that when the thickness of the lower layer increases from 7 cm to 9 cm. The effect of increasing the thickness of the lower layer on the tensile stress at the bottom of the stabilized layer of the inorganic binder is higher than that when the thickness of the lower layer is 7–9 cm. With the increase of the base modulus, the tensile stress at the bottom of the inorganic binder stable layer increases and the influence of the base modulus on the decreasing trend of the tensile stress at the bottom of the inorganic binder stable layer is uniform. It can be seen from Figure 5(b) that, with the increase of surface layer thickness, surface layer modulus, and subbase modulus, the permanent deformation of asphalt mixture surface layer first decreases and then increases, while with the increase of lower layer thickness, base layer thickness, base layer modulus, and subbase thickness, it first increases and then decreases. Among them, the influence trend of the increase of the thickness of the lower layer and the modulus of the base layer on the permanent deformation of the surface layer of the asphalt mixture layer is more similar, both of which are in the first half of the influence degree which is greater, and the latter half has little influence. The influence trend of the increase of the

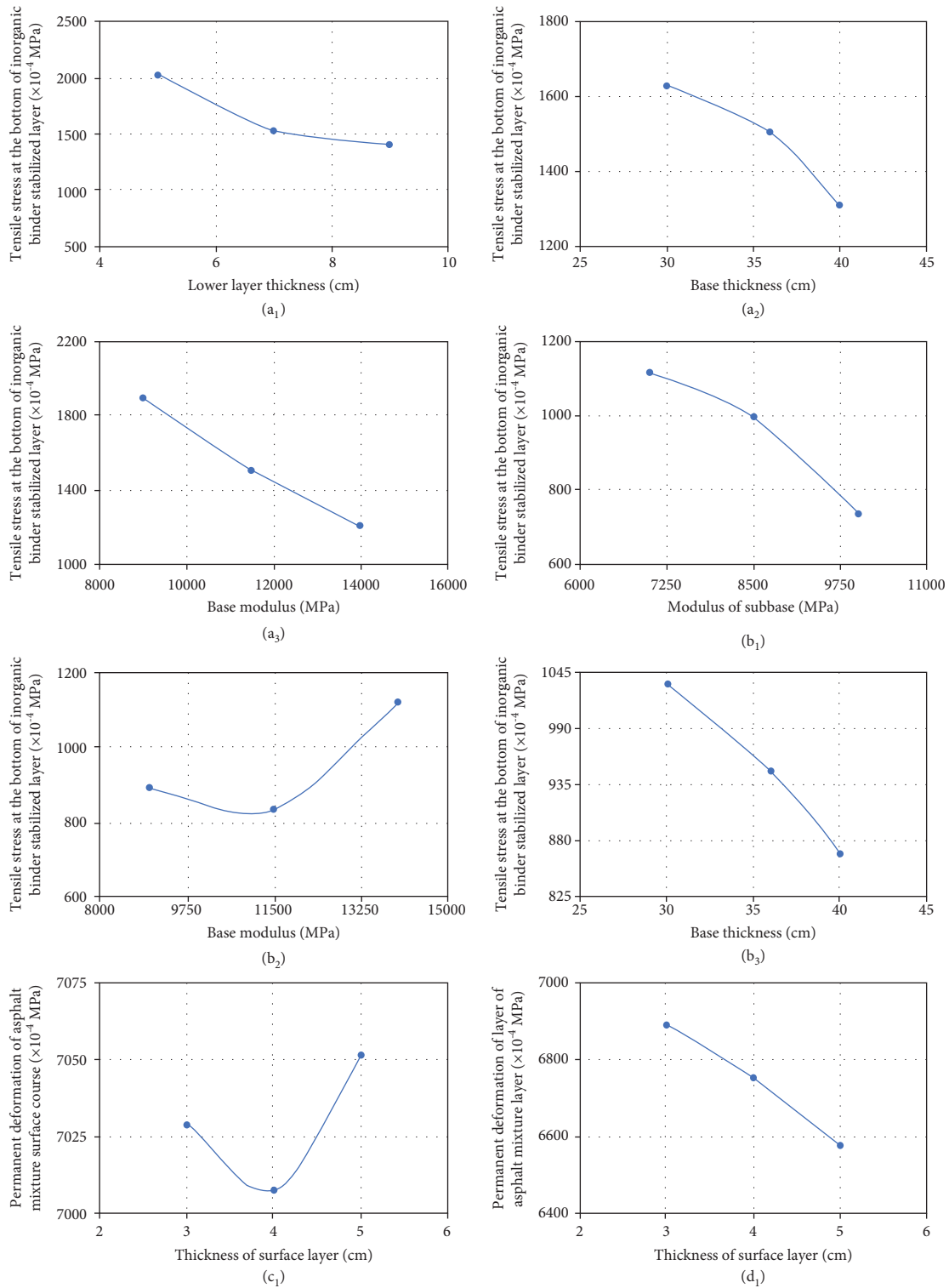
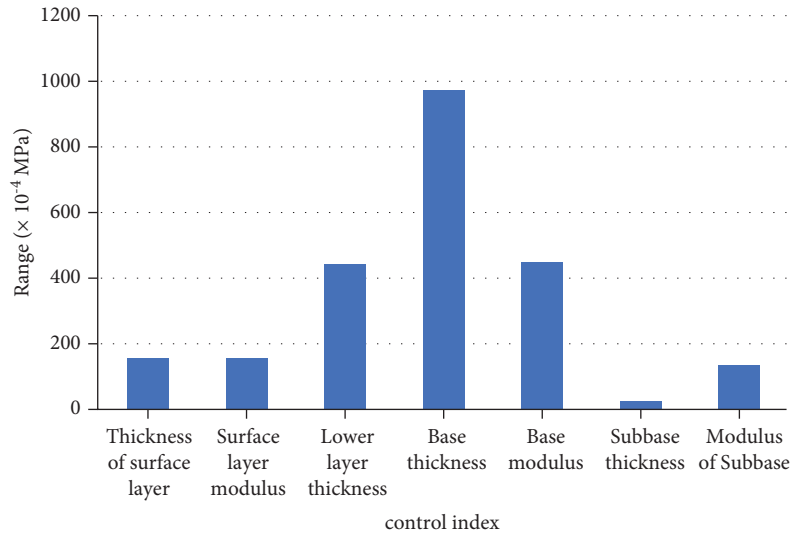


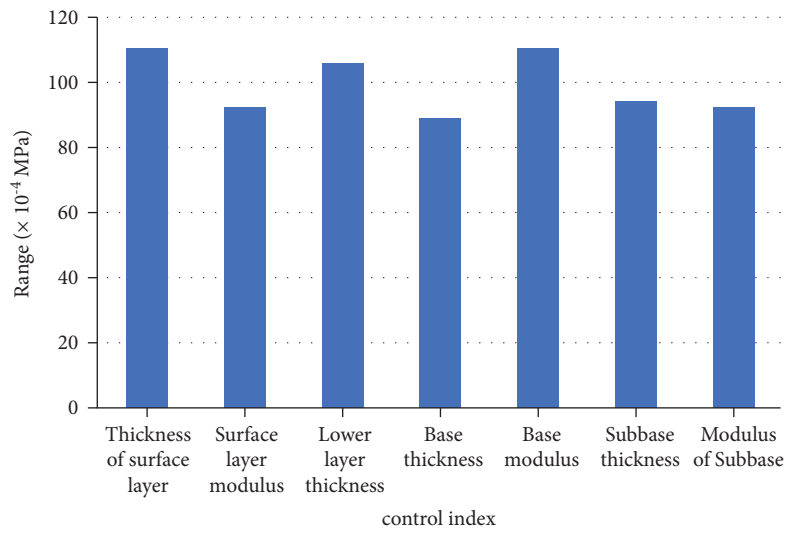
FIGURE 3: Trend chart of working condition I.

thickness of the base layer and subbase layer on the permanent deformation of the surface layer of the asphalt mixture layer is more similar, both of which are in the first half of the influence degree which has little influence, and the latter half is greater. It can be seen from Figure 5(c) that, with the increase of the surface layer thickness in the

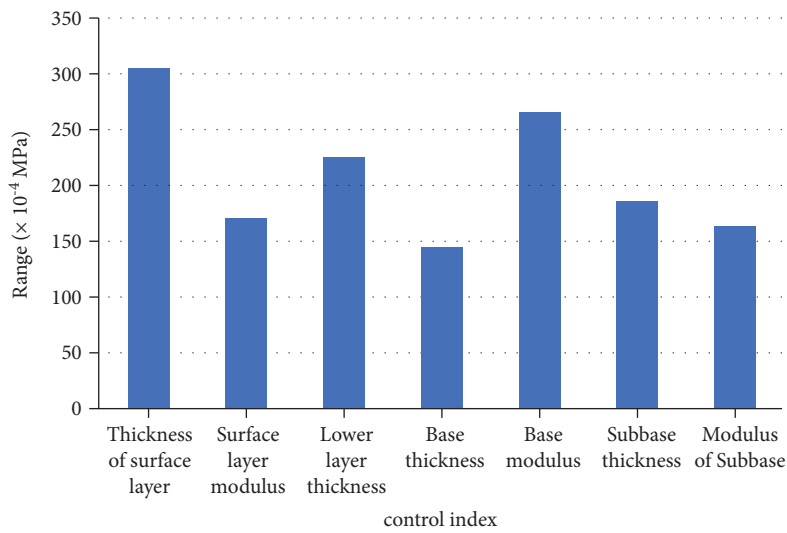
pavement structure, the permanent deformation of the surface layer of the asphalt mixture layer gradually decreases, and, when the surface layer thickness increases from 3 m to 4 m, the reduction rate of permanent deformation of asphalt mixture surface layer is 130.29 times that when the surface layer thickness increases from 4 cm



(a)

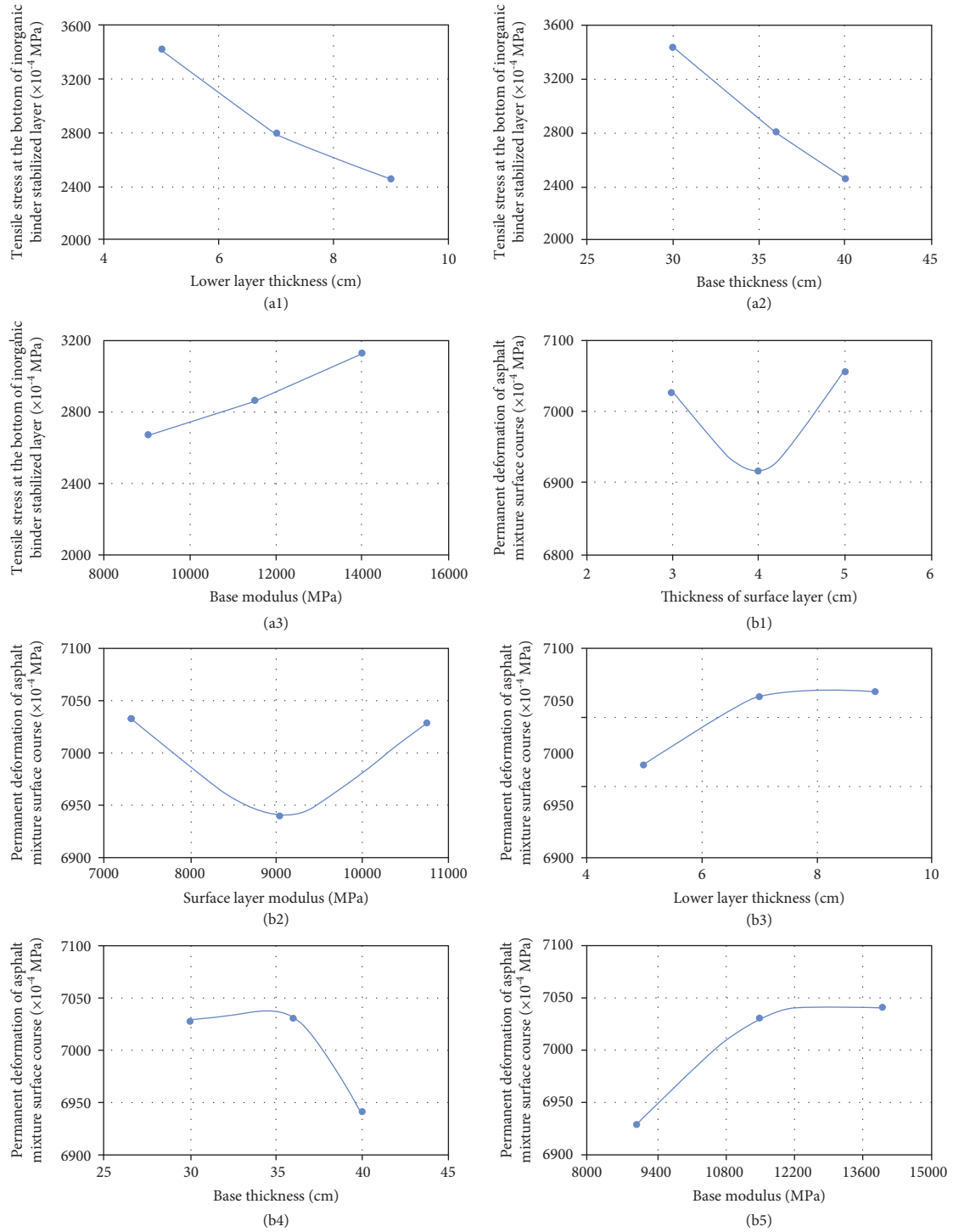


(b)



(c)

FIGURE 4: Range diagram of working condition II. (a) Bottom layer tensile stress of inorganic binder stabilizing layer. (b) Permanent deformation of asphalt concrete surface layer. (c) Permanent deformation of the lower layer of asphalt concrete layer.



(a)
FIGURE 5: Continued.

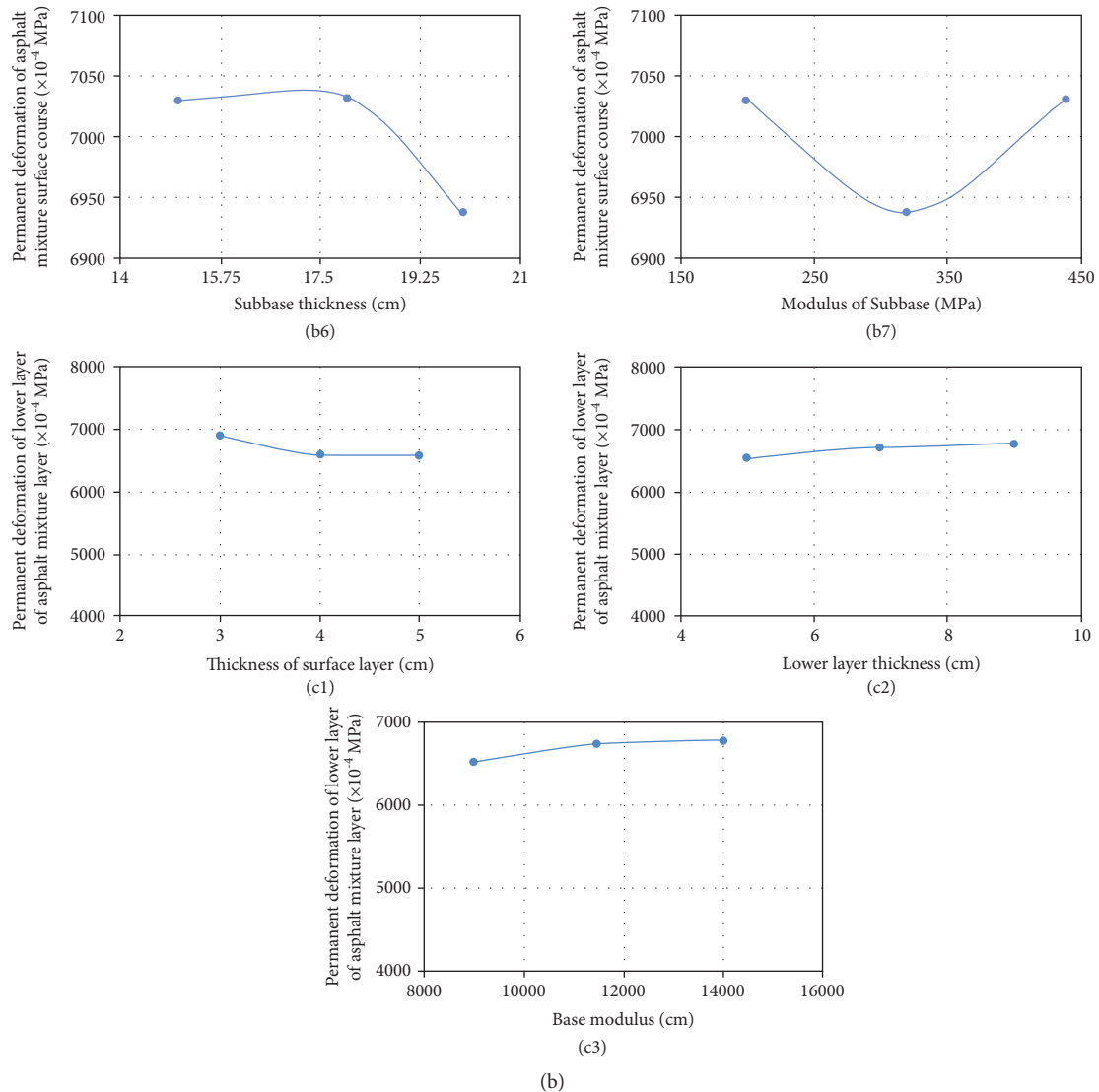


FIGURE 5: Trend chart of working condition II.

to 5 cm (the permanent deformation of asphalt mixture surface layer basically does not change when the surface layer thickness increases from 4 cm to 5 cm). The permanent deformation of the surface layer of the asphalt mixture layer increases gradually, and it increases rapidly in the first half and hardly changes in the second half. When the thickness of the lower layer increases from 5 m to 7 m, the increase rate of permanent deformation of the asphalt mixture surface layer is 3.35 times that of the surface layer from 7 cm to 9 cm. When the base modulus increases from 9000 MPa to 11,500 MPa, the increase rate of permanent deformation of the asphalt mixture surface layer is 5.77 times that when the base modulus increases from 11,500 MPa to 14,000 MPa. In conclusion, combined with economy, the recommended pavement structure is as

follows: the thickness of the surface layer is 4 cm + the thickness of the lower layer is 5 cm + the thickness of the base layer is 40 cm + the thickness of the subbase layer is 20 cm, the modulus of the base layer should be low, and the modulus of subbase layer and surface layer can be flexibly selected according to the actual situation of the project.

After analyzing Figures 2 to 4, we see that, under different working conditions, the degree of influence of the seven control indicators on the corresponding design index is shown in Table 5.

After integrating the mechanical response analysis results and economic aspects, the recommended pavement structure under the two working conditions is shown in Table 6.

TABLE 5: The influence degree of control indicators.

Working condition	Design index	Thickness of surface layer	Surface layer modulus	Lower layer thickness	Base thickness	Base modulus	Subbase thickness	Modulus of subbase
Working condition I	Tensile stress at the bottom of inorganic binder stabilized layer	The basic level Subbase		✓		✓		✓✓
	Permanent deformation of asphalt mixture layer	Surface layer Lower layer	✓			✓		
Working condition II	Tensile stress at the bottom of inorganic binder stabilized layer	—		✓	✓✓	✓		
	Permanent deformation of asphalt concrete layer	Surface layer Lower layer	✓	✓	✓	✓	✓	✓

TABLE 6: Recommended pavement structure.

Working condition	Thickness of surface layer (cm)	Surface layer modulus (MPa)	Lower layer thickness (cm)	Base thickness (cm)	Base modulus (MPa)	Subbase thickness (cm)	Modulus of subbase (MPa)
Working condition I	4	Flexible	7	36	Medium high value	15	High value
Working condition II	4	Flexible	5	40	Low value	20	Flexible

4. Conclusions

By changing different layer thickness and modulus, we can study the influence of the nanomodified asphalt pavement structure on pavement mechanics response and then propose the recommended pavement structure combination form of the nanomodified asphalt.

The bottom layer tensile stress of the inorganic binder stabilizing subbase layer is greatly affected by the thickness of the underlying layer and the modulus of the base layer, followed by the thickness of the base layer. The bottom layer tensile stress of the inorganic binder stabilizing subbase layer is more greatly affected by the modulus of the base layer and the modulus of the subbase layer, followed by the thickness of the base layer. The thickness of the surface layer has a significant effect on the permanent deformation of the asphalt concrete surface layer, and with the increase of the thickness, the permanent deformation first decreases and then increases. The thickness of the surface layer has a significant effect on the permanent deformation of the underlying layer of asphalt concrete, and as the thickness of the surface layer increases, the permanent deformation decreases uniformly.

Considering the economic aspect, the recommended pavement structure for working condition I is as follows: the thickness of the surface layer 4 cm + the thickness of the underlying layer 7 cm + the thickness of the base layer 36 cm + the thickness of the subbase layer 15 cm. For the modulus of the base layer, the value should be medium to

high, for the modulus of the subbase layer, the value should be as high as possible, and the modulus of the surface layer can be flexibly selected according to the actual situation of the project. The recommended pavement structure for working condition II is as follows: the thickness of the surface layer 4 cm + the thickness of the underlying layer 5 cm + the thickness of the base layer 40 cm + the thickness of the subbase layer 20 cm. For the modulus of the base layer, the value should be low, and for the modulus of the subbase layer and surface layer, it can be flexibly selected according to the actual situation of the project.

Data Availability

The data used to support the findings of this study are included within the article.

Conflicts of Interest

The authors declare that they have no conflicts of interest.

Acknowledgments

This study was sponsored in part by the Highway Construction Science and Technology Projects of Shandong Hi-Speed Co., Ltd. (Grant no. QLTD-2019-A-FW-0036), to which the authors are very grateful.

References

- [1] J. Ren, B. Xue, and L. Zhang, "Characterization and prediction of rutting resistance of rock asphalt mixture under the coupling effect of water and high-temperature," *Construction and Building Materials*, vol. 254, Article ID 119316, 2020.
- [2] Y. Jiang, Y. Yi, J. Fan, T. Tian, and C. Deng, "Laboratory investigation on the heat dissipation regularity and road performance of different pavement structure combinations by double-layer paving," *Construction and Building Materials*, vol. 284, Article ID 122785, 2021.
- [3] C. Deng, Y. Jiang, K. Yuan, T. Tian, and Y. Yi, "Mechanical properties of vertical vibration compacted lime-fly ash-stabilized macadam material," *Construction and Building Materials*, vol. 251, Article ID 119089, 2020.
- [4] Y. Jiang, K. Yuan, C. Deng, and T. Tian, "Fatigue performance of cement-stabilized crushed gravel produced using vertical vibration compaction method," *Journal of Materials in Civil Engineering*, vol. 32, no. 11, Article ID 04020318, 2020.
- [5] J. Ren, D. Li, and S. Wang, "Combined effect of compaction methods and loading conditions on the deformation behaviour of unbound granular material," *Advances in Civil Engineering*, vol. 2020, Article ID 2419102, 16 pages, 2020.
- [6] P. Caputo, M. Porto, R. Angelico, V. Loise, P. Calandra, and C. O. Rossi, "Bitumen and asphalt concrete modified by nanometer-sized particles: basic concepts, the state of the art and future perspectives of the nanoscale approach-science direct," *Advances in Colloid and Interface Science*, vol. 285, no. 275, Article ID 102283, 2020.
- [7] R. Li, F. Xiao, S. Amirkhanian, Z. You, and J. Huang, "Developments of nano materials and technologies on asphalt materials – a review," *Construction and Building Materials*, vol. 143, pp. 633–648, 2017.
- [8] L. Sun, X. Xin, and J. Ren, "Asphalt modification using nanomaterials and polymers composite considering high and low temperature performance," *Construction and Building Materials*, vol. 133, pp. 358–366, 2017.
- [9] Y. Ma, L. Li, H. Wang, W. Wang, and K. Zheng, "Laboratory study on performance evaluation and automobile exhaust degradation of nano-tio₂ particles-modified asphalt materials," *Advances in Materials Science and Engineering*, vol. 2021, no. 9, 13 pages, Article ID 5574013, 2021.
- [10] J. Hu and X. Yu, "Performance evaluation of solar-responsive asphalt mixture with thermochromic materials and nano-tio₂ scatterers," *Construction and Building Materials*, vol. 247, Article ID 118605, 2020.
- [11] C. Hu, J. Ma, H. Jiang, Z. Chen, and J. Zhao, "Evaluation of nano-TiO₂ modified waterborne epoxy resin as fog seal and exhaust degradation material in asphalt pavement," *Journal of Testing and Evaluation*, vol. 45, no. 1, Article ID 20160157, 2017.
- [12] R. Li, J. Pei, and C. Sun, "Effect of nano-zno with modified surface on properties of bitumen," *Construction and Building Materials*, vol. 98, no. 15, pp. 656–661, 2015.
- [13] S. Karahancer, "Effect of aluminum oxide nano particle on modified bitumen and hot mix asphalt," *Petroleum Science and Technology*, vol. 2020, Article ID 1783292, 12 pages, 2020.
- [14] A. Sarkar and F. Hojjati, "The effect of nano-silica material and alkali resistant glass fiber on the OGFC asphalt mixture," *International Journal of Pavement Engineering*, vol. 22, no. 29, pp. 1–13.
- [15] C. Li, S. Wu, Z. Chen, G. Tao, and Y. Xiao, "Improved microwave heating and healing properties of bitumen by using nanometer microwave-absorbers," *Construction and Building Materials*, vol. 189, no. 20, pp. 757–767, 2018.
- [16] K. Patchai Murugan, M. Balaji, S. Swaroopa Kar, S. Swarnalatha, and G. Sekaran, "Nano fibrous carbon produced from chromium bearing tannery solid waste as the bitumen modifier," *Journal of Environmental Management*, vol. 270, Article ID 110882, 2020.
- [17] S. N. A. Jeffry, R. Putra Jaya, N. Abdul Hassan, H. Yaacob, M. Z. H. Mahmud, and Z. H. Al-Saffar, "The influence of nano-carbon from coconut shell ash as modifier on the properties of bitumen," *Road Materials and Pavement Design*, vol. 2020, no. 4, 17 pages, Article ID 1809502, 2020.
- [18] A. Akbari and A. Modarres, "Fatigue response of hma containing modified bitumen with nano-clay and nano-alumina and its relationship with surface free energy parameters," *Road Materials and Pavement Design*, vol. 2018, Article ID 1553733, 24 pages, 2018.
- [19] A. A. Hussein, R. P. Jaya, H. Yaacob, N. A. Hassan, and M. Hasan, "Physical, chemical and morphology characterization of nano ceramic powder as bitumen modification," *International Journal of Pavement Engineering*, vol. 2, pp. 1–14, 2019.
- [20] X. Shi, L. Cai, W. Xu, J. Fan, and X. Wang, "Effects of nano-silica and rock asphalt on rheological properties of modified bitumen," *Construction and Building Materials*, vol. 161, no. 10, pp. 705–714, 2018.
- [21] J. Ren, S. Wang, and G. Zang, "Effects of recycled aggregate composition on the mechanical characteristics and material design of cement stabilized cold recycling mixtures," *Construction and Building Materials*, vol. 244, no. 3, Article ID 118329, 2020.
- [22] X. Wang, J. Ren, X. Gu, N. Li, Z. Tian, and H. Chen, "Investigation of the adhesive and cohesive properties of asphalt, mastic, and mortar in porous asphalt mixtures [J]," *Construction and Building Materials*, vol. 276, Article ID 122255, 2021.
- [23] J. Jiang, Y. Li, Y. Zhang, and H. U. Bahia, "Distribution of mortar film thickness and its relationship to mixture cracking resistance," *International Journal of Pavement Engineering*, vol. 2020, Article ID 1774767, 2020.
- [24] C. Wang, S. Wang, Z. Gao, and Z. Song, "Effect evaluation of road piezoelectric micro-energy collection-storage system based on laboratory and on-site tests," *Applied Energy*, vol. 287, Article ID 116581, 2021.
- [25] X. Ji, B. Han, H. Hu, S. Li, Y. Xiong, and E. Sun, "Application of the discrete element method and CT scanning to investigate the compaction characteristics of the soil-rock mixture in the subgrade," *Road Materials and Pavement Design*, vol. 2020, Article ID 1826350, 2020.
- [26] J. Ren and C. Yin, "Investigating mechanical characteristics of aggregate structure for road materials," *International Journal of Pavement Engineering*, vol. 2020, Article ID 1748189, 2020.
- [27] J. Huang, J. Zhang, J. Ren, and H. Chen, "Anti-rutting performance of the damping asphalt mixtures (DAMs) made with a high content of asphalt rubber (AR)," *Construction and Building Materials*, vol. 271, Article ID 121878, 2021.
- [28] J. Huang, Y. Sun, and J. Zhang, "Reduction of computational error by optimizing SVR kernel coefficients to simulate concrete compressive strength through the use of a human learning optimization algorithm," *Engineering with Computers*, 2021.
- [29] X. Wang, J. Ren, X. Hu, X. Gu, and N. Li, "Determining optimum number of gyrations for porous asphalt mixtures

using superpave gyratory compactor,” *KSCE Journal of Civil Engineering*, vol. 25, pp. 2010–2019, 2021.

- [30] J. Huang, G. Shiva Kumar, J. Ren, Y. Sun, Y. Li, and C. Wang, “Towards the potential usage of eggshell powder as bio-modifier for asphalt binder and mixture: workability and mechanical properties,” *International Journal of Pavement Engineering*, vol. 2021, Article ID 1905809, 13 pages, 2021.
- [31] J. Huang, G. S. Kumar, and Y. Sun, “Evaluation of workability and mechanical properties of asphalt binder and mixture modified with waste toner,” *Construction and Building Materials*, vol. 276, Article ID 122230, 2021.

Research Article

Environment Effect on the Rutting Resistance of Nano-SiO₂-Modified Asphalt Concrete: Temperature and Water

Luchuan Chen,¹ Wenjun Gu² ,² and Xuanyu Zhang³

¹Shandong Hi-Speed Group, Jinan, Shandong 250098, China

²Washington Institute for Advanced Study, 7835 Muirfield Court, Potomac, MD 20854, USA

³Shandong Hi-Speed Infrastructure Construction Co., Ltd., Jinan, Shandong 250098, China

Correspondence should be addressed to Wenjun Gu; gu_wenjun@hotmail.com

Received 6 May 2021; Revised 5 July 2021; Accepted 2 August 2021; Published 12 August 2021

Academic Editor: Jiaolong Ren

Copyright © 2021 Luchuan Chen et al. This is an open access article distributed under the Creative Commons Attribution License, which permits unrestricted use, distribution, and reproduction in any medium, provided the original work is properly cited.

Nanoparticles have been widely adopted to improve the high-temperature performance of asphalt binder. However, the influence of moisture on high-temperature performance is not clear. Hence, the water absorption performance of the nano-SiO₂-modified asphalt concrete is investigated. Based on this, to further analyze the pavement performance of the nano-SiO₂-modified asphalt concrete, the coupled effects of high-temperature, moisture content, and nanoparticles content on the rutting resistance of the nano-SiO₂-modified asphalt concrete are tested and revealed in this study. Results show that temperature has the most significant influence on the water absorption performance of the nano-SiO₂-modified asphalt concrete. The rutting resistance of the nano-SiO₂-modified asphalt concrete decreases as temperature and moisture content increase, especially for the temperature. The dynamic stability at the same temperature condition decreases approximately linearly as moisture content increases. The effect of the nano-SiO₂ content is the most nonobvious.

1. Introduction

Since the reform and opening-up, China's highway transportation construction has been changing rapidly and has developed quickly [1, 2], but rutting has always been one of the most important diseases of China's highway asphalt pavement [3, 4]. Rutting will greatly affect driving safety and road aesthetics and have a significant negative impact on highway operations [5]. How to improve the rutting resistance of asphalt pavement is a hot topic in recent years, and enhancing the high-temperature stability of asphalt is one of the effective ways [6–8]. In recent years, nanomaterials have been widely used to improve the performance of asphalt binder because of its large specific surface area, high surface free energy, and good dispersion ability [9–12]. Hasaninia and Haddadi investigated the rutting and fatigue damage of asphalt caused by nano-SiO₂ and found the correlation between modified binder and the engineering performance of asphalt mixture [13]. Wu et al. explored the temperature sensitivity of nanoparticles to cement mortar, the influence

of nano-SiO₂ on the strength of cement asphalt mortar, and the performance of nano-SiO₂ cement asphalt mortar at different temperatures [14]. Rezaei et al. modified asphalt with nano-SiO₂ and SBS polymer and analyzed its high-temperature performance [15]. Chen and Li have carried out engineering index tests on nano-SiO₂ emulsified asphalt. It reveals that the addition of nano-SiO₂ has the effect of improving stability, permeability, and softening point [16]. Shafabakhsh and Jafari Ani found that the addition of nano-TiO₂ and nano-SiO₂ improved the rheological properties of asphalt, increasing the toughness and viscosity by 30% and 109% on average while reducing the permeability grade. In addition, the rutting resistance and fatigue life of the asphalt are improved [17]. Saltan et al. measured the rutting and fatigue properties of modified nanometer asphalt materials [18]. Chen et al. studied the effect of SiO₂ phase change composite on the internal temperature of porous asphalt concrete [19]. Shafabakhsh et al. explored the effects of nano-SiO₂ on low-temperature cracks in asphalt mixtures, using a semicircular bending test (SCB) under the loading of I/II

mixture [20]. Qian et al. showed that the anti-UV aging property of asphalt is improved obviously due to the blocking function of nano-SiO₂ and carbon black in rubber powder, and the enhancing effect of nano-SiO₂ is found to be the most significant [21]. Yang et al. investigated the effects of nano-SiO₂ content on the Engler viscosity and storage stability of asphalt emulsion as well as the performances of asphalt emulsion residue [22]. Du et al. proposed that Al₂O₃ and SiO₂ chemical components played a leading role in improving the bearing capacity and rutting performance of porous asphalt pavement [23]. Moeini et al. investigated the modification effect of two morphologically different nano-SiO₂ materials: (i) a synthesised fibrous with porous structure and (ii) a commercial spherical with nonporous structure, on asphalt binder [24]. Leiva-Villacorta and Vargas-Nordbeck carried out the dynamic shear rheological test, asphalt fatigue test, rutting test, and adhesion work analysis to explore the influence of nano-SiO₂ [25]. Wan et al. explored that ceramic fiber has a great strengthening effect on asphalt, which makes the asphalt harder and can only withstand a small strain under the same stress. The thermal insulation effect of ceramic fiber will improve temperature stability. The results of complex modulus and phase Angle show that ceramic fiber can significantly improve the high-temperature resistance of soft binder [26].

Temperature is one of the main causes of rutting on asphalt pavement [27–29]. In high-temperature areas in China, the highest temperature of asphalt pavement can be higher than 60°C. When vehicles are driving, the road is prone to rutting [11, 12, 30]. At the same time, it is usually accompanied by continuous rainfall in some high-temperature areas (such as China's southeast coastal areas and southern China), such as the "meiyu period" in China. Due to the monsoon, there will be 30–40 days of high temperature in summer (such as in Zhejiang Province and Guangdong Province), and along with continuous light to moderate rain, it is easy to make the road surface buckle under conditions of water-high temperature, and the degradation of road performance will be the result of the combined effect of water and high temperature. When water enters the asphalt pavement from cracks or other ways, it will reduce asphalt's aggregate adhesion, resulting in loosening, peeling, potholes, and other diseases of the pavement. Under the combined effect of water and high temperature, the damage to asphalt is more serious than that of water or high temperature alone.

In order to solve the above problems, this study studied the influence of water and high-temperature coupling on the rutting resistance of nano-SiO₂-modified asphalt concrete through a wheel tracking test. The laboratory tests of 48 groups with different water conditions, temperatures, and nano-SiO₂-modified asphalt concrete were designed.

2. Materials and Methods

2.1. Materials. The aggregate is limestone, and the asphalt is grade Zhonghai 70# asphalt. All technical indexes of all kinds of aggregates and asphalt meet the relevant requirements of China's aggregate technical regulations.

2.1.1. Aggregates. The technical indexes of coarse aggregates, fine aggregates, and mineral powders are shown in Tables 1–3.

2.1.2. Asphalt Mixture Composition. The aggregate gradation is given in Table 4.

2.1.3. Base Asphalt Binder. The Zhonghai 70# base asphalt binder is used in this study, of which the technical indexes are displayed in Table 5.

2.2. Methods. The test process is shown in Figure 1.

2.2.1. The Specimen Preparation. Size of specimen: 300×150×150 (mm). The test temperature is 60°C. The wheel pressure is 0.7 MPa.

(1) Add the aggregate to the mixer and stir for 90 s; then, add asphalt and stir for 90 s at 177°C. (2) The well-mixed aggregate and asphalt mixture are added to the mill. First, the asphalt mixture is preliminarily compacted, mainly from the surrounding to the middle of the mill. The compacted samples are higher in the middle than around. (3) The prepared samples were rolled on a roller, first rolled twice in one direction and then rolled 24 times after rotating 90°. (4) The prepared samples were placed at room temperature and pressure for 48 h. The operation of the rutting test was carried out after 48 hours.

2.2.2. Test Process.

- (1) The specimen shall be placed together with the test mold in a constant temperature chamber up to 60°C and 1°C for not less than 5 hours or 24 hours. On the part where the test wheel does not walk, paste a thermoelectric corner thermometer and control the temperature of the specimen to be stable at $60 \pm 0.5^\circ\text{C}$.
- (2) The specimen together with the test model was placed on the test bench of the wheel point tester. The test wheel was in the central part of the specimen, and its walking direction should be consistent with the rolling or driving direction of the specimen. Start the rut deformation automatic recorder, and then start the test machine, so that the test wheel moves back and forth to walk for about 1 h or the maximum deformation reaches 25 mm. During the test, the recorder automatically records the deformation curve and specimen temperature.

The rutting test was carried out in accordance with the specification (JTGE20-2011, 2011). Fine-grain gradation AC-13 was selected in this study. Synthetic gradation of mineral aggregate is shown in Table 6. The optimum oil-aggregate ratios of nanomodified asphalt concrete with 1%, 2%, and 3% nano-SiO₂ particles are 5.0%, 5.0%, and 5.1%, respectively.

TABLE 1: Technical indexes of coarse aggregates.

Crushed stone value (%)	Los Angeles abrasion value (%)	Ruggedness (%)	Flat-elongated particles content (%)	<0.075 mm particle content (%)	Water absorption (%)
15.2	17.1	7.3	5.9	0.4	0.76

TABLE 2: Technical indexes of fine aggregates.

Silt content (%)	Angularity (s)	Ruggedness (%)	Hydrophilic coefficient
1	69	5.8	0.58

TABLE 3: Technical indexes of mineral powders.

Water content (%)	Hydrophilic coefficient	Plasticity index (%)	Heating stability	Particle size (%)		
				<0.6 mm	<0.15 mm	<0.075 mm
0.68	0.58	2.6	Unchanged	100	93.7	100

TABLE 4: Aggregate gradation.

Passing size (mm)	Mass ratio (%)
19	100
16	93.5
13.2	79.8
9.5	63.8
4.75	45.8
2.36	33.1
1.18	22.6
0.6	15.4
0.3	9.8
0.15	8.1
0.075	6.9

TABLE 5: Technical indexes of base asphalt binder.

25°C penetration (0.1 mm)	Softening point (°C)	10°C ductility (cm)	15°C ductility (cm)	60°C viscosity (Pa-s)
67.0	48.6	27.6	>100	216

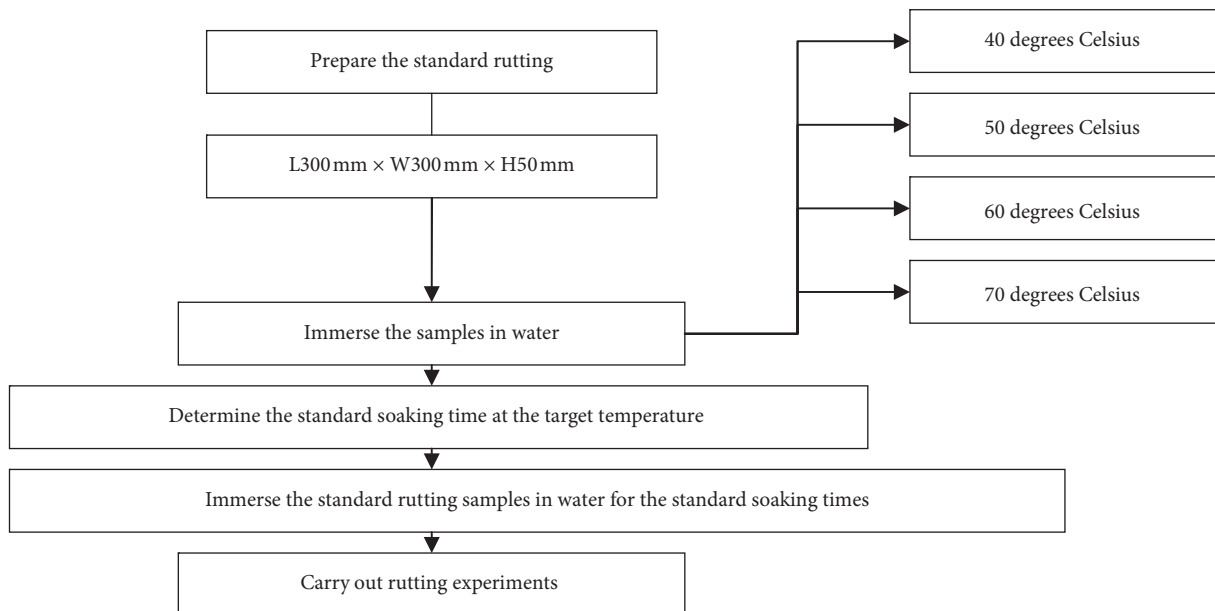


FIGURE 1: Flowchart of asphalt concrete immersion test under high temperature.

TABLE 6: Synthetic grading of mineral aggregate.

Grading type	Pass rate (%)										
	19	16	13.2	9.5	4.75	2.36	1.18	0.6	0.3	0.15	0.075
AC-13	100	100	91.7	72.3	49.0	34.8	23.6	16.0	10.0	8.2	6.9

TABLE 7: Saturated water ratios in the case of using different temperatures and content of nano-SiO₂.

Soaking time	Saturated water ratio (%)											
	40°C			50°C			60°C			70°C		
	3%	3.5%	4%	3%	3.5%	4%	3%	3.5%	4%	3%	3.5%	4%
10 min	26.61	26.67	26.59	18.68	18.60	18.71	15.33	15.32	15.36	11.87	11.89	11.89
20 min	38.26	38.33	38.40	29.16	29.07	29.09	24.29	24.32	24.37	19.66	19.58	19.51
0.5 h	48.31	48.33	48.34	37.15	37.21	37.16	31.51	31.53	31.61	26.45	26.57	26.55
1.5 h	63.37	63.33	63.21	48.80	48.84	48.91	40.53	40.54	40.44	33.61	33.57	33.66
3.5 h	73.29	73.33	73.55	55.77	55.81	55.71	46.69	46.85	46.60	39.09	39.16	39.18
5.5 h	80.09	80.00	80.16	61.36	61.63	61.67	51.69	51.35	51.70	44.99	44.76	44.71
9.5 h	86.69	86.67	86.91	69.62	69.77	69.83	60.01	60.36	60.37	53.01	53.15	53.09
15.5 h	89.99	90.00	90.11	79.99	79.87	79.66	72.88	72.97	73.07	67.18	67.13	67.27
22.5 h	93.19	93.33	93.38	89.61	89.53	89.21	87.41	87.39	87.16	79.72	79.81	79.89
30.5 h	96.77	96.67	96.46	95.53	95.35	95.61	94.50	94.59	94.61	92.91	93.01	93.11
44.5 h	98.61	98.33	98.18	97.72	97.67	97.99	97.39	97.30	97.46	95.70	95.80	95.91
60.5 h	100.0	100.0	100.0	98.83	98.84	98.89	99.00	99.10	99.33	97.90	97.90	97.88
72.5 h	100.0	100.0	100.0	100.0	100.0	100.0	100.0	100.0	100.0	100.0	100.0	100.0
84.5 h	100.0	100.0	100.0	100.0	100.0	100.0	100.0	100.0	100.0	100.0	100.0	100.0
96.5 h	100.0	100.0	100.0	100.0	100.0	100.0	100.0	100.0	100.0	100.0	100.0	100.0

3. Water Absorption Characteristics of Nanomodified Asphalt Concrete under High-Temperature Conditions

The nanomodified asphalt concrete and matrix asphalt concrete with different content of nano-SiO₂ particles were tested at 40°C, 50°C, 60°C, and 70°C for the corresponding moisture content of the specimens under water immersion conditions. Each group of experiments is carried out in four parallel experiments.

The experimental temperature of the rutting test in the Chinese test specification is 60°C. To further investigate the effect of temperature on the rutting resistance of the nano-SiO₂-modified asphalt concrete, a wide range of the experimental temperature is selected in this study.

The relationship between nanomodified asphalt concrete and immersion time at different temperatures is shown in Table 7.

The change law of the nanomodified asphalt concrete with water immersion time at different temperatures is shown in Figure 2.

As shown in Figure 2 and Table 7, under the same temperature and immersion time, the difference in moisture content between nanomodified asphalt concrete and matrix asphalt concrete does not exceed 1%. Therefore, the influence of nanomodifiers on the water absorption characteristics of asphalt concrete is not significant.

From the above analysis, it can be seen that the content of nano-SiO₂ particles has no significant effect on the moisture content of asphalt concrete; that is, the same test index is selected for matrix asphalt concrete and nanomodified asphalt concrete. Therefore, for matrix asphalt and

nanomodified asphalt concrete, when conducting rutting and fatigue tests, temperature is used as the influencing factor, and moisture content is used as the controlling factor. The immersion time corresponding to the water content of 0%, 50%, 80%, and 100% is selected as the test index. The results are shown in Table 8.

4. High-Temperature Stability of Nanomodified Asphalt Concrete under the Coupling Action of Water and High Temperature

In the test, dynamic stability is used as the evaluation standard, and each group of tests is carried out in three parallel tests. See Table 9 for the rutting test results of asphalt concrete with different moisture content.

4.1. Effect of Saturated Water Ratio. Figure 3 plots the relationship between saturated water ratio and dynamic stability of modified asphalt mixture at different temperatures and different contents of nano-SiO₂ particles.

Figure 3 shows us that, with the increase of water content, the dynamic stability of nanomodified asphalt concrete decreases significantly. Under AC-13 gradation, compared with the case of 0% water content, the dynamic stability of nanomodified asphalt concrete is reduced by 37.2%, 51.1%, and 61.5% on average when the water content is 50%, 80%, and 100%. At 40°C, 50°C, 60°C, and 70°C, the total attenuation is 52.2%, 56.3%, 60.8%, and 69.5%. The analysis results show that the water in the voids of the nanoasphalt mixture will erode the asphalt film in the asphalt-aggregate interface and affect the cementation of the aggregate and asphalt. Particularly under

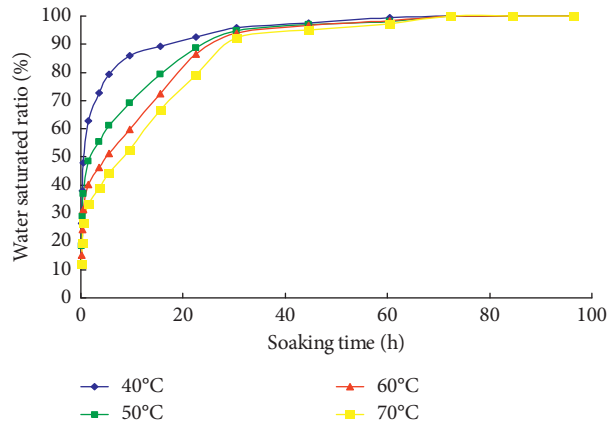


FIGURE 2: Relationship between saturated water ratio and soaking time.

TABLE 8: Time index of moisture content of asphalt concrete under AC-13 grading.

Water absorption (%)	Temperature (°C)	Immersion time (h)
0	40	0
	50	0
	60	0
	70	0
50	40	0.5
	50	1.5
	60	5.5
	70	9.5
80	40	5.5
	50	15.5
	60	19.5
	70	22.5
100	40	60
	50	72
	60	72
	70	72

TABLE 9: AC-13 nano-SiO₂-modified asphalt dynamic stability.

Temperature (°C)	Water absorption (%)	Content (%)	Dynamic stability (cycles/mm)
40	0	1	5625
		2	6215
		3	6841
	50	1	3485
		2	4278
		3	4521
	80	1	2805
		2	3182
		3	3514
	100	1	2018
		2	2420
		3	2655

TABLE 9: Continued.

Temperature (°C)	Water absorption (%)	Content (%)	Dynamic stability (cycles/mm)	
50	0	1	4781	
		2	5283	
		3	5815	
	50	50	1	2962
			2	3636
			3	3843
	80	80	1	2384
			2	2705
			3	2987
	100	100	1	1715
			2	2057
			3	2257
60	0	1	4585	
		2	5162	
		3	5474	
	50	50	1	2318
			2	2529
			3	2744
	80	80	1	1251
			2	1506
			3	1782
	100	100	1	982
			2	1123
			3	1515
70	0	1	3577	
		2	4369	
		3	4725	
	50	50	1	1743
			2	1710
			3	2198
	80	80	1	705
			2	804
			3	1141
	100	100	1	548
			2	649
			3	922

the action of the wheel pressure of the hydrodynamic pressure, the water damage will lead to the decline of the antirutting performance of the asphalt mixture and the degradation of the structural stability of the nano-SiO₂-modified asphalt concrete asphalt mixture. With the increase of water content, this negative effect of water will intensify, and rutting is apt to occur.

4.2. Effect of Temperature. Figure 4 displays the relationship between temperature and dynamic stability of modified asphalt mixture at different saturated water ratios.

Figure 4 shows the relationship between dynamic stability and temperature at different moisture contents. As the temperature increases, the dynamic stability of nanomodified asphalt concrete decreases significantly. Under AC-13 gradation, when the temperature of nanomodified asphalt concrete is 40°C, and the immersion time is 0.5 h, 5.5 h, and 44.5 h, the average dynamic stability is 2997 times/mm, 2063 times/mm, and 1571 times/mm, respectively. The dynamic stability decreased by 39.3%, 49.2%, and 57.1% for every 10°C increase in temperature.

From the above analysis, the following conclusions can be drawn: the dynamic stability of the three different contents of nanomodified asphalt concrete decreases after the temperature increases, indicating that high temperature can reduce the dynamic stability of the nanomodified asphalt concrete. Moreover, as the temperature increases, the asphalt film usually softens, and the above-mentioned effects of water will be correspondingly more significant. The results show that, under the combined action of water and high temperature, rutting is more likely to occur.

4.3. Influence of Content of Nano-SiO₂ Particles. Based on the data in Table 4, the dynamic stability curves of AC-13 nanosized modified asphalt concrete nano-SiO₂ particles with different mixing amounts at 40°C, 50°C, 60°C, and 70°C are drawn as follows:

It can be seen from Figure 5 that, as the content of nano-SiO₂ particles increases, the dynamic stability of nanomodified asphalt concrete increases and the relationship is basically linear. In consideration of economic benefits, the dynamic stability of 0.4% nano-SiO₂ particles increases by

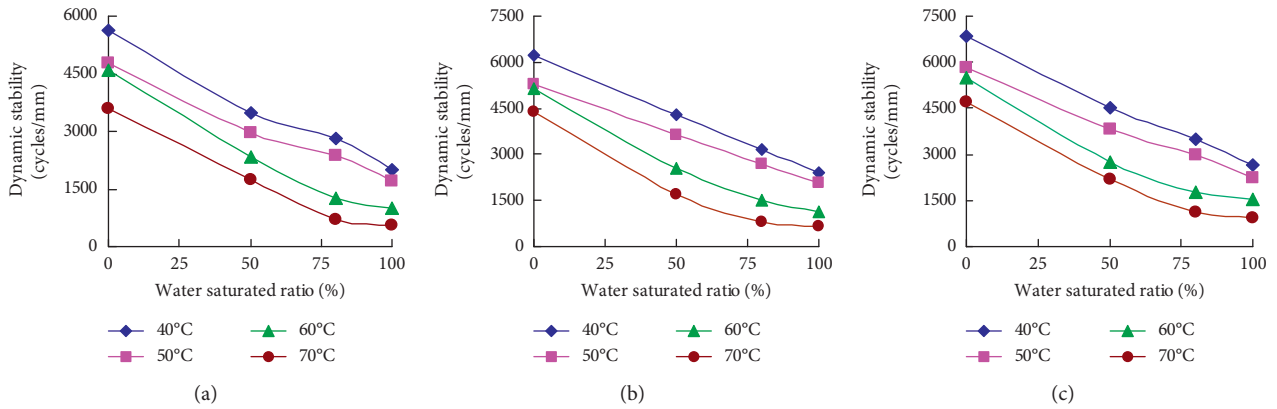


FIGURE 3: Relationship between dynamic stability and saturated water ratio at different temperatures. (a) 1% content. (b) 2% content. (c) 3% content.

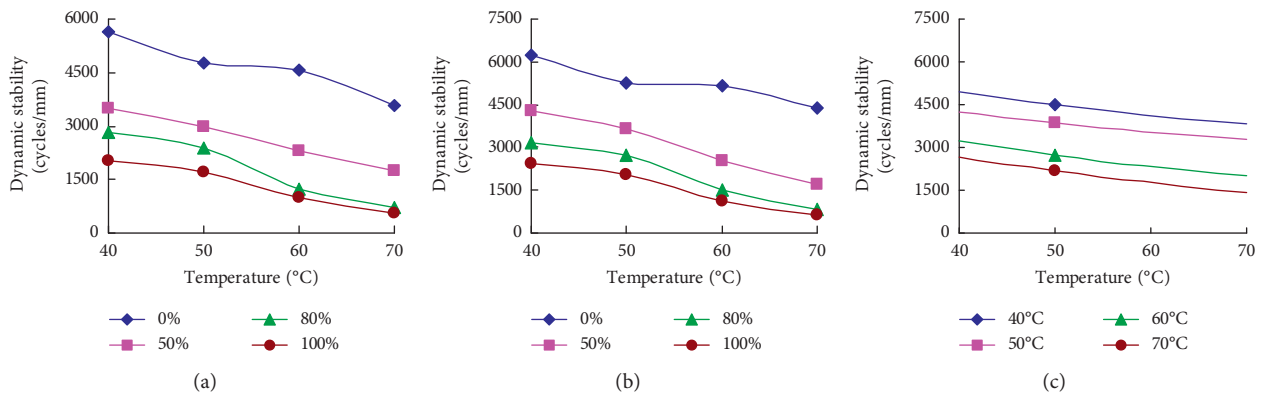


FIGURE 4: Relationship between dynamic stability and temperature at different saturated water ratios. (a) 1% content. (b) 2% content. (c) 3% content.

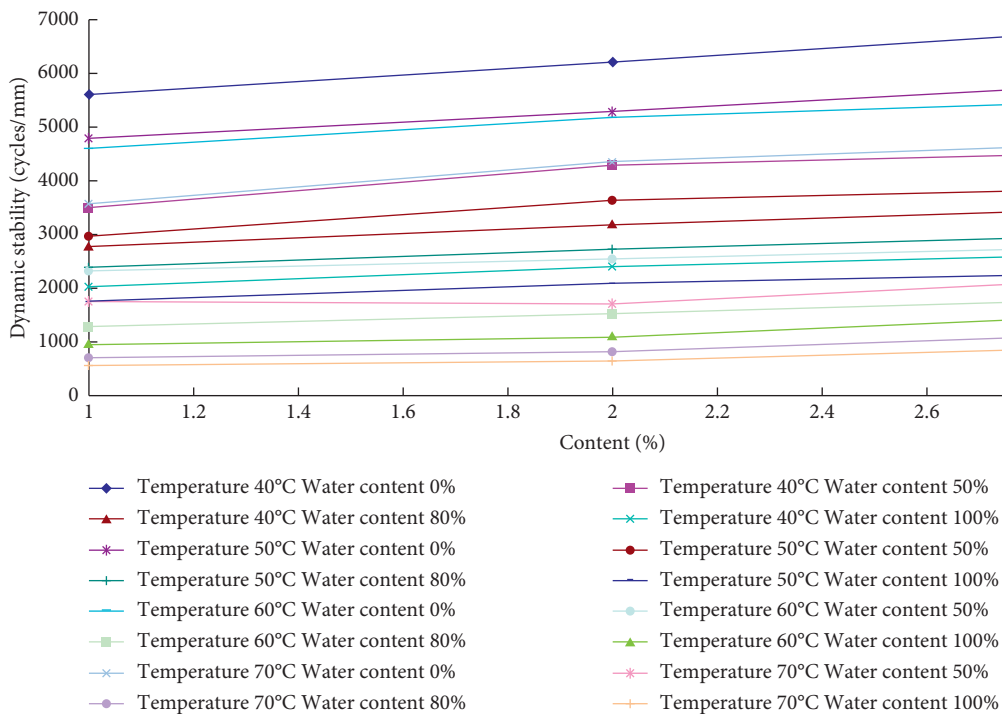


FIGURE 5: Effect of content on dynamic stability.

9.4% compared with 0.35%, and the dynamic stability only increases by 4.6% when the concentration is 0.45%. Therefore, the content of nano-SiO₂ particles is considered to be 0.4%.

5. Conclusion

This article provides a way to improve the antirutting performance of nanomodified asphalt concrete by using nano-SiO₂ particles. Research shows that the water absorption capacity and water absorption rate of nanomodified asphalt concrete are basically the same as those of matrix asphalt concrete. It shows that the addition of nano-SiO₂ particles will not affect the relationship between water absorption capacity and soaking time. This study is beneficial to design the nano-SiO₂-modified asphalt concrete during the coupled effect of high temperature and water.

- (1) According to the technical requirements of the specification, the raw materials used in asphalt concrete were tested, and the mix ratio of nanomodified asphalt concrete was designed when the raw materials met the requirements. The result shows, for AC-13 gradation, the addition of nano-SiO₂ particles will not affect the change of the optimal oil-stone ratio.
- (2) Temperature has a great influence on the water absorption performance of asphalt concrete. The higher the temperature, the longer it takes for the asphalt concrete to reach 100% moisture content. At the same time, when the moisture content reaches 100%, water absorption is higher. The dynamic stability of the three nanomodified asphalt concretes with different concentrations decreases with the increase of temperature, indicating that high temperature will reduce the dynamic stability of the nanomodified asphalt concrete. As the temperature increases, the asphalt film usually softens, and water's effect becomes correspondingly more significant. The results show that rutting is more likely to occur under the coupled action of water and high temperature.
- (3) The rutting test was carried out at 40°C, 50°C, 60°C, and 70°C, respectively. It was found that the dynamic stability under the same temperature condition decreases approximately linearly with the increase of water content. When the water content is greater than 50%, the rate of decrease gradually lessens, but with the increase of temperature, the linear trend becomes more and more obvious.

In the future, other pavement performance of the nano-SiO₂-modified asphalt concrete, for example, the fatigue behavior and skid resistance, should be addressed in the coupled effect of temperature and water.

Data Availability

The data used to support the findings of this study are included within the article.

Conflicts of Interest

The authors declare that they have no conflicts of interest.

Acknowledgments

The authors are very grateful for the support provided in part by the Highway Construction Science and Technology Projects of Shandong Hi-Speed Co. Ltd. (Grant no. QLTD-2019-A-FW-0036).

References

- [1] S. N. A. Jeffry, R. Putra Jaya, N. Abdul Hassan, H. Yaacob, M. Z. H. Mahmud, and Z. H. Al-Saffar, "The influence of nano-carbon from coconut shell ash as modifier on the properties of bitumen," *Road Materials and Pavement Design*, 2020.
- [2] J. Ren and C. Yin, "Investigating mechanical characteristics of aggregate structure for road materials," *International Journal of Pavement Engineering*, 2020.
- [3] Y. Jiang, Y. Yi, J. Fan, T. Tian, and C. Deng, "Laboratory investigation on the heat dissipation regularity and road performance of different pavement structure combinations by double-layer paving," *Construction and Building Materials*, vol. 284, Article ID 122785, 2021.
- [4] C. Deng, Y. Jiang, K. Yuan, T. Tian, and Y. Yi, "Mechanical properties of vertical vibration compacted lime-fly ash-stabilized macadam material," *Construction and Building Materials*, vol. 251, Article ID 119089, 2020.
- [5] Y. Jiang, K. Yuan, C. Deng, and T. Tian, "Fatigue performance of cement-stabilized crushed gravel produced using vertical vibration compaction method," *Journal of Materials in Civil Engineering*, vol. 32, no. 11, Article ID 04020318, 2020.
- [6] C. Wang, S. Wang, Z. Gao, and Z. Song, "Effect evaluation of road piezoelectric micro-energy collection-storage system based on laboratory and on-site tests," *Applied Energy*, vol. 287, Article ID 116581, 2021.
- [7] X. Ji, B. Han, J. Hu, S. Li, Y. Xiong, and E. Sun, "Application of the discrete element method and CT scanning to investigate the compaction characteristics of the soil-rock mixture in the subgrade," *Road Materials and Pavement Design*, 2020.
- [8] J. Jiang, Y. Li, Y. Zhang, and H. U. Bahia, "Distribution of mortar film thickness and its relationship to mixture cracking resistance," *International Journal of Pavement Engineering*, 2020.
- [9] X. Wang, J. Ren, X. Gu, N. Li, Z. Tian, and H. Chen, "Investigation of the adhesive and cohesive properties of asphalt, mastic, and mortar in porous asphalt mixtures," *Construction and Building Materials*, vol. 276, Article ID 122255, 2021.
- [10] X. Wang, J. Ren, X. Hu, X. Gu, and N. Li, "Determining optimum number of gyrations for porous asphalt mixtures using superpave gyratory compactor," *KSCE Journal of Civil Engineering*, vol. 25, pp. 2010–2019, 2021.
- [11] J. Huang, J. Zhang, J. Ren, and H. Chen, "Anti-rutting performance of the damping asphalt mixtures (DAMs) made with a high content of asphalt rubber (AR)," *Construction and Building Materials*, vol. 271, Article ID 121878, 2021.
- [12] J. Huang, Y. Sun, and J. Zhang, "Reduction of computational error by optimizing SVR kernel coefficients to simulate concrete compressive strength through the use of a human learning optimization algorithm," *Engineering with Computers*, 2021.

- [13] M. Hasaninia and F. Haddadi, "Studying engineering characteristics of asphalt binder and mixture modified by nano-silica and estimating their correlations," *Advances in Materials Science and Engineering*, vol. 2018, Article ID 4560101, 9 pages, 2018.
- [14] X. Wu, X.-L. Fan, and J.-F. Wang, "Temperature sensitivity of mechanical properties of cement asphalt mortar with nanoparticles," *Advances in Civil Engineering*, vol. 2020, Article ID 3109612, 14 pages, 2020.
- [15] S. Rezaei, M. Khordehbinan, S.-M.-R. Fakhrefatemi, S. Ghanbari, and M. Ghanbari, "The effect of nano- SiO₂ and the styrene butadiene styrene polymer on the high-temperature performance of hot mix asphalt," *Petroleum Science and Technology*, vol. 35, pp. 553–560, 2017.
- [16] Z. Chen and Z. Li, "Preparation and stabilisation mechanism of asphalt-in-water pickering emulsion stabilised by SiO₂ nanoparticles," *Road Materials and Pavement Design*, vol. 22, pp. 1679–1691, 2021.
- [17] G. H. Shafabakhsh and O. Jafari Ani, "Experimental investigation of effect of nano- TiO₂/SiO₂ modified bitumen on the rutting and fatigue performance of asphalt mixtures containing steel slag aggregates," *Construction and Building Materials*, vol. 98, pp. 692–702, 2015.
- [18] M. Saltan, S. Terzi, and S. Karahancer, "Performance analysis of nano modified bitumen and hot mix asphalt," *Construction and Building Materials*, vol. 173, pp. 228–237, 2018.
- [19] J. Chen, W. Zhang, X. Shi, C. Yao, and C. Kuai, "Use of PEG/SiO₂ phase change composite to control porous asphalt concrete temperature," *Construction and Building Materials*, vol. 245, Article ID 118459, 2020.
- [20] G. Shafabakhsh, M. Sadeghnejad, and R. Ebrahimnia, "Fracture resistance of asphalt mixtures under mixed-mode I/II loading at low-temperature: without and with nano SiO₂," *Construction and Building Materials*, vol. 266, Article ID 120954, 2021.
- [21] G. Qian, C. Yang, H. Huang, X. Gong, and H. Yu, "Resistance to ultraviolet aging of nano-SiO₂ and rubber powder compound modified asphalt," *Materials*, vol. 13, no. 22, p. 5067, 2020.
- [22] Y. Yang, W. Fan, Z. Wang, Q. Zhang, and G. Nan, "Effect of nano-SiO₂ on the performance of asphalt emulsion and its residue," *Advanced Materials Research*, vol. 413, pp. 331–335, 2012.
- [23] C. Du, G. Lu, H. Wang et al., "Effect of filler on performance of porous asphalt pavement using multiscale finite element method," *International Journal of Pavement Engineering*, 2021.
- [24] A. R. Moeini, A. Badiei, and A. M. Rashidi, "Effect of nanosilica morphology on modification of asphalt binder," *Road Materials and Pavement Design*, vol. 21, pp. 2230–2246, 2020.
- [25] F. Leiva-Villacorta and A. Vargas-Nordbeck, "Optimum content of nano-silica to ensure proper performance of an asphalt binder," *Road Materials and Pavement Design*, vol. 20, pp. 414–425, 2019.
- [26] J. Wan, S. Wu, Y. Xiao, Q. Liu, and E. Schlangen, "Characteristics of ceramic fiber modified asphalt mortar," *Materials (Basel, Switzerland)*, vol. 9, 2016.
- [27] J. Ren, S. Wang, and G. Zang, "Effects of recycled aggregate composition on the mechanical characteristics and material design of cement stabilized cold recycling mixtures using road milling materials," *Construction and Building Materials*, vol. 244, no. 3, Article ID 118329, 2020.
- [28] J. Huang, G. Shiva Kumar, J. Ren, Y. Sun, Y. Li, and C. Wang, "Towards the potential usage of eggshell powder as bio-modifier for asphalt binder and mixture: Workability and mechanical properties," *International Journal of Pavement Engineering*, 2021.
- [29] J. Huang, G. S. Kumar, and Y. Sun, "Evaluation of workability and mechanical properties of asphalt binder and mixture modified with waste toner," *Construction and Building Materials*, vol. 276, Article ID 122230, 2021.
- [30] J. Ren, D. Li, and S. Wang, "Combined effect of compaction methods and loading conditions on the deformation behaviour of unbound granular material," *Advances in Civil Engineering*, vol. 2020, Article ID 2419102, 16 pages, 2020.

Research Article

Coupled Dynamics of Vehicle-Bridge Interaction System Using High Efficiency Method

Lu Sun ¹ and Xingzhuang Zhao ²

¹Department of Civil Engineering Technology, Environmental Management and Safety, Rochester Institute of Technology, Rochester, NY, USA

²A. James Clark School of Engineering, University of Maryland, College Park 20740, MD, USA

Correspondence should be addressed to Lu Sun; lxsite@rit.edu

Received 6 May 2021; Accepted 14 July 2021; Published 11 August 2021

Academic Editor: Jiaolong Ren

Copyright © 2021 Lu Sun and Xingzhuang Zhao. This is an open access article distributed under the Creative Commons Attribution License, which permits unrestricted use, distribution, and reproduction in any medium, provided the original work is properly cited.

Vehicle-bridge interaction is the core for a variety of applications, including vehicle vibration, bridge vibration, bridge structural health monitoring, weight-in-motion, bridge condition inspection, and load rating. These applications give rise to a great interest in pursuing a high-efficiency method that can tackle intensive computation in the context of vehicle-bridge interaction. This paper studies the accuracy and efficiency of discretizing the beam in space as lumped masses using the flexibility method and as finite elements using the stiffness method. Computational complexity analysis is carried out along with a numerical case study to compare the accuracy and efficiency of both methods against the analytical solutions. It is found that both methods result in a similar level of accuracy, but the flexibility method overperforms the stiffness method in terms of computational efficiency. This high efficiency algorithm and corresponding discretization schema are applied to study the dynamics of vehicle-bridge interaction. A system of coupled equations is solved directly for a simply supported single-span bridge and a four-degree-of-freedom vehicle modeling. Pavement roughness significantly influences dynamic load coefficient, suggesting preventative maintenance or timely maintenance of pavement surface on a bridge, to reduce pavement roughness, is of significant importance for bridge's longevity and life-cycle cost benefit. For class A and B level pavement roughness, the dynamic load coefficient is simulated within 2.0, compatible with specifications of AASHTO standard, Australian standard, and Switzerland standard. However, the Chinese code underestimates the dynamic load coefficient for a bridge with a fundamental frequency of around 4 Hz. The proposed method is applicable to different types of bridges as well as train-bridge interaction.

1. Introduction

Vehicle-bridge interaction is the key to obtaining the interaction force between the tire and pavement. It has many applications in the weigh-in-motion system [1–32], bridge dynamics and vibration control [33–50], bridge structural health monitoring, bridge ambient testing, bridge damage identification [51–64], and high-speed railway [29, 65–68].

Due to the complexity of models of vehicle-bridge interaction, an analytical solution of vehicle-bridge interaction is normally beyond achievement for most cases. Therefore, numerical methods such as the finite difference method and finite element method (FEM) become indispensable for any realistic applications [1, 2, 69–76].

One of the essential components in modeling vehicle-bridge interaction is the bridge subsystem. In FEM, a bridge is typically discretized as finite elements and solved by the stiffness method [2, 4, 41, 73, 76–84]. Rieker et al. studied the influence of discretization of beams on the dynamic response of elastic beams under moving load [1]. And, they concluded that an acceptable level of accuracy (i.e., relative error within 1%) could be achieved when the number of elements in discretization for dynamic analysis should be 16 and be at least two to eight times greater than that used in static analysis. Law et al. [77] investigated the influence of the number of finite elements and argued that at least 8 elements were required to discretize the beam bridge.

The abovementioned applications require intensive computation of time-varying vehicle-bridge interaction, demanding high-efficiency methods. What is missing in the literature on vehicle-bridge interaction is the investigation of an efficient and accurate method for solving the vehicle-bridge interaction problem.

The innovative contributions of this study are three-fold. First of all, this study studies the accuracy and efficiency of discretizing the beam in space as lumped masses using the flexibility method and as finite elements using the stiffness method. Using computational complexity analysis, it is shown that both methods result in a similar level of accuracy, but the flexibility method is two to eight times faster than the stiffness method.

Secondly, based on the new finding of the advantage embedded in discretizing the beam in space as lumped masses using the flexibility method, this study develops a high efficiency method for solving the coupled dynamics of vehicle-bridge interaction using a 4-DOF vehicle model, a simply supported single-span bridge model and ISO pavement roughness model.

Lastly, this study reveals that pavement roughness significantly influences dynamic load coefficient (DLC) and Chinese code [85] underestimates the DLC for a bridge with fundamental frequency around 4 Hz, suggesting the importance of preventative and timely maintenance of the pavement surface on a bridge to reduce pavement unevenness for bridge's longevity and life cycle cost benefit.

2. Equation of Beam Motion

Without forfeiting the validity of the analysis, a moving vehicle is simplified as a dynamic load $q(x, t)$ in this study [86]. This simplification allows analytical solutions to be developed for a simple form of the dynamic load, therefore serving as a benchmark for comparison against the numerical solution.

In this section, the equation of motion of a beam is derived. Consider an Euler-Bernoulli beam, with unit width and length L subjected to an arbitrarily distributed force $q(x, t)$, as shown in Figure 1. The parameters of the beam are E which denotes Young's modulus, I_z which denotes the cross-section moment of inertia, ρ which denotes the density, and A which denotes the area of cross section. It is assumed that the beam bridge is uniform in cross section.

Taking out an infinitesimal segment from the beam, with which the force applied on this segment is shown in Figure 2. Here, M denotes the moment applied on left cross section, V denotes the shear force applied on left cross section, $M + (\partial M/\partial x)\delta x$ denotes the moment applied on right cross section, $V + (\partial V/\partial x)\delta x$ denotes the shear force applied on right cross section, $q(x, t)$ denotes the distributed force applied, m denotes the mass of the infinitesimal segment volume, $m = \rho A \delta x$, a denotes the acceleration of the infinitesimal segment volume, $a = \partial^2 w/\partial t^2$, where w is the deflection of the beam and t is time variable, f_d is the unit damping force caused by the ambience and material viscosity, which is proportional to the velocity, $f_d = c(\partial w/\partial t)$, where d is the damping coefficient of the unit length.

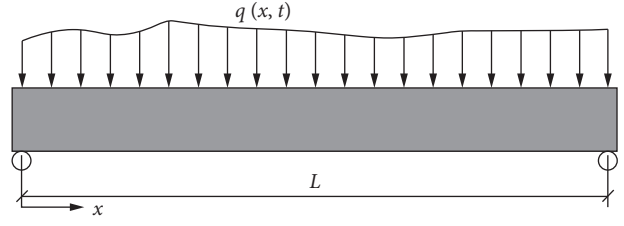


FIGURE 1: Euler-Bernoulli beam.

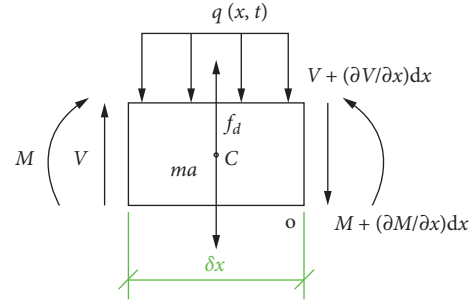


FIGURE 2: Infinitesimal segment analysis.

Similar to [87], it is plausible to assume that the distributed force be uniform and the inertial force is applied at the center of the segment because of the infinitesimal length of the segment. The equation of beam motion can be established by Newton's second law. Different from [87], an additional term of damping force proportional to the speed of beam motion is added to the equation.

Apply Newton's second law on the segment in the vertical direction:

$$\rho A \delta x \frac{\partial^2 w}{\partial t^2} = V + \frac{\partial V}{\partial x} \delta x - V + q(x, t) \delta x - c \frac{\partial w}{\partial t} \delta x, \quad (1a)$$

or equivalently

$$\rho A \frac{\partial^2 w}{\partial t^2} = \frac{\partial V}{\partial x} + q(x, t) - c \frac{\partial w}{\partial t}. \quad (1b)$$

Take moment with respect to point O. The moment balance equation can be obtained as follows:

$$M + V \delta x - M - \frac{q(x, t) \delta x^2}{2} - \frac{\partial M}{\partial x} \delta x - \frac{m a \delta x}{2} = 0. \quad (2)$$

Substituting $m = \rho A \delta x$ and $a = \partial^2 w/\partial t^2$ into (2) leads to

$$V \delta x - \frac{q(x, t) \delta x^2}{2} - \frac{\partial M}{\partial x} \delta x - \frac{\rho A \delta x^2}{2} = 0. \quad (3)$$

Divide both sides by δx and take the limit of $\delta x \rightarrow 0$, obtaining

$$V = \frac{\partial M}{\partial x}. \quad (4)$$

Substitution of V into (1b) leads to

$$\rho A \frac{\partial^2 w}{\partial t^2} = \frac{\partial^2 M}{\partial x^2} + q(x, t) - c \frac{\partial w}{\partial t}. \quad (5)$$

According to Euler–Bernoulli beam theory,

$$EI_z \frac{\partial^2 w}{\partial x^2} = -M. \quad (6)$$

The equation of motion for the beam bridge is obtained as follows:

$$\rho A \frac{\partial^2 w}{\partial t^2} + c \frac{\partial w}{\partial t} + \frac{\partial^2}{\partial x^2} \left(EI_z \frac{\partial^2 w}{\partial x^2} \right) = q(x, t), \quad (7)$$

where ρ , A , d , and EI_z could be functions of both position x and time t , that is, $\rho = \rho(x, t)$, $A = A(x, t)$, $c = c(x, t)$, and $(\partial^2/\partial x^2)(EI_z(\partial^2 w/\partial x^2)) = r(x, t)(\partial^4 w/\partial x^4)$, $r(x, t) \neq 0$. This generalization leads to

$$p(x, t) \frac{\partial^2 w}{\partial t^2} + c(x, t) \frac{\partial w}{\partial t} + r(x, t) \frac{\partial^4 w}{\partial x^4} = q(x, t). \quad (8)$$

The coefficient of the third term $\partial^4 w/\partial x^4$ in the continuous equation of motion (8) could be set to 1 by dividing $r(x, t)$ into both sides of (8), resulting in

$$\tilde{p}(x, t) \frac{\partial^2 w}{\partial t^2} + \tilde{b}(x, t) \frac{\partial w}{\partial t} + \frac{\partial^4 w}{\partial x^4} = \tilde{q}(x, t). \quad (9)$$

For a uniform beam with a constant EI_z , (7) can be further simplified as

$$\rho A \frac{\partial^2 w}{\partial t^2} + c \frac{\partial w}{\partial t} + EI_z \frac{\partial^4 w}{\partial x^4} = q(x, t), \quad (10)$$

where $\tilde{p}(x, t) = p(x, t)/r(x, t)$, $\tilde{b}(x, t) = b(x, t)/r(x, t)$, and $\tilde{q}(x, t) = q(x, t)/r(x, t)$.

When neglecting the damping, i.e., $c = 0$, (8) degrades to Euler–Lagrange equation [88]. For a beam bridge and the initial time is set at $t=0$, equations (7), (8), and (10) are defined for $t \geq 0$, $0 \leq x \leq L$, and L is the length of the bridge. The coefficients of $\partial^4 w/\partial x^4$, $\partial w/\partial t$, and $\partial^2 w/\partial t^2$ present stiffness, damping, and mass, respectively.

3. Discretization of Beam as Lumped Masses

A beam bridge can be discretized into lumped masses [89]. Each lumped mass is assigned to the node with an interval of Δx , as shown in Figure 3.

In the lumped mass discretization schema, only the vertical displacement at each of the lumped masses is considered. The deflection of the lumped mass can be obtained for both determinate and indeterminate structures [90]. For instance, the deflection of a simply supported beam due to static force is governed by the following formula given in the AISC steel construction manual [91]:

$$w = -\frac{Fbx}{6EI_z L} (L^2 - x^2 - b^2), \quad (11)$$

$$w = -\frac{Fb}{6EI_z L} \left[\frac{L}{b} (x-a)^3 + (L^2 - b^2)x - x^3 \right],$$

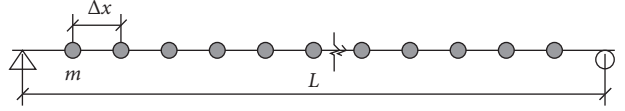


FIGURE 3: Discretization schema of the beam as lumped masses.

where F is the concentrated force acting on the beam, x , E , I_z , and L are defined the same way as before, a is the distance from the origin, and $b = L - a$.

The deflection of every lumped mass is obtained by applying a unit force to the mass to achieve the corresponding deflection. The stiffness matrix K in equation (13) can be computed as the reverse of the flexibility matrix F_d [84]. The mass matrix is obtained by constructing a diagonal matrix of size $n \times n$, with the element of value $\rho(x_i, t)A(x_i, t)\Delta x$. The force vector $F(t)$ applied on the lumped mass could be directly represented by $q(x_i, t)\Delta x$.

4. Discretization of Beam as Finite Elements

The beam bridge could also be discretized as n finite elements, with Δx being the length of the elements, as shown in Figure 4. The two ends of each element are defined as the nodes of the element. From the figure, it is observed that the distances between the nodes are Δx .

Multiplying Δx on both sides of equation (1a), discretizing the system into

$$\rho(x_i, t)A(x_i, t)\Delta x \frac{\partial^2 w_i}{\partial t^2} + c(x_i, t)\Delta x \frac{\partial w_i}{\partial t} + E(x_i, t)I_z(x_i, t) \frac{\partial^4 w_i}{\partial x^4} \Delta x = q(x_i, t)\Delta x \quad (i = 1, \dots, n). \quad (12)$$

Equation (12) can be written in a matrix form as

$$M(t)\ddot{w} + C(t)\dot{w} + K(t)w = F(t). \quad (13)$$

Here, $\rho(x_i, t)A(x_i, t)\Delta x (\partial^2 w_i/\partial t^2)$ is equivalent to $M(t)\ddot{w}$, $c(x_i, t)\Delta x (\partial w_i/\partial t)$ is equivalent to $C(t)\dot{w}$, $q(x_i, t)\Delta x$ is equivalent to $F(t)$, $E(t)I_z(t) (\partial^4 w_i/\partial x^4) \Delta x$ is equivalent to $K(t)w$, $M(t)$ is the mass matrix of the discretized system, $C(t)$ is the damping coefficient matrix, $K(t)$ is the stiffness matrix, $F(t) = q(x_i, t)\Delta x$ is the excitation force that is applied on each lumped mass, and w is the deflection vector of the beam.

In Figure 5, the nodes of the element are located on two clamped ends. An external exciting force applied to the element is transferred onto the nodes of the elements. For a concentrated load, as shown in Figure 5, the equivalent node force vector in the local coordinate is $[-Pb/\Delta x, -Pab^2/\Delta x, -Pa/\Delta x, Pab^2/\Delta x]^T$. For a distributed load, as shown in Figure 6, the equivalent node force vector in the local coordinates is $[-q\Delta x/2, -q\Delta x^2/12, -q\Delta x/2, q\Delta x^2/12]^T$. Here, P and q are respective the concentrated force and the distributed force applied locally on the element.

The local stiffness matrix and mass matrix can be written as

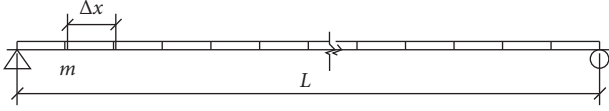


FIGURE 4: Discretization schema of the beam as finite elements.

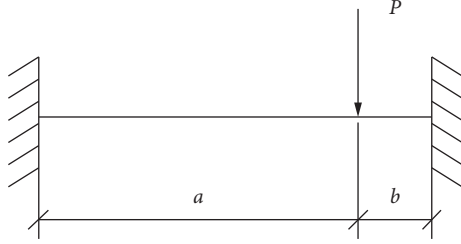


FIGURE 5: The concentrated force.

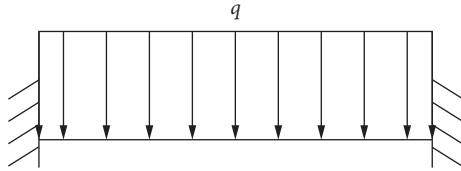


FIGURE 6: The distributed force.

$$[k]_i = \frac{2E_i I_i}{\Delta x^3} \left[63\Delta x - 63\Delta x 3\Delta x_i 2\Delta x^2 - 3\Delta x \Delta x^2 - 6 \right. \\ \left. - 3\Delta x 6 - 3\Delta x 3\Delta x_i 2\Delta x^2 - 3\Delta x 2\Delta x^2 \right], \quad (14)$$

$$[m]_i = \frac{\rho_i A_i \Delta x}{420} \left[15622\Delta x 54 - 13\Delta x 22\Delta x 4\Delta x^2 13\Delta x \right. \\ \left. - 3\Delta x^2 5413\Delta x 156 - 22\Delta x - 13\Delta x \right. \\ \left. - 3\Delta x^2 - 22\Delta x 4\Delta x^2 \right]. \quad (15)$$

Besides, the damping matrix is constructed in a similar way as the mass matrix in (17):

$$[c]_i = \frac{c_i A_i \Delta x}{420} \left[15622\Delta x 54 - 13\Delta x 22\Delta x 4\Delta x^2 13\Delta x \right. \\ \left. - 3\Delta x^2 5413\Delta x 156 - 22\Delta x - 13\Delta x - 3\Delta x^2 - 22\Delta x 4\Delta x^2 \right]. \quad (16)$$

The exciting force can be written accordingly as follows:

$$[F]_i = \left[\frac{q\Delta x}{2}, \frac{q\Delta x^2}{12}, \frac{q\Delta x}{2}, \frac{q\Delta x^2}{12} \right]^T \text{ for a distributed load,} \quad (17)$$

$$[F]_i = \left[-\frac{Pb}{\Delta x}, -\frac{Pab^2}{\Delta x}, -\frac{Pa}{\Delta x}, \frac{Pab^2}{\Delta x} \right]^T \text{ for a concentrated load.} \quad (18)$$

The global stiffness matrix, the global mass matrix, and the global force vector could be obtained by assembling all the local stiffness matrices (15), the local mass matrices (16), and the local force vectors [92].

5. Computational Complexity

The following equation can be constructed for the dynamic response of the beam bridge:

$$M(t)\ddot{w} + C(t)\dot{w} + K(t)w = F(t). \quad (19)$$

For the discretization schema of the beam bridge as lumped masses, the stiffness matrix is obtained by inverting the flexibility matrix. For the discretization schema of the beam bridge as finite elements, the stiffness matrix is obtained by assembling the local stiffness matrices of elements. The coefficients using the flexibility method and the stiffness method are given in Table 1. Here, d_{ij} is the deflection at lumped mass j when the unit force is applied to the beam at lumped mass i .

Equation (17) could be solved using classical numerical methods, such as the central finite difference method, Houbolt method, Wilson theta method, and Newmark's Beta method [93]. In this study, the Newmark method [94] is implemented. The procedures for solving (20) are given as follows.

- Step 1: compute coefficient matrix, $M(t)$, $C(t)$, and $K(t)$ using the lumped masses and the finite elements, respectively
- Step 2: compute the excitation force vector $F(t)$
- Step 3: solve equation (19) using Newmark's method

The size of the coefficient matrix M , C , and K for the discretization of the beam as lumped masses is $n \times n$, whereas the size of the coefficient matrix M , C , and K for the discretization of the beam as finite elements is $2n \times 2n$. Here, n is the number of lumped masses or finite elements after discretization. The matrices involved in the computation of the lumped masses are four times the size of the matrices involved in the computation of the finite elements.

Neglecting the initialization step described in Table 2, the computational operations (addition/subtraction and multiplication/division) for the algorithm are approximately $2n^3/3$ and $16n^3/3$, respectively. Therefore, the difference between the flexibility method and the stiffness method is due to the size of their coefficient matrices, which mainly account for the number of operations of the flexibility method and stiffness method. Theoretically, the efficiency of discretizing the beam as lumped masses in the flexibility method is roughly eight times more efficient than discretizing the beam as finite elements using the stiffness method.

6. Performance Comparison

A numerical case study is provided in this section to illustrate and compare the computational accuracy and efficiency of two different discretization schemas.

TABLE 2: Computational schema of Newmark's method using (9).

Algorithm	Discretization of the beam as lumped masses (the flexibility method)	Discretization of the beam as finite elements (the stiffness method)
1.0 initialization		
1.1 $\ddot{u}_0 = p_0 - c\dot{u}_0 - ku_0/m$		
2.2 set Δt	$O(1)$	$O(1)$
3.3 calculate a_1, a_2, a_3		
4.4 calculate \tilde{k}		
2.0 loop		
for $i = 1$ to T_t		
5.5 calculate \tilde{p}_{i+1}	$O(n)$	$O(2n)$
6.6 calculate u_{i+1}	$(2n^3/3) + O(n^2)$	$(16n^3/3) + O(4n^2)$
7.7 calculate \tilde{u}_{i+1}	$O(n)$	$O(2n)$
8.8 calculate \ddot{u}_{i+1}	$O(n)$	$O(2n)$
End		

The case study involves a forced vibration of the beam bridge without the damping term. The equation of motion is shown in (19). The beam bridge is excited by an external force which varies in time and space; the coefficients of the term $\partial^2 w / \partial t^2$ and $\partial^4 w / \partial x^4$ are constant. The parameters of the bridge are adopted from Law et al. [77]; the total length of the beam bridge: $L = 30$ m, $EI = 2.5 \times 10^{10}$ N·m², and $\rho A = 5.0 \times 10^3$ kg/m:

$$\rho A \frac{\partial^2 w}{\partial t^2} + EI \frac{\partial^4 w}{\partial x^4} = \frac{1}{10} \left[2\rho A + EI t^2 \left(\frac{\pi}{L} \right)^2 \right] \sin \left(\frac{\pi}{L} x \right), \quad (20)$$

$$\begin{aligned} w(0, t) &= 0, \\ w(L, t) &= 0, \\ w''(0, t) &= 0, \\ w''(L, t) &= 0. \end{aligned} \quad (21)$$

The boundary conditions and the initial conditions are given in equations (21) and (22):

$$\begin{aligned} w(x, 0) &= 0, \\ \dot{w}(x, 0) &= 0. \end{aligned} \quad (22)$$

The theoretical solution for this beam bridge is provided in (23), which can be verified by directly substituting (23) into (19):

$$w = \frac{1}{10} t^2 \sin \left(\frac{\pi}{L} x \right). \quad (23)$$

Dynamic displacement for the first 1 second is computed at three different time steps: 0.01 s, 0.005 s, and 0.001 s and plotted in Figures 4 and 5. Due to the symmetry of the geometry and the boundary condition, only two locations on the beam bridge are computed and compared: $0.3L$ and $0.5L$. The relative error ε_x is defined as

$$\varepsilon_x = \text{abs} \left[\frac{(\text{calculated value} - \text{theoretical value})}{\text{theoretical value}} \right] \times 100\%, \quad (24)$$

where the subscript x of ε stands for the method, f stands for the flexibility method, and s stands for the stiffness method.

Figures 7 and 8 show the relative error of both methods at $0.3L$ and $0.5L$. The horizontal axis of both figures is

computation time duration from the beginning into the simulation. Newmark's method is a stable computational method when the time step is small enough, say, smaller than 10% of the overall time duration, [94]. Therefore, the cumulated error would not increase without bound as the computation time duration increases.

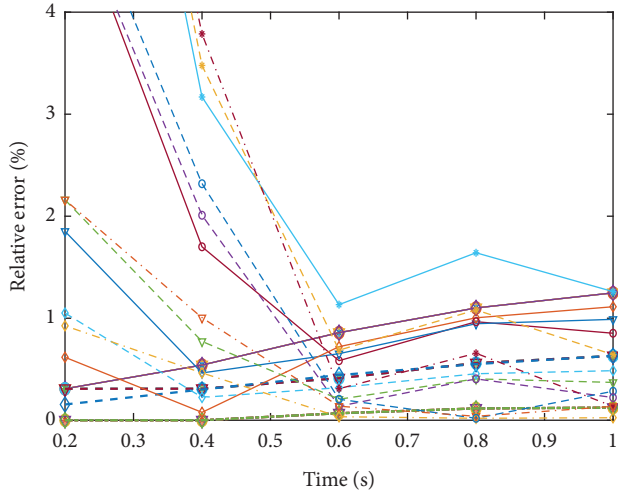
According to Figures 7 and 8, the relative errors of both methods are approximately at the same level for the same number of elements and the same time step, though the accuracy of the flexibility method is slightly better than that of the stiffness method. The variations of flexibility methods for a different number of elements are very small when the time step is the same.

Increasing the number of elements or nodes not only slightly improves the accuracy of the flexibility method but also improves considerably the accuracy of the stiffness method.

The time step plays a significant role in improving accuracy. Decreasing the time step improves significantly the accuracy for both methods at the cost of increased computation time. When the time step is small and the element number is over 50, the increase of element number does not improve the accuracy considerably for both methods. When the time step is small enough, even a small number of elements (e.g., 20 elements or nodes for a beam bridge of the length of 30 m) could achieve satisfactory accuracy.

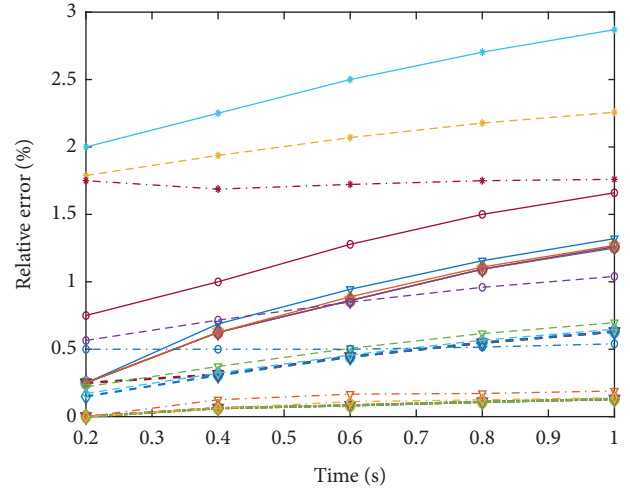
Figure 9 plots the computation time of two discretization schemas versus the number of elements or nodes. It is evident that the computation time for the flexible method increases slightly with the increase in the number of elements, while the computation time for the stiffness method increases significantly with the increase in the number of elements.

Figure 10 shows the time ratio, defined as the ratio between the time used by the flexibility method over the stiffness method, versus the number of elements or nodes. As the number of elements increases from 10 to 100, the time ratio increases from roughly 1.8, 2.2, and 3.2 for time steps 0.01 s, 0.005 s, and 0.001 s, respectively, to 4.9, 5.6, and 5.7. This is in general consistent with and slightly lower than the theoretical prediction on the computational complexity of the two methods, which suggests 8.0 computational efficiency differences between the two methods. The reason for such discrepancy between theoretical prediction and



- * Flexibility (dt = 0.01 s): n = 10
- o Flexibility (dt = 0.01 s): n = 20
- v Flexibility (dt = 0.01 s): n = 50
- d Flexibility (dt = 0.01 s): n = 100
- * Flexibility (dt = 0.005 s): n = 10
- o Flexibility (dt = 0.005 s): n = 20
- v Flexibility (dt = 0.005 s): n = 50
- d Flexibility (dt = 0.005 s): n = 100
- * Flexibility (dt = 0.001 s): n = 10
- o Flexibility (dt = 0.001 s): n = 20
- v Flexibility (dt = 0.001 s): n = 50
- d Flexibility (dt = 0.001 s): n = 100
- * Stiffness (dt = 0.01 s): n = 10
- o Stiffness (dt = 0.01 s): n = 20
- v Stiffness (dt = 0.01 s): n = 50
- d Stiffness (dt = 0.01 s): n = 100
- * Stiffness (dt = 0.005 s): n = 10
- o Stiffness (dt = 0.005 s): n = 20
- v Stiffness (dt = 0.005 s): n = 50
- d Stiffness (dt = 0.005 s): n = 100
- * Stiffness (dt = 0.001 s): n = 10
- o Stiffness (dt = 0.001 s): n = 20
- v Stiffness (dt = 0.001 s): n = 50
- d Stiffness (dt = 0.001 s): n = 100

FIGURE 7: The relative error at 0.3L.



- * Flexibility (dt = 0.01 s): n = 10
- o Flexibility (dt = 0.01 s): n = 20
- v Flexibility (dt = 0.01 s): n = 50
- d Flexibility (dt = 0.01 s): n = 100
- * Flexibility (dt = 0.005 s): n = 10
- o Flexibility (dt = 0.005 s): n = 20
- v Flexibility (dt = 0.005 s): n = 50
- d Flexibility (dt = 0.005 s): n = 100
- * Flexibility (dt = 0.001 s): n = 10
- o Flexibility (dt = 0.001 s): n = 20
- v Flexibility (dt = 0.001 s): n = 50
- d Flexibility (dt = 0.001 s): n = 100
- * Stiffness (dt = 0.01 s): n = 10
- o Stiffness (dt = 0.01 s): n = 20
- v Stiffness (dt = 0.01 s): n = 50
- d Stiffness (dt = 0.01 s): n = 100
- * Stiffness (dt = 0.005 s): n = 10
- o Stiffness (dt = 0.005 s): n = 20
- v Stiffness (dt = 0.005 s): n = 50
- d Stiffness (dt = 0.005 s): n = 100
- * Stiffness (dt = 0.001 s): n = 10
- o Stiffness (dt = 0.001 s): n = 20
- v Stiffness (dt = 0.001 s): n = 50
- d Stiffness (dt = 0.001 s): n = 100

FIGURE 8: The relative error at 0.5L.

realization could be caused by coefficients embedded in computational complexity analysis in Table 2 and the actual computer used to execute the computation.

7. Vehicle Model

Figure 11 shows a vehicle traversing a single span simply supported beam bridge. A four-degree-of-freedom (4-DOF) half-car model is utilized for analysis in this paper. Taking

advantage of Lagrange formulation, the equation of motion of the vehicle can be derived as follows.

The kinetic energy equation of the vehicle model is

$$K = \frac{1}{2} m_v \dot{y}_v^2 + \frac{1}{2} m_f \dot{y}_1^2 + \frac{1}{2} m_r \dot{y}_r^2 + \frac{1}{2} I_v \dot{\theta}^2. \quad (25)$$

The potential energy equation of the vehicle model is

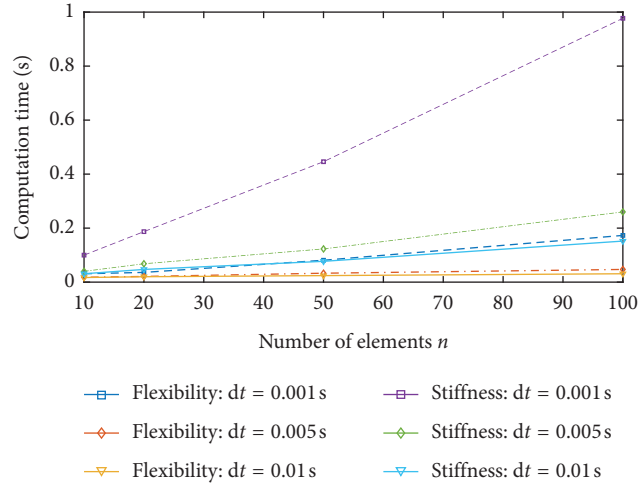


FIGURE 9: Efficiency comparison between the flexibility method and the stiffness method.

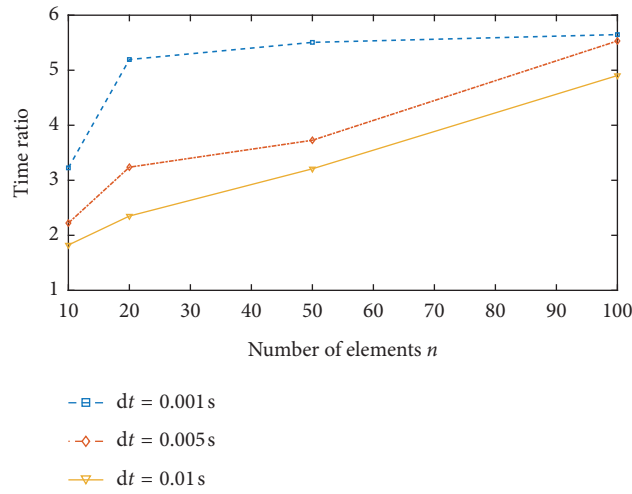


FIGURE 10: The time ratio between the stiffness method over the flexibility method.

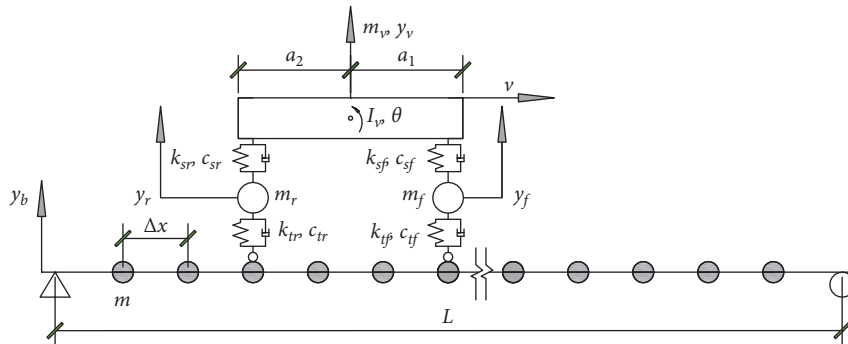


FIGURE 11: A 4-DOF model of the vehicle-bridge interaction system.

$$\begin{aligned}
 V &= \frac{1}{2} k_{tf} (y_f - y_{bf})^2 + \frac{1}{2} k_{tr} (y_r - y_{br})^2 + \frac{1}{2} k_{sf} (y_v - y_f + a_1 \theta)^2 \\
 &+ \frac{1}{2} k_{sr} (y_v - y_r - a_1 \theta)^2. \\
 D &= \frac{1}{2} c_{tf} (\dot{y}_f - \dot{y}_{bf})^2 + \frac{1}{2} c_{tr} (\dot{y}_r - \dot{y}_{br})^2 + \frac{1}{2} c_{sf} (\dot{y}_v - \dot{y}_f + a_1 \dot{\theta})^2 \\
 &+ \frac{1}{2} c_{sr} (\dot{y}_v - \dot{y}_r - a_1 \dot{\theta})^2.
 \end{aligned}
 \tag{26}$$

(27)

The energy dissipation equation is

Substituting into Lagrange formation.

$$\frac{d}{dt} \left(\frac{\partial K}{\partial \dot{q}_i} \right) - \left(\frac{\partial K}{\partial q_i} \right) + \left(\frac{\partial d}{\partial \dot{q}_i} \right) + \left(\frac{\partial V}{\partial q_i} \right) = f_i \quad (i = 1, 2, 3, 4), \quad (28)$$

equation of motion of the vehicle model is obtained, presenting in the matrix form,

$$M_v \ddot{y} + C_v \dot{y} + K_v y = F_v, \quad (29)$$

where

$$y = \begin{Bmatrix} y_v \\ \theta \\ y_f \\ y_r \end{Bmatrix}, \quad (30)$$

$$M_v = \begin{bmatrix} m_v & 0 & 0 & 0 \\ 0 & I_v & 0 & 0 \\ 0 & 0 & m_f & 0 \\ 0 & 0 & 0 & m_r \end{bmatrix}, \quad (31)$$

$$C_v = \begin{bmatrix} c_{sf} + c_{sr} & -c_{sf}a_1 + c_{sr}a_2 & -c_{sf} & -c_{sr} \\ -c_{sf}a_1 + c_{sr}a_2 & c_{sf}a_1^2 + c_{sr}a_2^2 & c_{sf}a_1 & -c_{sr}a_2 \\ -c_{sf} & c_{sf}a_1 & c_{sf} + c_{tf} & 0 \\ -c_{sr} & -c_{sr}a_2 & 0 & c_{sr} + c_{tr} \end{bmatrix}, \quad (32)$$

$$K_v = \begin{bmatrix} k_{sf} + k_{sr} & -k_{sf}a_1 + k_{sr}a_2 & -k_{sf} & -k_{sr} \\ -k_{sf}a_1 + k_{sr}a_2 & k_{sf}a_1^2 + k_{sr}a_2^2 & k_{sf}a_1 & -k_{sr}a_2 \\ -k_{sf} & k_{sf}a_1 & k_{sf} + k_{tf} & 0 \\ -k_{sr} & -k_{sr}a_2 & 0 & k_{sr} + k_{tr} \end{bmatrix}, \quad (33)$$

$$F_v = \begin{Bmatrix} 0 \\ 0 \\ k_{tf}y_{bf} + c_{tf}\dot{y}_{bf} \\ k_{tr}y_{br} + c_{tr}\dot{y}_{br} \end{Bmatrix}, \quad (34)$$

$$y_{bf}(t) = w(x_f(t), t) + r(x_f(t), t), \quad (35)$$

$$y_{br}(t) = w(x_r(t), t) + r(x_r(t), t), \quad (36)$$

Here, $y_{bf}(t)$ and $y_{br}(t)$ are, respectively, the absolute vertical displacements of the front wheel and the rear wheel evaluated at the contact points along the route of the vehicle, which are determined based on pavement roughness and deflection of the bridge. In this study, it is assumed that the vehicle and bridge always keep full contact during the entire interaction process, which is reflected through equations (35) and (36). In these two equations, $w(x, t)$ and $r(x, t)$ stand

for bridge deflection and pavement roughness, respectively. The values of $y_{bf}(t)$ and $y_{br}(t)$ are dependent on the location on the bridge x during the motion of the vehicle. For a moving vehicle at a constant speed, $x = vt$; therefore, $y_{bf}(t)$ and $y_{br}(t)$ are also functions of time.

8. Bridge Model

The bridge considered herein is a uniform cross-section beam. For varied cross-section beams, the same method is applied. The beam is discretized into mn lumped mass, as shown in Figure 3. In this study, only the vertical displacement of each lumped mass is considered. In other words, the total number of degree-of-freedom of the bridge is mn , excluding boundary conditions.

The mass matrix M_b for the bridge model can be conveniently obtained as a diagonal matrix. For the stiffness matrix K_b , the flexibility method is implemented. Taking advantage of knowledge from mechanics, the vertical deflection at each of the aforementioned lumped masses is calculated, resulting in the flexibility matrix. Taking the inverse of the flexibility matrix, the stiffness matrix K_b is obtained.

In establishing the damping matrix, the classical Rayleigh damping for structure dynamics is adopted. The damping matrix is C_b , which is a combination of both mass matrix M_b and stiffness matrix K_b :

$$C_b = \alpha M_b + \beta K_b, \quad (37)$$

where $\alpha = 2\xi\omega_1\omega_2/\omega_1 + \omega_2$, $\beta = 2\xi/\omega_1 + \omega_2$, ξ is the damping ratio and $\xi = 0.02$ is used in this study, and ω_1 and ω_2 are the first and second fundamental frequency, respectively.

The equation of motion of the beam can be derived by Newton's second law and reads

$$M_b \ddot{w} + C_b \dot{w} + K_b w = F_b(t), \quad (38)$$

where M_b is the mass matrix of the discretized system, which is a $mn \times mn$ diagonal matrix, C_b is damping coefficient matrix, K_b is the stiffness matrix $y_{bf}(t)$ and $y_{br}(t)$, $F_b(t)$ is excitation force, concentrated on each lumped mass, which is induced by the motion of the vehicle, and w is the deflection vector at each of the lumped mass of the beam, the size of which is $mn \times 1$.

The excitation force $F_b(t)$ applied on the bridge model at each of the vehicle wheels is consisted of static and dynamic interaction load, which can be written as

$$F_b(t) = \begin{Bmatrix} 0 \\ 0 \\ k_{tf}(y_f - y_{bf}(t)) + c_{tf}(\dot{y}_f - \dot{y}_{bf}(t)) - \left(m_f + \frac{a_2 m_v}{a}\right)g \\ k_{tr}(y_r - y_{br}(t)) + c_{tr}(\dot{y}_r - \dot{y}_{br}(t)) - \left(m_r + \frac{a_1 m_v}{a}\right)g \end{Bmatrix}. \quad (39)$$

9. Pavement Roughness Model

Pavement roughness is an important parameter affecting the dynamic response of the vehicle-bridge interaction system [95–97]. When the wheels are separated from the road surface [98], the dynamic response of the vehicle-bridge interaction system is dramatically different. While many studies ignore pavement roughness in analyzing vehicle-bridge interaction systems due to its complexity, we do take into account pavement roughness in this study.

Dodds and Robson [99] proposed a method to generate pavement roughness by inverse Fast Fourier Transformation (FFT) based on displacement power spectral density (PSD) function. Pavement roughness in the spatial domain can be determined by

$$r(x) = \sum_{i=1}^m \sqrt{4G_d(n_i)/(\Delta m)} \cos(2\pi n_i x + \theta_i). \quad (40)$$

Here, $r(x)$ is the pavement surface profile function, $x = vt$ is the location indicator, which is time dependent, θ_i is the random phase angle uniformly distributed from 0 to 2π , n_i is the wavenumber (cycle/m), $n_i = i/\Delta m$, $\varphi(n_i)$ is the PSD function for the pavement surface profile ($m^3/(\text{cycle}/m)$), Δ is the interval of successive points of the pavement surface profile, m is the total number of sample points of the surface profile, and $G_d(n_i)$ is the PSD function.

In this paper, the PSD function recommended by ISO-8608 [100] is employed:

$$G_d(n_i) = G_d(n_0) \left(\frac{n_i}{n_0} \right)^{-w} \quad (n_l < n_i < n_u), \quad (41)$$

where n_0 is the reference spatial frequency (= 0.1 cycles/m), $G_d(n_0)$ is the roughness coefficient (m^3/cycle), n_u and n_l are upper and lower cut-off frequencies, w is the exponent of the fitted PSD, and $w = 2$ is adopted according to ISO-8608 [100].

Roads are classified into eight categories from A to H (very good to very poor) in ISO-8608 [100] according to pavement roughness, which is represented by $G_d(n_0)$. Of the eight categories, the first four categories are used for describing pavement road surface while the last four are used for unpaved road surface [101]. The first three categories of pavement roughness shown in Table 3 are examined in this study.

10. Equation of Motion of Vehicle-Bridge Interaction System

For a coupled vehicle-bridge interaction system, the vehicle and the bridge models are coupled by the relative displacement. To make sure that the vehicle is coupled

TABLE 3: ISO-8608 road roughness classification [100].

Road class	$G_d(n_0) \times 10^{-6} \text{ m}$		
	Lower limit	Geometric mean	Upper limit
A	—	16	32
B	32	64	128
C	128	256	512

with the corresponding lumped mass on the bridge, there exists an implicit bound, $dx = vdt$, in the discretization of the beam if velocity is constant though not mandatory. In order to obtain the dynamic response of the vehicle-bridge interaction system, the vehicle model and bridge model should be efficiently coupled together through contact points between the wheel and bridge pavement surface.

The vehicle model needs to be transformed using more convenient variables before coupling with the bridge model. The dynamic motion of the vehicle is described by new variables, as shown in Figure 12. The relation between the variables is as follows:

$$\begin{aligned} \theta &= \frac{u_3 - u_4}{a}, \\ y_v &= \frac{a_1 u_4 + a_2 u_3}{a}, \\ y_f &= u_1, \\ y_r &= u_2, \end{aligned} \quad (42)$$

where u_i ($i = 1, 2, 3, 4$) are the absolute displacement of the bodies and a_1 and a_2 are shown in Figure 1, and $a = a_1 + a_2$.

The conversion is conducted through the following transformation matrix:

$$\begin{Bmatrix} y_v \\ \theta \\ y_f \\ y_r \end{Bmatrix} = \begin{bmatrix} \frac{a_2}{a} & \frac{a_1}{a} & 0 & 0 \\ a & -\frac{1}{a} & 0 & 0 \\ 0 & 0 & 1 & 0 \\ 0 & 0 & 0 & 1 \end{bmatrix} \begin{Bmatrix} u_3 \\ u_4 \\ u_1 \\ u_2 \end{Bmatrix}. \quad (43)$$

After transformation, the equation of motion is written as

$$M_{vt} \ddot{u} + C_{vt} \dot{u} + K_{vt} u = F_v, \quad (44)$$

where

$$F_b(t) = \begin{Bmatrix} 0 \\ 0 \\ k_{tf}z_1 + c_{tf}\dot{z}_1 - \left(m_f + \frac{a_2m_v}{a}\right)g \\ k_{tr}z_2 + c_{tr}\dot{z}_2 - \left(m_r + \frac{a_1m_v}{a}\right)g \end{Bmatrix}, \quad (51)$$

where $\ddot{w}(x_f(t), t)$ and $\ddot{w}(x_r(t), t)$ are acceleration at the lumped mass of the beam at the front wheel and the rear wheel, respectively, locating at $x_f(t)$ and $x_r(t)$; $\dot{r}(x_r(t), t)$ and $\ddot{r}(x_r(t), t)$ are second derivatives, with respect to time t , of the road surface profile at the contacting points at $x_f(t)$ and $x_r(t)$, which is derived according to (32), as

$$\ddot{r}(x) = -(2\pi v)^2 \sum_{i=1}^m \sqrt{\frac{4G_d(n_i)}{(\Delta m)}} n_i^2 \cos(2\pi n_i x + \theta_i). \quad (52)$$

Combining vehicle model in (47) and bridge model in (38), the equation of motion for the coupled vehicle-bridge interaction system can be concisely written as

$$\begin{bmatrix} M_{vz} & M_{4mn} \\ 0 & M_b \end{bmatrix} \begin{Bmatrix} \ddot{z} \\ \ddot{w} \end{Bmatrix} + \begin{bmatrix} C_{vz} & 0 \\ C_{mn4} & C_b \end{bmatrix} \begin{Bmatrix} \dot{z} \\ \dot{w} \end{Bmatrix} + \begin{bmatrix} K_{vz} & 0 \\ K_{mn4} & K_b \end{bmatrix} \begin{Bmatrix} z \\ w \end{Bmatrix} = \begin{Bmatrix} F_{vzr}(t) \\ F_b(t) \end{Bmatrix}, \quad (53)$$

where M_{4mn} is a sparse matrix of size $4 \times mn$ with six nonzeros elements. The two nonzero elements of the first row are a_2m_v/a and a_1m_v/a , corresponding to $w(x_f(t), t)$ and $w(x_r(t), t)$, respectively; the two nonzero elements of the second row are I_v/a and $-I_v/a$, pairing with $w(x_f(t), t)$ and $w(x_r(t), t)$ separately; each nonzero entry for the third and fourth row are m_f and m_r , matching with $w(x_f(t), t)$ and $w(x_r(t), t)$, respectively. C_{mn4} is a sparse matrix of size $mn \times 4$ with two nonzero entries. The two nonzero entries are c_{tf} and c_{tr} , corresponding to $w(x_f(t), t)$ and $w(x_r(t), t)$, in column 3 and column 4, respectively. Similarly, the two nonzero entries for K_{mn4} are $-k_{tf}$ and $-k_{tr}$, occupying the same location as in C_{mn4} .

Using Newmark's method, (53) can be solved and time responses of both the bridge model and vehicle model are obtained. With the known relative displacement from (53), the axle loads at both of the wheels are hence achieved through (51). Given the parameters of the models, M_b , C_b , and K_b for the bridge model, M_{vz} , C_{vz} , and K_{vz} for the vehicle model, the speed of the vehicle, the pavement surface roughness, and the dynamic responses of vehicle-bridge interaction are readily solvable.

11. Case Study

In this section, we use a single-span simply supported beam bridge for a case study. The fundamental frequency of the 30 m single-span bridge is 3.78 Hz. The parameters of the vehicle-bridge interaction system are presented in Table 4.

Parameters of the 4-DOF vehicle model are adopted from [102], which are measurements from the actual vehicle and have been utilized by [77].

11.1. Influence of Number of Elements on Accuracy. In this section, pavement roughness is not considered. In order to select a proper number of elements to represent the bridge to achieve an acceptable level of accuracy, the displacement and the acceleration of the bridge at typical locations of the bridge are calculated with different numbers of elements, while the vehicle velocity remains a constant. It can be seen from Figures 13 and 14 that when the element number is above 300, the influence on it is insignificant.

11.2. Dynamic Force. In this section, pavement roughness is not considered. The dynamic responses of the front wheel and the rear wheel described by relative displacement with respect to the road surface are shown in Figure 15, which incorporate responses at different velocities. It can be observed that when speed increases, the magnitude of relative displacement goes up accordingly. Displacement of the middle span of the bridge when the vehicle traverses the bridge at a constant speed is plotted in Figure 16. The maximum displacement at the middle span of the bridge does not vary significantly. Displacement of the bridge when the front wheel is at $L/2$ is shown in Figure 17. It shows that, at an increasing vehicle velocity, the displacement of the bridge does not necessarily increase accordingly. The interaction force between the vehicle wheel and the bridge is presented in Figure 18. It is observed that peak interaction force grows when vehicle speed increases.

11.3. Dynamic Load Coefficient (DLC). In this section, dynamic load coefficient (DLC) [101] is used to analyze the influence of vehicle speed and pavement roughness. DLC is defined as the ratio between maximum dynamic axle loads and static vehicle load (F_{static}) as follows:

$$DLC = \frac{F_{bmax}}{F_{static}}. \quad (54)$$

For pavement surface roughness levels A, B, and C, the simulated moving force of the front and the rear wheel is shown in Figure 19, and the DLC is shown in Figure 20. DLC is usually in the range of [1.0, 2.0], as shown in Figures 19 and 20. It is noted that, for the dynamic load, coefficient of the front wheel is commonly higher than that of the rear wheel.

For a smooth pavement, the DLC is in the magnitude of 1.01. Clearly, pavement roughness has a significant influence on DLC. At the same velocity, moving force and DLC generally grow with pavement roughness, while for the same pavement roughness, moving force and DLC generally grow with vehicle velocity.

11.4. DLC Standard. Different countries have adopted different criteria for allowable DLC [101]. American Association of Highways and Transportation Officials [103]

TABLE 4: Parameters for the vehicle-bridge interaction system.

Bridge parameters		Vehicle parameters	
$L = 30$ m	$m_v = 17735$ kg	$m_f = 1500$ kg	$m_r = 1000$ kg
$EI = 2.5 \times 10^{10}$ N · m ²	$I_v = 1.47 \times 10^5$ kg · m ²	$c_{sf} = 3.00 \times 10^4$ NM/S	$c_{sr} = 4.00 \times 10^4$ N/m/s
$\rho A = 5.0 \times 10^3$ kg/m	$a_1 = 2.2$ m	$c_{tf} = 3.90 \times 10^3$ N/m/s	$c_{tr} = 4.30 \times 10^3$ N/m/s
$\xi = 0.02$	$a_2 = 1.1$ m	$k_{sf} = 2.47 \times 10^6$ N/m	$k_{sr} = 4.23 \times 10^6$ N/m
		$k_{tf} = 3.74 \times 10^6$ N/m	$k_{tr} = 4.60 \times 10^6$ N/m

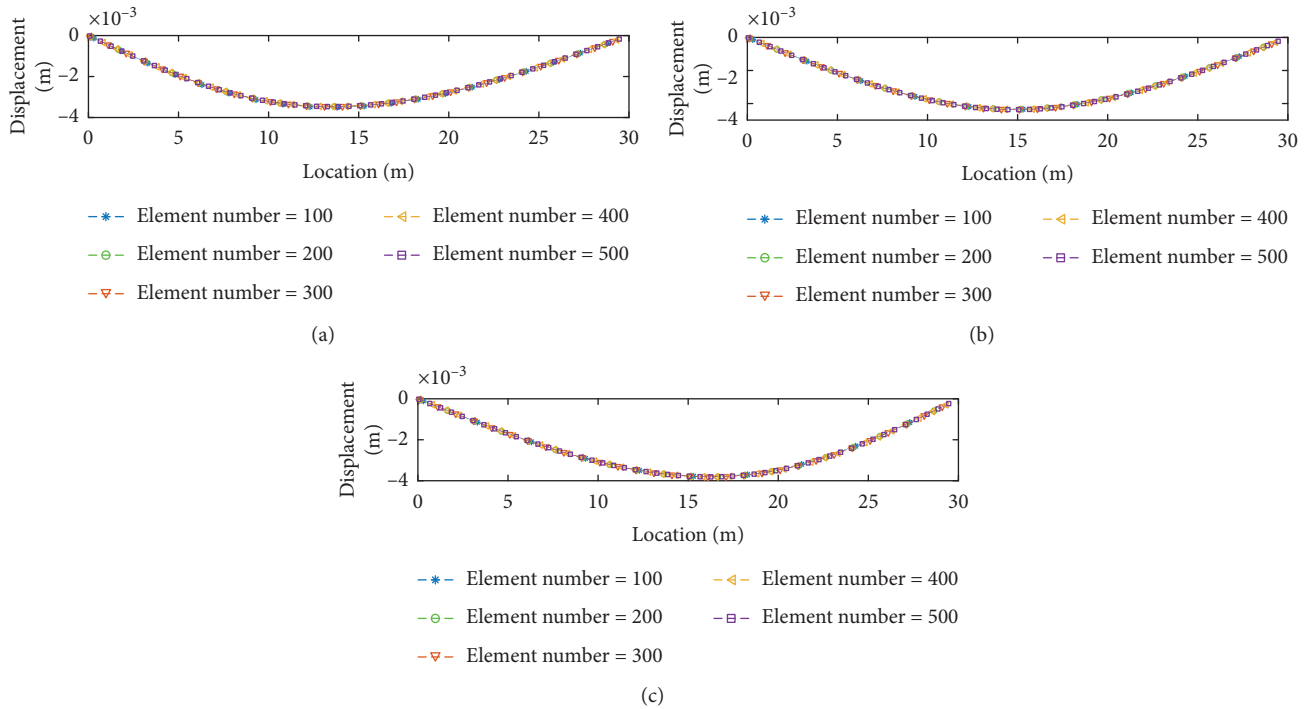


FIGURE 13: Bridge displacement x bridge location (m) and y displacement (m). (a) Front wheel at $L/3$. (b) Front wheel at $L/2$. (c) Front wheel at $2L/3$.

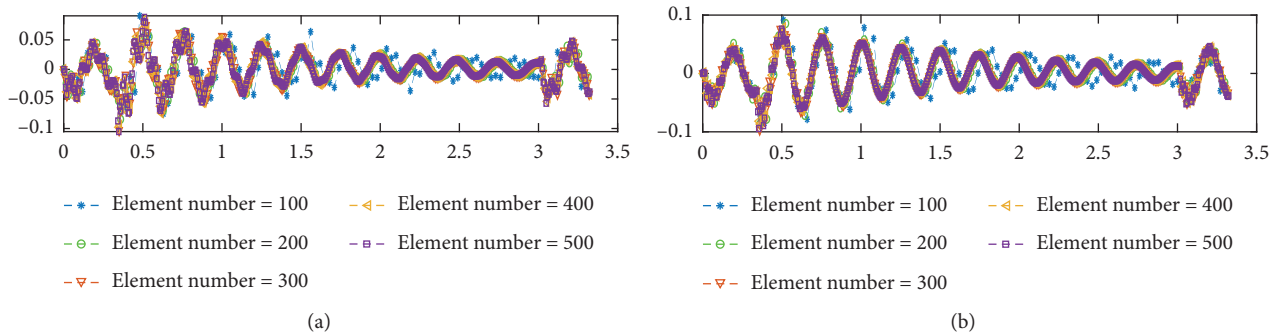


FIGURE 14: Continued.

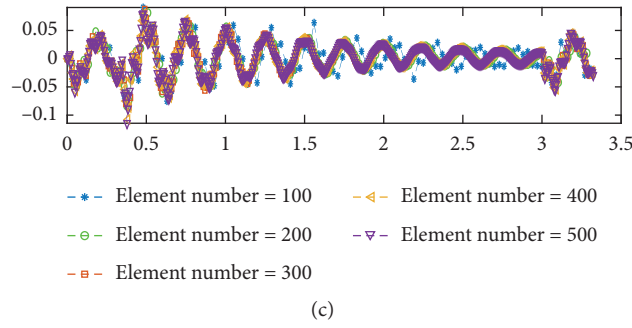


FIGURE 14: Bridge acceleration history x time (s) and y acceleration (m^2/s). (a) At $L/3$. (b) At $L/2$. (c) At $2L/3$.

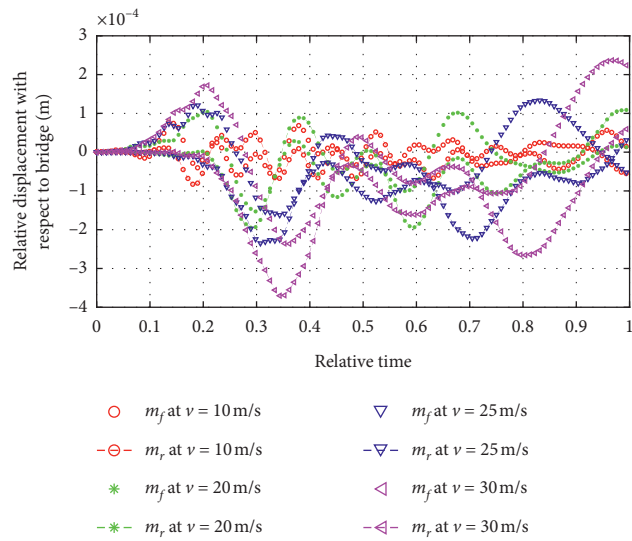


FIGURE 15: The relative displacement of the front wheel and the rear wheel.

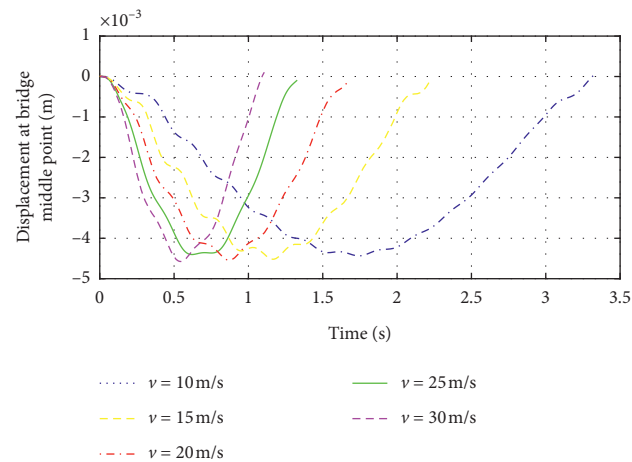


FIGURE 16: Dynamic response of bridge at the middle span.

technical specification uses 0.75 for deck joints, 0.15 for fatigue and fracture limit state, and 0.33 for all other limit states for all other components except joints. Australian technical specification [104] recommends a factor of 0.4 based on static wheel and axle load. Switzerland technical

specification [105] adopts a factor of 0.8 for the bridge with a fundamental frequency between 2 and 4 Hz and 0.4 for frequency above 5 Hz. Chinese technical specification [85] recommends the following impact factor μ (i.e., allowable DLC):

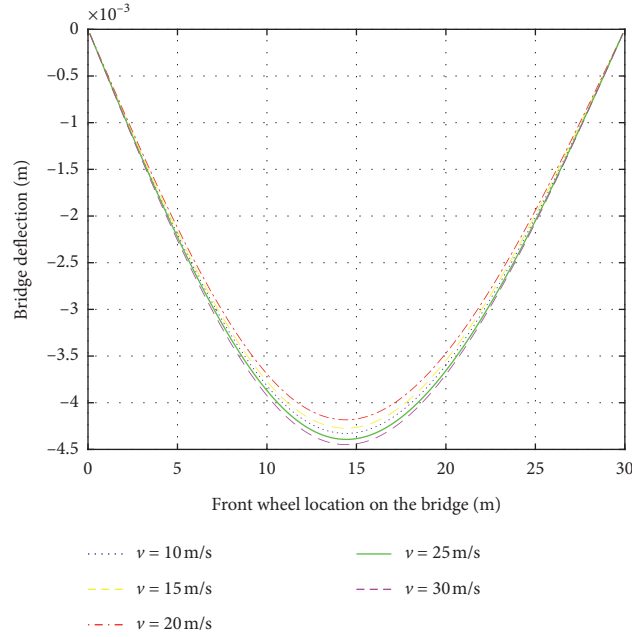


FIGURE 17: Displacement of the bridge with different vehicle velocities.

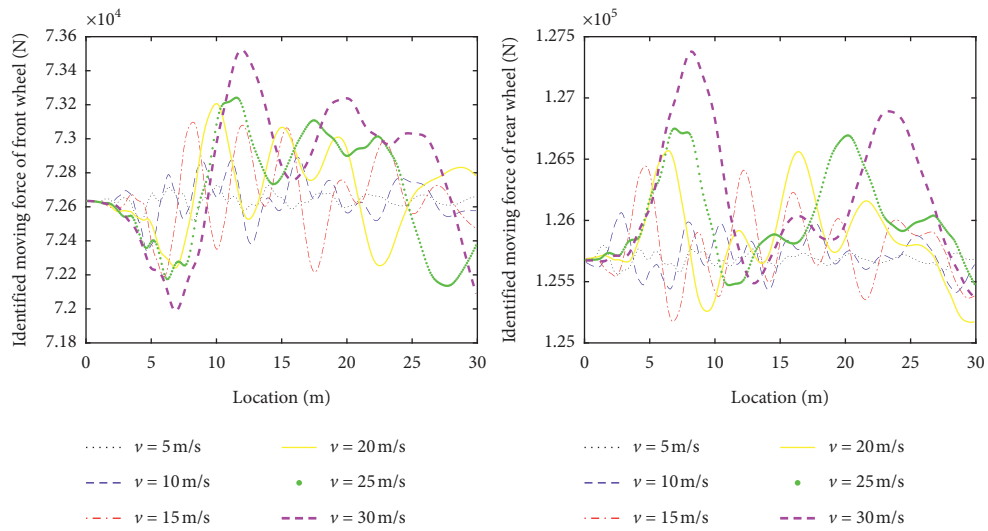


FIGURE 18: Moving force at different vehicle velocities.

$$\mu = \begin{cases} 0.05, & f < 1.5 \text{ Hz}, \\ 0.1767 \ln(f) - 0.0157, & 1.5 \text{ Hz} \leq f \leq 14 \text{ Hz}, \\ 0.45, & f > 14 \text{ Hz}. \end{cases} \quad (55)$$

Here, f is the fundamental frequency of the bridge. For pavement roughness in classes A and B, this study conforms

with specifications of ASSHTO, Australia standard [104] and Switzerland standard [105]. However, the allowable DLC recommended by Chinese technical specification [85] is a little smaller for a bridge with a fundamental frequency of around 4 Hz. For a 30m long single-span bridge, Table 5 shows the recommended DLC based on technical specifications from different countries.

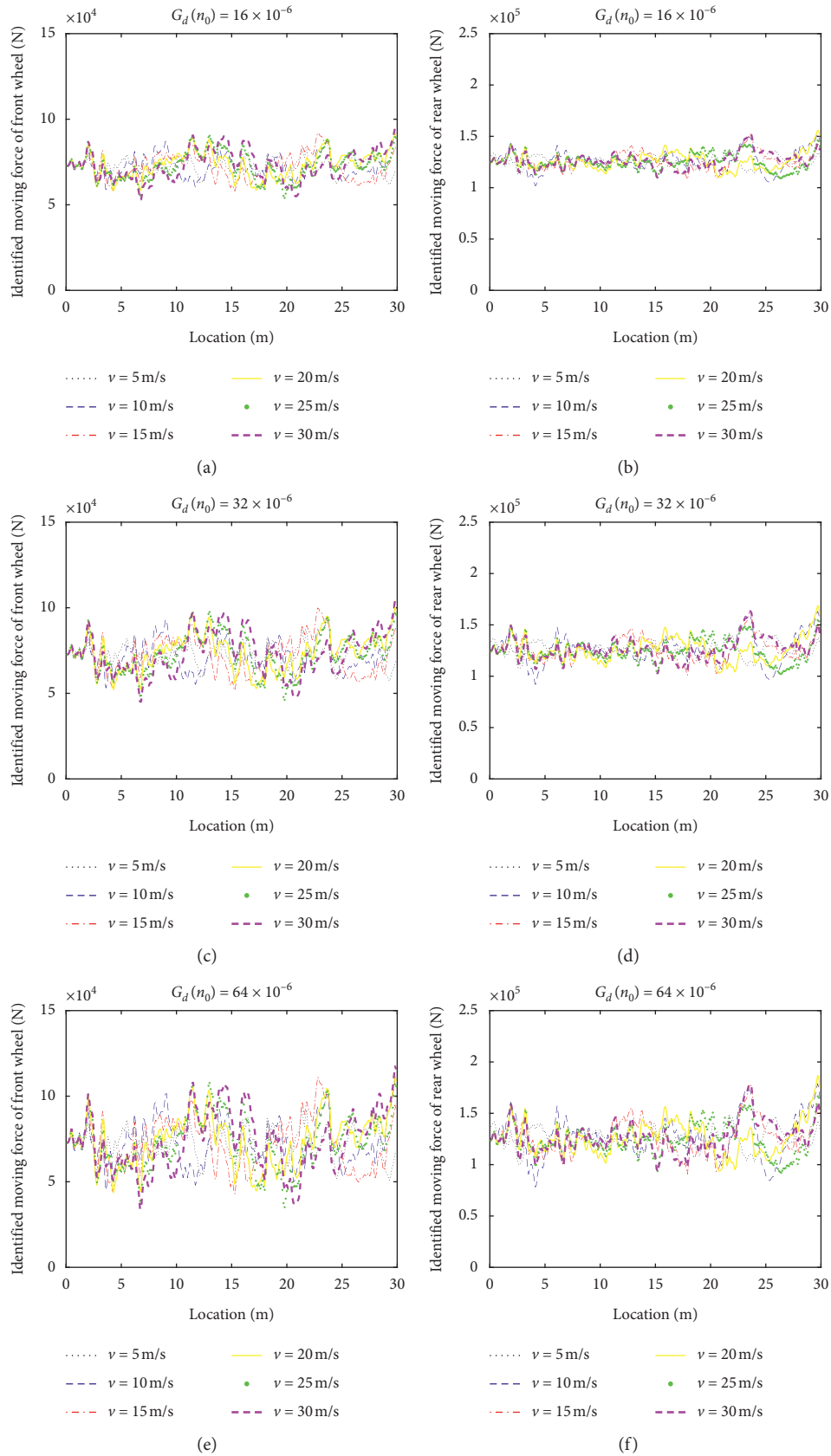


FIGURE 19: Continued.

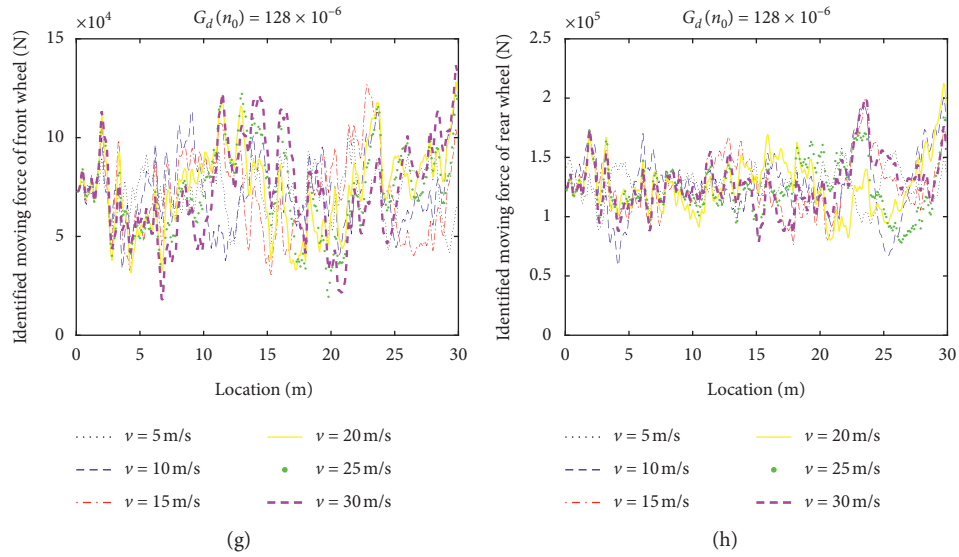


FIGURE 19: Moving force at different velocities and different pavement roughness.

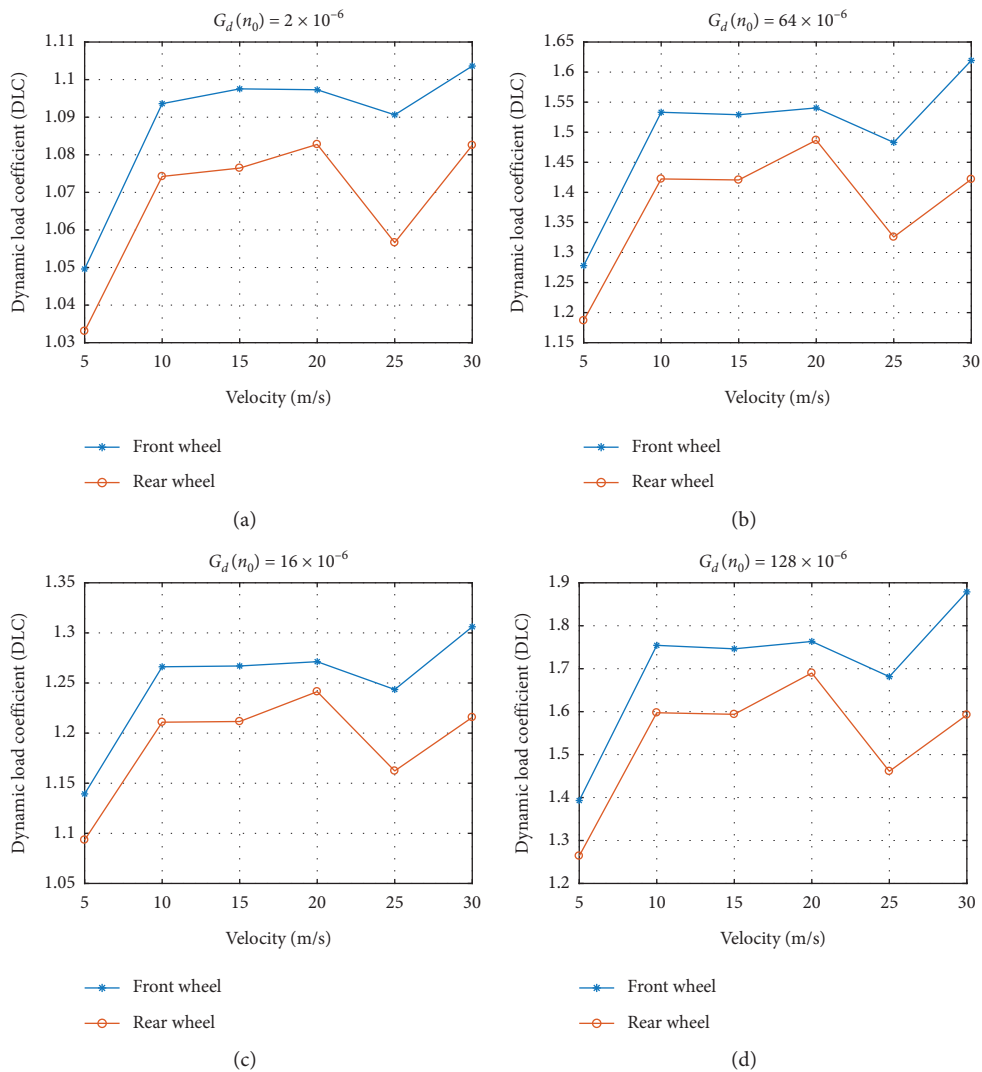


FIGURE 20: Continued.

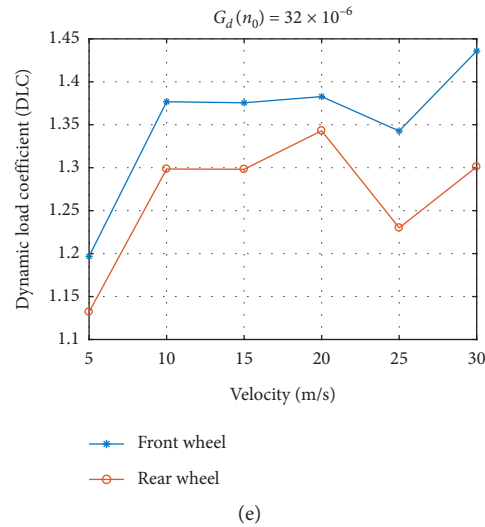


FIGURE 20: Peak dynamic load coefficient of the front wheel and rear wheel.

TABLE 5: Recommended DLC based on technical specifications from different countries.

Code	Specifications for considering dynamic effect	DLC
ASSHTO [103]	0.75 for deck joints, 0.15 for fatigue and fracture limit state, and 0.33 for all other limit states, for all other components except joints	1.33
Chinese code [85]	$\mu = \begin{cases} 0.05, & f < 1.5 \text{ Hz}, \\ 0.1767 \ln(f) - 0.0157, & 1.5 \text{ Hz} \leq f \leq 14 \text{ Hz}, \\ 0.45, & f > 14 \text{ Hz} \end{cases}$	1.22
Australian standard [104]	Recommends a factor of 0.4 based on static wheel and axle load	1.4
Switzerland standard [105]	A factor of 0.8 is adopted for a bridge with a fundamental frequency between 2 and 4 Hz and 0.4 for frequency above 5 Hz	1.8
EN 1991-2 [106]	For carefully maintained track $\Phi_3 = (1.44/\sqrt{L_\Phi} - 0.2) + 0.82$, $1.0 \leq \Phi_3 \leq 1.67$ for a track with standard maintenance $\Phi_3 = (2.16/\sqrt{L_\Phi} - 0.2) + 0.73$ $1.0 \leq \Phi_3 \leq 2.0$ is determinant length depending on the structural element type	1.14 (standard maintenance)

12. Concluding Remarks

The accuracy and efficiency of discretizing the beam in space as lumped masses using the flexibility method and as finite elements using the stiffness method are studied and compared against the analytical solutions of a case study. In general, both methods result in a similar level of accuracy for the same number of elements or nodes as well as the same time step, though the former is slightly better than that of the latter.

The time step plays a significant role in improving accuracy. Decreasing the time step improves significantly the accuracy for both methods at the cost of increased computation time.

Increasing the number of elements or nodes not only slightly improves the accuracy of the flexibility method but also improves considerably the accuracy of the stiffness method.

When the time step is small and the element number is over 50, the increase of the element number does not improve the accuracy considerably for both methods. When the time step is small enough, even a small number of elements could achieve satisfactory accuracy.

In terms of computation efficiency, discretizing the beam as lumped masses will be in theory eight times or in reality two to six times faster than discretizing the beam as finite elements. The former is, even more, faster than the latter when the number of elements or nodes increases. This conclusion paves the way for developing a high efficiency algorithm for the dynamics of vehicle-bridge interaction.

This high efficiency algorithm and corresponding discretization schema are applied to study vehicle-bridge interaction systems, in which a 4-DOFs vehicle model, a simply supported single-span bridge, and ISO pavement roughness model are used. The coupled equation of the vehicle-bridge interaction system is solved directly.

When pavement is smooth, peak interaction force of the front wheel and the rear wheel in general increases when vehicle speed increases, and the DLC is typically below 1.01 for vehicle speed in the range of [0, 30 m/s].

Pavement roughness significantly influences DLC. Therefore, preventative maintenance or timely maintenance of the pavement surface on a bridge to reduce pavement roughness while the bridge is still in a good condition is of

significant importance for the bridge's longevity and life cycle cost benefit.

For class A and B level pavement roughness, DLC is simulated within 2.0, compatible with specifications of ASSHTO, Australian standard [104], and Switzerland standard [105]. However, the Chinese code [85] underestimates the DLC for a bridge with a fundamental frequency of around 4 Hz.

Data Availability

The data, models, or code generated or used during the study are proprietary or confidential in nature and can be obtained from the corresponding author upon request.

Conflicts of Interest

The authors declare that they have no conflicts of interest.

Acknowledgments

This study was sponsored in part by the National Science Foundation, under Grant CMMI-0644552, by the National Natural Science Foundation of China, under grant U1134206, by Yunnan Department of Transportation (7921000079), and by Shangdong Expressway Co. Ltd, under Grant 2017-BLKY4, to which the authors are very grateful.

References

- [1] J. R. Rieker, Y.-H. Lin, and M. W. Trethewey, "Discretization considerations in moving load finite element beam models," *Finite Elements in Analysis and Design*, vol. 21, no. 3, pp. 129–144, 1996.
- [2] L. Wang, X. Kang, and P. Jiang, "Vibration analysis of a multi-span continuous bridge subject to complex traffic loading and vehicle dynamic interaction," *Ksce Journal of Civil Engineering*, vol. 20, no. 1, pp. 323–332, 2016.
- [3] M. Asgari, "Vibration interaction analysis of non-uniform cross-section beam structure under a moving vehicle," *International Journal of Acoustics and Vibration*, vol. 21, pp. 429–439, 2016.
- [4] D. Feng, H. Sun, and M. Q. Feng, "Simultaneous identification of bridge structural parameters and vehicle loads," *Computers & Structures*, vol. 157, pp. 76–88, 2015.
- [5] A. Camara and A. M. Ruiz-Teran, "Multi-mode traffic-induced vibrations in composite ladder-deck bridges under heavy moving vehicles," *Journal of Sound and Vibration*, vol. 355, pp. 264–283, 2015.
- [6] Q. Gao, Z. Wang, H. Jia et al., "Dynamic responses of continuous girder bridges with uniform cross-section under moving vehicular loads," *Mathematical Problems in Engineering*, vol. 2015, Article ID 951502, 29 pages, 2015.
- [7] Q. F. Gao, Z. L. Wang, B. Q. Guo, and C. Chen, "Dynamic responses of simply supported girder bridges to moving vehicular loads based on mathematical methods," *Mathematical Problems in Engineering*, vol. 2014, Article ID 514872, 22 pages, 2014.
- [8] P. Asnachinda, T. Pinkaew, and J. A. Laman, "Multiple vehicle axle load identification from continuous bridge bending moment response," *Engineering Structures*, vol. 30, no. 10, pp. 2800–2817, 2008.
- [9] T. H. T. Chan, L. Yu, S. S. Law, and T. H. Yung, "Moving force identification studies, I: theory," *Journal of Sound and Vibration*, vol. 247, no. 1, pp. 59–76, 2001.
- [10] T. H. T. Chan, S. S. Law, and T. H. Yung, "Moving force identification using an existing prestressed concrete bridge," *Engineering Structures*, vol. 22, no. 10, pp. 1261–1270, 2000.
- [11] T. H. T. Chan, S. S. Law, T. H. Yung, and X. R. Yuan, "An interpretive method for moving force identification," *Journal of Sound and Vibration*, vol. 219, no. 3, pp. 503–524, 1999.
- [12] T. H. T. Chan, L. Yu, S. S. Law, and T. H. Yung, "Moving force identification studies, II: comparative studies," *Journal of Sound and Vibration*, vol. 247, no. 1, pp. 77–95, 2001.
- [13] Y. Chen, M. Q. Feng, and C.-A. Tan, "Modeling of traffic excitation for system identification of bridge structures," *Computer-Aided Civil and Infrastructure Engineering*, vol. 21, no. 1, pp. 57–66, 2006.
- [14] M. Fafard, M. Bennur, and M. Savard, "A general multi-axle vehicle model to study the bridge-vehicle interaction," *Engineering Computations*, vol. 14, 1997.
- [15] A. González, C. Rowley, and E. J. O'Brien, "A general solution to the identification of moving vehicle forces on a bridge," *International Journal for Numerical Methods in Engineering*, vol. 75, no. 3, pp. 335–354, 2008.
- [16] S. Law, T. H. Chan, and Q. Zeng, "Moving force identification—a frequency and time domains analysis," *Journal of Dynamic Systems, Measurement, and Control*, vol. 121, 1999.
- [17] S. S. Law, T. H. T. Chan, Q. X. Zhu, and Q. H. Zeng, "Regularization in moving force identification," *Journal of Engineering Mechanics*, vol. 127, no. 2, pp. 136–148, 2001.
- [18] S. S. Law and X. Q. Zhu, "Study on different beam models in moving force identification," *Journal of Sound and Vibration*, vol. 234, no. 4, pp. 661–679, 2000.
- [19] S. S. Law and Y. L. Fang, "Moving force identification: optimal state estimation approach," *Journal of Sound and Vibration*, vol. 239, no. 2, pp. 233–254, 2001.
- [20] S. S. Law, T. H. T. Chan, and Q. H. Zeng, "Moving force identification: a time domain method," *Journal of Sound and Vibration*, vol. 201, no. 1, pp. 1–22, 1997.
- [21] C. W. Rowley, E. J. O'Brien, A. González, and A. Žnidarič, "Experimental testing of a moving force identification bridge weigh-in-motion algorithm," *Experimental Mechanics*, vol. 49, no. 5, pp. 743–746, 2009.
- [22] S. Q. Wu and S. S. Law, "Moving force identification based on stochastic finite element model," *Engineering Structures*, vol. 32, no. 4, pp. 1016–1027, 2010.
- [23] S. Q. Wu and S. S. Law, "Vehicle axle load identification on bridge deck with irregular road surface profile," *Engineering Structures*, vol. 33, no. 2, pp. 591–601, 2011.
- [24] S. Q. Wu and S. S. Law, "Statistical moving load identification including uncertainty," *Probabilistic Engineering Mechanics*, vol. 29, pp. 70–78, 2012.
- [25] X. Q. Zhu and S. S. Law, "Moving forces identification on a multi-span continuous bridge," *Journal of Sound and Vibration*, vol. 228, no. 2, pp. 377–396, 1999.
- [26] X. Q. Zhu and S. S. Law, "Orthogonal function in moving loads identification on a multi-span bridge," *Journal of Sound and Vibration*, vol. 245, no. 2, pp. 329–345, 2001.
- [27] X. Q. Zhu and S. S. Law, "Practical aspects in moving load identification," *Journal of Sound and Vibration*, vol. 258, no. 1, pp. 123–146, 2002.
- [28] X. Q. Zhu and S. S. Law, "Identification of moving interaction forces with incomplete velocity information," *Mechanical Systems and Signal Processing*, vol. 17, no. 6, pp. 1349–1366, 2003.

- [29] H. Gou, C. Liu, W. Zhou, Y. Bao, and Q. Pu, "Dynamic responses of a high-speed train passing a deformed bridge using a vehicle-track-bridge coupled model," *Proceedings of the Institution of Mechanical Engineers—Part F: Journal of Rail and Rapid Transit*, vol. 235, no. 4, pp. 463–477, 2021.
- [30] D. Huang and T.-L. Wang, "Vibration of highway steel bridges with longitudinal grades," *Computers & Structures*, vol. 69, no. 2, pp. 235–245, 1998.
- [31] P. Cahill, V. Jaksic, J. Keane et al., "Effect of road surface, vehicle, and device characteristics on energy harvesting from bridge-vehicle interactions," *Computer-Aided Civil and Infrastructure Engineering*, vol. 31, no. 12, pp. 921–935, 2016.
- [32] J. Kim and J. P. Lynch, "Experimental analysis of vehicle-bridge interaction using a wireless monitoring system and a two-stage system identification technique," *Mechanical Systems and Signal Processing*, vol. 28, pp. 3–19, 2012.
- [33] D. Stancioiu and H. Ouyang, "Optimal vibration control of beams subjected to a mass moving at constant speed," *Journal of Vibration and Control*, vol. 22, no. 14, pp. 3202–3217, 2016.
- [34] Y. Pi and H. Ouyang, "Vibration control of beams subjected to a moving mass using a successively combined control method," *Applied Mathematical Modelling*, vol. 40, no. 5–6, pp. 4002–4015, 2016.
- [35] J. Hu, W. Ma, and S. Luo, "Coupled dynamic analysis of low and medium speed maglev vehicle-bridge interaction using SIMPACK," *Proceedings of the Institution of Mechanical Engineers—Part F: Journal of Rail and Rapid Transit*, vol. 235, no. 3, pp. 377–389, 2021.
- [36] S. S. Law and X. Q. Zhu, "Bridge dynamic responses due to road surface roughness and braking of vehicle," *Journal of Sound and Vibration*, vol. 282, no. 3–5, pp. 805–830, 2005.
- [37] E. J. O'Brien, P. Rattigan, A. González, J. Dowling, and A. Žnidarič, "Characteristic dynamic traffic load effects in bridges," *Engineering Structures*, vol. 31, no. 7, pp. 1607–1612, 2009.
- [38] L. Sun, "Dynamic displacement response of beam-type structures to moving line loads," *International Journal of Solids and Structures*, vol. 38, no. 48–49, pp. 8869–8878, 2001.
- [39] L. Sun, W. Gu, and F. Luo, "Steady-state wave propagation in multilayered viscoelastic media excited by a moving dynamic distributed load," *Journal of Applied Mechanics*, vol. 76, 2009.
- [40] L. Sun and F. Luo, "Steady-state dynamic response of a Bernoulli–Euler beam on a viscoelastic foundation subject to a platoon of moving dynamic loads," *Journal of Vibration and Acoustics*, vol. 130, 2008.
- [41] S. Q. Wu and S. S. Law, "Dynamic analysis of bridge with non-Gaussian uncertainties under a moving vehicle," *Probabilistic Engineering Mechanics*, vol. 26, no. 2, pp. 281–293, 2011.
- [42] H. Xia, Y. Deng, C. Xia, G. De Roeck, L. Qi, and L. Sun, "Dynamic analysis of coupled train - ladder track - elevated bridge system," *Structural Engineering & Mechanics*, vol. 47, no. 5, pp. 661–678, 2013.
- [43] V. Pakrashi, A. O'Connor, and B. Basu, "Effect of tuned mass damper on the interaction of a quarter car model with a damaged bridge," *Structure and Infrastructure Engineering*, vol. 6, no. 4, pp. 409–421, 2010.
- [44] B. A. D. Piombo, A. Fasana, S. Marchesiello, and M. Ruzzene, "Modelling and identification of the dynamic response of a supported bridge," *Mechanical Systems and Signal Processing*, vol. 14, no. 1, pp. 75–89, 2000.
- [45] L. Sun, "Closed-form representation of beam response to moving line loads," *Journal of Applied Mechanics*, vol. 68, no. 2, pp. 348–350, 2001.
- [46] L. Sun, "Time-harmonic elastodynamic green functions of plates for line loads," *Journal of Sound and Vibration*, vol. 246, no. 2, pp. 337–348, 2001.
- [47] L. Sun and F. Luo, "Transient wave propagation in multi-layered viscoelastic media: theory, numerical computation, and validation," *Journal of Applied Mechanics*, vol. 75, 2008.
- [48] G. H. Tan, G. H. Brameld, and D. P. Thambiratnam, "Development of an analytical model for treating bridge-vehicle interaction," *Engineering Structures*, vol. 20, no. 1–2, pp. 54–61, 1998.
- [49] Z.-P. Zeng, F.-S. Liu, Z.-H. Lu, Z.-W. Yu, P. Lou, and L.-K. Chen, "Three-dimensional rail-bridge coupling element of unequal lengths for analyzing train-track-bridge interaction system," *Latin American Journal of Solids and Structures*, vol. 13, no. 13, pp. 2490–2528, 2016.
- [50] N. Zhang, S. Zhou, H. Xia, and L. Sun, "Evaluation of vehicle-track-bridge interacted system for the continuous CRTS-II non-ballast track slab," *Science China Technological Sciences*, vol. 57, no. 10, pp. 1895–1901, 2014.
- [51] H. Aied, A. González, and D. Cantero, "Identification of sudden stiffness changes in the acceleration response of a bridge to moving loads using ensemble empirical mode decomposition," *Mechanical Systems and Signal Processing*, vol. 66–67, pp. 314–338, 2016.
- [52] E. O'Brien, C. Carey, and J. Keenahan, "Bridge damage detection using ambient traffic and moving force identification," *Structural Control and Health Monitoring*, vol. 22, no. 12, pp. 1396–1407, 2015.
- [53] K. Nguyen, B. Freytag, M. Ralbovsky, and O. Rio, "Assessment of serviceability limit state of vibrations in the UHPFRC-Wild bridge through an updated FEM using vehicle-bridge interaction," *Computers & Structures*, vol. 156, pp. 29–41, 2015.
- [54] Q. Zhang, Ł. Jankowski, and Z. Duan, "Simultaneous identification of moving masses and structural damage," *Structural and Multidisciplinary Optimization*, vol. 42, no. 6, pp. 907–922, 2010.
- [55] V. Jaksic, A. O'Connor, and V. Pakrashi, "Damage detection and calibration from beam-moving oscillator interaction employing surface roughness," *Journal of Sound and Vibration*, vol. 333, no. 17, pp. 3917–3930, 2014.
- [56] L. Majumder and C. S. Manohar, "A time-domain approach for damage detection in beam structures using vibration data with a moving oscillator as an excitation source," *Journal of Sound and Vibration*, vol. 268, no. 4, pp. 699–716, 2003.
- [57] W. Xiang, D. Wang, and H. Zhu, "Damage identification in a plate structure based on strain statistical moment," *Advances in Structural Engineering*, vol. 17, no. 11, pp. 1639–1655, 2014.
- [58] H. A. Nasrallah and C. S. Manohar, "A particle filtering approach for structural system identification in vehicle-structure interaction problems," *Journal of Sound and Vibration*, vol. 329, no. 9, pp. 1289–1309, 2010.
- [59] R. Sieniawska, P. Śniady, and S. Żukowski, "Identification of the structure parameters applying a moving load," *Journal of Sound and Vibration*, vol. 319, no. 1–2, pp. 355–365, 2009.
- [60] H. Sun and R. Betti, "Simultaneous identification of structural parameters and dynamic input with incomplete output-only measurements," *Structural Control and Health Monitoring*, vol. 21, no. 6, pp. 868–889, 2014.

- [61] P. Chang and X. Zhao, "Exact solution of vibrations of beams with arbitrary translational supports using shape function method," *Asian Journal of Civil Engineering*, vol. 21, no. 7, pp. 1269–1286, 2020.
- [62] X. Zhao, "Free vibration analysis of cracked Euler-Bernoulli beam by Laplace transformation considering stiffness reduction," *Romanian Journal of Acoustics and Vibration*, vol. 16, pp. 166–173, 2019.
- [63] X. Zhao, "Exact vibration analysis of beams with arbitrary intermediate elastic supports, concentrated masses and non-classical boundary conditions under an axial force using shape function method," *Romanian Journal of Acoustics and Vibration*, vol. 17, pp. 57–76, 2020.
- [64] X. Zhao, "Solution to vibrations of double-beam systems under general boundary conditions," *Journal of Engineering Mechanics*, vol. 147, no. 10, 2021.
- [65] D. F. Zhang and N. Zhang, "Image-based crack detection and properties retrieval for high-speed railway bridge," *Information Technology and Computer Application Engineering*, Taylor & Francis, Milton Park, UK, 2014.
- [66] P. Antolín, N. Zhang, J. M. Goicolea, H. Xia, M. Á. Astiz, and J. Oliva, "Consideration of nonlinear wheel-rail contact forces for dynamic vehicle-bridge interaction in high-speed railways," *Journal of Sound and Vibration*, vol. 332, no. 5, pp. 1231–1251, 2013.
- [67] F. Zeng, H. Xie, Q. Liu, F. Li, and W. Tan, "Design and optimization of a new composite bumper beam in high-speed frontal crashes," *Structural and Multidisciplinary Optimization*, vol. 53, no. 1, pp. 115–122, 2016.
- [68] Y. Hu, S. Wu, P. J. Withers et al., "Corrosion fatigue lifetime assessment of high-speed railway axle EA4T steel with artificial scratch," *Engineering Fracture Mechanics*, vol. 245, Article ID 107588, 2021.
- [69] Y.-B. Yang and J.-D. Yau, "Vehicle-bridge interaction element for dynamic analysis," *Journal of Structural Engineering*, vol. 123, no. 11, pp. 1512–1518, 1997.
- [70] K. Henchi, M. Fafard, M. Talbot, and G. Dhatt, "An efficient algorithm for dynamic analysis of bridges under moving vehicles using a coupled modal and physical components approach," *Journal of Sound and Vibration*, vol. 212, no. 4, pp. 663–683, 1998.
- [71] B. Yang, C. A. Tan, and L. A. Bergman, "Direct numerical procedure for solution of moving oscillator problems," *Journal of Engineering Mechanics*, vol. 126, no. 5, pp. 462–469, 2000.
- [72] Z. R. Lu and J. K. Liu, "Identification of both structural damages in bridge deck and vehicular parameters using measured dynamic responses," *Computers & Structures*, vol. 89, no. 13–14, pp. 1397–1405, 2011.
- [73] S. Q. Wu and S. S. Law, "Dynamic analysis of bridge-vehicle system with uncertainties based on the finite element model," *Probabilistic Engineering Mechanics*, vol. 25, no. 4, pp. 425–432, 2010.
- [74] H. Moghimi and H. R. Ronagh, "Development of a numerical model for bridge-vehicle interaction and human response to traffic-induced vibration," *Engineering Structures*, vol. 30, no. 12, pp. 3808–3819, 2008.
- [75] A. González, P. Rattigan, E. J. O'Brien, and C. Caprani, "Determination of bridge lifetime dynamic amplification factor using finite element analysis of critical loading scenarios," *Engineering Structures*, vol. 30, no. 9, pp. 2330–2337, 2008.
- [76] P. Lou and Q.-y. Zeng, "Formulation of equations of motion of finite element form for vehicle-track-bridge interaction system with two types of vehicle model," *International Journal for Numerical Methods in Engineering*, vol. 62, no. 3, pp. 435–474, 2005.
- [77] S. S. Law, J. Q. Bu, X. Q. Zhu, and S. L. Chan, "Vehicle axle loads identification using finite element method," *Engineering Structures*, vol. 26, no. 8, pp. 1143–1153, 2004.
- [78] S. Q. Wu and S. S. Law, "Evaluating the response statistics of an uncertain bridge-vehicle system," *Mechanical Systems and Signal Processing*, vol. 27, pp. 576–589, 2012.
- [79] T. H. T. Chan, L. Yu, and S. S. Law, "Comparative studies on moving force identification from bridge strains in laboratory," *Journal of Sound and Vibration*, vol. 235, no. 1, pp. 87–104, 2000.
- [80] L. Deng and C. S. Cai, "Identification of parameters of vehicles moving on bridges," *Engineering Structures*, vol. 31, no. 10, pp. 2474–2485, 2009.
- [81] L. Lu Deng and C. S. Cai, "Identification of dynamic vehicular axle loads: theory and simulations," *Journal of Vibration and Control*, vol. 16, no. 14, pp. 2167–2194, 2010.
- [82] X. Q. Zhu and S. S. Law, "Damage detection in simply supported concrete bridge structure under moving vehicular loads," *Journal of Vibration and Acoustics*, vol. 129, no. 1, pp. 58–65, 2007.
- [83] A. Yan and J.-C. Golinval, "Structural damage localization by combining flexibility and stiffness methods," *Engineering Structures*, vol. 27, no. 12, pp. 1752–1761, 2005.
- [84] S. Weng, H.-P. Zhu, Y. Xia, L. Ye, and X.-Y. Hu, "Construction of stiffness and flexibility for substructure-based model updating," *Mathematical Problems in Engineering*, vol. 2013, Article ID 706798, 14 pages, 2013.
- [85] L. Cccc Highway Consultants Co, *General Specifications for Design of Highway Bridges and Culverts (JTG D60-2015)* China Communication Press, Beijing, China, 2015.
- [86] M. Olsson, "On the fundamental moving load problem," *Journal of Sound and Vibration*, vol. 145, no. 2, pp. 299–307, 1991.
- [87] A. Shabana, *Vibration of Discrete and Continuous Systems*, Springer Science & Business Media, Berlin, Germany, 2012.
- [88] J. N. Reddy, "Nonlocal theories for bending, buckling and vibration of beams," *International Journal of Engineering Science*, vol. 45, no. 2–8, pp. 288–307, 2007.
- [89] E. Reynders and G. De Roeck, "A local flexibility method for vibration-based damage localization and quantification," *Journal of Sound and Vibration*, vol. 329, no. 12, pp. 2367–2383, 2010.
- [90] A. Jensen and H. H. Chenoweth, *Statics and Strength of Materials*, McGraw-Hill, New York, NY, USA, 1975.
- [91] A. I. o.S. Construction, *Steel Construction Manual*, Amer Institute of Steel Construction, Chicago, IL, USA, 2005.
- [92] K. C. Rockey, H. R. Evans, D. W. Griffiths, and D. A. Nethercot, "The finite element method-A basic introduction," *Strain*, vol. 11, no. 3, p. 140, 1975.
- [93] K.-J. Bathe, *Finite Element Procedures in Engineering Analysis*, Massachusetts Institute of Technology, Cambridge, MA, USA, 1982.
- [94] A. K. Chopra, *Dynamics of Structures: Theory and Applications to Earthquake Engineering*, Prentice-Hall, Hoboken, NJ, USA, 4th edition, 2011.
- [95] A. Rezaiguia, N. Ouelaa, D. F. Laefer, and S. Guenfoud, "Dynamic amplification of a multi-span, continuous orthotropic bridge deck under vehicular movement," *Engineering Structures*, vol. 100, pp. 718–730, 2015.

- [96] H. H. Nassif, M. Liu, and O. Ertekin, "Model validation for bridge-road-vehicle dynamic interaction system," *Journal of Bridge Engineering*, vol. 8, no. 2, pp. 112–120, 2003.
- [97] H. H. Nassif and M. Liu, "Analytical modeling of bridge-road-vehicle dynamic interaction system," *Journal of Vibration and Control*, vol. 10, no. 2, pp. 215–241, 2004.
- [98] Y. S. Cheng, F. T. K. Au, Y. K. Cheung, and D. Y. Zheng, "On the separation between moving vehicles and bridge," *Journal of Sound and Vibration*, vol. 222, no. 5, pp. 781–801, 1999.
- [99] C. J. Dodds and J. D. Robson, "The description of road surface roughness," *Journal of Sound and Vibration*, vol. 31, no. 2, pp. 175–183, 1973.
- [100] S. Iso 8608, *Mechanical Vibration—Road Surfaces Profiles—Reporting of Measured Data*, International Organization for Standardization, Geneva, Switzerland, 1995.
- [101] L. Ding, H. Hao, and X. Zhu, "Evaluation of dynamic vehicle axle loads on bridges with different surface conditions," *Journal of Sound and Vibration*, vol. 323, no. 3-5, pp. 826–848, 2009.
- [102] N. L. Mulcahy, "Bridge response with tractor-trailer vehicle loading," *Earthquake Engineering & Structural Dynamics*, vol. 11, no. 5, pp. 649–665, 1983.
- [103] L. Aashto, *AASHTO LRFD Bridge Design Specifications*, American Association of State Highway Transportation Officials, Washington DC, USA, 2010.
- [104] A. S. AS5100.2, *Bridge Design Part2: Design Loads*, Standards Australia International Ltd., Sydney, Australia, 2004.
- [105] S. 160E, *Einwirkungen auf Tragwerke, Entwurf, Schweiz*, Ingenieur und Architekten-Verein, Zurich, Switzerland, 1988.
- [106] E. Cen, *2 Eurocode 1: Actions on Structures-Part 2: Traffic Loads on Bridges*, Paris, France, 2003.

Research Article

Using Continuum-Discontinuum Element Method to Model the Foliation-Affected Fracturing in Rock Brazilian Test

Qunlei Zhang,^{1,2} Zihan Zhi,¹ Chun Feng,³ Ruixia Li,¹ Jinchao Yue ,¹ and Junyu Cong⁴

¹School of Water Conservancy Engineering, Zhengzhou University, Zhengzhou 450001, China

²School of Civil Engineering and Communication, North China University of Water Resources and Electric Power, Zhengzhou 450045, China

³Institute of Mechanics, Chinese Academy of Sciences, Beijing 100190, China

⁴Gdem Technology, Beijing, Co., Ltd., Beijing 100096, China

Correspondence should be addressed to Jinchao Yue; yuejc@zzu.edu.cn

Received 28 April 2021; Accepted 26 June 2021; Published 7 July 2021

Academic Editor: Adolfo Preciado

Copyright © 2021 Qunlei Zhang et al. This is an open access article distributed under the Creative Commons Attribution License, which permits unrestricted use, distribution, and reproduction in any medium, provided the original work is properly cited.

In this study, the continuum-discontinuum element method (CDEM) was used to investigate the tensile fracture mechanism of rock materials. An isotropic rock disk model and models considering different foliation inclinations were established, and three schemes were used to simulate the rock fracturing in Brazilian test. Then, the influences of the rock matrix and foliation strengths on anisotropy rock fracturing were investigated. Furtherly, simulation results were verified, and the rock fracture mechanisms were discussed. The results show that the rock fracturing in Brazilian test can be accurately simulated by CDEM, which is in accordance with the experimental results. For isotropic and horizontal foliation rock, the stress concentration in loading positions causes a local fracture of rock sample, and application of a local strengthening scheme can simulate the integral tension fracture of sample middle. As the foliation angle varies from 15° to 45°, the rock fracturing is affected by the stress concentration and foliation distribution. In splitting simulation, a strengthening scheme should be adopted to overcome this influence. As a result, the rock sample generates the sliding and compression-shear fracture. As the foliation angle changes from 45° to 75°, the foliation, rather than the matrix, dominates the fracture behavior of rock sample. For vertical foliations' rock, as the middle foliation thickness is appropriately broadened, the simulation results are reasonable. In general, the tensile strength of anisotropic rock entirely decreases with an increase of foliation angle, and the effect of foliation strength on the tensile strength rock sample is larger than that of the rock matrix.

1. Introduction

Because the fracture resistance of rock material is weaker under tension than under compression, so the investigation of rock tensile fracturing is important. The Brazilian disk testing method is usually used to obtain the tensile strength of rock material [1–3]. Meanwhile, rock anisotropy such as fissuring, jointing, and foliation are the important factors in studying the situ stress measurements, displacement control in rock, and excavation damage development. Currently, investigating the fracture mechanism of anisotropy rock materials by Brazilian testing has caused more and more attention.

In experimental research of rock with weak structures, the plastic deformation and failure mechanisms of shale are highly dependent on the orientation of the bedding planes [4–7]. By observing the crack initiation and propagation in the rock, the effect of anisotropy on the failure mechanism was studied, and the failure modes were classified into sliding and nonsliding failure [8–10]. In uniaxial and triaxial compressive strength tests, the shear sliding along the weak planes could reduce the strength of anisotropic rock [11, 12]. Due to the complexity of rock failure, the comprehensive observation and data acquisition of rock fracture process are easily achieved by simulation. The fracturing of the rock sample with a hole was simulated by

the boundary element code DIGS, and the influence of a tensile stress gradient on the rock fracture initiation and crack growth was discussed [13]. The dynamic fracturing characteristics of rock and concrete materials were investigated by the finite element method (FEM) [14, 15]. The extended finite element method (XFEM) was used to evaluate the effect of the specimen flat end in dynamic Brazilian tests [16]. In anisotropic rock mass, due to the interaction of intact rock fracture and joint face sliding, the failure mechanism of rock mass has been discussed by certain studies using the discrete element method (DEM) [17, 18]. Based on the nanoscale structure of shale, a model simulating nanoscale rock anisotropy was proposed [19, 20]. The failure characteristics of phyllite specimens under Brazilian tests are investigated by the particle discrete element method, and the influence of rock foliation strength and matrix microstructure was also studied numerically [21]. A modified smooth joint model was proposed to simulate the failure behavior of jointed rock mass, and the roughness effect of the joint face under different normal stresses was discussed [22–25]. The mechanics behavior of foliated rock samples in the Brazilian tests was simulated using Universal Distinct Element Code (UDEC) [26]. In general, the continuum mechanics method is suitable for analyzing the small deformation and damage behavior of materials, and the discrete element method can easily analyze the rock fracturing and motion. A continuum-discontinuum element method (CDEM) combines the advantages of the finite element method and the discrete element method, which has gradually become an effective simulation method to study the failure mechanisms of rock materials [27–33].

In this context, based on CDEM, the force and deformation of a loading plate in the Brazilian test were analyzed by the continuum element method, and the discontinuum element method was used to study the fracturing of rock samples. An isotropic rock disk model and models considering different foliation angles were sequentially established. The splitting simulations of rock samples were conducted by three simulation schemes. Furthermore, the effects of matrix and foliation strengths on rock fracturing were investigated. Finally, simulation results were verified, and the fracturing mechanisms of rock materials were discussed.

2. Simulation Program

2.1. Simulation Method. In this paper, a coupling method of particle-block element based on the continuum-discontinuum element method (CDEM) is used to investigate the tensile fracture mechanism of rock materials. The simulation method is indicated in Figure 1. CDEM adopts a time-stepping, explicit scheme, and the equilibrium equations are as follows:

$$\begin{aligned} [M]\{\ddot{u}\} + [C]\{\dot{u}\} &= \{F\}_{\text{ext}}, \\ \{F\}_{\text{ext}} &= \{F\}_p + \{F\}_t [F_k], \end{aligned} \quad (1)$$

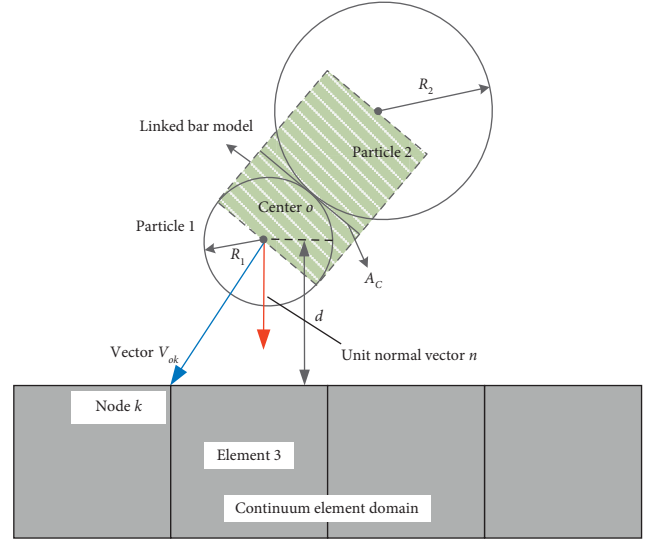


FIGURE 1: Continuum-discontinuum element model.

where $[M]$ denotes the nodal mass matrix, $[C]$ is the damping matrix, $\{u\}$ denotes the displacement vector, and $\{F\}_{\text{ext}}$ denotes the vector of external forces, which includes the node internal force matrix $[F_k]$, the particle contact force $\{F\}_p$, and external loading force $\{F\}_t$.

For the block elements of the continuum element method, the internal force of the element node in the continuum element method is calculated by

$$[F_k] = [F_k^0] + \sum_{i=1}^N [B_i^T] \cdot [D] \cdot [B_i] \cdot [\Delta u] \cdot \omega_i \cdot J_i, \quad (2)$$

where $[F_k^0]$ is the node internal force matrix at the previous step, i is the element Gaussian point, N is the number of Gaussian points, $[B_i]$ is the strain matrix, $[\Delta u]$ is the node incremental displacement vector, $[D]$ is the element elastic matrix, ω_i is the integral coefficient, and J_i is the Jacobian determinant value.

For the particle elements of the discontinuum element method, the linked bar model combined with the Mohr–Coulomb criterion and maximum tensile stress criterion is used to simulate the rock breaking and moving [30–32].

The contact forces between two contact particles are calculated by

$$\begin{aligned} F_i(t + \Delta t) &= F_i(t) - K_i \Delta u_i, \quad i = 1, 2, \\ A_c &= \min(2R_i), \quad i = 1, 2, \\ K_i &= \tilde{E}_i A_c (R_1 + R_2), \quad i = 1, 2, \end{aligned} \quad (3)$$

where $F_i(t + \Delta t)$ and $F_i(t)$ are the contact forces at the time of $t + \Delta t$ and t , F_1 and F_2 are the normal and tangential contact forces, Δu_1 and Δu_2 are the normal and tangential increments of contact displacement, R_1 and R_2 represent the radius of contact particles, K_1 and K_2 represent the normal and tangential stiffness, \tilde{E}_1 and \tilde{E}_2 represent elastic and shear modulus, and A_c is the contact area of particles.

The contact forces of equations (3) are modified by

$$\begin{aligned} \text{if } F_1 - TA_c \geq 0, \text{ then } F_1 = F_2 = 0, T = C = 0, \\ \text{if } F_2 - F_1 \tan(\varphi) - CA_c \geq 0, \text{ then } F_2 = F_1 \tan(\varphi), T = C = 0. \end{aligned} \quad (4)$$

In a 2D numerical model, the contact state between block element and particle element is determined by the relative position between particle center and block element boundary. The contact pair will be created when the distance between particle center and block edge is less than or equal to the radius of the particle, that is,

$$d = |V_{ok} \cdot n| \leq R_1, \quad (5)$$

where d is the distance between particle center and block edge, k is the node of block element, V_{ok} is the relative position vector for particle center o to node k , n is the unit normal vector of continuum element domain boundary, and R_1 is the radius of the particle close to target block element.

2.2. Numerical Models and Parameters. The schematic diagram of Brazilian disk test and isotropic and anisotropic rock models are shown in Figure 2. The rock sample consists of 14154 particles, each with a radius of 0.2 mm. The bearing plate consists of 320 finite element elements. The loading velocity of the top bearing plate is 1 nm/step, and the bottom nodes of the lower bearing plate are fixed. For the anisotropic rock sample, the spacing between foliation planes is 5 mm.

Based on CDEM, the equivalent macrostrain energy of particles with macroscale mechanical parameters coincides well with the strain energy computed by FEM, when the number of contact particles reaches a certain value [32]. The fracturing and moving process of rock is well simulated with macroscale mechanical parameters [31, 32]. The numerical parameters in this study are shown in Table 1 [21].

2.3. Simulation Scheme. To investigate the fracture mechanism of rock materials in Brazilian test, the failure of isotropic rock sample was firstly simulated. Then, the fracturing simulations of rock samples with 0° , 15° , 30° , 45° , 60° , 75° , and 90° foliations were conducted. Finally, the splitting simulations of rock samples with different matrices and foliation strengths were conducted, which were used to investigate the effect of strength parameters on the anisotropic rock failure.

3. Results and Analysis

3.1. Simulation Results of Isotropic Rock and Horizontal Foliation Rock. Adopting different simulation schemes in the Brazilian test, the failure results of isotropic and horizontal foliation rock samples are shown in Figure 3. During the stiff wire loading, the stress concentration near the loading positions causes a local failure of rock sample as shown in model I, and the tensile strength obtained by Brazilian test is smaller than the actual tension strength of rock materials. To solve this problem, a scheme strengthening the local zone of numerical sample is adopted to simulate the splitting of

isotropic and horizontal foliation rock. In this scheme, the strengthening zone size is $2 \text{ mm} \times 4 \text{ mm}$, and the local strength parameters are 8 times the strength parameters of Table 1. As shown in model II and III of Figure 3, the integral tensile fracture through the specimen middle can be well simulated. As indicated in the strength histogram, a proper tensile strength of the rock sample in the Brazilian test can be obtained by the splitting simulation, and the tensile strength of isotropic rock sample is slightly larger than that of horizontal foliation rock sample.

3.2. Simulation Results of Rock with Oblique Foliations. For the anisotropic rock with 15° , 30° , 45° , 60° , and 75° foliations, the fracturing processes of rock samples in the Brazilian test were simulated, as shown in Figure 4. To comprehensively analyze the fracture mechanism of anisotropic rock, the strengthening scheme of Section 3.1 was adopted, and simulations without a strengthening scheme were also conducted.

In simulations without a strengthening scheme, as the foliation angle is 15° , the vertical fracture penetrates the entire rock sample, and there only exists a shorter crack propagating along the foliation near the lower loading location of the sample. As the foliation angles are 30° and 45° , two symmetrical cracks generate in two foliations near the upper and lower loading locations. As the foliation angles continue to increase, the orientation of main crack will be closer to the vertical central axis. In simulations with a strengthening scheme, the 15° foliation rock sample fractures along the foliations near the strengthening zone. As the foliation angle is 30° , the strengthening zone covers the foliation near the loading positions, so the cracks propagate along the foliation below the strengthening zone. Meanwhile, the rock sample is crushed in the area between two foliations. As the foliation angles continuously increase from 45° to 75° , the fracture forms of strengthened samples are similar to the fracture forms without a strengthening scheme.

To analyze the effect of foliation angles on the rock tensile strength, the failure strengths of anisotropic rock under two simulation schemes were compared, as shown in Figure 5. For the rock samples with different foliation angles, the failure strengths with a strengthening scheme are entirely larger than those without a strengthening scheme. With a strengthening scheme, the failure strength of rock obviously decreases when the foliation angle changes from 15° to 45° , and then, the failure strength slightly decreases as the foliation angle changes from 45° to 60° . However, the failure strength slightly increases as the foliation angle changes from 60° to 75° . Without a strengthening scheme, the failure strength continuously decreases as the foliation angles increase from 15° to 75° ; moreover, the decrease rate of the failure strength of rock with 15° to 30° foliations is obviously larger than that of rock with 30° to 75° foliations.

As indicated in the trend line of Figure 5, studies indicate that the failure strengths of rock with different foliation angles decrease as the foliation angle increases [25, 26]. From Figure 5, as the foliation angle changes from 0° to 45° ,

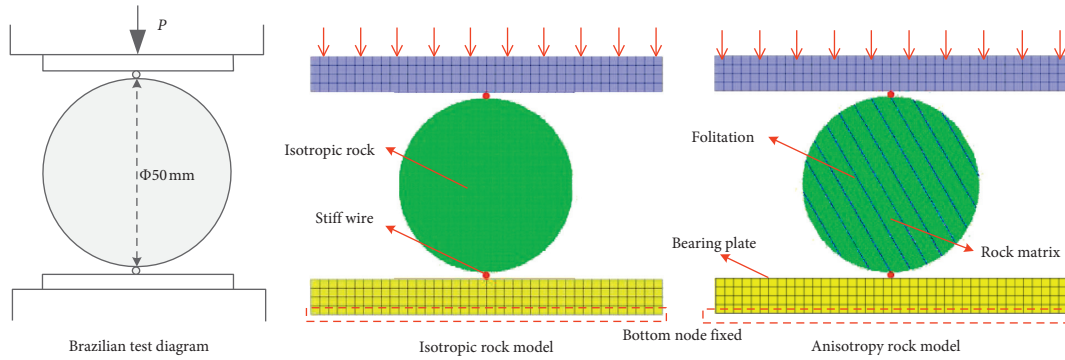


FIGURE 2: Test diagram and numerical models.

TABLE 1: Numerical parameters in the simulation of Brazilian test.

	Density (kg/m^3)	Elastic modulus (GPa)	Poisson's ratio	Tensile strength (MPa)	Cohesion (MPa)
Bearing plate	7850	200	0.25	—	—
Rock matrix	2800	30	0.25	6	6
Foliation	2519	24	0.25	2.1	2.16

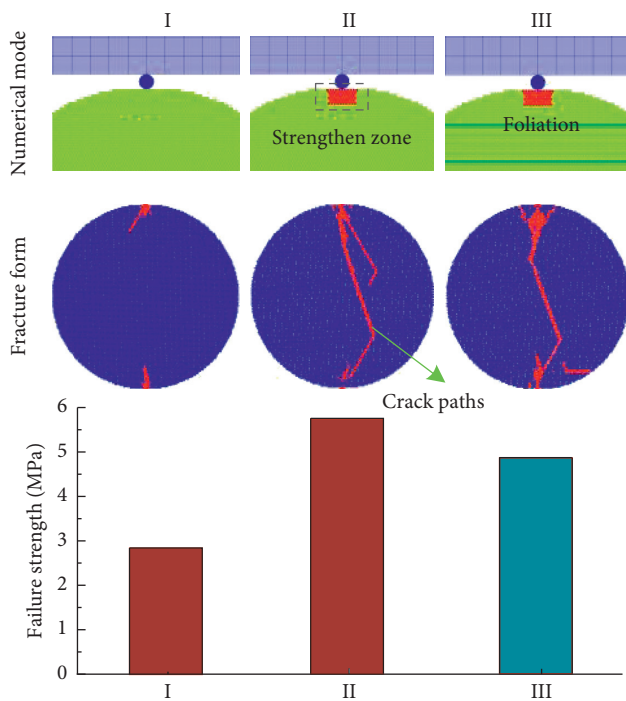


FIGURE 3: Splitting simulation of isotropic and horizontal foliation rock.

simulation results with a strengthening scheme relatively follow the trend line. However, because the failure strength will continue to decrease as the foliation angle increases from 45° to 75° , simulation results without a strengthening scheme more closely follow the trend line.

3.3. Simulation Results of Rock with Vertical Foliations. Figure 5 of Section 3.2 shows that, as the foliation angle is higher than 75° , the failure strength of the rock sample under

a strengthening scheme is obviously higher than the trend line. Therefore, for the splitting of vertical foliation rock, the simulations without a strengthening scheme were conducted, and the effect of foliation thickness in sample middle were also considered, as shown in Figure 6. As the foliation thickness is 0.4 mm, the sample with 90° foliations is crushed near the loading positions, and the main cracks propagate along two foliations near the vertical middle axis of sample. However, as the foliation thickness is 0.8 mm or 1.2 mm, the rock sample is directly split along the middle foliation, and there is only one main crack in the sample. Moreover, the crushing degree near the sample loading positions also decreases. As the foliation thickness increases, the failure strengths of 90° foliation rock obviously decrease, which is consistent with the trend line of Figure 5.

In summary, the effects of different rock foliation angles on the fracture forms and failure strengths of rock samples are significant. For the fracturing simulation of anisotropic rock in the Brazilian test, the splitting process of horizontal foliation rock can be well simulated by a strengthening scheme. The strengthening scheme is also suitable for investigating the fracturing of rock samples with the smaller foliation angle; however, simulations without a strengthening scheme are more suitable for investigating the fracturing of rock samples with the larger foliation angle. Further, the fracturing of the rock sample with vertical foliations can be well simulated by adjusting the foliation thickness of sample middle.

3.4. Simulation Results with Different Rock Matrices and Foliation Strengths. From Figure 5, the failure strength of 45° foliation rock with a strengthening scheme is close to the failure strength without a strengthening scheme. To investigate the effect of foliation and matrix strengths on the rock fracturing, the splitting of 45° foliation rock sample in the Brazilian test was simulated. The tensile and cohesive

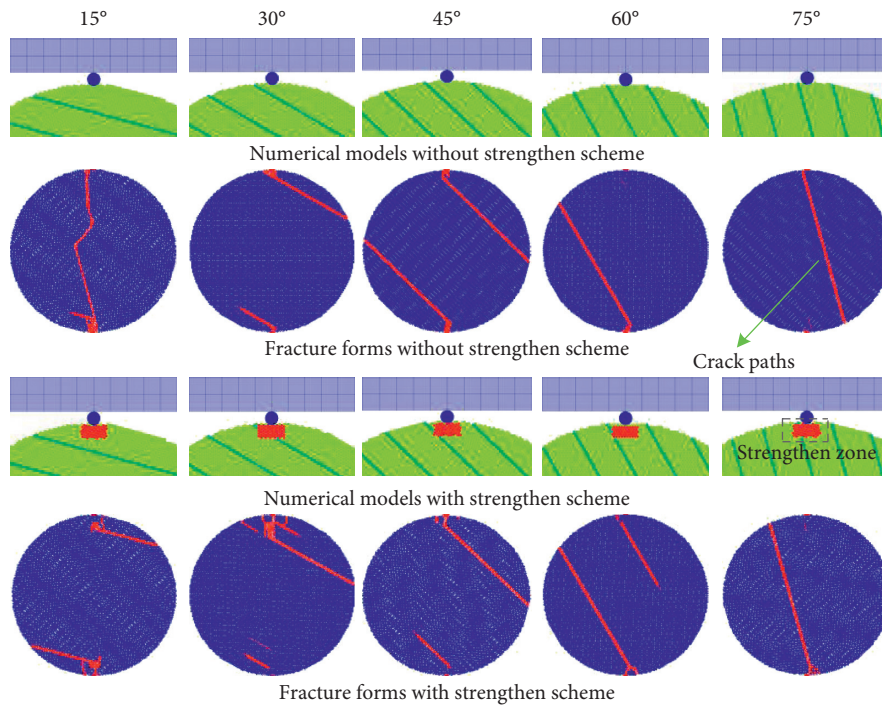


FIGURE 4: Fracturing simulation of rock with different foliation angles.

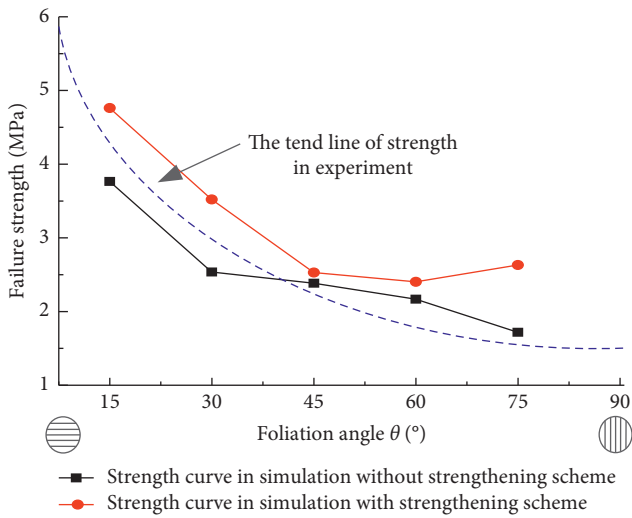


FIGURE 5: The relationship between foliation angle and failure strength.

strengths of rock foliation were taken as 1 MPa, 1.5 MPa, 2 MPa, 2.5 MPa, and 3 MPa, respectively. The tensile and cohesive strengths of the rock matrix were taken as 4 MPa, 6 MPa, 8 MPa, 10 MPa, and 12 MPa, respectively.

Under different strength parameters, the tensile failure strengths of the rock sample in the splitting simulation produce significant differences, as shown in Figure 7. As the foliation strengths increase, the failure strengths of the rock sample increase. Specifically, as the foliation tensile strength varies from 1 MPa to 3 MPa, the tensile failure strength of rock sample changes from 2.28 MPa to 2.44 MPa. As the foliation cohesive strength varies from 1 MPa to 3 MPa, the

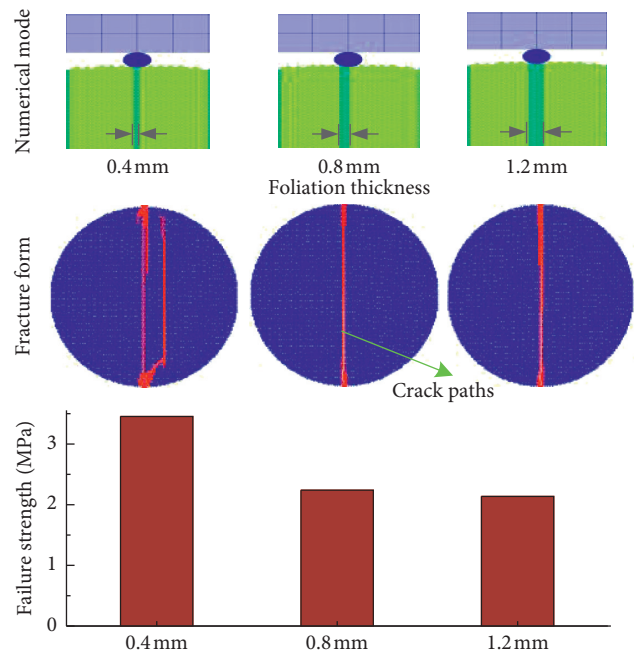


FIGURE 6: Splitting simulation of vertical foliation rock.

tensile failure strength of the rock sample changes from 2.2 MPa to 2.43 MPa. Moreover, the tensile failure strength of the rock sample also increases with an increase of rock matrix strength. As the matrix tensile strength varies from 4 MPa to 12 MPa, the tensile failure strength of the rock sample increases from 2.1 MPa to 2.9 MPa. As the matrix cohesive strength varies from 4 MPa to 12 MPa, the tensile failure strength of rock sample changes from 2.2 MPa to 2.7 MPa.

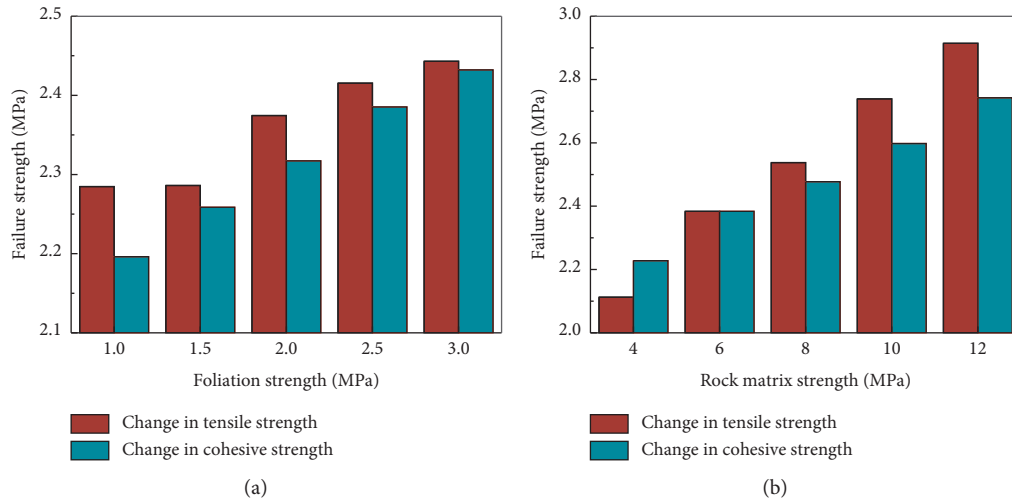


FIGURE 7: Failure strengths of rock samples with different foliation and matrix strengths.

In general, for the splitting simulations of 45° foliation rock sample, the variation range of rock matrix strengths is 4 MPa to 12 MPa; however, the foliation strengths vary from 1 MPa to 3 MPa. As the results of the splitting simulation, the tensile failure strengths of rock samples only change from 2.1 MPa to 2.9 MPa. This indicates the effect of matrix strength variation on the tensile strength of the rock sample is not obvious; however, the foliation strength variation significantly affects the tensile strength of the rock sample.

4. Verification and Discussion

4.1. Verification. To verify the simulation results, the current works are compared with [25, 26], as shown in Figure 8. In general, the fracture patterns of foliation rock in current simulation are consistent with those of laboratory tests. As the foliation angle is 0° , the rock sample fractures along the vertical middle axis. As the foliation angle increases, the cracks of rock samples mainly propagate along rock foliations. Specifically, as the foliation angle is 0° , the loading positions of the rock sample are crushed in current work, and a corner breakage also occurs near the loading positions of 0° foliation rock in [25]. Meanwhile, there is a short horizontal crack in the lower part of the rock sample in current work, and there is also a crack along the foliation of rock sample in [26].

4.2. Discussion. In this study, the fracturing processes of isotropic and anisotropic rock samples in the Brazilian test were simulated, and simulation results are consistent with the experiment results. The fracture mechanism of the rock sample in the Brazilian test can be well depicted by the continuum-discontinuum element method.

In Brazilian splitting test, the vertical load firstly applies to the rock matrix near the sample loading positions, and then, the vertical load gradually translates into the sample middle. For the isotropic and horizontal foliation rock in the splitting simulation of Brazilian test, the failure tensile

strengths of rock samples are larger than those of the inclined and vertical foliation rock, so the isotropic and horizontal foliation rock samples relatively easily generate the compression-shear fracture and the integral tensile fracture. During the stiff wire loading, the stress concentration near the loading positions easily causes the local failure of the rock sample, and the tensile strength obtained by splitting simulation is smaller than the actual tension strength of rock materials. Therefore, for the isotropic and horizontal foliation rock, a local strengthening scheme should be adopted to simulate the splitting of rock samples, which can simulate the integral tensile fracture and obtain the proper tension strength of the rock sample in the Brazilian test. As rock foliation angles vary from 15° to 45° , the tensile strength variation of numerical samples with a strengthening scheme is consistent with the trend of Figure 5, and the rock samples generate the compression-shear fracture and the sliding fracturing along the foliations. This indicates as the foliation angle is smaller, the stress concentration and rock foliation both affect the splitting results of the rock sample. As rock foliation angles varies from 45° to 75° , the rock samples only generate the fracturing along the foliations; moreover, the tensile strength variation in simulation with a strengthening scheme is obviously different from the trend of Figure 5. This indicates the effect of larger angle foliations on sample splitting is larger than the rock matrix. The fracturing of vertical foliation rock can be well simulated by adjusting the foliation thickness of sample middle, which can be because, in the complex geological processes, the geometric width of rock foliation appears to be very small; however, the influence area of the weak layer structure on the rock sample may be much larger than that of its geometric size.

With the strength parameter variation of the rock foliation and matrix, the weak layer structures have a significant influence on the fracture form and failure strength of anisotropic rock, although rock matrix strengths are much higher than foliation strengths. Therefore, the adjustment of rock matrix strength cannot obviously change the tensile failure strength of the numerical sample, while the

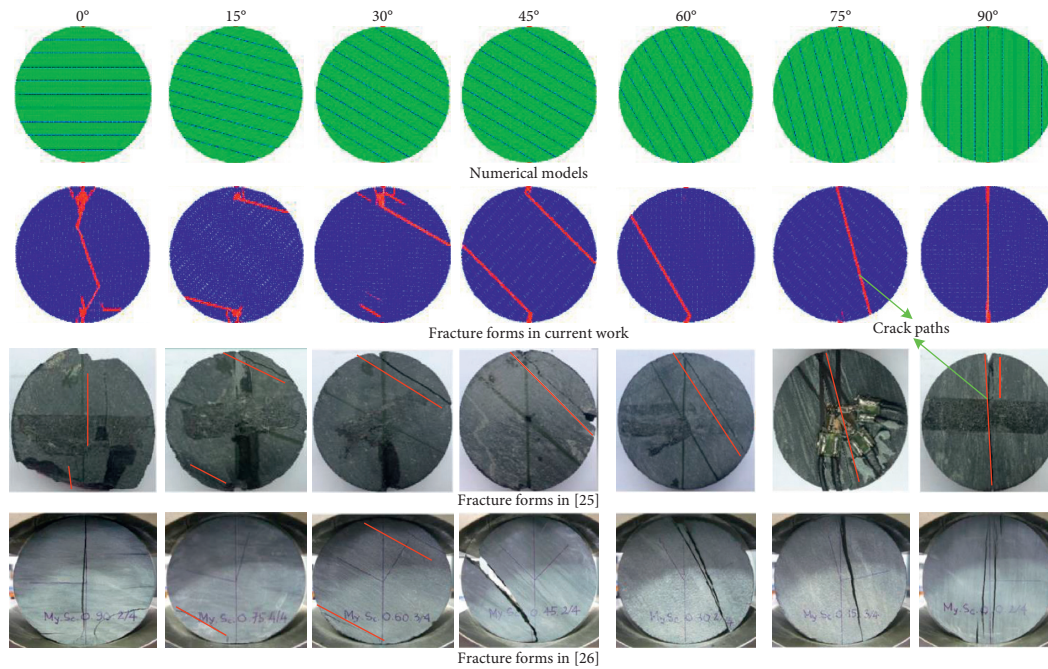


FIGURE 8: Comparison of simulation and experiment.

variation in the foliation strength can significantly affect the tensile failure strength of the rock sample.

5. Conclusions

- (1) The fracturing of rock samples in the Brazilian test can be well simulated by the continuum-discontinuum element method (CDEM), and simulation results are consistent with the literatures. For isotropic and horizontal foliation rock samples, the stress concentration easily causes the local failure of the sample, and the effect of the rock matrix on splitting of numerical samples is larger than rock foliation. The splitting of the rock sample can be simulated by a strengthening scheme. Isotropic and horizontal foliation rock easily generates the compression-shear fracture near loading positions and integral tensile fracture in sample middle.
- (2) As foliation angle varies from 15° to 45° , the foliations and the stress concentration near loading positions both affect the splitting results of the rock sample. Rock samples easily generate the sliding fracturing along foliations and the compression-shear fracturing near loading positions. As foliation angles varies from 45° to 75° , the tensile strength variation of the rock sample without a strengthening scheme is consistent with experiment results, the effect of rock foliation on sample splitting is larger than the rock matrix, and the rock samples mainly generate the fracturing along foliations. The fracturing of vertical foliation rock can be well simulated by adjusting the foliation thickness of sample middle, and the

influence area of the foliation on the rock sample may be larger than that of its geometric size.

- (3) For the fracturing of the rock sample with 45° foliations, as the tensile strength of foliation varies from 1 MPa to 3 MPa, the rock failure strength increases from 2.28 MPa to 2.44 MPa. The rock failure strength changes from 2.2 MPa to 2.43 MPa as the cohesive strength of foliation varies from 1 MPa to 3 MPa. However, as the tensile strength of the rock matrix varies from 4 MPa to 12 MPa, the rock failure strength changes from 2.1 MPa to 2.9 MPa. The rock failure strength changes from 2.2 MPa to 2.7 MPa as the cohesive strength of rock matrix changes from 4 MPa to 12 MPa. This indicates the rock foliation rather than the rock matrix dominates the failure strength of the rock sample.

Data Availability

The data used to support the findings of this study are included within the article.

Conflicts of Interest

The authors declare that they have no conflicts of interest to report regarding the present study.

Acknowledgments

This work was supported by the National Key R&D Program of China (Grant nos. 2018YFC0604502 and 2018YFC1505504) National Natural Science Foundation of China (Grant no. 51708513), China Postdoctoral Science Foundation (Grant no. 2020M672227), and Henan

Provincial Department of Transportation (Grant nos. 2018J4 and 2019J1). The authors gratefully acknowledge Dr. Shen Wang and Professor Ruifu Yuan in Henan Polytechnic University, who provided language help and writing assistance.

References

- [1] C.-S. Chen, E. Pan, and B. Amadei, "Determination of deformability and tensile strength of anisotropic rock using Brazilian tests," *International Journal of Rock Mechanics and Mining Sciences*, vol. 35, no. 1, pp. 43–61, 1998.
- [2] Q. Z. Wang, W. Li, and H. P. Xie, "Dynamic split tensile test of flattened Brazilian disc of rock with SHPB setup," *Mechanics of Materials*, vol. 41, no. 3, pp. 252–260, 2009.
- [3] K. H. Li, Y. M. Cheng, and X. Fan, "Roles of model size and particle size distribution on macro-mechanical properties of Lac du Bonnet granite using flat-joint model," *Computers and Geotechnics*, vol. 103, pp. 43–60, 2018.
- [4] G. Barla and L. Goffi, "Direct tensile testing of anisotropic rocks," in *Proceedings of the 3rd Congress of the International Society for Rock Mechanics*, Denver, CO, USA, 1974.
- [5] H. Niandou, J. F. Shao, J. P. Henry, and D. Fourmaintraux, "Laboratory investigation of the mechanical behaviour of Tournemire shale," *International Journal of Rock Mechanics and Mining Sciences*, vol. 34, no. 1, pp. 3–16, 1997.
- [6] J.-W. Cho, H. Kim, S. Jeon, and K.-B. Min, "Deformation and strength anisotropy of Asan gneiss, Boryeong shale, and Yeoncheon schist," *International Journal of Rock Mechanics and Mining Sciences*, vol. 50, pp. 158–169, 2012.
- [7] B. Debecker and A. Vervoort, "Experimental observation of fracture patterns in layered slate," *International Journal of Fracture*, vol. 159, no. 1, pp. 51–62, 2009.
- [8] T. Meier, E. Rybacki, T. Backers, and G. Dresen, "Influence of bedding angle on borehole stability: a laboratory investigation of transverse isotropic oil shale," *Rock Mechanics and Rock Engineering*, vol. 48, no. 4, pp. 1535–1546, 2015.
- [9] A. Tavallali and A. Vervoort, "Effect of layer orientation on the failure of layered sandstone under Brazilian test conditions," *International Journal of Rock Mechanics and Mining Sciences*, vol. 47, no. 2, pp. 313–322, 2010.
- [10] B. Debecker and A. Vervoort, "Two-dimensional discrete element simulations of the fracture behaviour of slate," *International Journal of Rock Mechanics and Mining Sciences*, vol. 61, pp. 161–170, 2013.
- [11] B. Park and K.-B. Min, "Bonded-particle discrete element modeling of mechanical behavior of transversely isotropic rock," *International Journal of Rock Mechanics and Mining Sciences*, vol. 76, pp. 243–255, 2015.
- [12] U. Kuila, D. N. Dewhurst, A. F. Siggins, and M. D. Raven, "Stress anisotropy and velocity anisotropy in low porosity shale," *Tectonophysics*, vol. 503, no. 1, pp. 34–44, 2011.
- [13] B. V. D. Steen, A. Vervoort, and J. A. L. Napier, "Observed and simulated fracture pattern in diametrically loaded discs of rock material," *International Journal of Fracture*, vol. 131, no. 1, pp. 35–52, 2005.
- [14] S. H. Cho, Y. Ogata, and K. Kaneko, "Strain-rate dependency of the dynamic tensile strength of rock," *International Journal of Rock Mechanics and Mining Sciences*, vol. 40, no. 5, pp. 763–777, 2003.
- [15] Y. Hao and H. Hao, "Finite element modelling of mesoscale concrete material in dynamic splitting test," *Advances in Structural Engineering*, vol. 19, no. 6, pp. 1027–1039, 2016.
- [16] M. R. Khosravani, M. Silani, and K. Weinberg, "Fracture studies of ultra-high performance concrete using dynamic Brazilian tests," *Theoretical and Applied Fracture Mechanics*, vol. 93, pp. 302–310, 2018.
- [17] D. O. Potyondy and P. A. Cundall, "A bonded-particle model for rock," *International Journal of Rock Mechanics and Mining Sciences*, vol. 41, no. 8, pp. 1329–1364, 2004.
- [18] N. Cho, C. D. Martin, and D. C. Segol, "A clumped particle model for rock," *International Journal of Rock Mechanics and Mining Sciences*, vol. 44, no. 7, pp. 997–1010, 2007.
- [19] B. E. Hornby, L. M. Schwartz, and J. A. Hudson, "Anisotropic effective-medium modeling of the elastic properties of shales," *Geophysics*, vol. 59, no. 10, pp. 1570–1583, 1994.
- [20] R. N. Vasin, H. R. Wenk, W. Kanitpanyacharoen, S. Matthies, and R. Wirth, "Elastic anisotropy modeling of Kimmeridge shale," *Journal of Geophysical Research: Solid Earth*, vol. 118, no. 8, pp. 3931–3956, 2013.
- [21] G. Xu, C. He, Z. Chen, and A. Su, "Transverse isotropy of phyllite under Brazilian tests: laboratory testing and numerical simulations," *Rock Mechanics and Rock Engineering*, vol. 51, no. 4, pp. 1111–1135, 2018.
- [22] C.-C. Chiu, T.-T. Wang, M.-C. Weng, and T.-H. Huang, "Modeling the anisotropic behavior of jointed rock mass using a modified smooth-joint model," *International Journal of Rock Mechanics and Mining Sciences*, vol. 62, pp. 14–22, 2013.
- [23] X.-X. Yang, H.-W. Jing, C.-A. Tang, and S.-Q. Yang, "Effect of parallel joint interaction on mechanical behavior of jointed rock mass models," *International Journal of Rock Mechanics and Mining Sciences*, vol. 92, pp. 40–53, 2017.
- [24] X.-X. Yang, H.-W. Jing, and W.-G. Qiao, "Numerical investigation of the failure mechanism of transversely isotropic rocks with a particle flow modeling method," *Processes*, vol. 6, no. 9, p. 171, 2018.
- [25] G. Xu, C. He, Z. Chen, and D. Wu, "Effects of the micro-structure and micro-parameters on the mechanical behaviour of transversely isotropic rock in Brazilian tests," *Acta Geotechnica*, vol. 13, no. 4, pp. 887–910, 2018.
- [26] X. Tan, H. Konietzky, T. Frühwirth, and D. Q. Dan, "Brazilian tests on transversely isotropic rocks: laboratory testing and numerical simulations," *Rock Mechanics and Rock Engineering*, vol. 48, no. 4, pp. 1341–1351, 2015.
- [27] L. Wang, S. Li, G. Zhang, Z. Ma, and L. Zhang, "A GPU-based parallel procedure for nonlinear analysis of complex structures using a coupled FEM/DEM approach," *Mathematical Problems in Engineering*, vol. 2013, Article ID 618980, 15 pages, 2013.
- [28] Q. L. Zhang, Z. H. Zhi, C. Feng, Y. C. Cai, G. H. Pang, and J. C. Yue, "Investigation of concrete pavement cracking under multi-head impact loading via the continuum-discontinuum element method," *International Journal of Impact Engineering*, vol. 135, Article ID 103410, 2020.
- [29] Z. Chen, W. Gong, G. Ma et al., "Comparisons between centrifuge and numerical modeling results for slope toppling failure," *Science China Technological Sciences*, vol. 58, no. 9, pp. 1497–1508, 2015.
- [30] Q. L. Zhang, R. F. Yuan, S. Wang, D. Y. Li, H. M. Li, and X. H. Zhang, "Optimizing simulation and analysis of automated top-coal drawing technique in extra-thick coal seams," *Energies*, vol. 13, no. 1, 2020.
- [31] Q. L. Zhang, J. C. Yue, C. Liu, C. Feng, and H. M. Li, "Study of automated top-coal caving in extra-thick coal seams using the continuum-discontinuum element method," *International*

Journal of Rock Mechanics and Mining Sciences, vol. 122, Article ID 104033, 2019.

- [32] C. Feng, S. H. Li, and X. Y. Liu, "Particle-dem based linked bar strain softening model and its application," *Chinese Journal of Theoretical and Applied Mechanics*, vol. 48, pp. 76–85, 2016.
- [33] R. Yuan and B. Shen, "Numerical modelling of the contact condition of a Brazilian disk test and its influence on the tensile strength of rock," *International Journal of Rock Mechanics and Mining Sciences*, vol. 93, pp. 54–65, 2017.

Research Article

Decision Method of Bridge Deck Pavement Maintenance Based on the Decision Maker's Objective

Xiaofei Liang , Jun Shi , and Zhongmei Li

School of Civil and Architectural Engineering, Shandong University of Technology, Zibo 255000, China

Correspondence should be addressed to Jun Shi; sjun@sdut.edu.cn

Received 28 January 2021; Revised 7 March 2021; Accepted 22 May 2021; Published 7 June 2021

Academic Editor: Luigi Aldieri

Copyright © 2021 Xiaofei Liang et al. This is an open access article distributed under the Creative Commons Attribution License, which permits unrestricted use, distribution, and reproduction in any medium, provided the original work is properly cited.

The performance of reinforced concrete bridge deck pavement will be gradually reduced with the increase of operation time, so the reasonable maintenance measures should be taken to ensure the performance and safety of the bridge structures. The objectives and their hierarchical structures from both state position and enterprise position of the decision makers in bridge engineering decision-making problems were discussed. By the existing deterioration model, this paper studies the bridge operation safety maintenance strategy, establishes the mathematical model of the influence of different degrees of maintenance measures on the structural performance, combines with the cost-benefit theory, establishes the maintenance risk decision criteria for the decision makers with different objectives, and makes the decision on the selection of the bridge deck pavement scheme based on the enterprise position through an example.

1. Introduction

With the aging of existing bridges, the maintenance of operating bridges becomes very important [1]. Through the detection of the operating bridge, the deterioration of the bridge can be found in time, and the corresponding repair measures can be taken to ensure the safe operation of the bridge [2, 3]. To make a reasonable inspection and maintenance scheme, several investigations on the bridge operation management under normal degradation conditions have been done. Bian et al. studied the maintenance and reinforcement decision-making of service bridges based on reliability and the influence of maintenance on reliability and maintenance cost [4]. Combining with the optimal reliability of the structure, Qin et al. discussed in detail based on the group decision-making theory [5]. Shao et al. carried out research on structural safety and economic optimization from different angles [6–9]. Based on the two maintenance control indexes of bridge reliability and bridge condition, Cao et al. proposed a multiobjective optimization method for bridge maintenance decision-making, which can

comprehensively consider the total maintenance cost, bridge life after maintenance, bridge reliability, and bridge condition [10, 11].

Most of the above research studies are based on the reliability theory of bridge safety and take the cost-benefit theory of the lowest cost in the broad sense as the control condition to establish the model to solve the optimal remaining service life of the operating bridge. This kind of research mainly focuses on the theoretical framework construction level, and the research on the maintenance strategy based on time-varying reliability is still in its infancy. Through combining and integrating the existing research results, this paper forms a bridge maintenance decision-making method based on the goal of the decision maker. Based on the deterioration model of reliability index, this method studies the maintenance strategy of bridge operation safety, establishes the mathematical model of the influence of different degrees of maintenance measures on the structural performance, and establishes the maintenance risk decision-making methods for decision makers with different objectives combined with the cost-benefit theory.

2. Types and Objectives of Decision Makers

Decision makers are individuals or groups of individuals who directly or indirectly provide the most important value judgments. In China, the decision-making of bridge construction projects planned by the state needs to be considered from both the state and enterprises [12]. Although the decision makers do not change, their goals and preferences are different due to different starting points. Therefore, they can be regarded as two kinds of decision makers with different natures. In addition, with the continuous exploration of the financing mode of bridge engineering, the private enterprises of bridge engineering have an increasing trend; the decision makers should be the person in charge of the private enterprise, the general meeting of shareholders, or similar institutions, which should be treated as a completely consistent collective and treated as a person. The positions and characteristics of decision makers are shown in Table 1.

The value of the bridge is realized through operation. If the decision maker does not have a clear operation goal, it will lead to the lack of continuity of maintenance measures, which will lead to the lack of understanding of the bridge maintainability and sustainable development ability [13–15]. Different decision makers must scientifically establish the goal of its operation period to realize the value of the bridge. However, no matter the state government units, state-owned enterprises, or private enterprises, the maintenance of bridges should at least include the following aspects:

- (i) After maintenance, the bridge must meet a certain safety level
- (ii) After maintenance, the bridge must have conditions to reach a certain safe service life
- (iii) During and after the maintenance, the influence of the structure on the environment should be controlled
- (iv) Maintenance programs minimize or avoid the disruption of traffic

After meeting the basic objectives, as a national capital construction project, the overall goal of the bridge's operation in the national position is to improve people's living standards, while the decision maker in the enterprise position will make value judgment from the interests obtained. In the application, the objective function is represented by money. The objective function selected in this paper has the maximum profit for the enterprise position decision-making and the minimum loss for the state position decision-making.

3. Decision-Making Process

In theory, different schemes have different risks. It is of positive significance for the safe operation of bridges to consider the cost and subsequent risks when making decisions. Objectively, it is unrealistic to require "zero risk" of bridges. In general, a safe bridge refers to the risk of bridge crash, which is acceptable to individuals or the society

[16–18]. Any bridge has the possibility of damage to varying degrees. It is necessary to take measures to control this possibility within the allowable range. Different measures will lead to different costs and effects. To balance risk reduction and cost, bridge risk decision is required. Conditions for risk decision-making are as follows: setting the target expected by the decision maker, more than two alternatives available, decision-making criteria, the benefit value of each scheme can be calculated, and the probability of failure after the implementation of each scheme can be calculated. The risk decision process is shown in Figure 1.

4. Deterioration Model

Reliability (or the probability of failure) is one of the most representative probabilistic structural performance indicators [2]. The reliability of a deteriorating bridge decreases over time due to external loadings and various environmental stressors under uncertainty [20]. Deterioration is a complex process. In this paper, referring to the research results of Frangopol and others [21–23], a two-stage linear model with three parameters (initial reliability index β_0 , deterioration initial time t_I , and deterioration rate α) is adopted for the reliability index of bridges in the operation period, as shown in Figure 2 and the following equation.

$$\beta(t) = \begin{cases} \beta_0, & 0 \leq t \leq t_I, \\ \beta_0 - \alpha(t - t_I), & t > t_I. \end{cases} \quad (1)$$

The value of β_0 is affected by many factors such as design, material, and construction. According to Cao et al. [10], β_0 is 7.0. The physical deterioration, concrete carbonization, and steel corrosion in the course of bridge operation reduce the reliability of the bridge. Imai and Frangopol [24] took the time when the steel bars in the structure began to rust as the deterioration initial time t_I , as shown in the following equation:

$$t_I = \frac{(c - x_0)^2}{k^2}, \quad (2)$$

where c is the concrete cover thickness, k is the carbonation coefficient of concrete, and x_0 is the carbonation remains.

5. Maintenance Strategy Model

Under different maintenance measures, the deterioration process of the bridge structure is very different. For the convenience of analysis, it is assumed that the time interval of preventive maintenance t_p is the same; the duration of preventive maintenance effect t_{pD} is the same; each preventive maintenance has the same jump γ in reliability; there is $\beta(t) \leq \beta_0$ at any time [25].

5.1. Preventive Maintenance Based on Time Control. After the completion of maintenance measures, the bridge will deteriorate along the deterioration rate θ within the duration of maintenance effect t_{pD} , and the maintenance interval t_p is required to be less than the duration of maintenance effect t_{pD} , such as small-scale repair. $t_{pI} \geq t_I$ and $t_{pD} \geq t_p$. The

TABLE 1: The positions and characteristics of decision makers.

Organization type	Decision maker	Position of the decision maker	Decision-making basis
Government units	Public officials of the state	The state position	The state interests
State-owned enterprises	Public officials in enterprises	The enterprises' position	The enterprises' interests
Private enterprises	The head of private enterprises	The enterprises' position	Value judgment of the decision maker

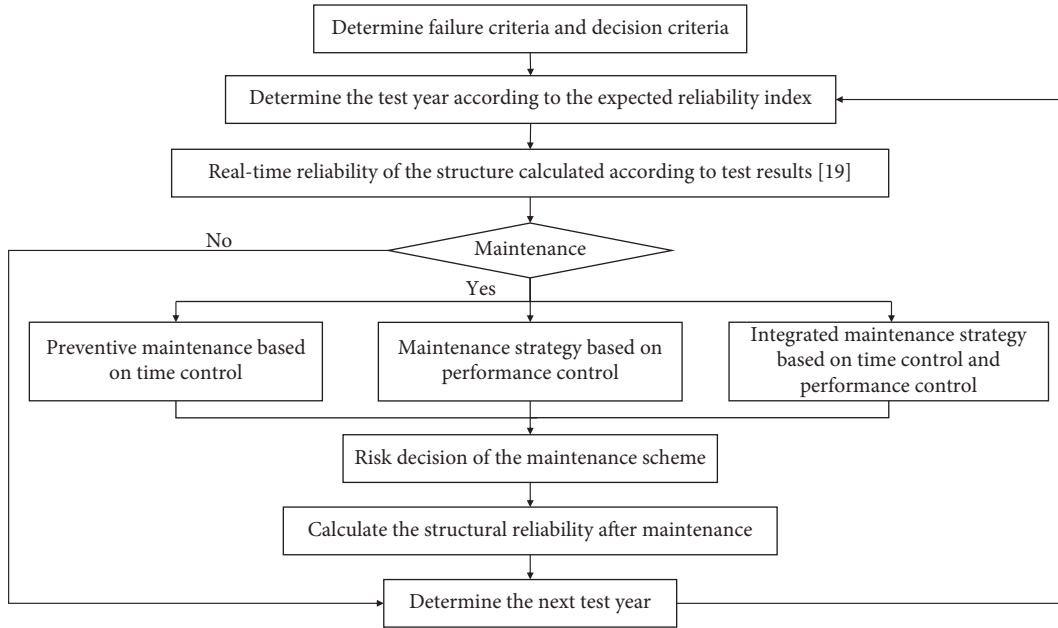


FIGURE 1: Maintenance decision flowchart [19].

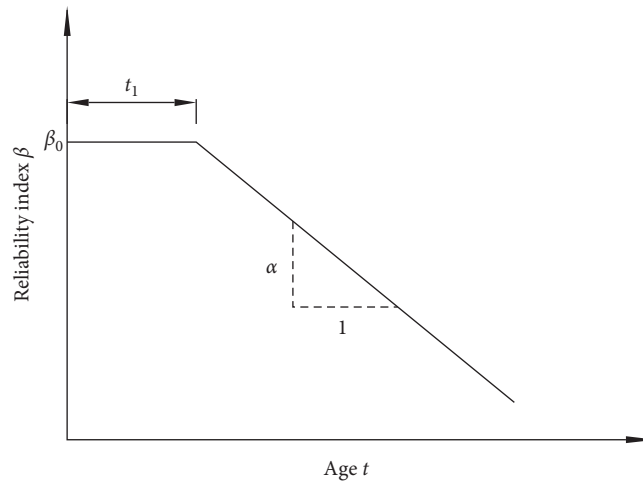


FIGURE 2: Two-stage linear model of the reliability index.

change of the reliability index of the bridge is shown in Figure 3, and the expression of deterioration reliability is as follows:

$$\beta(t) = \begin{cases} \beta_0, & t < t_I, \\ \beta_0 - \alpha(t - t_I), & t_I \leq t < t_{PI}, \\ \beta_1 - \theta(t - t_{PI}), & t_{PI} \leq t < t_{PI} + t_P, \\ \beta_n - \theta\{t - [t_{PI} + (n-1)t_P]\}, & t_{PI} + (n-1)t_P \leq t < t_{PI} + nt_P, \end{cases} \quad (3)$$

where $\beta_1 = -\alpha(t - t_I) + \gamma$, $t = t_{PI}$, and $\beta_n = \beta_{n-1} - \theta t_P + \gamma$, $t = t_{PI} + (n-1)t_P$.

5.2. Maintenance Strategy Based on Performance Control.

Maintenance measures are taken when the performance of the bridge is reduced to the specified allowable performance index, that is, $\beta \leq \beta'_{\text{target}}$. The change of the reliability index of the bridge is shown in Figure 4, and the expression of deterioration reliability is as follows:

$$\beta(t) = \begin{cases} \beta_0, & t < t_I, \\ \beta_0 - \alpha(t - t_I), & t_I \leq t < t_{PI}, \\ \beta_1 - \alpha(t - t_{PI}), & t_{PI} \leq t < t_{PI} + t_1, \\ \beta_n - \alpha \left\{ t - \left[t_{PI} + \sum_{i=1}^{n-1} t_i \right] \right\}, & t_{PI} + \sum_{i=1}^{n-1} t_i \leq t < t_{PI} + \sum_{i=1}^n t_i, \end{cases} \quad (4)$$

where $\beta_1 = \beta_0 - \alpha(t - t_I) + \Delta\beta_1$, $t = t_{PI}$, and $\beta_n = \beta_{n-1} - \alpha t_{n-1} + \Delta\beta_{n-1}$, $t = t_{PI} + \sum_{i=1}^{n-1} t_i$.

5.3. Integrated Maintenance Strategy. In the preventive maintenance strategy based on time control, in order to ensure that the bridge can operate to the design life, the condition of $t_{PI} \geq t_I$ and $t_{PD} \geq t_P$ should be met, which directly affects the maintenance times. Because the bridge needs to control traffic while it is being maintained, more maintenance reduces the benefits of the bridge. However, when each new maintenance starts, the last maintenance effect is still there, so the damage degree of the bridge is low, the driving comfort is high, and the corresponding single maintenance cost is also low.

The maintenance strategy of performance control has long maintenance cycle, low maintenance frequency, and little influence on traffic revenue. However, when the bridge needs to be maintained, the state of the bridge is at the lowest

allowable value, and the bridge often suffers relatively large damage and low driving comfort. In order to ensure the safe operation of the bridge, it is necessary to adopt relatively high-cost reinforcement and renovation measures to improve the performance of the bridge.

The integrated maintenance strategy combining time control and performance control is to adopt time control at the early stage of operation and carry out maintenance and repair after the maintenance effect continues to disappear but before the bridge performance reaches the minimum allowable value. When $t_{PD} < t_P$, the deterioration rate of the bridge in $[0, t_{PD}]$ is θ , and the deterioration rate of the bridge in $[t_{PD}, t_P]$ is α . When $\beta \leq \beta'_{\text{target}}$, the performance control is adopted to greatly improve the bridge performance. The performance of the bridge changes is shown in Figure 5, and the reliability of deterioration is expressed as follows:

$$\beta(t) = \begin{cases} \beta_0, & t < t_I, \\ \beta_0 - \alpha(t - t_I), & t_I \leq t < t_{PI}, \\ \beta_1 - \alpha(t - t_{PI}), & t_{PI} \leq t < t_{PI} + t_1, \\ \beta'_1 - \alpha[t - (t_{PI} + t_{PI})], & t_{PI} + t_{PD} \leq t < t_{PI} + t_P, \\ \vdots & \vdots \\ \beta_m - \theta\{t - [t_{PI} + (m-1)t_P]\}, & t_{PI} + (m-1)t_P \leq t < t_{PI} + (m-1)t_P + t_{PD}, \\ \beta'_m - \alpha\{t - [t_{PI} + (m-1)t_P]\}, & t_{PI} + (m-1)t_P + t_{PD} \leq t \leq t_{PI} + (m-1)t_P + t_{m1}, \end{cases} \quad (5)$$

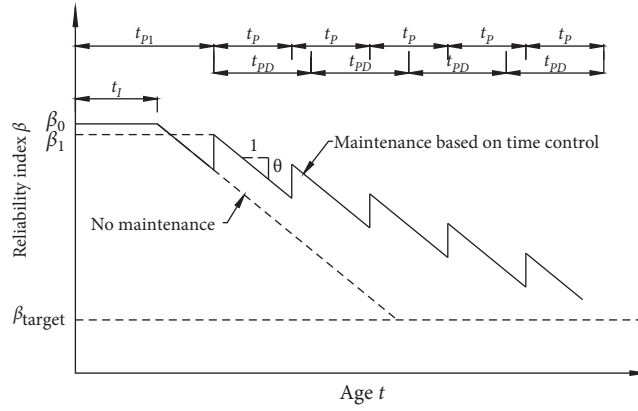


FIGURE 3: Reliability index change chart of the time-based maintenance.

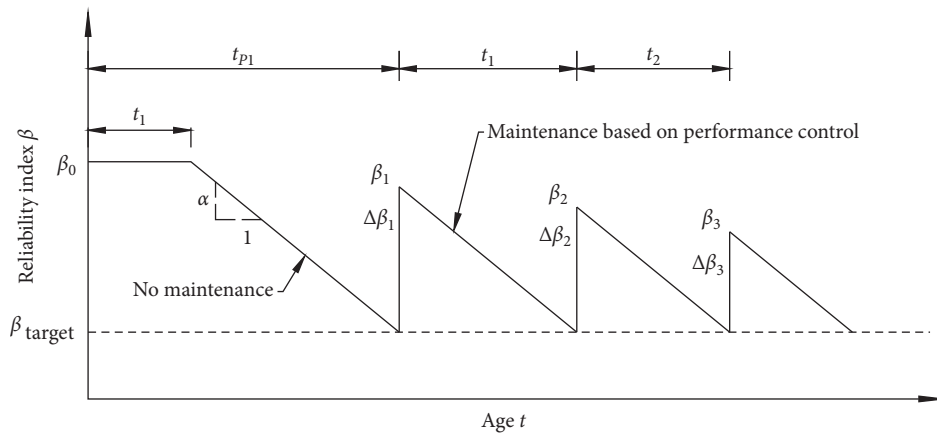


FIGURE 4: Reliability index change chart of the performance-based maintenance.

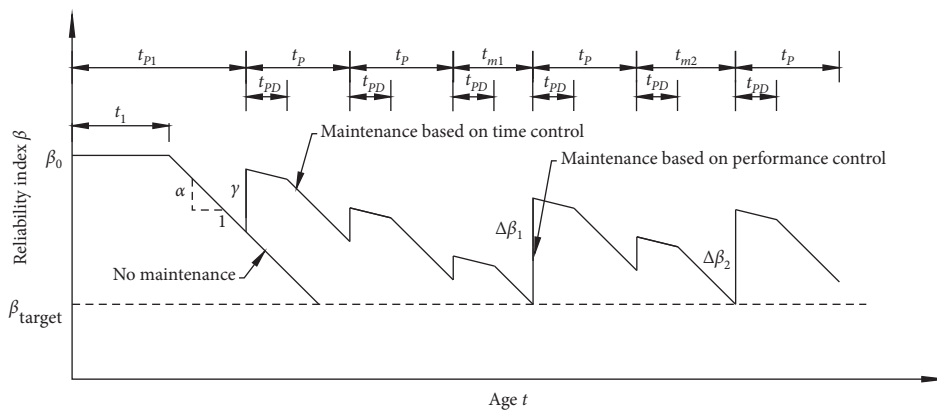


FIGURE 5: Reliability index change chart of the integrated maintenance.

where $\beta_1 = \beta_0 - \alpha(t - t_I) + \gamma$, $t = t_{PI}$, $\beta'_1 = \beta_1 - \theta t_{PD}$, $\beta_m = \beta'_{m-1} - \alpha\{t - [t_{PI} + (n-1)t_P]\} + \gamma$, and $\beta'_m = \beta_m - \theta t_{PD}$.

$$\beta(t) = \begin{cases} \beta_n - \theta\{t - [t_{PI} + (n-1)t_P]\}, & t_{PI} + (n-1)t_P + \Delta t \leq t < t_{PI} + (n-1)t_P + t_{PD} + \Delta t, \\ \beta'_n - \alpha\{t - [t_{PI} + (n-1)t_P]\}, & t_{PI} + (n-1)t_P + t_{PD} + \Delta t \leq t < t_{PI} + nt_P + \Delta t, \end{cases} \quad (6)$$

where $\beta_n = \beta'_{n-1} - \alpha\{t - [t_{PI} + (n-1)t_P]\} + \Delta\beta$ and $\beta'_n = \beta_n - \theta t_{PD}$.

6. Decision Criteria for Bridge Deck Pavement Maintenance Based on the Decision Maker Objective

The purpose of decision analysis is to make the “best” decision. Different stances, experiences, and degrees of risk aversion of decision makers determine different “best” decisions, whose essence is to meet decision makers’ expectations. Therefore, the decision matrix can be expressed as the following equation [26]:

$$E(A)_{\text{def}} = \begin{bmatrix} E(A_1) \\ E(A_2) \\ \vdots \\ E(A_m) \end{bmatrix} = \begin{bmatrix} A_1 \\ A_2 \\ \vdots \\ A_m \end{bmatrix} \begin{bmatrix} a_{11} & a_{12} & a_{1m} \\ a_{21} & a_{22} & a_{2m} \\ \vdots & \vdots & \vdots \\ a_{m1} & a_{m2} & a_{mm} \end{bmatrix}_{m \times n}. \quad (7)$$

The decision-making criterion of bridge deck pavement maintenance based on the decision maker’s objective is to quantify the corresponding benefits, costs, and losses of each scheme into the economic value. On the premise of ensuring safety, the maximum expectation calculation model is as follows:

$$\begin{cases} u(A_{\text{opt}}) = \max\{E(A_i)\} \\ \text{s.t. } u(A_{\text{opt}}) \geq 0 \\ \beta(t) \geq \beta(T) \\ C_{\text{Man}} \leq C_{\text{Man},m} \end{cases} \quad (8)$$

where $C_{\text{Man}} \leq C_{\text{Man},m}$ is the pavement maintenance cost and the allowable maintenance cost.

When the decision-making body is the state, in addition to the charging benefit, more benefits of national economy will be generated during the operation of the bridge. National economic benefits have no specific material products. Therefore, it is difficult to quantify the benefits brought by bridge operation to the national economy and society and the contribution to the economic development of the whole society or region. In this case, the adoption of the maximum expected benefit criterion will produce relatively unobjective results due to the preference of the decision maker. At this point, the consequence value $\theta_{ik}^{(1)}, \theta_{ik}^{(2)}, \dots, \theta_{ik}^{(n)}$ only represents the cost $C_{ik}^{(1)}, C_{ik}^{(2)}, \dots$ and loss $L_{ik}^{(1)}, L_{ik}^{(2)}, \dots$, but does not contain the benefit $B_{ik}^{(1)}, B_{ik}^{(2)}, \dots$. Therefore, based on the

After m times of maintenance, major maintenance is needed, so the reliability of deterioration is expressed as the following equation:

national position, it should be expressed as follows according to the minimum expected cost criterion:

$$\begin{cases} d(A_{\text{opt}}) = \min\{E(A_I)\} \\ \beta(t) \geq \beta(T). \end{cases} \quad (9)$$

7. Model Validations

The bridge was completed and opened to traffic in 2001, with an annual growth rate of 8% and a 25-year concession period. The bridge deck is paved with 8 cm thick cement concrete. At present, the damage of bridge deck pavement is relatively serious on the whole, and the connection state of some concrete pavement layers and the beam body is poor, which leads to rainwater infiltration into the main beam and affects the safety of the bridge structure. The heavy traffic and damaged road surface increase the risk of traffic accident rate. It is planned to overhaul the bridge deck pavement to ensure the safety of road traffic and bridge structure. Since it is still within the concession period, this paper will refer to equation (9) and make a risk decision on the operation and safety maintenance of the bridge from the standpoint of the enterprise based on the cost-benefit criterion. When the bridge is repaved, double width and half width are each closed, and 2~5 types of passenger and freight vehicles are separated. It is estimated that the proportion of toll loss is 33.1%, and the daily toll loss is about 210,700 yuan. The bridge deck treatment scheme is shown in Table 2.

The bridge has been in operation for 20 years, and the bridge deck renovation carried out at this time belongs to performance-based bridge maintenance. Therefore, the expression of deterioration can be referred to equation(4). $t_I = 4$ [24], $t_{PI} = 20$, $t_{PI} = t_I + ((\beta_0 - \beta_{\text{target}})/\alpha)$, $\beta_0 = 7.0$ [10], and $\beta_{\text{target}} = 3.7$, so $\alpha = (\beta_0 - \beta_{\text{target}})/(t_{PI} - t_I) = 0.21$.

Because the pavement of the renovated bridge deck belongs to protective maintenance, the reliability of the bridge surface after the pavement is installed with ordinary cement concrete is improved to $\beta = 4.494$, and the reliability of the bridge surface after the pavement is installed with steel fiber concrete is improved to $\beta = 5.263$ [29]. The number of years that bridge deck pavement can maintain its service performance is 7.78 years for schemes A and C and 11.44 years for schemes B and D.

In 2019, the total toll will be 216 million yuan, and the benefit value will increase by 8% in the same year as the traffic volume. According to equations (1) and (7), the calculated result is $E(A)_A > E(A)_B > E(A)_D > E(A)_C$. Therefore, from the standpoint of the enterprise, facing the

TABLE 2: Bridge deck pavement maintenance scheme.

	Scheme A	Scheme B	Scheme C	Scheme D
Maintenance mode	8 cm thick ordinary concrete	8 cm thick steel fiber concrete	8 cm thick quick cement concrete	6 cm thick steel fiber concrete and MRK + 2 cm thick ultrathin wear layer; steel fiber-reinforced concrete (85%); MRK (15%)
Maintenance costs	6.14 million yuan	6.83 million yuan	17.54 million yuan	10.28 million yuan
Maintenance cycle	150 d	150 d	140 d	160 d
Traffic loss	31.61 million yuan	31.61 million yuan	29.50 million yuan	33.71 million yuan
Maintenance characteristics	Mature process; weak tensile and shear strength	Good crack resistance; good integrity of the bridge deck, high toughness, and tensile strength; steel fibers rust easily [27]	Time is short; the price is more expensive; new materials; new technology; performance and durability are not widely proven	The landscape effect is good; good durability; more material types; complicated construction technology [28]

concession period of 5 years, the choice of scheme A is the most appropriate.

Decisions based on national positions are not affected by the concession period. After the bridge deck pavement is renovated, the bridge using schemes A and C will need to reinvest in maintenance after 7.78 years of operation, and the total cost and loss of re-repair will inevitably exceed those of other schemes. Therefore, according to equation (9), schemes B and D are given priority. The deterioration trend of schemes B and D is the same, and the total cost expenditure of scheme D is higher than that of scheme B. However, after 11.44 years, the bridge deck pavement in schemes B and D also needs to be renovated again. At this time, scheme D can take a small repair to improve the safety of the bridge deck pavement by milling off the 2 cm covering and re-covering it with less cost. Therefore, based on the national position, scheme D is the most appropriate.

8. Conclusions

This paper has presented a risk decision method of bridge operation safety maintenance based on the decision maker's goal. The mathematical model of the influence of maintenance measures on the structural performance under different control conditions was established. Combined with the cost-benefit theory, the decision criteria of maintenance risk were established for decision makers with different objectives. Based on this investigation, the following conclusions are drawn:

- (i) Based on the analysis of the characteristics and objective hierarchy of different decision makers, a bridge maintenance decision-making method based on decision makers' objectives is proposed by classifying decision makers related to bridge maintenance units and departments into national decision makers and enterprise decision makers.
- (ii) Based on the existing deterioration model, the mathematical model of the influence of maintenance measures on the structural performance

under different control conditions is established. For bridge maintenance, three maintenance strategies can exist simultaneously. What maintenance mode to take depends on the situation of the maintenance object itself and should be determined according to the maintenance technology and maintenance means, so as to achieve both economic and effective purposes.

- (iii) The performance of bridge deck pavement decreases gradually with the increase of operation time, so reasonable maintenance measures should be taken to ensure the safety of the bridge. According to the decision-making process of this paper, for different decision makers' goals, combined with examples, this paper has carried on the risk decision-making of the choice of the bridge deck pavement scheme.
- (iv) The risk decision method in this paper can be used for the maintenance management of similar reinforced concrete structures. As for the complex structure, its degradation is complex and changeable, so the decision optimization problem is very complex, which is worthy of further study.

Data Availability

The data used to support the findings of this study are included within the article.

Conflicts of Interest

The authors declare that they have no conflicts of interest.

References

- [1] Y. Yoon and M. Hastak, "Condition improvement measurement using the condition evaluation criteria of concrete bridge decks," *Journal of Transportation Engineering*, vol. 142, 2016.
- [2] D. M. Frangopol and D. Saydam, "Structural performance indicators for bridges," in *Bridge Engineering Handbook*,

- W.-F. Chen and L. Duan, Eds., pp. 185–206, CRC Press, Boca Raton, FL, USA, 2nd edition, 2014.
- [3] D. Honfi, I. Björnsson, O. L. Ivanov et al., “Informed successive condition assessments in bridge maintenance,” *Journal of Civil Structural Health Monitoring*, vol. 10, pp. 729–737, 2020.
- [4] J. Bian, F. Zhu, and Y. Kang, “A review on decision-making of service bridge maintenance and reinforcement based on reliability,” *Chinese and Foreign Highways*, vol. 28, no. 1, pp. 133–138, 2008.
- [5] J. Qin, X. Liu, Y. Zuo, and J. Wang, “Effects of optimal reliability selection model and economic benefits and maintenance strategies on structural,” *Journal of Rock Mechanics and Engineering*, vol. 24, no. 1, pp. 97–104, 2005.
- [6] X. Shao, J. Peng, and B. Yan, “Cost optimization of maintenance scheme for degraded bridge,” *Reliability Engineering Mechanics*, vol. 25, no. 9, pp. 149–155, 2008.
- [7] A. Arzhang, P. Shahram, and M. F. Christopher, “Probabilistic performance-based optimal design of steel moment resisting frames II: applications,” *Journal of Structural Engineering*, vol. 133, no. 6, pp. 767–776, 2007.
- [8] B. Fabio, B. Franco, M. F. Dan et al., “Probabilistic service life assessment and maintenance planning of concrete structure,” *Journal of Structural Engineering*, vol. 132, no. 5, pp. 810–825, 2006.
- [9] G. F. Sirca, H. Adeli and F. Asce, Cost optimization of prestressed concrete bridges,” *Journal of Structural Engineering*.ASCE, vol. 131, no. 3, pp. 0733–9445, 2005.
- [10] M. Cao, S. Zhang, H. Chen, and Q. Huang, “A study on multi-objective optimization method for bridge maintenance decision,” *Chinese and Foreign Highways*, vol. 33, no. 5, pp. 93–97, 2013.
- [11] J. X. Peng, *Macroscopic Characteristics of Dense Road Networks*, The University of Hong Kong, HongKong, China, 2013.
- [12] National Development and Reform Commission and Ministry of Construction, *Methodology of Economic Evaluation and Parameters for Construction Projects*, China Planning Press, Beijing, China, 2006.
- [13] A. Farahani, H. Wallbaum, and J. O. Dalenbäck, “Cost-optimal maintenance and renovation planning in multifamily buildings with annual budget constraints,” *Journal of Construction Engineering and Management*, vol. 146, no. 3, 2020.
- [14] S. Soheil and A. Payam, “Life-cycle cost optimization of semiactive magnetorheological dampers for the seismic control of steel frames,” vol. 29, no. 18, Article ID e1807, 2020.
- [15] M. Feng and Z. Zhao, “Methodology of bridge engineering operation and maintenance,” *Engineering Research - Engineering in an Interdisciplinary Perspective*, vol. 8, no. 6, pp. 644–653, 2016.
- [16] J. K. Vriling, H. G. Voortman, and M. D. Pandey, “A framework for risk criteria for critical infrastructures. Fundamentals and case studies in The Netherlands,” *Journal of Risk Research*, vol. 7, no. 6, pp. 569–579, 2003.
- [17] P. H. Bottelberghs, “Risk analysis and safety policy developments in The Netherlands,” *Journal of Hazardous Materials*, vol. 71, no. 1–3, pp. 59–84, 2000.
- [18] T. Vrouwenvelder, “Stochastic modeling of extreme action events in structural engineering,” *Probabilistic Engineering Mechanics*, vol. 15, no. 15, pp. 109–111, 2000.
- [19] A. Chen, Y. Pan, D. Wang, and R. Ma, “Bridge maintenance and security in the big data age,” *Shanghai Highway*, vol. 1, no. 01, pp. 17–23, 2014.
- [20] D. M. Frangopol and S. Kim, *Life-Cycle of Structures under Uncertainty: Emphasis on Fatigue-Sensitive Civil and marine Structures*, CRC Press, Boca Raton, FL, USA, 2019.
- [21] D. Collings, “An environmental comparison of bridge forms,” *Proceedings of the Institution of Civil Engineers*, vol. 12, pp. 163–168, 2006.
- [22] J. S. Kong and D. M. Frangopol, “Life-cycle reliability-based maintenance cost optimization of deteriorating structures with emphasis on bridges,” *Journal of Structural Engineering*, vol. 129, no. 6, pp. 818–828, 2003.
- [23] J. S. Kong and D. M. Frangopol, “Cost-reliability interaction in life-cycle cost optimization of deteriorating structures,” *Journal of Structural Engineering*, vol. 130, no. 11, pp. 1704–1712, 2004.
- [24] K. Imai and D. M. Frangopol, “System reliability of suspension bridges,” *Structure Safety*, vol. 24, no. 4, pp. 219–259, 2002.
- [25] X. Shao, J. Peng, and B. Yan, “Cost optimization of maintenance scheme for degraded bridge based on reliability,” *Engineering Mechanics*, vol. 197, no. 9, pp. 149–155, 2008.
- [26] X. Liang, *Research on the Risk Management Method of Bridge Operation Safety*, Chang’an University, X’ian China, 2018.
- [27] A. Kamel M, “Quantification of benefits of steel fiber reinforcement for rigid pavement,” *Materials Science*, vol. 4, no. 6, pp. 189–198, 2016.
- [28] Y. Sun and Y. Cao, “Development and application of rapid repairing materials in cement concrete deck repair,” *Highway*, vol. 60, no. 6, pp. 218–223, 2015.
- [29] X. Shao and X. Liu, “Relationship between probability-based bridge deterioration model and maintenance strategy,” *Journal of Chongqing Jiaotong University (Natural Science Edition)*, vol. 26, no. 5, pp. 32–36, 2007.

Research Article

Analysis and Research on Energy-Saving Reconstruction of Building Heating System

Yongqiang Liu  and Zhanfang Huang

School of Construction Engineering, Shandong University of Technology, Zibo 255049, Shandong, China

Correspondence should be addressed to Yongqiang Liu; yongqiangliu110@163.com

Received 14 January 2021; Revised 9 February 2021; Accepted 14 March 2021; Published 14 April 2021

Academic Editor: Di Wang

Copyright © 2021 Yongqiang Liu and Zhanfang Huang. This is an open access article distributed under the Creative Commons Attribution License, which permits unrestricted use, distribution, and reproduction in any medium, provided the original work is properly cited.

A building heating system had high energy consumption and did not meet the requirements of environmental protection, so it was needed to be reformed. After recalculating the heat load, it was found that the heat source, pipe network specification, and radiator area of the original heating system were oversized. After comparing with a gas-fired boiler, the heat source was transformed into the water source heat pump system. The water supply temperature of the water source heat pump was lower than that of the boiler. Generally, it seemed necessary to increase the radiator area. However, after calculation and verification, when the supply and return water temperature was 65/58°C, the system operated continuously and the original pipe network and radiator could still ensure the indoor temperature of 16°C. The total cost of transformation was 11.5 million Chinese Yuan. After analyzing the operation data of the new system, the water source heat pump system could save 82.6% energy compared with the original system and 29.6% cost compared with the central heating system. The transformation is successful, and the experience is worth popularizing.

1. Introduction

In recent years, with more stringent environmental policies, coal-fired boilers for heating are restricted. Many places have been actively promoting “coal to electricity” or “coal to gas” [1, 2]. For buildings outside the scope of central heating, the selection of heat source type needs to consider the factors of technology, environmental protection, energy conservation, and economy. This requires engineers to determine the form of heat source according to local conditions, not mechanically.

Many professionals have studied the heating transformation. Zhang [3] summarized the appropriate technologies and application characteristics of energy-saving renovation of public buildings in hot summer and cold winter zones. Wang et al. [4] took a university located in Jinan Shandong province as an example to investigate the performance of the energy-saving transformation system. He et al. [5] analyzed the problems from various aspects in Karamay Experimental High School, such as heat source, primary circuit, secondary circuit, indoor heating system, and building envelope

structure and put forward the corresponding solutions. After taking measures, the system reached the heating standard. After investigating the cold and heat source system of a middle school in cold area, Zhi-yong et al. [6] carried out energy-saving transformation of the original cold and heat source system from three aspects of load forecasting, transformation scheme design, and transformation benefit analysis. Li [7] used water source heat pump to heat the shaft, which reduced the operating cost by 1.1086 million Chinese Yuan per year.

The application of heat pump in different occasions had also been studied by many scholars. Wu et al. [8] studied the operation characteristics of a closed-loop surface river source heat pump. Li et al. [9] studied the application of seawater-source heat pump in aquaculture. Sun and Li [10, 11] used the technology of mine water source heat pump to supply the heating and cooling of industrial area, which had achieved remarkable economic benefits. Liu et al. [12–14] had studied the application of sewage source heat pump in heating.

In this paper, taking the heating system reconstruction of a waterworks as an example, this paper analyzes the process and thinking of determining the heat source according to the actual situation of the project and comprehensively considers various factors and analyzes the transformation effect.

2. Project Overview

A waterworks, located in Linfen City, Shanxi Province, China, was built in the 1980s with a water supply capacity of 2500 m³/h. All the water comes from underground. There are 2530 square meters of living buildings such as office building (three floors), 6544 square meters of production buildings such as various water treatment workshops (one floor), 3926 square meters of various water pools, with a total construction area of 13000 square meters, including 9970 square meters of heating construction area. There is no central heating pipe network near the plant area. The heat source was a coal-fired hot water boiler with a rated thermal power of 1400 kW, and the indoor radiator heating system was adopted. When the outdoor temperature was lower than 0°C, the boiler system started up and run in intermittent heating mode, and the heating lasted for 5 months every year. During the operation, the average indoor temperature was maintained at 16°C. The average annual consumption of coal was about 700 tons, and the average annual heating cost is 55.1 Chinese Yuan per square meter. The local central heating cost standard is only 23.2 Chinese Yuan per square meter. Thus, the operation cost of the system was very high and the energy waste was serious. At the same time, the local environmental protection policy also began to limit the use of coal-fired boilers, so the energy-saving transformation of heating source was considered.

3. Determination of Heat Source Type

The heating load was recalculated according to the enclosure structure, as shown in Table 1. According to the calculation, the heating load is 648.55 kW, less than half of the original boiler heating power (1400 kW).

There was no central heating pipe network around the plant area, but there was a natural gas pipeline network. At the same time, the plant was rich in water resources, so gas-fired boilers or water source heat pumps were mainly considered as heat sources. According to the investigation, the local natural gas price was 3.2 Chinese Yuan per cubic meter. Gas cost was calculated as shown in Table 2. The cost of gas is 60.28 Chinese Yuan per square meter, even higher than the original coal cost (55.1 Chinese Yuan per square meter).

The water source of the waterworks is well water with a temperature of (17 ± 1)°C, which is suitable for the operation of water source heat pump units in winter. In addition, the waterworks purifies 60000 cubic meters of water every day and operates 24 hours, which can meet the requirements of water source heat pump units. Based on the above analysis, the feasibility of water source heat pump was mainly considered.

4. Determination of Water Source Heat Pump Heating Scheme

4.1. Problems and Analysis of Inconsistency of Supply and Return Water Temperature between Water Source Heat Pump System and Boiler System. According to the actual situation, the water supply temperature of the original boiler system is 80°C, and the temperature difference between supply and return water was 25°C. However, for water source heat pump, the highest temperature of heating water is 65°C, and the temperature difference between supply and return water is generally between 5°C and 15°C (obtained by investigating the manufacturers of heat pump units). Therefore, if the water source heat pump is used to replace the boiler, the water supply temperature will be reduced, and the water temperature difference between supply and return will be smaller. The decrease of water temperature will lead to the decrease of heat dissipation capacity of the radiator; to keep the heat dissipation constant, it seems necessary to increase the radiator area. At the same time, the smaller temperature difference means more flow.

4.1.1. Determination of Temperature Difference between Supply and Return Water of Heat Pump System. The greater the temperature difference of the heat pump system, the smaller the system resistance loss, the more likely to use the old pipe network. According to the excavation investigation, the main pipe of outdoor heating pipe network in the plant is made of DN 125 welded steel pipe. The specific friction is calculated by taking the temperature difference between supply and return water at 5°C, 7°C, and 10°C, and the calculation results are shown in Table 3. When the temperature difference is 7°C and 10°C, the flow meets the requirements of economic specific friction resistance range (30–100 Pa/m [19]).

4.1.2. The Influence of the Decrease of Water Temperature on the Number of Radiators. Two-pipe heating system was used in most buildings of this project. For the convenience of analysis, the inlet and outlet water temperatures of radiator are equal to the temperature of water supply and return of heat source in the following analysis.

According to formulas (1)–(3) [18], the decrease of Inlet water temperature of radiator will lead to the decrease of heat dissipation of single radiator. In order to keep the indoor heat supply constant, it is necessary to increase the number of radiators. From this point of view, it is necessary to reform the indoor heating system after using heat pump:

$$t_{pj} = \frac{t_{sg} + t_{sh}}{2}, \quad (1)$$

$$q = 0.657(t_{pj} - t_n)^{1.306}, \quad (2)$$

$$n = \frac{Q}{q}, \quad (3)$$

TABLE 1: Head load of buildings.

Building	Floorage (m ²)	Heat load (kW)	Heating index (W/m ²)
Office building	2700	183.6	68
Advanced water treatment workshop	2300	138	60
Chemical feed room	1300	88.4	68
Other workshops	3670	238.55	65
Total	9970	648.55	65.1

TABLE 2: Calculation of gas cost.

Parameter name	Parameter value	Unit
Days of heating period	150	d
Heating load	648.55	kW
Inside air calculating temperature for heating	18 [15]	°C
Outdoor mean air temperature during heating period	1.1 [15]	°C
Outdoor air temperature for heating calculating	-6.6 [15]	°C
Annual consumption of heat	6525.99 [16]	GJ
Calorific value of natural gas	38.6 [17]	MJ/m ³
Thermal efficiency of boiler	0.9	
Natural gas consumption	187790.09	m ³
Overall floorage	9970	m ²
Gas fee	60.28	Chinese Yuan/m ²

TABLE 3: Calculation of specific friction under different temperature difference.

Heat load (kW)	Supply water temperature (°C)	Return water temperature (°C)	Temperature difference between supply and return water (°C)	Flow (m ³ /h)	Pipe diameter (mm)	Specific frictional resistance (Pa/m)
648.55	65	60	5	111.5	150	218.81 [18]
		58	7	79.5		110.3 [18]
		55	10	55.7		55.08 [18]

where n is the number of radiators per group, slice/group; Q is the heat release of radiator, W/group; q is the heat release of each radiator, W/piece; t_{pj} is the average water temperature in radiator, °C; t_n is the indoor design temperature for heating, °C; t_{sg} is the inlet water temperature of radiator, °C; and t_{sh} is the outlet water temperature of radiator, °C.

However, by investigating the number of radiators and calculating their heating capacity, as shown in Table 4, it can be found that the number of radiators exceeds the actual demand under the original heating conditions ($Q_S > D_{HL}$). At the same time, the heating capacity under the condition of heat pump is calculated. As shown in Table 4, when the supply and return water temperature is 65/58°C, the indoor temperature is 16°C, which can meet the standard of the original system.

For the heat pump system, on the one hand, in order to use the original radiator, the temperature of supply and return water should be increased; on the other hand, in order to use the original pipe network, the temperature difference of supply and return water should be increased. If the water supply temperature of the heat pump unit is higher than 65°C, its working efficiency will decrease significantly. When the water supply temperature is constant and the water temperature difference between supply and return is enlarged, the flow resistance loss of the pipe network will be reduced, but the heat dissipation capacity of the original radiator will also be reduced. When the supply and return

water temperature is 65/58°C, the original pipe network and radiator can be used to meet the requirements, and the operation energy consumption can be reduced to the greatest extent.

4.2. Measures to Prevent Heat Pump System from Polluting Water. Using water source heat pump unit, the well water should be directly connected to the evaporator in the unit. In the evaporator, the refrigerant and water exchange heat through the copper tube, which will not pollute the water under normal conditions. However, if there is a rupture of the copper tube, resulting in the leakage of refrigerant, it will cause pollution. In order to prevent this situation, water-water heat exchanger can be added to completely isolate water source system and refrigerant system. In order to prevent the pollution caused by the pipeline system, high-density polyethylene is selected as the pipe material, and copper or stainless steel material is selected for the valve.

4.3. Heat Source Reconstruction Scheme of the Waterworks. There are not only static water sources such as pools but also flowing water sources such as various pipelines. The initial investment and operation cost of intake pump can be saved by using the water in the pipeline. The use of the flowing water source can save the cost by not using intake pump. Through field investigation and analysis, it is determined

TABLE 4: The number of radiators in each building and its heating capacity.

Building	Number of radiators per square meter, n (slice/m ²)	Heat release of each radiator when the supply and return water temperatures are 65/58°C and the indoor temperature is 16°C, q_2 (W/piece)	The heat supply per square meter when the supply and return water temperatures are 65/58°C and the indoor temperature is 16°C ($Q_{s2} = q_2 * n$, (W/m ²))
Office building	0.69	63.48	66.7
Advanced water treatment workshop	0.63	57.96	60.9
Chemical feed room	0.71	65.32	68.6
Other workshops	0.63	57.96	60.9

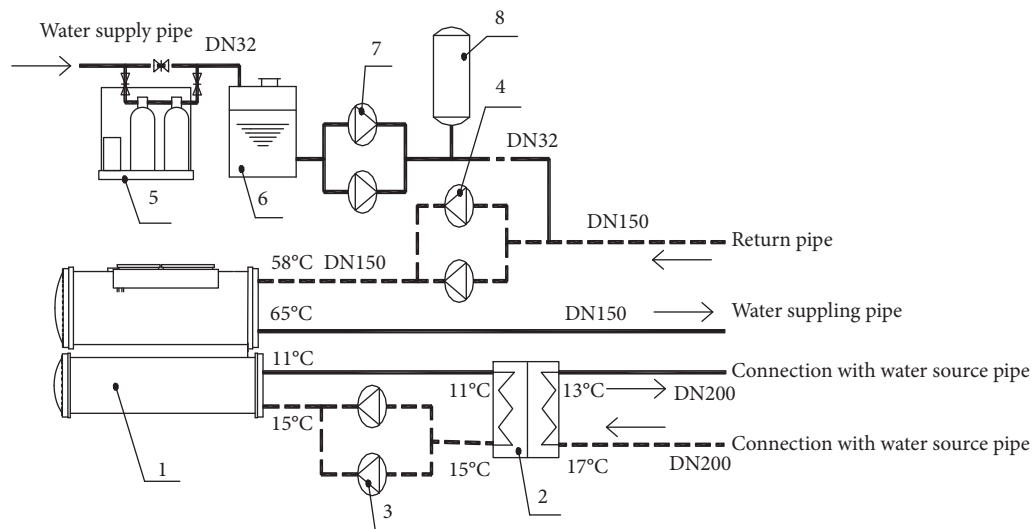


FIGURE 1: Flow chart of water source heat pump system.

that part of the water from the underground pump house to the advanced water treatment workshop is led out from the water supply pipeline as the water source of the heat pump unit. Based on the above analysis, the process flow of the water source heat pump system was determined, as shown in Figure 1, and the main equipment parameters are shown in Table 5. The system can automatically adjust the water supply temperature according to the outdoor air temperature, which can not only save energy but also save labor management costs.

5. Economic Analysis of Water Source Heat Pump System

5.1. Initial Investment and Operation Cost of Water Source Heat Pump System. The reconstruction cost of the system included the equipment, pipeline, and electrical system of the heat pump room, as well as the water intake pipeline, with a total cost of 1.15 million Chinese Yuan.

The water source heat pump system was completed in October 2014 and put into use in November of the same year. It runs 24 hours and lasts for 5 months in each heating season (the central heating time is 4 months). So far, the water source heat pump system has been operating well. The indoor temperature has been kept in the range of 16–18°C.

After the transformation, the power consumption of the system is shown in Table 6.

5.2. Energy-Saving Analysis Compared with the Original System. Before reconstruction, the annual energy consumption of heating system is 2154000 kW h (as shown in Table 7), at present, the annual power consumption of heat pump heating system is 374126.7 kW h (as shown in Table 6). The energy consumption of the heat pump system is only 17.4% of that of the original boiler system, and the energy-saving rate reaches 82.6%.

5.3. Economic Analysis Compared with Central Heating. The heat pump system runs five months a year, but the local central heating system runs four months a year. In order to compare the operation costs of the two heating modes, half of the energy in the first month and the last month of the heat pump system operation period is converted, as shown in Table 8. Obviously, the converted system operation cost is only 16.35 Chinese Yuan/(m²•year), but the cost of central heating in this city is 23.2 Chinese Yuan/(m²•year), and the operation cost of the heat pump system is only 70.4% of the central heating cost. All in all, the heat source transformation is very successful, saving energy and money.

TABLE 5: Parameters of main equipment.

Equipment number	Equipment name	Equipment parameters
1	Water-source heat pumps	The heating capacity under design condition is 702 kW
2	Plate heat exchanger	The heat transfer capacity under design condition is 550 kW
3	Circulating water pump	The flow rate is 120 m ³ /h, the lift is 8 m H ₂ O
4	Circulating water pump	The flow rate is 73 m ³ /h, the lift is 32 m H ₂ O
5	Water softener	The water treatment capacity is 1.0 m ³ /h
6	Soft water tank	The volume is 1.0 m ³
7	Make-up water pump	The flow rate is 1.0 m ³ /h, the lift is 22 m H ₂ O
8	Pressure tank	The regulating volume is 0.2 m ³

TABLE 6: Power consumption statistics of the system after transformation.

Month	Power consumption (kW·h)				Subtotal	Average value
	The first year	The second year	The third year			
November	54560	39980	56340		150880	50293.33
December	93860	83520	89540		266920	88973.33
January	93480	107160	133100		333740	111246.67
February	66460	86800	80200		233460	77820.00
March	34700	56480	46200		137380	45793.33
Total	343060	373940	405380		1122380	374126.67

TABLE 7: Energy consumption of original system.

Name	Number/power	Coal consumption rate of power supply/operation time of circulating pump	Equivalent electric energy consumption
Coal	700 t	333 g/kW·h [20]	2100000 kW·h
Circulating pump	20 kW	2700 hours	54000 kW·h
Equivalent power consumption of original system			2154000 kW·h

TABLE 8: Converted operating cost of heat pump system.

Month	Actual power consumption in three years (kW·h)	Converted power consumption in three years (kW·h)	Unit price of electricity (Chinese Yuan/kW·h)	Average annual converted electric charge (Chinese Yuan)	Floorage (m ²)	Average annual electricity charge per unit area (Chinese Yuan/(m ² ·year))
November	150880	75440		37720		1.26
December	266920	266920		133460		4.46
January	333740	333740		166870		5.58
February	233460	233460	0.5	116730	9970	3.90
March	137380	68690		34345		1.15
Total	1122380	978250		489125		16.35

6. Conclusion

- (1) For projects with abundant water resources, such as waterworks, it is a relatively economic scheme to use water source heat pump in winter. The operation cost of water source heat pump system is only 70.4% of the cost of central heating in local cities.
- (2) In some heating transformation projects of heat pump replacing boiler, although the temperature of supply and return water decreases, it is not necessary to increase the number of radiators, which needs to be calculated and verified according to the actual situation. This is caused by the excessive number of radiators in the original system.

- (3) For waterworks, when water source heat pump unit is used as heating source, it is necessary to take measures to prevent water pollution, such as setting heat exchanger.

Data Availability

The data used to support the findings of this study are included within the article.

Conflicts of Interest

The authors declare that there are no conflicts of interest regarding the publication of this article.

References

- [1] H. Chunxu, A. Qu, Z. Dong, J. Qin, Z. Go, and R. Hu, "Study on subsidy policy of clean heating environment in North China," *Ecological Economy*, vol. 36, no. 4, pp. 151–155, 2020, (in Chinese).
- [2] W. Yu, R. Jia, X. Xia, H. Zheng, and B. Hu, "Analysis of the current situation and marketing for "Coal to electricity" in Shanxi province," *Shandong Electric Power*, vol. 47, no. 270, pp. 61–64, 2020, (in Chinese).
- [3] W. Zhang, "Technical analysis and energy efficiency evaluation of energy saving renovation of public buildings in hot summer and cold winter zone," *HV&AC*, vol. 50, no. 5, pp. 67–70, 2020, (in Chinese).
- [4] X. Wang, X. Zhou, and P. Cui, "A case study for the energy-saving transformation of an existing heating system in an university," *District Heating*, vol. 2, pp. 33–42, 2019, (in Chinese).
- [5] J. He and X. Guo, "Analysis and solutions of heating system problems in Karamay experimental high school," *Energy and Energy Conservation*, vol. 171, no. 12, pp. 88–90, 2019, (in Chinese).
- [6] L. Zhi-yong, D. Nai-ren, and F. Liu, "Feasibility analysis of a high school in cold regions design project for energy retrofit," *Energy Conservation*, vol. 379, no. 4, pp. 29–32, 2014, (in Chinese).
- [7] X. Li, "Analysis of heat source reforming scheme of anti-freezing heating in zhaogu No. 2 Mine," *Coal and Chemical Industry*, vol. 43, no. 8, pp. 95–97, 2020, (in Chinese).
- [8] S. Wu, F. Yun-zhun, and C. Li-jie, "Experimental study on refrigeration operation characteristics of a close-loop surface river source heat pump system," *Fluid Machinery*, vol. 46, no. 10, (in Chinese), 2018.
- [9] X. Li, W. Deng, D. Zhang, Z. G. MuGan, S. Chen, and Q. Che, "Engineering application of seawater-source heat pump for waste heat recovery in sea cucumber breeding system," *Transactions of the Chinese Society of Agricultural Engineering*, vol. 33, no. 9, pp. 218–223, 2017, (in Chinese).
- [10] X. Sun and S. Zhu, "Analysis of winter operating performance and economy of a mine water source heat pump system," *Building Science*, vol. 34, no. 2, pp. 49–54, 2018, (in Chinese).
- [11] K.-r. Li, "Mine water waste heat utilization in Tangjiahui Coal Mine," *Coal Engineering*, vol. 52, no. 7, pp. 24–26, 2020, (in Chinese).
- [12] X. Liu, Z. Yin, C. Liang, Z. Li, and C. Wang, "Study on the actual application effect of sewage source heat pump in a green building in a cold region during the heating season," *Building Science*, vol. 34, no. 8, pp. 10–17, 2018, (in Chinese).
- [13] X. Jia, M. Duan, and H. Shu, "Field measurement and energy-saving potential analysis on the performance of a sewage-water heat pump system," *Journal of Refrigeration*, vol. 38, no. 6, pp. 66–72, 2017, (in Chinese).
- [14] P. Chun-ying, K. Liu, J. Zheng, H. Deng-yue, G. Wen-bao, and L. Yu-hong, "Application research of sewage source heat pump for heating of WWTP," *China Water&Wastewater*, vol. 27, no. 17, pp. 91–95, 2011, (in Chinese).
- [15] Ministry of Housing and Urban-Rural Development of the People's Republic of China, *Design Code for Heating Ventilation and Air Conditioning of Civil Buildings(GB 50736-2012)*, China Architecture & Building Press, Beijing, China, 2012pp. 6–107, (in Chinese).
- [16] Ministry of Housing and Urban-Rural Development of the People's Republic of China, *Design Code for City Heating network(CJJ34-2010)*, China Architecture & Building Press, Beijing, China, 2011pp. 9–11, (in Chinese).
- [17] X. Liu and J. Zhu, "Water-loop heat pump was applied in space heating in winter," *Acta Energeiae Solaris Sinica*, vol. 26, no. 2, pp. 262–265, 2005, (in Chinese).
- [18] Y. Lu, *Practical Heating and Air Conditioning Design Manual* China Architecture Publishing Press, Beijing, China, Second edition, pp. 53–401, Beijing, China, 2008, (in Chinese).
- [19] Department of Construction Engineering Quality & Safety Supervision Ministry of Housing and Urban-Rural Development of the P. R. China, "China Institute of Building Standard Design & Research," in *National Technical Measures for Design of Civil Construction(2009)-Heating, Ventilation and Air Conditioning*, pp. 50-51, China Planning Press, Beijing, China, 2009, (in Chinese).
- [20] Y. Yang, Z. Yang, G. Xu, and N. Wang, "Situation and prospect of energy consumption for China's thermal power generation," in *Proceedings of the CSEE*, vol. 33, no. 23, pp. 1–12, 2013, (in Chinese).

Research Article

Research on Fatigue Model of Semi-Rigid Base Asphalt Pavement before and after Polymer Grouting

Bei Zhang , Xu Zhang, Yanhui Zhong , Xiaolong Li , Meimei Hao , Xianwei Sang, Xiaoliang Wang, and Jianyang Liu

College of Water Conservancy and Engineering, Zhengzhou University, Zhengzhou 450001, China

Correspondence should be addressed to Yanhui Zhong; zhong_yanhui@163.com and Xiaolong Li; wennuandeshang@hotmail.com

Received 9 December 2020; Revised 26 January 2021; Accepted 2 February 2021; Published 22 February 2021

Academic Editor: Di Wang

Copyright © 2021 Bei Zhang et al. This is an open access article distributed under the Creative Commons Attribution License, which permits unrestricted use, distribution, and reproduction in any medium, provided the original work is properly cited.

To improve the service life of a semirigid base asphalt pavement and prolong its service cycle, it is imperative to conduct long-term performance research before and after pavement disease repair. This study proposes a fatigue damage model for pavement and polymer materials and uses the finite element method to establish a three-dimensional numerical model of a semirigid base asphalt pavement structure. Moreover, it compares and analyzes the mechanical response and fatigue damage of this pavement before and after polymer repair. The evolution law is verified by indoor fatigue tests. The results show that, under a standard load of 0.7 MPa, the vertical displacement and the Mises stress of the vacant position after the polymer repair are reduced by 61% and 69%, respectively. Under a cyclic load of 1.2 MPa, the number of load actions increases from 500,000 to more than 5 million, and the fatigue damage factor of the polymer is reduced by 29%. With the increase in the number of fatigue test loads, the cumulative evolution trend of the fatigue damage is basically consistent with the results of the numerical simulation, which verifies the rationality of the numerical model. This research is relevant for providing a reference for extending the service life of expressways and improving the technical level of expressway maintenance.

1. Introduction

In recent years, highway construction in China has developed rapidly, and the scale and number of constructions have increased swiftly. In 2019, the total mileage of highways reached 5 million km, of which 143,000 km corresponded to expressways. Semirigid base pavement structures are the most extensively used ones in expressways owing to their high stiffness and high stability [1]. Under the cyclic effect of vehicle load and the rapid increase in traffic volume, a semirigid base layer undergoes a certain degree of plastic deformation, and some voids or even vacancies form at the bottom of the base layer, causing fatigue damage. Thus, in turn, results in the road structure no longer serving as a continuous and uniform support structure, which severely affects opening an expressway to traffic and its normal use, thereby threatening the healthy development of the society and the economy [2].

Numerous scholars have conducted studies on the fatigue characteristics of semirigid base asphalt pavement structures. In 2014, Maitra et al. established a numerical model based on fictitious crack and stress degradation approaches to theoretically study the internal crack growth and fatigue characteristics of a concrete pavement under cyclic loading [3]. In 2016, Hu et al. used digital image processing to detect the microstructure of asphalt mixtures, studied and analyzed the changes in their internal structure morphology, and obtained the relationship between the microstructure and the fatigue damage [4]. In 2018, Cheng et al. studied the fatigue characteristics of in-service cold central-plant recycling (CCPR) and hot mix asphalt (HMA) mixtures by indirect tensile fatigue tests and obtained their fatigue failure characteristics and fatigue life. Moreover, they proposed a method to calculate CCPR based on the fatigue test results, on-site traffic load, and HMA mixture displacement factor method [5]. In 2018, Barman et al. used the fatigue index f_i to

characterize the fatigue resistance of asphalt mixtures and tested the fatigue resistance of five different types using the indirect tension test data [6]. In 2019, Lv et al. conducted unconfined compressive strength, indirect tensile strength, and four-point bending strength tests on cement-stabilized crushed stone specimens under various loading rates to obtain the fatigue test stress ratio related to the loading rate and solve various problems. There exist uncertainty and nonuniqueness of fatigue characteristics in the single-load mode [7]. In 2019, Zhang et al. introduced loading frequency into the classic Chaboche damage evolution model, conducted theoretical analysis and laboratory tests, and established a new damage evolution model [8]. In 2020, Wei et al. studied the effects of frequency, load displacement, asphalt aggregate ratio, and aging degree on the fatigue performance and disturbance changes of large stone asphalt mixtures based on the viscoelastic continuum damage model method [9]. In summary, it can be seen that relatively there are many studies on the fatigue characteristics of road materials using traditional fatigue test methods; however, they have disadvantages, such as long test cycles, high capital investment, and lack of theoretical basis.

The traditional methods for repairing semirigid base asphalt pavement diseases include excavation and reconstruction, paving, grouting, and cement-based grouting repair technology. However, these methods have long construction and maintenance times; consume substantial manpower, material resources, and financial resources; and severely affect traffic [10]. In recent years, polymer grouting repair technology has been an emerging nonexcavation repair technology. It has been extensively used in the treatment of many hidden road diseases in China and achieved good results [11]. Shi et al. studied the compressive strength of polymer grouting materials having different densities and at different temperatures by uniaxial compression tests [12]. Liu et al. studied the compressive mechanical properties of polyurethane polymer grouting materials of different densities, and the results showed that polyurethane polymer grouting materials of low densities possess elastoplastic characteristics [13]. Bezazi and Scarpa comparatively analyzed the cyclic load tensile behaviors of conventional and expanded thermoplastic polyurethane polymers and studied the relationship between the decrease in their stiffness and the accumulation of energy dissipation and the number of cycles [14]. Pulungan et al. proposed a viscoelastic-viscoplastic damage model for polypropylene-based polymers, which was verified by three-point bending tests conducted at different loading speeds [15]. From the above studies, it can be seen that polymer materials have good mechanical properties and fatigue resistance.

In summary, although polymer grouting repair technology has been widely used in the treatment of many road diseases in my country and has achieved good repair results. However, there are relatively few studies on the long-term service performance of polymer grouting repaired roads, and the evolution of fatigue damage of the pavement structure after polymer grouting repair is not clear. Therefore, in this study, polymer grouting technology is used to repair the vacancy disease of a semirigid base asphalt

pavement, and a fatigue damage model suitable for semirigid base materials and polymer grouting materials is proposed. A finite element software is used to modify the pavement structure before and after the repair. Mechanical response analysis, the repair effect of the polymer grouting to repair the void disease of the semirigid base, and the evolution law of the fatigue damage were studied, and the model was verified by indoor fatigue tests. This study has theoretical reference significance for the prediction of the remaining life of a semirigid base asphalt pavement and the repair of hollow semirigid base asphalt pavements by polymer grouting.

2. Material Fatigue Damage Model

2.1. Two-Stage Fatigue Damage Model of Pavement Structure Materials. In this study, based on the simplified Chaboche nonlinear fatigue damage model, the evolution process of the fatigue damage of semirigid base asphalt pavement structural materials is corrected. Moreover, a two-stage fatigue damage model suitable for the rapid and steady growth of pavement structural material damage variables is established to study the evolution law of structural fatigue damage of a semirigid base asphalt pavement.

- (1) Cumulative law of damage evolution in Chaboche nonlinear fatigue damage model

The simplified Chaboche nonlinear fatigue damage model is [16]

$$\frac{dD}{dN} = a \left[\frac{\sigma}{(1-D)} \right]^p, \quad (1)$$

where a and p are the characteristic damage parameters of the material, N is the number of cyclic loading, D is the current damage, and σ is the load stress during the cyclic loading.

The fatigue damage model can describe the phenomena of different loading sequences and different damage conditions when multilevel loads are applied sequentially, which is highly convenient in finite element calculation. The damage evolution and accumulation rules of the simplified Chaboche nonlinear fatigue damage model are listed in Table 1.

It can be seen from Table 1 that the initial damage of the material is assumed to be $D_0 = 0$, the stress during the first cyclic loading is σ , and the damage caused by the first cyclic loading is $D_1 = a\sigma^p$. Assuming that the cyclic stress remains unchanged, the damage caused by the second cyclic loading is $D_2 = a(\sigma/(1-D_1))^p$. Thus, the damage caused by the n th cycle loading is $D_n = a(\sigma/(1-D_{n-1}))^p$, and the total damage caused by the n th cycle is $D_M = D_1 + D_2 + \dots + D_n = a\sigma_1^p + a(\sigma_2/(1-D_1))^p + \dots + a(\sigma_n/(1-D_{n-1}))^p$.

- (2) Chaboche nonlinear fatigue damage model correction

The destruction of pavement structure materials is divided into two stages: crack formation and

TABLE 1: Simplified Chaboche nonlinear fatigue damage model damage evolution and accumulation law.

N	σ	D_N	D_M
0	0	0	0
1	σ_1	$a\sigma_1^p$	$a\sigma_1^p$
2	σ_2	$a(\sigma_2/(1-D_1))^p$	$a\sigma_1^p + a(\sigma_2/(1-D_1))^p$
...
n	σ_n	$a(\sigma_n/(1-D_{n-1}))^p$	$a\sigma_1^p + a(\sigma_2/(1-D_1))^p + \dots + a(\sigma_n/(1-D_{n-1}))^p$

macrocrack propagation. When the fatigue damage reaches the critical value, DC, cracks are formed and macroscopic cracks begin to grow. In this study, the critical value of the fatigue damage DC=0.5 [17]. The semirigid base material is brittle, and the fatigue life of the macroscopic crack propagation stage is relatively short. Therefore, this study mainly examines the crack formation stage and approximates the fatigue life of the used pavement structure material to the fatigue life of the crack formation stage.

In this study, the elastic modulus loss is used to define the material damage variable D as follows:

$$D = 1 - \frac{\tilde{E}}{E} \quad (2)$$

where \tilde{E} is the modulus of the damaged state and E is the modulus of the nondestructive state.

The simplified Chaboche nonlinear fatigue damage model has a certain impact on the simulation analysis of the pavement structure damage field and the fatigue damage evolution process, and the model needs to be modified to a certain extent. From the simplified Chaboche nonlinear fatigue damage model, it can be found that, in the controlled stress fatigue test method, the damage accumulation rate is determined by $1/(1-D)$. In this study, it is revised to $1/(1-D)^\alpha$, so that, by changing the size of α , the material damage accumulation rate is changed. The revised fatigue damage model is

$$\frac{dD}{dN} = \begin{cases} a \left[\frac{\sigma}{(1-D)^{\alpha_1}} \right]^p & (0 \leq D \leq D_m), \\ a \left[\frac{\sigma}{(1-D)^{\alpha_2}} \right]^p & (D_m \leq D \leq D_c), \end{cases} \quad (3)$$

where D_m is 0.35 and D_c is 0.5.

(3) Two-stage fatigue damage model parameters

(a) Fatigue damage model material characteristic parameters a and p

In this study, the pavement structure is simplified as a single beam specimen. Moreover, the beam specimen is analyzed and deduced under a fixed load based on the damage evolution characteristics of a two-stage fatigue damage model and the material classic fatigue life formula to determine model parameters a and p [18–20].

- ① The empirical formula for the fatigue life of the pavement structure trabecular material under the controlled stress mode is

$$N_f = A\sigma^{-B}. \quad (4)$$

- ② Material characteristic parameters a and p are calculated assuming that $\alpha = 1$. Specifically,

$$\frac{dD}{dN} = a \left[\frac{\sigma}{(1-D)} \right]^p. \quad (5)$$

- ③ The constitutive formula of the damaged material can be obtained from equation (2) as follows:

$$\sigma = E(1-D)\varepsilon. \quad (6)$$

- ④ The relationship between the deformation and displacement of the static trabeculae can be derived as follows:

$$\varepsilon = \frac{y}{\rho},$$

$$\sigma = \frac{E(1-D)y}{\rho}, \quad (7)$$

$$\frac{dD}{dN} = aE^p \varepsilon^p,$$

where ρ is the radius of curvature of the beam, ε is the plane section strain of the beam, and y is the distance from a point on the beam section to the neutral axis of the section.

- ⑤ Point C represents the point at the bottom of the beam on the cross section of the trabeculae:

$$\varepsilon_c = \frac{y_c}{\rho},$$

$$\frac{dD_c}{dN} = aE^p \varepsilon_c^p, \quad (8)$$

$$\frac{dD}{dD_c} = \frac{\varepsilon^p}{\varepsilon_c^p} = \frac{y^p}{y_c^p}.$$

- ⑥ Assuming that the position of the neutral axis does not change with the damage process, integrating equation (8) yields

$$D = \frac{y^p}{y_c^p} D_c, \quad (9)$$

$$\sigma = \frac{E(1 - (y^p/y_c^p)D_c)y}{\rho}.$$

- ⑦ The bending moment balance formula on the cross section is

$$M = \int y\sigma dA, \quad (10)$$

$$M = \int \frac{E(1 - (y^p/y_c^p)D_c)y^2}{\rho dA}.$$

- ⑧ If $\bar{I} = \int y^2(1-D)dA = \int y^2(1 - (y^p/y_c^p)D_c)dA$ represents the moment of inertia after the section is damaged, then

$$\frac{1}{\rho} = \frac{M}{E\bar{I}} \quad (11)$$

- ⑨ When the trabeculae are not damaged,

$$\sigma_0 = \frac{My}{I_0}, \quad I_0 = \int y^2 dA,$$

$$D = \frac{p+3}{p} \left\{ 1 - \left[1 - aN(\sigma_0)^p \frac{p+1}{p+3} \right]^{1/(p+1)} \right\}. \quad (12)$$

- ⑩ Considering the initial stress at point C as σ_c ,

$$D_c = \frac{p+3}{p} \left\{ 1 - \left[1 - aN(\sigma_c)^p \frac{p+1}{p+3} \right]^{1/(p+1)} \right\}. \quad (13)$$

When $D_c = 0.5$, the corresponding number of cycles, N_{cr} , is the fatigue crack formation life.

$$N_{cr} = \frac{p+3}{3a(p+1)(0.5)^p} \left[1 - \left(\frac{p}{p+3} \right)^{p+1} \right] (\sigma_c)^{-p}. \quad (14)$$

Comparing equation (1) with the empirical formula of fatigue life yields

$$A = \frac{p+3}{3a(p+1)(0.5)^p} \left[1 - \left(\frac{p}{p+3} \right)^{p+1} \right], \quad (15)$$

$$B = p. \quad (16)$$

From equations (15) and (16), it can be seen that determining the classic fatigue life equation of the trabecular material can yield the two-stage fatigue damage model parameters of a and p .

Based on the parameter determination method used in this study and the empirical formula of

the fatigue life of different pavement structure materials, parameters a and p of different pavement structure materials can be obtained, which are listed in Table 2.

- (b) Fatigue damage model correction parameter α
The accumulation rate of the material fatigue damage is determined by the current stress σ and $1/(1-D)^\alpha$. When the stress is a fixed value, the larger the value of $1/(1-D)^\alpha$, the higher the accumulation rate of the fatigue damage; the smaller the value of $1/(1-D)^\alpha$, the lower the accumulation rate of the fatigue damage. This study defines $1/(1-D)^\alpha$ as the sensitivity coefficient of the fatigue damage rate to the current stress.
- ① When $\alpha > 1$, the sensitivity coefficient of the fatigue damage rate to the stress increases, which increases the damage field gradient. When $\alpha < 1$, the sensitivity coefficient of the fatigue damage rate to the stress decreases, which reduces the damage field gradient to correct the damage model effect. Therefore, $\alpha < 1$ during the model revision process.
- ② This study uses a trial algorithm to determine the specific values of the two-stage fatigue damage model parameters: α_1 and α_2 . To this end, first α_1 and α_2 are assumed, and they are combined with parameters a and p . Subsequently numerical simulations are conducted, and the simulation results are compared with the test data. If the results are close, then the hypothetical values of α_1 and α_2 are valid; otherwise, they are re-assumed. Following many trial calculations, this study yields $\alpha_1 = 0.4$ and $\alpha_2 = 0.2$.

- (4) Two-stage fatigue damage model verification

Substituting the model parameters to obtain the two-stage fatigue damage model of a semirigid base asphalt pavement structure material can be expressed as

$$\frac{dD}{dN} = \begin{cases} a \left[\frac{\sigma}{(1-D)^{0.4}} \right]^p & (0 \leq D \leq D_m), \\ a \left[\frac{\sigma}{(1-D)^{0.2}} \right]^p & (D_m \leq D \leq D_c). \end{cases} \quad (17)$$

In this study, a two-dimensional finite element simulation of a typical semirigid base asphalt pavement structure material cement-stabilized gravel is conducted, and the simulation results of the fatigue damage evolution are compared with those of the indoor fatigue tests, as shown in Figure 1.

It can be seen from Figure 1 that the finite element simulation results of the cement-stabilized gravel material are in good agreement with the test results. This proves that the two-stage fatigue damage model used in this study can

TABLE 2: Summary of material damage parameters a and p for different pavement structures.

Pavement structure materials	a	p
SMA-13	$2.81e-3$	4
AC-20	$2.81e-3$	4
AC-25	$2.81e-3$	4
Cement-stabilized macadam	$1.36e+4$	2.02
Cement-stabilized gravel	$9.52e+7$	2.02

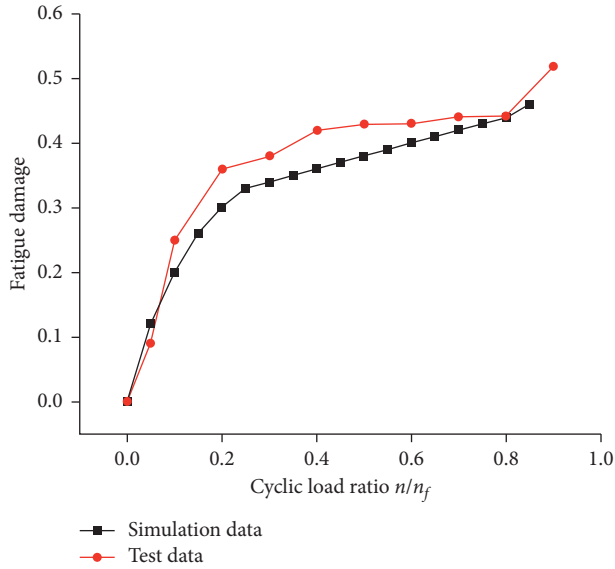


FIGURE 1: Comparison of results of fatigue damage accumulation curves of cement-stabilized gravel.

effectively predict the fatigue damage evolution process of semirigid base materials.

2.2. $D-N$ Fatigue Damage Model of Polymer Grouting Material. Compared with polymer materials, the stress generated by a road surface under a traffic load is low. According to the phenomenological theory, this study adopts a 0.7 stress ratio level $D-N$ fatigue damage model as the fatigue damage model of the polymer grouting materials.

As per [21], the microdamage evolution of same-density polymer material specimens under various stress levels can be divided into three stages. This study selects a 0.3 g/cm^3 polymer material to analyze the measured data of the cyclic compression fatigue test and obtains the fatigue damage equation for its each stage when the stress ratio is 0.7, as shown in Figure 2.

From the regression analysis, the $D-N$ fatigue damage evolution model of the above-mentioned polymer grouting material can be obtained as

$$D = \begin{cases} -0.03207 \times e^{-(N/29.7877)} + 0.03192 & (N < 100), \\ -0.01616 \times e^{-(N/2450.51)} + 0.04014 & (100 < N < 10000), \\ 0.03474 \times e^{-(N/173249.44)} + 0.00838 & (N > 10000). \end{cases} \quad (18)$$

The three-stage correlation coefficients, R^2 , are 0.9185, 0.8249, and 0.7607, respectively. It can be seen that the fitting equations of the first two stages are highly correlated. Owing to the cyclic hardening of the polymer material in the third stage of damage evolution, the fatigue damage value is reduced to a certain extent. This study does not consider the third stage of damage evolution [22].

Therefore, the polymer $D-N$ fatigue damage model used in expressway grouting repair is

$$D = \begin{cases} -0.03207 \times e^{-(N/29.7877)} + 0.03192 & (N < 100), \\ a(-0.01616 \times e^{-(N/2450.51)} + 0.04014) & (100 < N), \end{cases} \quad (19)$$

where a is 0.626 to ensure the continuity of the damage curve.

3. Research on Fatigue Characteristics of Semirigid Base Pavement

3.1. Numerical Simulation Research. In the engineering field, in the process of studying the fatigue characteristics of the actual pavement structure, the method of finite element numerical analysis is usually used to realize it. In this section, based on the ABAQUS finite element software, the user material subroutine of the damaged material is written, the damage variable is introduced into the constitutive equation of the damaged material, and the fatigue characteristics of the pavement structure under the traffic load are numerically simulated and analyzed.

(1) Basic assumptions

This study makes the following assumptions about the pavement structure model based on the theory of a multilayer elastic system of asphalt pavements [23]:

- ① Each structural layer is composed of isotropic materials, which are continuous and uniform elastic layered systems.
- ② The soil foundation is infinite in the horizontal and vertical directions, and the other structural layers are infinite in the horizontal direction.
- ③ Only the vertical displacement and stress are continuous between the layers, without considering frictional resistance.

(2) Model description

In this study, considering the symmetry of the pavement structure and load, the fatigue damage calculation time is extremely long [24]. A 1/2 pavement model is selected for the analysis. The size of the model is length \times width \times height = $6 \text{ m} \times 6 \text{ m} \times 3 \text{ m}$. The pavement structure consists of six parts: SMA-13, AC-20, AC-25, cement-stabilized macadam base, cement-stabilized gravel base, and soil base, as shown in Figure 3.

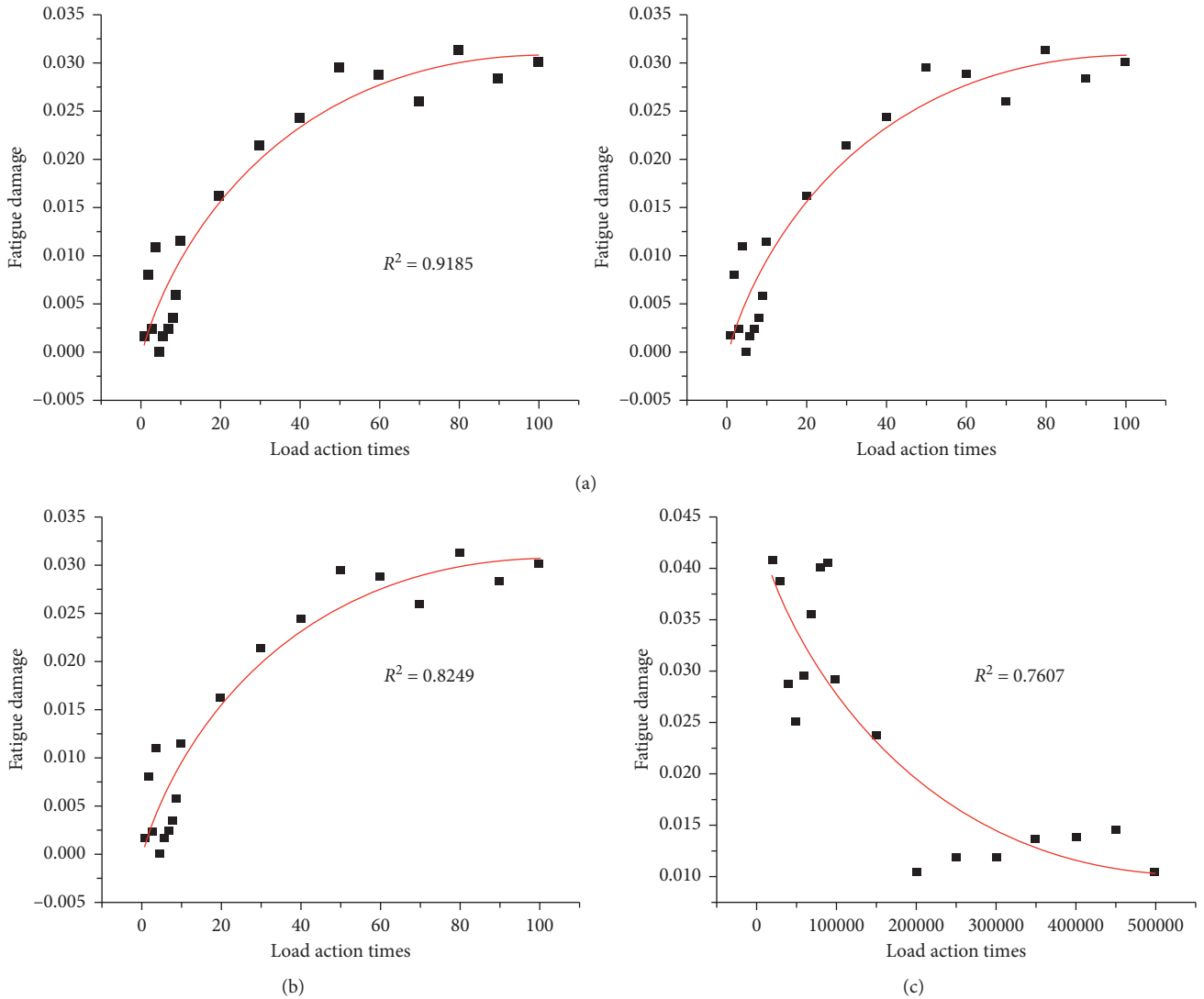


FIGURE 2: Accumulation of fatigue damage at each stage of 0.3 g/cm³ polymer at a stress ratio of 0.7. (a) The first stage of fatigue damage of 0.3 g/cm³ polymer under 0.7 stress level. (b) The second stage of fatigue damage of 0.3 g/cm³ polymer under 0.7 stress level. (c) The third stage of fatigue damage of 0.3 g/cm³ polymer under 0.7 stress level.

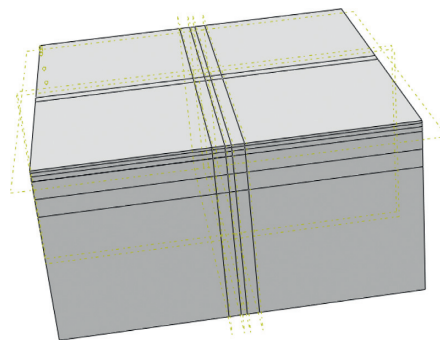


FIGURE 3: Overall structure diagram of semirigid base asphalt pavement.

A void area of size 50 cm × 20 cm × 0.5 cm is set in the middle of the bottom of the base layer, as shown in Figure 4.

The parameters of the semirigid base asphalt pavement structure materials and polymer grouting materials are listed in Table 3 [25].

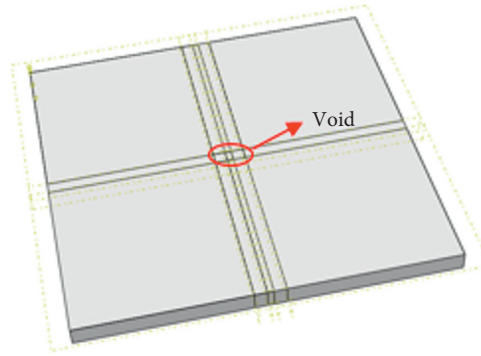


FIGURE 4: Layout of void area at bottom of base layer.

TABLE 3: Road structure and related parameters of polymer grouting materials.

Structural layer	Material	Thickness (cm)	Modulus of elasticity (MPa)	Poisson's ratio	Density (kg/m ³)
Upper surface	SMA-13	4	1400	0.35	2400
Middle surface	AC-20	6	1200	0.30	2400
Under surface	AC-25	8	1000	0.30	2400
Base	Cement-stabilized macadam	30	1500	0.25	2300
Subbase	Cement-stabilized gravel	30	1300	0.30	1800
Subgrade	Compacted soil	—	50	0.4	1920
—	Polymer	0.5	80	0.4	300

(3) Model boundary conditions and mesh division

The bottom of the model is completely fixed. The left and right sides of the model limit the displacement in the Z direction and the rotation in the XY direction, and the front and rear sides limit the displacement in the X direction and the rotation in the YZ direction. Contact surfaces between the surface layer and the base layer and between the base layer and the base layer are established. It is assumed that the two contact surfaces will not be separated and are in a bound state to ensure the continuous transmission of their vertical stress and displacement, as shown in Figure 5.

In the dynamic response analysis, the model uses a $0.1\text{ m} \times 0.1\text{ m}$ grid division, and the semirigid base asphalt pavement structure and the polymer material model use C3D8R hexahedral-reduced integral units.

(4) Cyclic traffic load setting

In this study, the vehicle wheel load is simplified as a double rectangular vertical uniform load, and the rectangular size is $0.2\text{ m} \times 0.167\text{ m}$. The load surface is a load moving belt based on a single-axle two-wheel group. With reference to the standard wheel diameter of 21.3 cm, the center distance between the two wheels is 31.9 cm, and the two-wheel track of the load moving belt is set as 20 cm. The wheel track distance is 10 cm. The traffic load is directly applied to the vacant area, and FORTRAN programming is used to compile subroutines to realize the cyclic movement of the load. The speed of the vehicle load is set as 6 m/s. A schematic of the traffic load action area is shown in Figure 6.

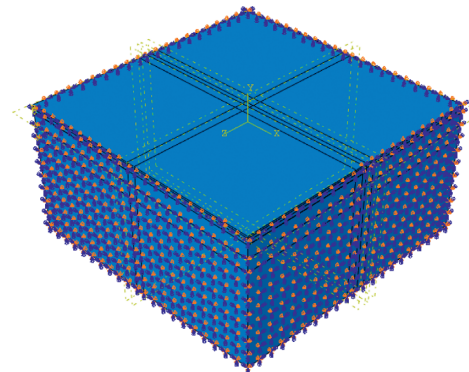


FIGURE 5: Boundary condition setting diagram of pavement structure model.

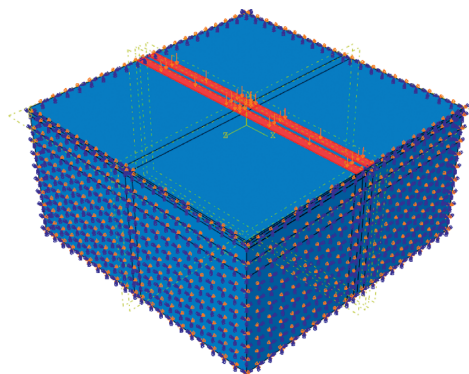


FIGURE 6: Schematic of traffic load action area.

3.2. Indoor Fatigue Test. In order to verify the accuracy and rationality of FEM, this paper has produced the semirigid base asphalt pavement structure model specimens under three working conditions: complete, voided, and polymer grouting repair. The servohydraulic fatigue test system is used for cyclic compression fatigue test operation, by collecting the number of load actions under fatigue failure of each working condition and the mechanical response change data under repeated loads and comparing and analyzing the fatigue damage evolution law of the three test conditions.

3.2.1. Production of Model Specimens. Considering the limitations of actual pavement structures and the indoor fatigue test conditions, this study uses semirigid base asphalt pavement structure model specimens to simplify the SMA-13 supper layer, AC-20 lower layer, cement-stabilized macadam base, and cement-stabilized macadam base. The four parts have thicknesses of 5 cm, 5 cm, 10 cm, and 10 cm, respectively.

(1) Fabrication of test piece of asphalt surface model

Asphalt surface course model specimens are formed of rut plates. The dimensions of the rut plates are 300 mm × 300 mm × 50 mm. Asphalt, SBS-modified asphalt, and 70# ordinary asphalt are used. The rut plate mold and the rut plate rolling machine are as shown in Figure 7.

The gradation of the SMA-13 asphalt concrete aggregate is summarized in Table 4.

The SMA-13 asphalt concrete production mix ratio is 0–0.6 mm mineral powder : 0–3 mm gravel : 3–5 mm gravel : 5–10 mm gravel (basalt) : 10–15 mm gravel (basalt) = 11% : 11% : 5% : 30% : 43%. The best oil-stone ratio is 6%; the amount of lignin fiber is 0.35% of the total mineral aggregate. The relative density of the asphalt mixture gross volume is 2.457 g/cm³, and the porosity is 4%.

The grading of the AC-20 asphalt concrete aggregate is summarized in Table 5.

The AC-20 asphalt concrete production mix ratio is 15–20 mm gravel : 10–15 mm gravel : 5–10 mm gravel : 3–5 mm gravel : stone powder = 6% : 29% : 20% : 14% : 31%. The best oil-stone ratio is 4.7%, the relative density of the asphalt mixture gross volume is 2.431 g/cm³, and the porosity is 4.5%.

After producing the rut plate test piece, the rut board is cut into a small test piece of 300 mm × 100 mm × 50 mm, as shown in Figure 8.

(2) Production of model specimens of cement-stabilized macadam base course

The middle beam mold is used to form the cement-stabilized crushed stone semirigid base course specimen, of size 100 mm × 100 mm × 400 mm, as shown in Figure 9.

The gradation of the cement-stabilized crushed stone is provided in Table 6.

The production mix ratio of the cement-stabilized crushed stone semirigid base is 20–30 mm crushed stone : 10–20 mm crushed stone : 5–10 mm crushed stone : 0–5 mm crushed stone = 27% : 23% : 17% : 33%. The cement content is 5%, the cement strength is 32.5, the best water content is 5.5%, and the maximum dry density is 2.33 g/cm³.

After the static pressure test piece is formed, it is cured under standard conditions for three months. The test piece is as shown in Figure 10.

(3) Composition of the pavement structure model

This study uses a 5 cm SMA-13, 5 cm AC-20, 10 cm cement-stabilized macadam, and 10 cm cement-stabilized macadam as the upper surface, under surface, base layer, and subbase layer, respectively, to simulate the semirigid base asphalt pavement structure. Between the upper and under surfaces, petroleum asphalt is used as the adhesive layer to bond the two layers into a whole. A void area is set at the bottom of the base layer, and the void size is set as 10 cm × 5 cm × 3 cm. It is shown in Figure 11.

3.2.2. Test Process. In this study, the repeated compression fatigue test method under a controlled load mode is used for testing. The test instrument is MTS-250 kN (servo hydraulic fatigue testing machine), the stress load is 1.2 MPa, the load frequency is 10 Hz, and the minimum load P_{\min} of the sine wave load is set to 10% of the maximum load P_{\max} . The test instrument is shown in Figure 12.

The basic process of the test is as follows:

- (1) The layout of the sensor is as follows. The strain sensor is set directly under the load; to the bottom of the base layer, two resistance strain gauges are attached. On the top of both the base layer and the fixture below the base layer, thin-film pressure sensors are fixed. The sensor layout diagram is shown in Figure 13, where the yellow box represents the empty area, a blue triangle symbol denotes the location of a resistance strain gauge, and the blue circle symbol represents the location of a pressure sensor.
- (2) Repeated fatigue compression operations are performed on the three structural model specimens of the complete pavement structure, voiding, and polymer grouting repair, respectively, as shown in Figure 14.
- (3) The number of load actions and the mechanical response data of the pavement structure are detected, extracted, and analyzed for the fatigue failure under each working condition, and the results are compared to the numerical simulation fatigue damage evolution.

4. Result Analysis

4.1. Analysis of Calculation Results

- (1) Comparative analysis of dynamic response of pavement structure models under three working conditions

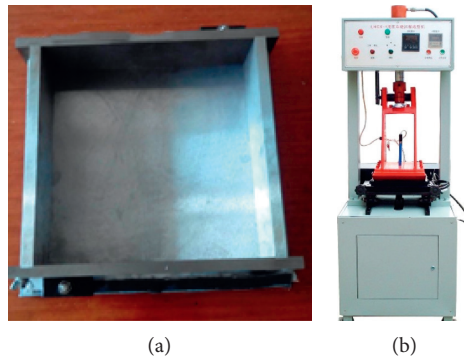


FIGURE 7: (a) Rutting plate mold and (b) rutting plate rolling machine.

TABLE 4: SMA-13 asphalt concrete gradation.

Mesh size (mm)	19	12.5	9.5	4.75	2.36	0.3	0.075
Passing rate	100	85-100	50-75	20-28	16-14	10-12	8-12

TABLE 5: AC-20 asphalt concrete gradation.

Mesh size (mm)	26.5	19	16	13.2	9.5	4.95	2.36	1.18	0.6	0.3	0.15	0.075
Passing rate	100	95.1	87.6	73.3	59.6	37.8	26.1	19.1	17.1	9.2	6.2	3.6



FIGURE 8: Specimen after cutting rut plate.

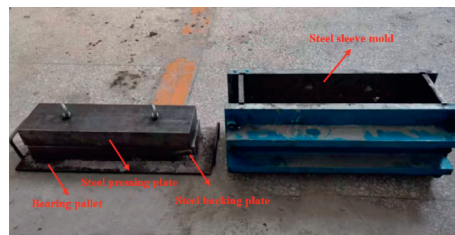


FIGURE 9: Cement-stabilized crushed stone beam mold.

TABLE 6: The gradation of cement-stabilized crushed stone.

Mesh size (mm)	31.5	26.5	19	16	13.2	9.5	4.95	2.36	1.18	0.6	0.3	0.15	0.075
Passing rate	100	95	73	67	63	50	33	20	13	9	5	4	2



FIGURE 10: Cement-stabilized crushed stone molding test piece.

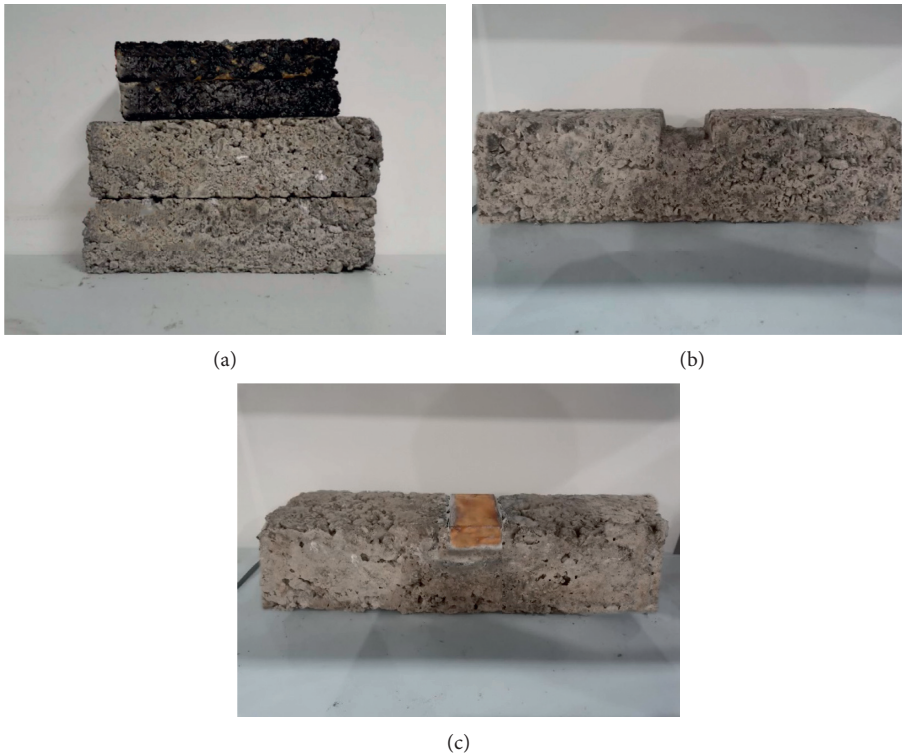


FIGURE 11: Different working conditions for structural layer model specimens. (a) Complete model test piece of pavement structure. (b) Model test piece of structural layer void. (c) Structural layer repair model test piece.



FIGURE 12: MTS-250 kN (servo hydraulic fatigue testing machine).

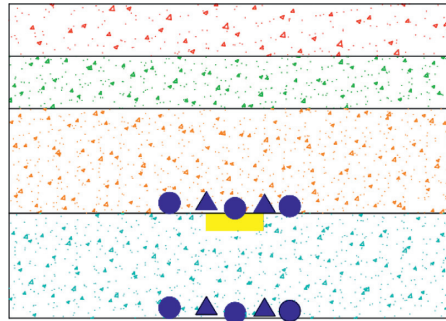


FIGURE 13: Schematic diagram of layout.

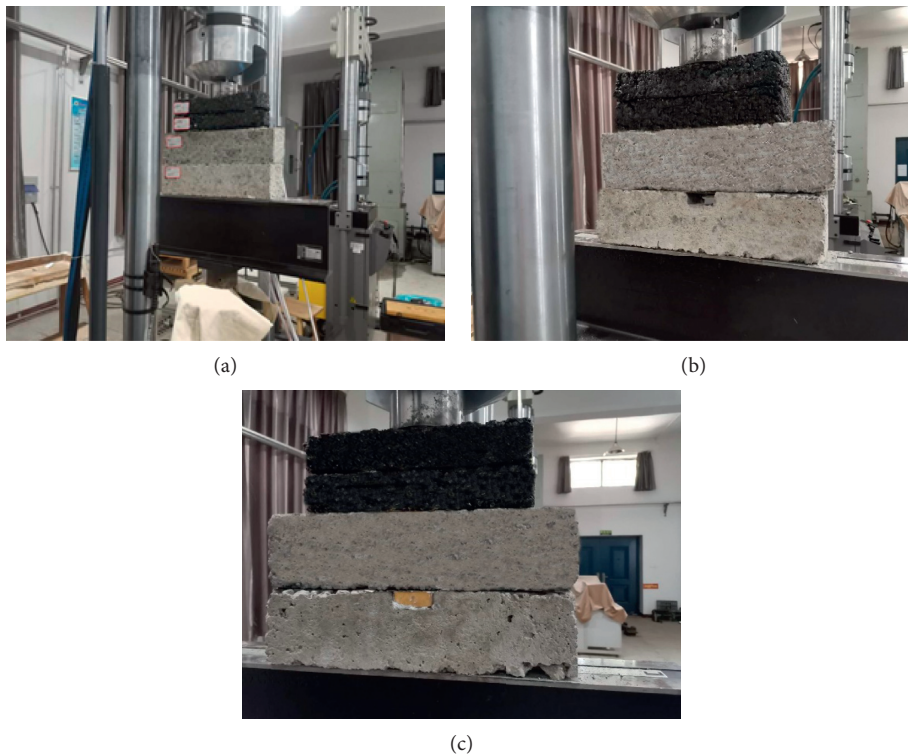


FIGURE 14: Repeated compression fatigue test diagram of structural model. (a) Compression fatigue test of complete structure model. (b) Compression fatigue test diagram of void structure model. (c) Compression fatigue test diagram of repaired structure model.

A standard load of 0.7 MPa was applied to the vacant area for a single movement, and three working conditions, complete base course, vacant, and polymer grouting repairs, were compared and analyzed. This study selects the three working conditions when the moving load moves to the top surface of the void to draw the Mises stress and vertical displacement comparison diagrams, as shown in Figures 15 and 16, respectively.

It can be seen from Figure 15 that the Mises stress in the void position of the pavement structure base layer is 217 kPa and that stress concentration occurs. After the polymer grouting repair, the Mises stress at the void position is reduced to 176 kPa.

Compared to the void condition, after the repair, the Mises stress is reduced by 69%, which proves that polymer grouting is effective in repairing the void in the base layer.

It can be seen from Figure 16 that the vertical displacement of the empty position of the pavement structure under the empty condition is 480 μm , which after the polymer grouting repair is 319 μm . Compared to the vacant condition, the vertical displacement after the repair is reduced by 61%, which proves that polymer grouting repair can significantly reduce the vertical displacement of the semirigid base asphalt pavement.

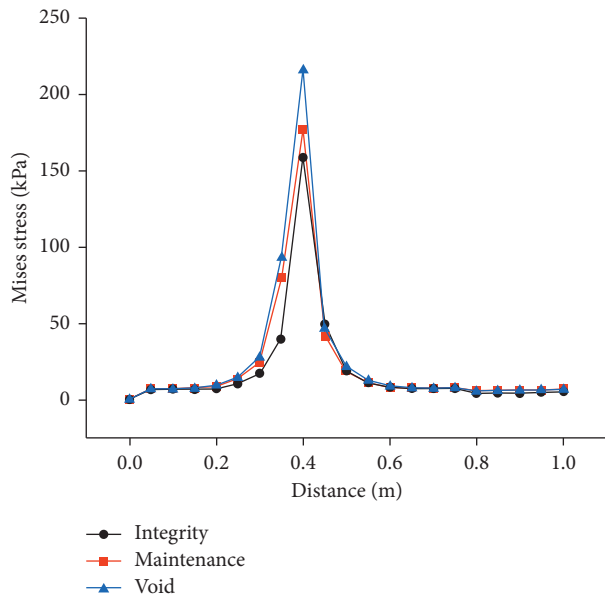


FIGURE 15: Mises stress comparison diagram of three working conditions.

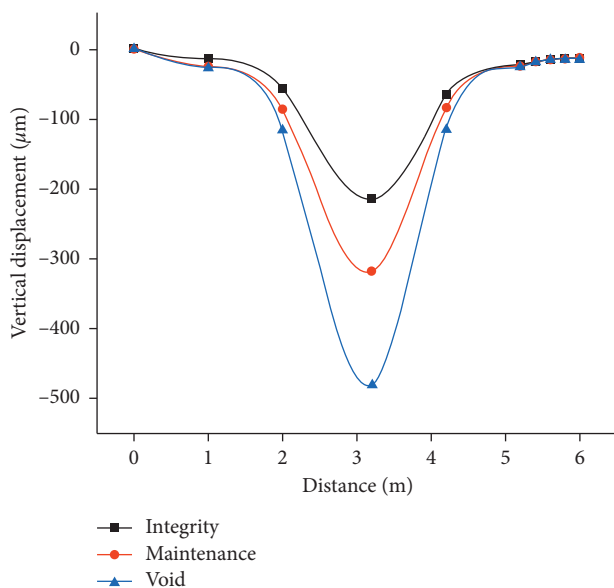


FIGURE 16: Comparison analysis diagram of vertical displacement under three working conditions.

(2) Comparative analysis of distribution law of fatigue damage field of pavement structure model under three conditions

This study selects a 1.2 MPa cyclic load to analyze the fatigue damage field distribution law of the semirigid base asphalt pavement structure. In view of the three working conditions of the pavement structure base course integrity, voiding, and polymer grouting repair, a pavement structure with repeated loads of 4.65 million times is selected as the research object (when the repeated load is 4.65 million times, the fatigue damage basically reaches

0.5). The element integration point where the fatigue damage variable D first accumulates to 0.5 is selected as the origin to establish a three-dimensional coordinate system. The vehicle travel direction is the X direction, the road plane perpendicular to the vehicle travel direction is the Y direction, and the vertical direction is the Z direction. The distribution diagrams of the fatigue damage field on the x -, y -, and z -axes of the three working conditions of the road structure model are shown in Figures 17–19, respectively.

From Figure 17, in the X direction, when the road bears 4.65 million repeated loads, the fatigue damage D at the bottom of the base layer directly above the void area is the highest. At the bottom of the base layer 0.5 m away from the void area, the three types of works of the fatigue damage of the condition model are not much different, indicating that the void disease has a limited impact on the overall road. After the polymer grouting repair, the fatigue damage D in the X direction is significantly reduced, indicating that the polymer grouting has voided the bottom of the semirigid base asphalt pavement base. The long-term repair effect is remarkable.

It can be seen from Figure 18 that, in the Y direction, when the road is subjected to 4.65 million repetitive loads, the fatigue damage D presents a single-peak curve, and D is the highest at the bottom of the base layer directly above the void area. At the center line of the wheel track, the road damage is the most significant, where the load is approximately 0.75 m on both sides of the load. The impact of the load on the road fatigue damage is reduced; after the polymer grouting repair, the fatigue damage D in the Y direction is significantly reduced, indicating that the polymer grouting affects the base. The long-term repair effect of voiding is remarkable.

It can be seen from Figure 19 that, in the Z direction, when the road bears 4.65 million repeated loads, the fatigue damage D reaches the maximum at the bottom of the base layer and gradually decreases upwards. The fatigue damage D at the bottom of the base layer is relatively significant, and the upward fatigue damage D decreases, being basically reduced to 0. The impact range of the cyclic load on the road is from the road surface to 0.8 m below the surface, with a greater impact being on the bottom base layer and above the structural layers of the pavement structure. The Z direction fatigue damage D is noticeable after the polymer grouting repair decreases, indicating that polymer grouting has a significant effect on the long-term repair of the voids at the bottom of the semirigid base asphalt pavement base.

(3) Comparative analysis of cumulative evolution law of fatigue damage of pavement structure models under three conditions

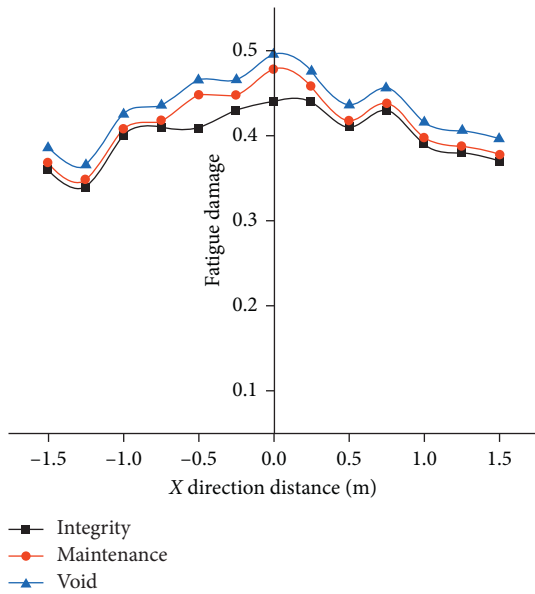


FIGURE 17: Fatigue damage distribution in X direction at bottom of base under three conditions.

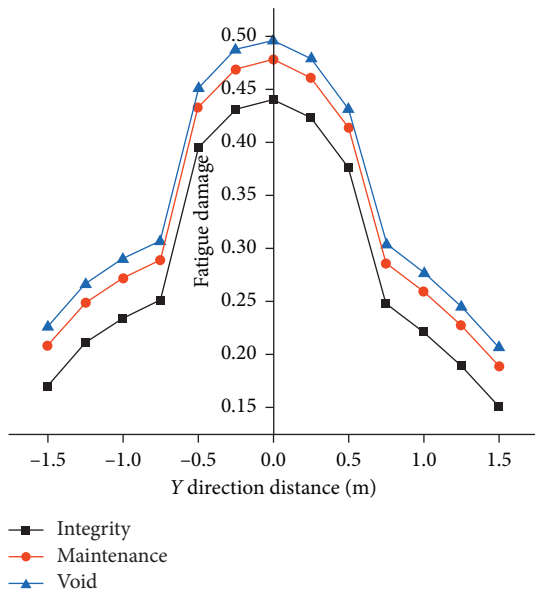


FIGURE 18: Fatigue damage distribution in Y direction at bottom of base under three conditions.

Under the action of the traffic cyclic load, a semirigid base asphalt pavement structure will experience accumulation of fatigue damage. As the number of loads continues to increase, the fatigue damage will develop until macro cracks appear. In this study, a 1.2 MPa cyclic load is used to analyze the cumulative evolution of the fatigue damage under three working conditions: bottom of the pavement structure base is completed, voided, and polymer grouting repaired. The fatigue damage degree under the three working conditions varies with the number of loads, as shown in Figure 20.

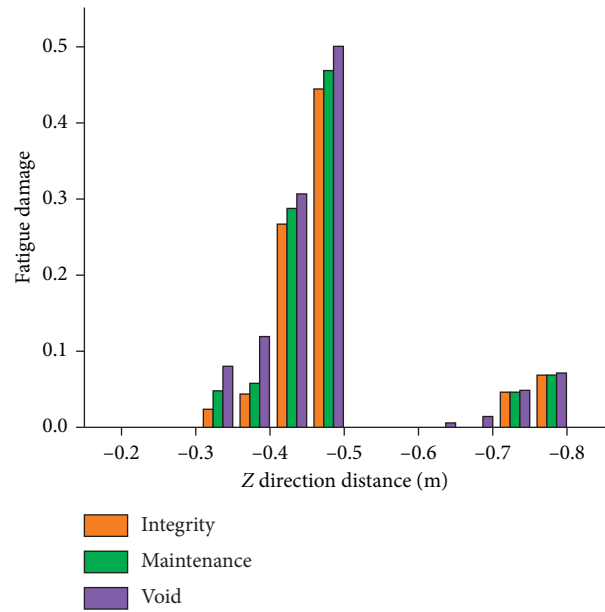


FIGURE 19: Fatigue damage distribution in Z direction corresponding to three working conditions.

It can be seen from Figure 20 that, under the action of a 1.2 MPa cyclic load, when the number of load actions is 5,00,000, the fatigue damage degree of the hollow pavement structure model reaches 0.2813. When the number of load actions is increased from 5,00,000 to 2 million, the fatigue damage D is increased to 0.423; when it is increased from 2 million to 5 million, the fatigue damage variable D reaches 0.5223. With the increase in the number of loads, the development rate of the fatigue damage in the void position of the pavement structure decreases. After the polymer grouting repair, when the number of loads is 5,00,000, the growth rate of the fatigue damage D decreases, and the cumulative development of fatigue damage is relatively slow. When the number of load actions reaches 5 million, the cumulative fatigue damage of the pavement structure is 0.3691, which is reduced by 29% compared to that of the hollow structure, which significantly reduces the degree of fatigue damage. This proves that the polymer grouting has a good repair effect of the semirigid base layer hollow disease effect.

To analyze the impact of different loads on the fatigue damage of the semirigid base asphalt pavement structure, this study uses 1.0 MPa and 1.4 MPa tire ground pressures to act under the three working conditions, as shown in Figures 21 and 22, respectively.

It can be seen from Figures 20–22 that the greater the tire ground pressure, the fewer the number of load actions required for the fatigue damage factor of the pavement structure to reach 0.5. When the tire ground pressure is 1.4 MPa, the cyclic load acts 1,00,000 times. Subsequently, the fatigue damage of the intact pavement structure exceeds that of the

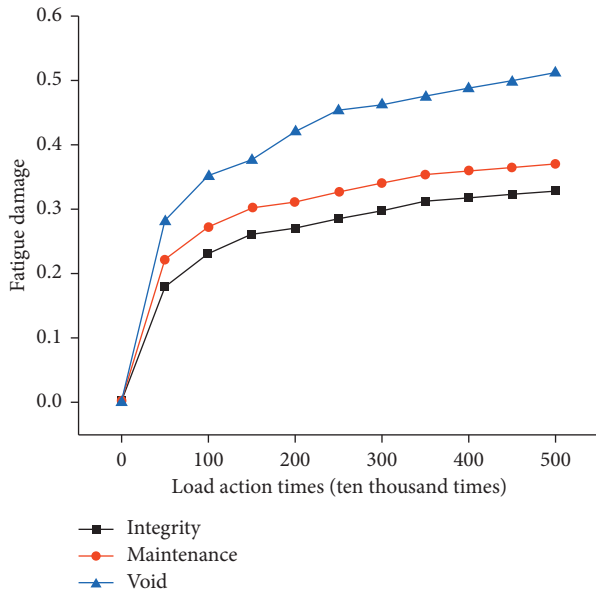


FIGURE 20: Cumulative evolution of fatigue damage under three working conditions under 1.2 MPa tire pressure.

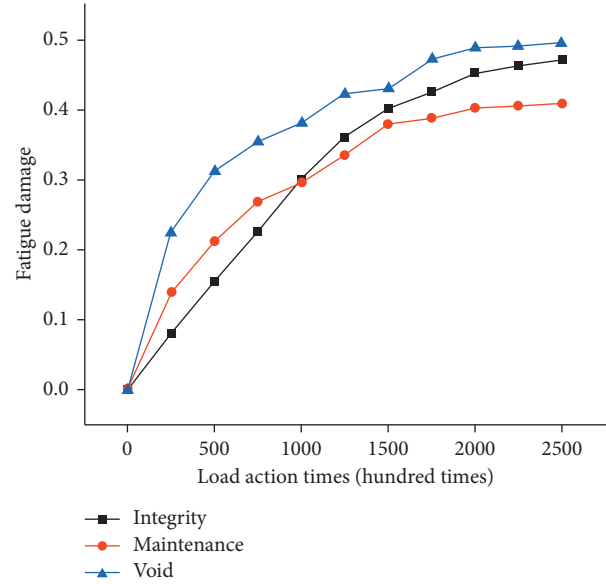


FIGURE 22: Cumulative evolution of fatigue damage under three working conditions under 1.4 MPa tire pressure.

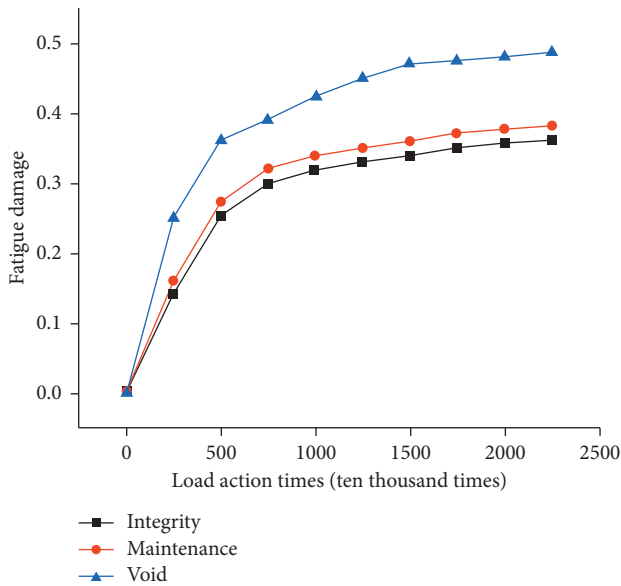


FIGURE 21: Cumulative evolution of fatigue damage under three working conditions under 1.0 MPa tire pressure.

polymer grouting to repair the pavement structure. This is mainly because the polymer material fatigue damage model is reoriented after the repeated compression of the polyurethane molecular chain under a low-stress ratio, resulting in crystallization and cyclic hardening.

4.2. Analysis of Test Results. The number of load actions required for the three pavement structure model working conditions to reach failure is shown in Figure 23.

It can be seen from Figure 23 that the number of load actions required for the complete, repair, and void structure models to reach failure is 269416, 244318, and 117215, respectively. The formula for calculating the repair effect N is $(N_r - N_v)/(N_c - N_v)$, and the long-term use performance repair effect of the pavement structure model can reach 83.51%.

Based on the strain value extracted from the test and the corresponding load action times, the tensile stress values of the same load acting under the three working conditions corresponding to the same position are not much different. Moreover, the relationship between the fatigue damage variable D and the load action times can be obtained. The bottom is the research object, and the cumulative evolution law of the fatigue damage under the three working conditions is compared and analyzed. The specific analysis is as follows.

It can be seen from Figure 24 that when the number of load actions is less than 100, the fatigue damage value does not change much. When the number of load actions is greater than 100, the more the number of load actions, the greater the fatigue damage value of the pavement structure, showing a two-stage change. The fatigue damage value of the pavement structure base layer has the fastest increase in the empty condition, and the number of load actions is the least at the end of the second stage. The growth rate of the fatigue damage value of the polymer-repaired pavement structure is significantly reduced compared to that of the empty pavement structure. At the end of the second stage, the number of load actions is basically the same as that of the complete pavement structure. Similar to the numerical simulation results, at the same location, under the comparison of the three working conditions, it is reflected in the fatigue damage accumulation level. Compared with the polymer grouting condition, the void damage accumulation is slower. The cumulative evolution trend of the fatigue damage in the

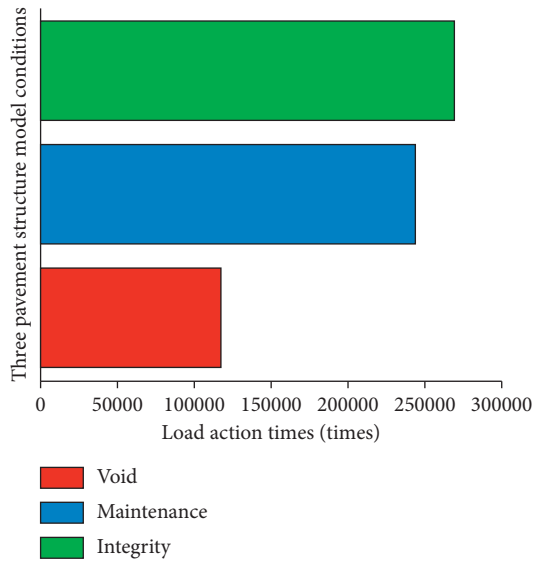


FIGURE 23: Compression fatigue failure load action times of three pavement structure models.

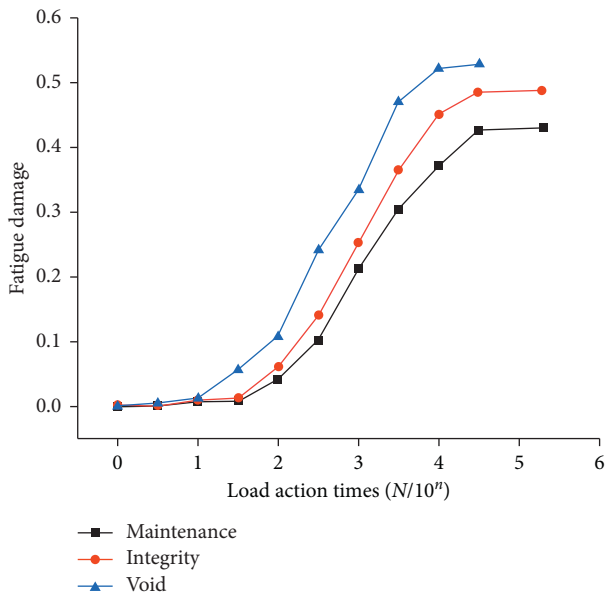


FIGURE 24: Cumulative evolution of fatigue damage under three basic working conditions.

three working conditions is basically consistent with the numerical simulation results, which verifies the rationality of the numerical model.

5. Conclusion

This study uses the finite element method to establish a three-dimensional numerical model of a semirigid base asphalt pavement structure and compares and analyzes the mechanical response and fatigue damage evolution law of the pavement before and after vacant polymer repair. The

model is verified by indoor fatigue tests. The following conclusions are drawn:

- (1) The simplified Chaboche nonlinear fatigue damage model is revised, and a two-stage fatigue damage model suitable for semirigid base materials is established. The cyclic compression fatigue test data of polymer grouting materials are subjected to regression analysis and shown to be suitable for high $D - N$ damage evolution model of polymer materials.
- (2) Under the action of a 0.7 MPa standard load, the vertical displacement and Mises stress value of the vacant position of the vacant polymer-repaired pavement structure base layer are reduced by 61% and 69%, respectively. This indicates that polymer grouting technology repairs the semirigid base layer, and the effect of voiding disease on the asphalt pavement base is good.
- (3) Under a 1.2 MPa cyclic load, the fatigue damage factor increases with the increase in the number of repeated loads, but the development rate of fatigue damage of pavement structure is decreasing. When the repeated loads increase from 5,00,000 times to 5 million times, the fatigue damage factor of the pavement structure is 0.5223 when the base layer of the pavement structure is empty. The fatigue damage factor of the pavement structure after the polymer repair is 0.3691, which is 29% lower than that of the empty structure. Prove that the polymer grouting repair method can effectively reduce the degree of fatigue damage.
- (4) Under different the tire contact pressure, the fatigue damage of the pavement structure after the polymer repair is lower than that of the empty pavement structure. And the greater the tire contact pressure, the fewer the number of load actions required for the fatigue damage factor of the pavement structure to reach 0.5 and the shorter the time for the fatigue failure of the pavement structure. Under the action of 1.4 MPa cyclic load, the accumulation of fatigue damage of polymer-repaired pavement structure is smaller than that of complete pavement structure.
- (5) With the increase of the number of fatigue test loads, the development rate of the fatigue damage degree of the three working conditions at the bottom of the base layer basically shows a downward trend. Moreover, at the same location, the accumulation of fatigue damage under polymer grouting conditions is slower than that under void conditions. It can be seen that the cumulative evolution trend of fatigue damage is basically consistent with the numerical simulation results, which verifies the rationality of the numerical model.

Data Availability

The data used to support the findings of this study are included within the article.

Conflicts of Interest

The authors declare that they have no conflicts of interest.

Acknowledgments

The authors acknowledge the support received from the National Key Research and Development Plan (Grant no. 2018YFB1600200), the National Natural Science Foundation of China (Grant nos. 51878624 and 51878622), Major Scientific and Technological Special Project in Henan (Grant no. 181100310400), Henan Science Fund for Distinguished Young Scholars (Grant no. 202300410354), Natural Science Foundation of Henan Province (Grant no. 202300410746), the Program for Science and Technology Innovation Talents in Universities of Henan Province (Grant no. 19HAS-TIT041), and Key Research Projects of Higher Education in Henan Province (Grant no. 18A580001).

References

- [1] X. Wang, X. Ma, and D. Baraldi, "Responses of semi-rigid base asphalt pavement with interlayer contact bonding model," *Advances in Civil Engineering*, vol. 2020, Article ID 8841139, 13 pages, 2020.
- [2] X. Yan, L. Chen, Q. You, and Q. Fu, "Experimental analysis of thermal conductivity of semi-rigid base asphalt pavement," *Road Materials and Pavement Design*, vol. 20, no. 5, pp. 1215–1227, 2019.
- [3] S. R. Maitra, K. S. Reddy, and L. S. Ramachandra, "Numerical investigation of fatigue characteristics of concrete pavement," *International Journal of Fracture*, vol. 189, no. 2, pp. 181–193, 2014.
- [4] J. Hu, P. Liu, D. Wang, M. Oeser, and Y. Tan, "Investigation on fatigue damage of asphalt mixture with different air-voids using microstructural analysis," *Construction and Building Materials*, vol. 125, pp. 936–945, 2016.
- [5] H. Cheng, L. Sun, L. Liu, and H. Li, "Fatigue characteristics of in-service cold recycling mixture with asphalt emulsion and HMA mixture," *Construction and Building Materials*, vol. 192, pp. 704–714, 2018.
- [6] M. Barman, R. Ghabchi, D. Singh, M. Zaman, and S. Commuri, "An alternative analysis of indirect tensile test results for evaluating fatigue characteristics of asphalt mixes," *Construction and Building Materials*, vol. 166, pp. 204–213, 2018.
- [7] S. Lv, C. Xia, L. You, X. Wang, J. Li, and J. Zheng, "Unified fatigue characteristics model for cement-stabilized macadam under various loading modes," *Construction and Building Materials*, vol. 223, pp. 775–783, 2019.
- [8] J. Zhang, Y. D. Wang, and Y. Su, "Fatigue damage evolution model of asphalt mixture considering influence of loading frequency," *Construction and Building Materials*, vol. 218, pp. 712–720, 2019.
- [9] J. Wei, T. Fu, Y. Meng et al., "Investigating the fatigue characteristics of large stone asphalt mixtures based on the disturbed state concept," *Advances in Materials Science and Engineering*, vol. 2020, Article ID 3873174, 10 pages, 2020.
- [10] Q. Chen, G. Wang, and W. Pan, "Research on relationships among different disease types of cement concrete pavement based on structural formula model," *Mathematical Problems in Engineering*, vol. 2020, Article ID 9580616, 13 pages, 2020.
- [11] C. Guo and F. Wang, "Mechanism study on the constructing of ultra-thin antiseepage wall by polymer injection," *Journal of Materials in Civil Engineering*, vol. 24, no. 9, pp. 1183–1192, 2012.
- [12] M. Shi, F. Wang, and J. Luo, "Compressive strength of polymer grouting material at different temperatures," *Journal of Wuhan University of Technology*, vol. 25, no. 6, pp. 962–965, 2010.
- [13] K. Liu, W. Liang, F. Ren, J. Ren, F. Wang, and H. Ding, "The study on compressive mechanical properties of rigid polyurethane grout materials with different densities," *Construction and Building Materials*, vol. 206, pp. 270–278, 2019.
- [14] A. Bezazi and F. Scarpa, "Tensile fatigue of conventional and negative Poisson's ratio open cell PU foams," *International Journal of Fatigue*, vol. 31, no. 3, pp. 488–494, 2008.
- [15] D. Pulungan, A. Yudhanto, S. Goutham, G. Lubineau, R. Yaldiz, and W. Schijve, "Characterizing and modeling the pressure- and rate-dependent elastic-plastic-damage behavior of polypropylene-based polymers," *Polymer Testing*, vol. 68, pp. 433–445, 2018.
- [16] M. Nazari, R. Ghabchi, and M. Zaman, "Flexural properties of chemically stabilised subgrade in designing semi-rigid pavements," *Road Materials and Pavement Design*, vol. 20, no. 4, pp. 836–858, 2019.
- [17] H. Liu and R. Luo, "Development of failure criterion and fatigue model to characterize the fatigue resistance of asphalt binders under controlled-stress time sweep tests," *Materials and Structures*, vol. 53, no. 4, pp. 141–149, 2019.
- [18] H. Wen, "Use of fracture work density obtained from indirect tensile testing for the mix design and development of a fatigue model," *International Journal of Pavement Engineering*, vol. 14, no. 6, pp. 561–568, 2013.
- [19] J. Füssl and R. Lackner, "Multiscale fatigue model for bituminous mixtures," *International Journal of Fatigue*, vol. 33, no. 11, pp. 1435–1450, 2011.
- [20] I. Farreras-Alcover, M. K. Chryssanthopoulos, and J. E. Andersen, "Data-based models for fatigue reliability of orthotropic steel bridge decks based on temperature, traffic and strain monitoring," *International Journal of Fatigue*, vol. 95, pp. 104–119, 2017.
- [21] X. Gao, Ya Wei, F. Wang et al., "Fatigue performance and microstructure evolution of polyurethane grouting material under cyclic compression loading," *Journal of Composite Materials*, vol. 34, no. 3, pp. 550–556, 2017.
- [22] G. Bosurgi and W. Perlongo, "Numerical analysis of fatigue cracks growth in flexible pavements with the elastoplastic fracture mechanics method," *Structure and Infrastructure Engineering*, vol. 10, no. 8, pp. 1027–1037, 2014.
- [23] F. Homsí, D. Bodin, S. Yotte, D. Breysse, and J. M. Balay, "Fatigue life modelling of asphalt pavements under multiple-axle loadings," *Road Materials and Pavement Design*, vol. 13, no. 4, pp. 749–768, 2012.
- [24] F. Moreno-Navarro, M. Sol-Sánchez, and M. C. Rubio-Gámez, "Exploring the recovery of fatigue damage in bituminous mixtures: the role of healing," *Road Materials and Pavement Design*, vol. 16, no. 1, pp. 75–89, 2015.
- [25] J. Hu, P. Liu, and B. Steinauer, "A study on fatigue damage of asphalt mixture under different compaction using 3D-microstructural characteristics," *Frontiers of Structural and Civil Engineering*, vol. 11, no. 3, pp. 329–337, 2017.

Research Article

Temperature Correction for FWD Deflection in Cement Pavement Void Detection

Bei Zhang , Xiaoliang Wang, Yanhui Zhong , Xiaolong Li , Meimei Hao ,
Yuanhao Ding, Jianyang Liu, and Xu Zhang

College of Water Conservancy and Engineering, Zhengzhou University, Zhengzhou 450001, China

Correspondence should be addressed to Yanhui Zhong; zhong_yanhui@163.com and Xiaolong Li; wenuandeshang@hotmail.com

Received 9 December 2020; Revised 20 January 2021; Accepted 27 January 2021; Published 10 February 2021

Academic Editor: Jiaolong Ren

Copyright © 2021 Bei Zhang et al. This is an open access article distributed under the Creative Commons Attribution License, which permits unrestricted use, distribution, and reproduction in any medium, provided the original work is properly cited.

The use of the falling weight deflectometer (FWD) for detecting pavement voids is based on the principle that, under the same impact load, the deflection of pavements with voids increases significantly. Under the effect of temperature, the cement pavement becomes warped, which affects the deflection detection accuracy. In order to improve the accuracy of FWD detection of cement pavement voids, a three-dimensional numerical model of cement pavement on a multilayered elastic foundation under the coupled action of temperature and load is established in this paper. In addition, under different pavement void, climatic, and load conditions, the influence of temperature difference between top and bottom of the plate on the deflection of the center point of plate angle load is studied. Considering the temperature difference between top and bottom, the temperature correction coefficient is established and experimentally verified the accuracy of the temperature correction coefficient. The results showed that, within the ranges of positive and negative temperature differences, the fitting degree of the temperature correction coefficient for the cement pavement exceeded 0.99, which was consistent with the variation trend of the temperature correction coefficient obtained through field tests. The error was lower than 7%, which verified the applicability of the temperature correction coefficient for the dynamic deflection of cement pavements based on FWD. The accuracy of the FWD method in detecting cement pavement voids was improved, and this study demonstrated theoretical reference value and practical engineering significance.

1. Introduction

Cement concrete pavement structures have advantages of extended service life, strong load diffusion capacity, easy constructability, accessibility of constituent materials, and low cost, and they are widely used for all types of highways [1]. However, during the service life of cement pavement, the pavement is prone to experience cracks, disconnections, voids, and other problems, owing to the combined action of the driving load and external environment. These problems have a significant impact on driving comfort and human safety [2]; the most significant impact on traffic is attributed to the voids in the cement concrete pavement [3, 4]. After concrete pavement voids are formed, the accurate and rapid detection of void damage in the concrete pavement is the focus of several studies.

Scholars have investigated the detection of voids in cement pavements, among which the most widely used technique is the void determination method based on the deflection. The void determination method is mainly divided into two types: falling weight deflectometer detection and Benkelman beam test [5, 6]. The FWD detection is used more widely because of its established technique and easy implementation. FWD detection is based on the principle that, under the same impact load, the deflection of the void area increases significantly [7–12]. Because of the influence of climatic factors, such as solar radiation and ambient temperature, cement pavement panels experience temperature warping at different degrees [13–15], which affect the accuracy of actual pavement detection results. Wen et al. systematically analyzed the impact of pavement voids under the coupled action of environment and load, described the

formation process of voids, and highlighted the significant causes of cement concrete bottom voids [16]. Zeng et al. used ANSYS and the FWD method to measure the deflection data of the panel center and panel angle of cement pavement and developed a method of estimating the scope of the panel angle void of cement pavements [17]. Chen et al. established a three-dimensional model of cement concrete pavement voids, verified the accuracy of the model by comparing its results with theoretical solutions and measured values, and proposed an analytical method for identifying cement concrete pavement voids [18]. Toth et al. evaluated the four-year meteorological data and deflection measurements of a section in Hungary, analyzed the variation of deflection parameters at different periods, and formulated correction factors based on the assessment results [19]. Through field observations, theoretical analysis, and relevant calculations, Jing et al. developed a method to determine the pavement temperature gradient using local meteorological data of several years [20]. Duan et al. performed simulation calculations on cement concrete pavement, analyzed the variation trend of the temperature stress of the plate angle under the conditions of complete contact with the pavement and plate angle void, and determined the main factors that influenced the temperature stress of the plate angle [21]. Based on a systematic analysis of the warping deformation of the sidewalk panel under a positive temperature gradient, Zhao et al. determined the modifiable temperature gradient of the internal deflection of a sidewalk panel. They established the correction method and the corresponding regression expression of the FWD test panel internal deflection [22]. Sheng et al. proposed improvement measures for the deflection test on old cement concrete pavements, evaluated the deflection of the solid engineering plate angle, plate center, and joint edge, and determined the reasonable temperature of the deflection test [23]. Dou et al. adopted the stress intensity factor as the evaluation criterion to perform three-dimensional finite element simulation of early pavement fracture expansion based on the theory of linear-elastic fracture mechanics. They analyzed the effects of fracture depth, overload, and temperature on fracture expansion [24]. Currently, studies on cement pavement temperature fields and FWD on pavement void detection have been conducted, but research on FWD pavement void detection under the coupled action of temperature and load have not been conducted in detail.

Therefore, through the establishment of a three-dimensional numerical model for cement pavements under temperature and load coupling and the pavement plate deflection under the temperature and load coupling under different climatic and void conditions, the temperature difference between the top and bottom was analyzed. The correlation of deflection temperature correction coefficient was established, and the temperature correction coefficient was developed by considering the temperature difference between the top and bottom. Furthermore, the accuracy of the temperature correction coefficient was verified experimentally. The research results are useful for improving the accuracy of the FWD method for detecting cement pavement voids in different climates.

2. Three-Dimensional Numerical Model of Cement Pavement under Coupling of Temperature and Load

2.1. Basic Assumptions. In this study, a three-dimensional numerical model of cement concrete pavement was established for the analysis of the influence of the temperature field on the deformation of a cement concrete pavement slab. The following basic assumptions were made:

- (1) The material layers are homogeneous and isotropic linear elastomers, characterized by the elastic modulus and Poisson's ratio
- (2) Except for the panel, each layer in the horizontal direction is an infinite elastomer, while the lowest layer is a homogeneous semi-infinite body
- (3) The displacements and stresses in all directions of the contact surfaces between layers are entirely continuous, and the transfer of the force and displacement only occurs when the contact surfaces are in the void region

2.2. Establishment of Void Model. In this study, two types of pavement bottom void were used: the plate angle void and the plate edge void. The plate angle void area was set as a cylindrical sheet with the corner vertex as the center of the circle, whereas the plate edge void was set as a cuboid sheet with a length, width, and height and the panel width adopted as the long side. The voids were combined into 16 (4×4) plate angle void conditions and 16 (4×4) plate edge void conditions. Table 1 lists the size setting of the void condition, and Figure 1 shows the plate angle and plate edge of the void model.

2.3. Material Parameters. The model size and material parameter setting of each structure layer were determined (Table 2) to simulate the actual cement concrete pavement structure better.

2.4. Load and Boundary Conditions

2.4.1. Temperature and Load Applications. The temperature stress was applied to input the corresponding value directly into the plate top and bottom of the cement concrete pavement during the initial step of the load setting. Based on the data for the measured temperature and temperature difference between the top and bottom of the plate in each season listed in Table 3, 25°C and -25°C were selected as the upper and lower limits of the temperature difference between the top and bottom, and the temperature gradient was set as 5°C .

The temperatures of the cement concrete pavement slab for a monitoring period of one year in four seasons were analyzed. There was a significant linear relationship between the top temperature of the plate and the bottom temperature difference of the plate [25, 26]. The correlation equations between the top temperature of the plate and the bottom temperature difference of the plate for the cement concrete pavement in each season are listed in Table 4.

TABLE 1: Size setting of void conditions.

Plate angle void		Plate edge void	
Radius (m)	Height (cm)	Width (m)	Height (cm)
0.25	0.50	0.25	0.50
0.50	1.00	0.50	1.00
0.75	1.50	0.75	1.50
1.00	2.00	1.00	2.00

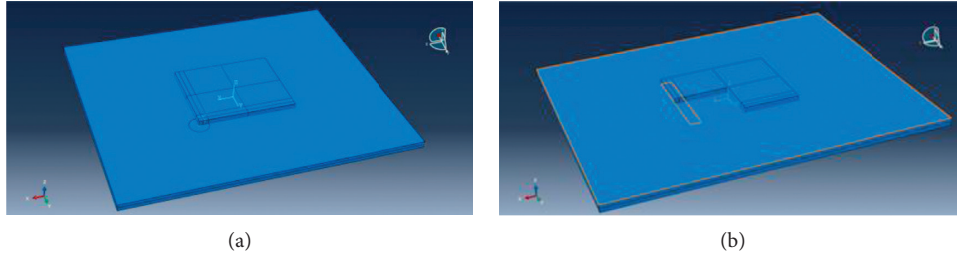


FIGURE 1: Schematic of plate angle and edge voids of the cement pavement. (a) Plate angle void of cement pavement. (b) Plate edge void of cement pavement.

TABLE 2: Material parameters of each structure layer of cement concrete pavement.

Structure layer	Plane dimension (m ²)	Thickness (cm)	Modulus of elasticity (MPa)	Poisson's ratio	Thermal conductivity ($\omega \cdot m^{-1} \cdot ^\circ C^{-1}$)
Surface	5 × 4	24	30000	0.15	1.34
Base	15 × 12	16	500	0.3	—
Subbase	15 × 12	18	400	0.3	—

TABLE 3: Measured temperature and temperature difference between top and bottom of the plate in each season.

Season	Maximum temperature (°C)		Minimum temperature (°C)		Average temperature (°C)		Temperature range (°C)	Mean temperature difference (°C)
	Top	Bottom	Top	Bottom	Top	Bottom		
Spring	51.60	37.30	1.00	5.20	22.46	21.34	-6.80 to 16.00	4.46
Summer	57.20	49.70	18.90	23.80	33.36	32.44	-9.90 to 19.50	0.81
Autumn	44.10	35.30	2.76	8.30	18.79	18.13	-2.00 to 10.00	1.87
Winter	18.80	5.00	-5.50	1.20	2.70	3.38	-7.10 to 15.00	-0.68

TABLE 4: Correlation equations expressing the relationship between the top temperature of cement concrete pavement plate and bottom temperature difference of plate.

Season	Plate top temperature T_{top} -plate bottom temperature difference ∇T relationship
Spring	$\nabla T = 0.5039 \cdot T_{top} - 6.8963$ $R^2 = 0.8828$
Summer	$\nabla T = 0.8761 \cdot T_{top} - 28.4320$ $R^2 = 0.9161$
Autumn	$\nabla T = 0.3261 \cdot T_{top} - 4.2576$ $R^2 = 0.9244$
Winter	$\nabla T = 0.9609 \cdot T_{top} - 3.0845$ $R^2 = 0.9584$

The load was simplified to that on a square area with a side length of 26.6 cm at the top of the panel and 25 cm from the corner edge of the panel under static loads. The third-grade loads were 50, 70, and 90 kN.

2.4.2. *Boundary Conditions.* In the initial analysis step, the panel boundary conditions were set as follows:

$$\begin{aligned} \text{Slab - X: } U_2 = U_{R_2} = U_{R_3} = 0, \\ \text{Slab - Y: } U_1 = U_{R_1} = U_{R_3} = 0, \end{aligned} \quad (1)$$

where U_1 and U_2 are the translational displacements in the directions of Models 1 and 2, respectively, and U_{R_1} , U_{R_2} , and U_{R_3} are the rotation angles centered on axes 1, 2, and 3, respectively.

In this model, the soil base was not set. Instead, an elastic modulus of 50 MPa was directly set at the bottom of the subbase as the boundary condition.

2.5. *Model Meshing.* Nonuniform grid technology is applied in this model, considering that this paper is mainly to study the variation law of deflection at the center point of plate angle load under the coupled action of temperature and load. Therefore, the mesh division of cement concrete pavement slab is more intensive than that of the base layer. Considering the particularity of the loading area, the cement concrete pavement slab was split several times, and the three-dimensional finite element overall model of the cement concrete pavement and the partition effect of the pavement slab mesh were obtained as shown in Figure 2.

3. Temperature Correction for Dynamic Deflection of Cement Pavement

3.1. *Pavement Plate Angle Deflection under Coupled Effect of Temperature and Load under Different Climatic Conditions.* In Table 3, data for each season cement pavement, the measured top plate temperature, bottom plate temperature, and temperature difference indicated that the average temperature of the season's plate for the top and bottom temperature difference was significant. However, the difference between the average temperature of the plate bottom for each season was not significant. Hence, the coupled effects of the pavement void deflection in four seasons at the same temperature difference and load were analyzed.

The deformation of the plate angle load center point in the finite element model of cement concrete pavement under the temperature stress and the coupled temperature-load effect was determined. Equation (2) was then introduced to calculate the corresponding deflection of the plate angle load center point at various temperature differences:

$$D_1 = L_1 - L_2. \quad (2)$$

In equation (2), D_1 is the deflection value of the center point of the plate corner load, considering the effect of the temperature stress field (μm). L_1 is the deformation of the

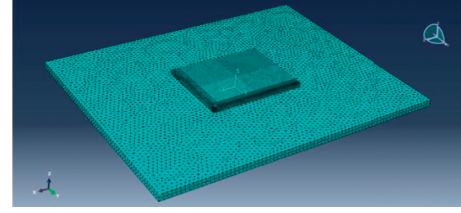


FIGURE 2: Overall meshing effect of three-dimensional finite element model for cement pavement.

center point of the plate corner load, considering the combined action of the temperature and load stress field (μm). L_2 is the deflection value of the center point of the plate corner load, considering only the temperature stress (μm).

Equation (2) was used to compute the load center point for each season and the values of the corresponding deflection at the temperature difference (Figure 3). The following observations were made.

- (1) The deflection under the coupled action of the temperature stress and the tertiary load at the negative and positive temperature differences at the center point of the plate angle load in each season was significant.
- (2) At the same temperature difference, there was no significant difference in deflection between the four seasons, and the deflection fluctuated slightly above and below the mean value in each season.
- (3) At the same temperature difference, the deflection of the plate angle load center point increased with the load.
- (4) Under the coupled action of temperature and load, the average error of the deflection value of the plate angle load center point in each season relative to the deflection value of the annual plate angle load center point is less than 3%. Therefore, under the action of temperature and load coupling, the average deflection of the center point of angle load in four seasons is taken as the deflection of the center point of angle load in the whole year.

The variation trend of deflection at the center point of the plate angle load under the coupled action of temperature and three-stage loading was analyzed (Figure 4). The following was found:

- (1) At the same temperature difference and under the same load, the effect of the void depth on the deflection could be ignored. The void depth increased with the void radius, and the deflection variation range between different void radii was broad.
- (2) At the same temperature difference, the deflection under each void condition decreased with increasing temperature difference when the temperature difference was negative but increased with increasing temperature difference when the temperature difference was positive.

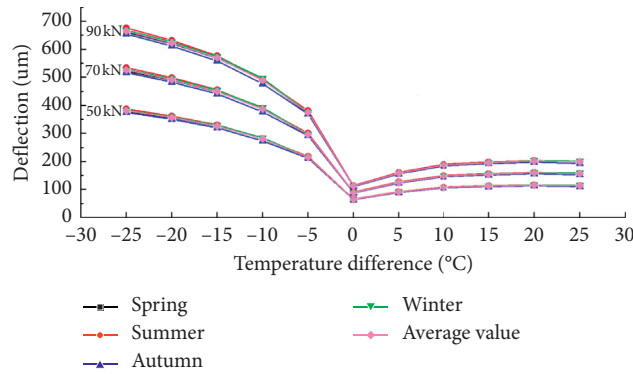


FIGURE 3: Deflection of plate angle load center point under coupled action of temperature and three-stage load for each season.

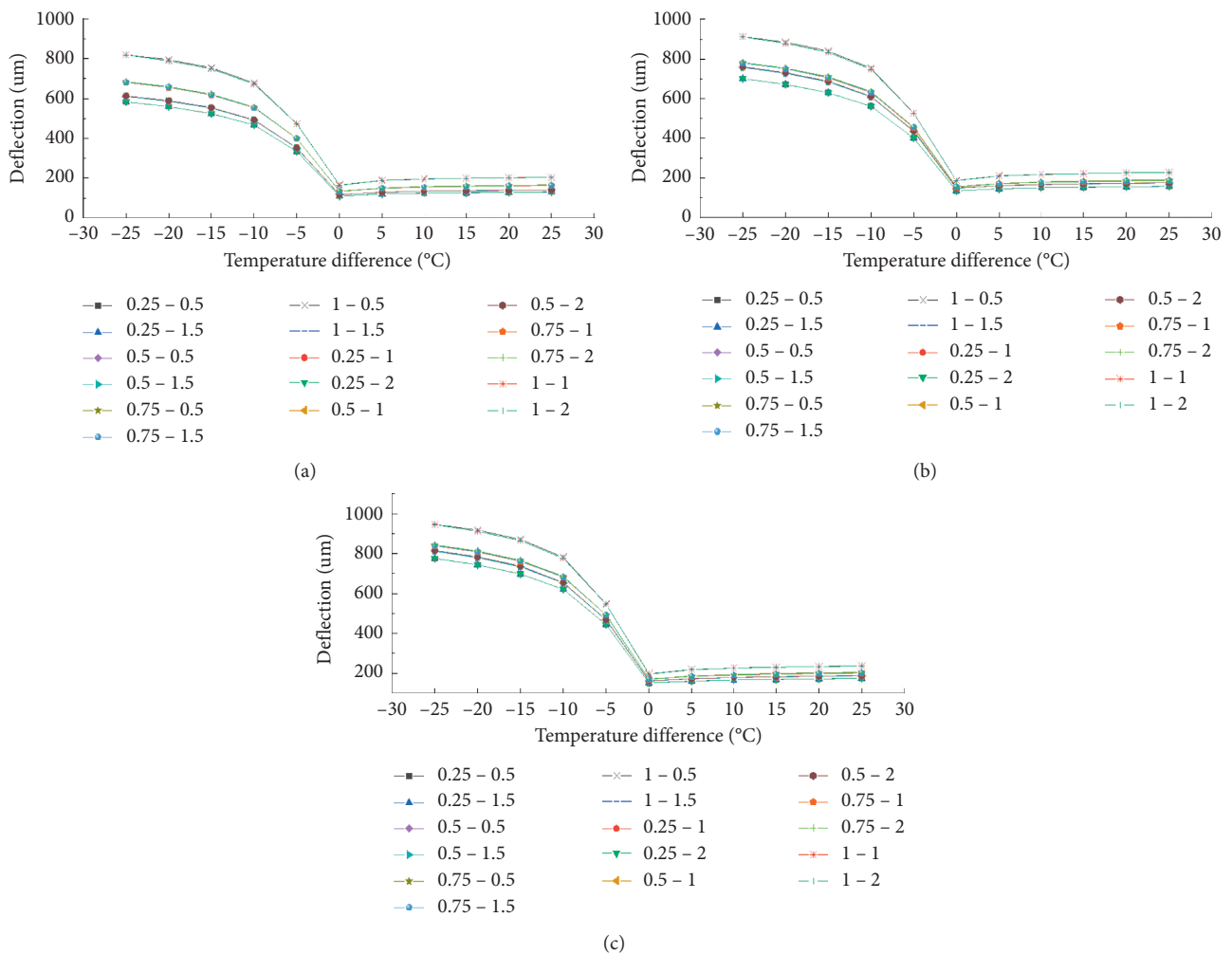


FIGURE 4: Deflection of plate angle load center point for plate angle voids. (a) 50 kN. (b) 70 kN. (c) 90 kN.

(3) Under the same void condition, the deflection increased with the load at the same temperature difference.

Figure 5 shows the variation of the deflection at the center point of the plate angle load for each plate edge void

under the coupled action of temperature and three-stage load. The following observations were made:

- (1) At the same temperature difference and under the same load, the deflection increased with the void depth but within a narrow range; the deflection

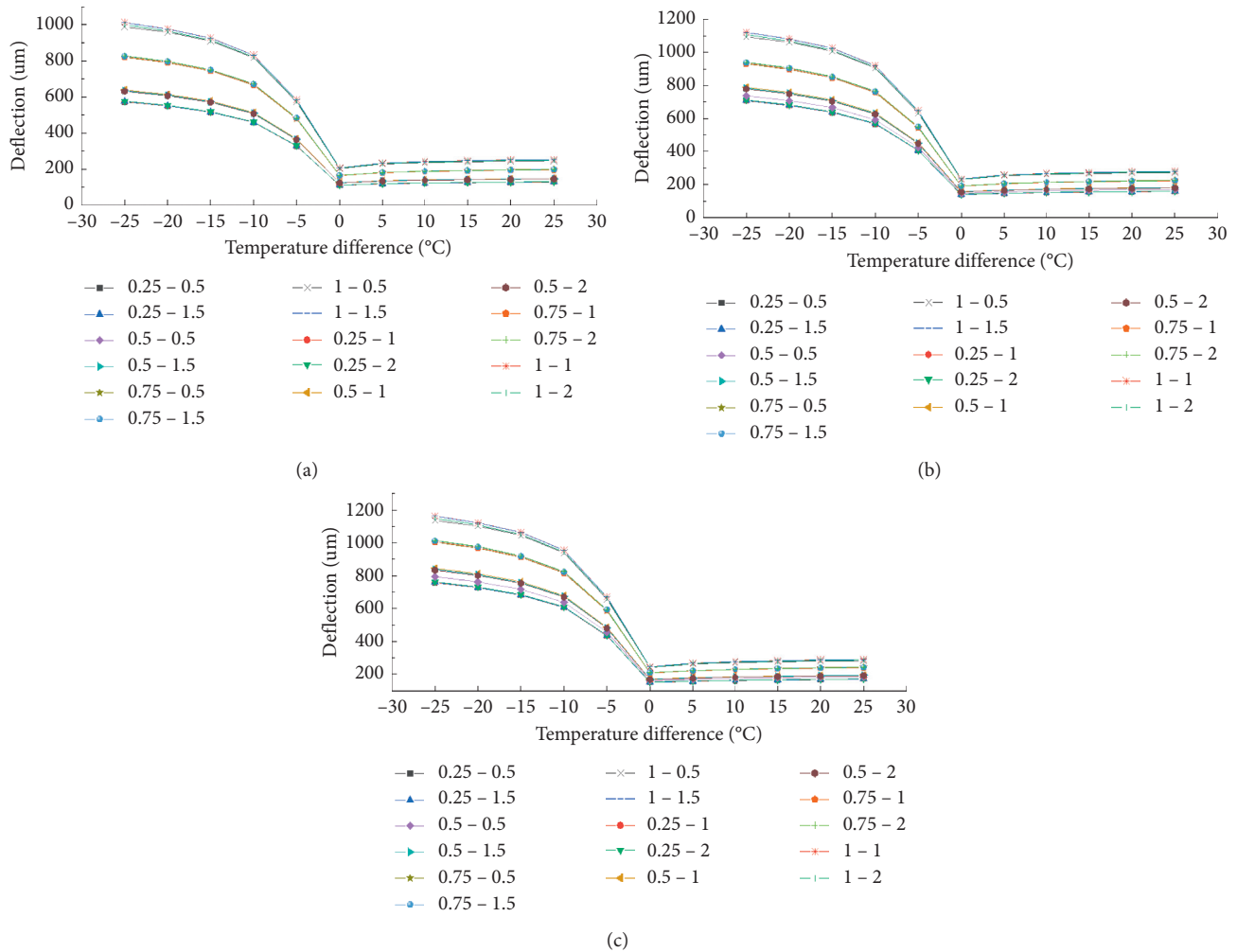


FIGURE 5: Deflection at plate angle load center point under plate edge void conditions. (a) 50 kN. (b) 70 kN. (c) 90 kN.

increased with the void width; and the deflections among the different void widths exhibited significant variations

- (2) At the same temperature difference, the deflection under each void condition decreased with increasing temperature difference when the temperature difference was negative but increased with increasing temperature difference when the temperature difference was positive
- (3) Under the same void condition, the deflection increased with the load at the same temperature difference

The comparison between Figures 4 and 5 shows that, at the same temperature difference and under the same load, the deflection under the plate edge void condition is larger than that under the plate angle void condition.

3.2. Correlation Analysis between Pavement Temperature Difference and Correction Coefficient. In this study, the modification coefficient of the influence degree of temperature difference on the deflection of the center point of the

plate angle load was introduced and denoted as φ . The coefficient is calculated using

$$\varphi = \frac{D_1}{D_2}, \quad (3)$$

where φ is the correction coefficient of the temperature difference to the deflection value of the center point of the plate angle load and D_2 is the deflection value of the center point of the plate corner load, ignoring the effect of the temperature stress field (μm).

The deflection values for the center point of the plate angle loads of 50, 70, and 90 kN (without considering the temperature effect) obtained through numerical simulation are listed in Table 5.

The correction coefficient distributions and the corresponding fitting curves for the deflections at the center point of the plate angle loads of 50, 70, and 90 kN were calculated and plotted (Figure 6).

The following results were obtained.

- (1) Within the negative temperature range, the correction coefficient decreased with an increase in the

TABLE 5: Deflections at plate angle load center point under three-stage loads (without considering temperature effect).

Load/kN	50	70	90
Deflection at load center point/ μm	66.12	92.57	119.02

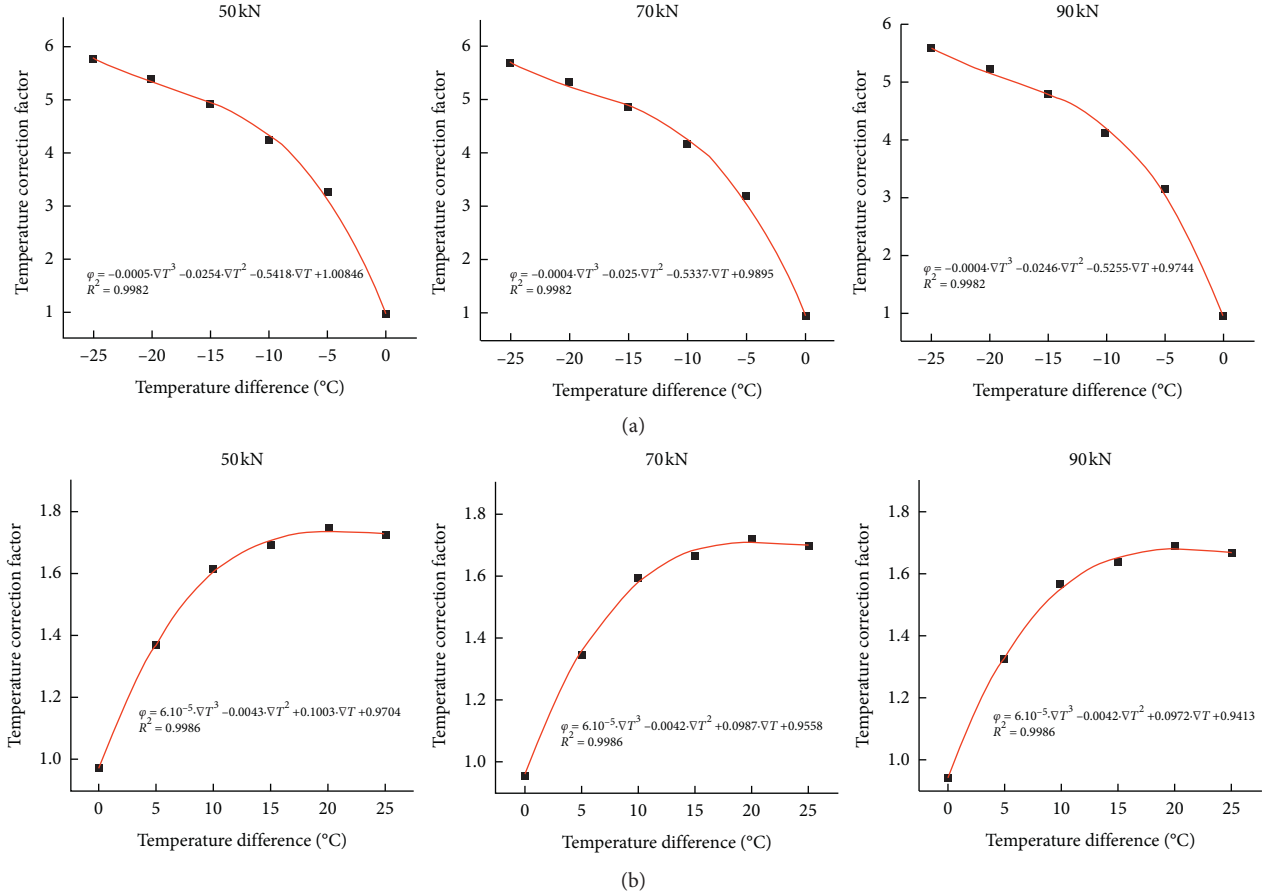


FIGURE 6: Correlation between temperature difference and correction coefficient under three loads. (a) Negative temperature range. (b) Positive temperature range.

temperature difference; in the positive temperature range, however, the correction coefficient increased with increasing temperature difference, and finally tended to be stable

- (2) At the same temperature difference, the correction coefficient did not change significantly with an increase in the load

The relative error between the correction coefficients that corresponded to different temperature differences and their mean values under the three-stage load was not more than 5%. Therefore, the average correction coefficient under the three-stage load represented the temperature correction coefficient under different loads, the calculated average temperature correction coefficient was sorted out, and the fitting curves were plotted, as shown in Figure 7.

When the positive and negative temperature differences were obtained, the correlation between the temperature difference and the correction coefficient could be expressed as follows.

Negative temperature range:

$$\varphi = -0.0004 \cdot \nabla T^3 - 0.025 \cdot \nabla T^2 - 0.5337 \cdot \nabla T + 0.9895, \quad R^2 = 0.9982. \quad (4)$$

Positive temperature range:

$$\varphi = 6 \cdot 10^{-5} \cdot \nabla T^3 - 0.0042 \cdot \nabla T^2 + 0.0987 \cdot \nabla T + 0.9558, \quad R^2 = 0.9986. \quad (5)$$

Based on the plate angle deflection values of the cement concrete pavement plate that corresponds to the difference in temperature obtained during the temperature field variation tests, equations (4) and (5) were used to calculate the corresponding plate angle center deflections. The comparison is depicted in Figure 8. It was found that the actually detected deflection value fluctuates up and down the

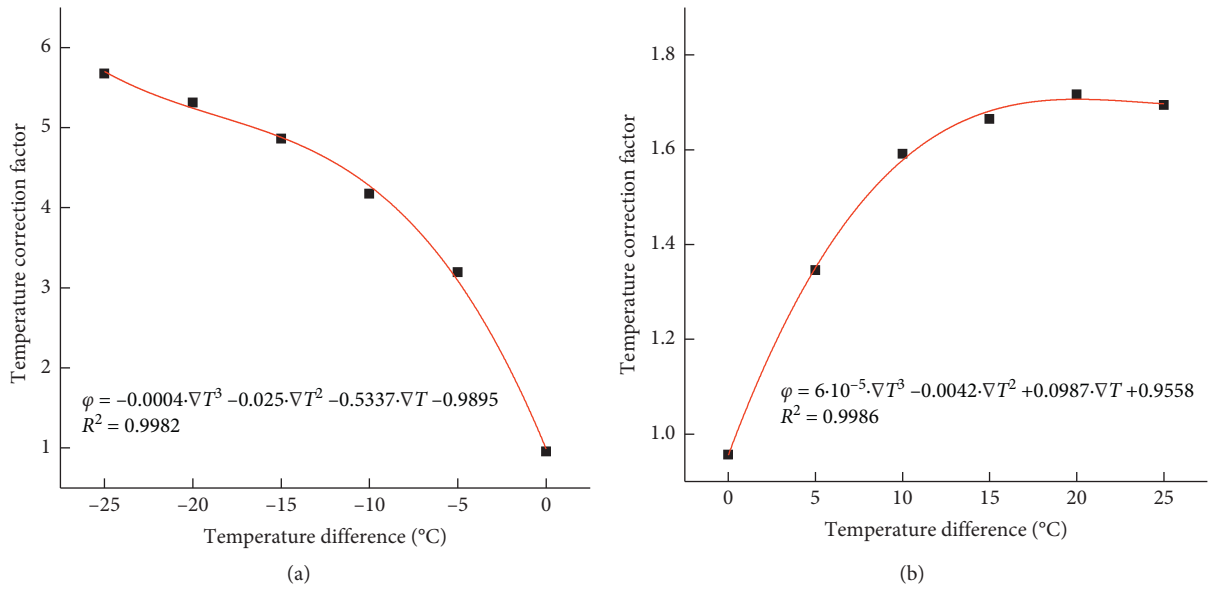


FIGURE 7: Correlation between positive and negative temperature differentials and mean correction coefficient. (a) Negative temperature range. (b) Positive temperature range.

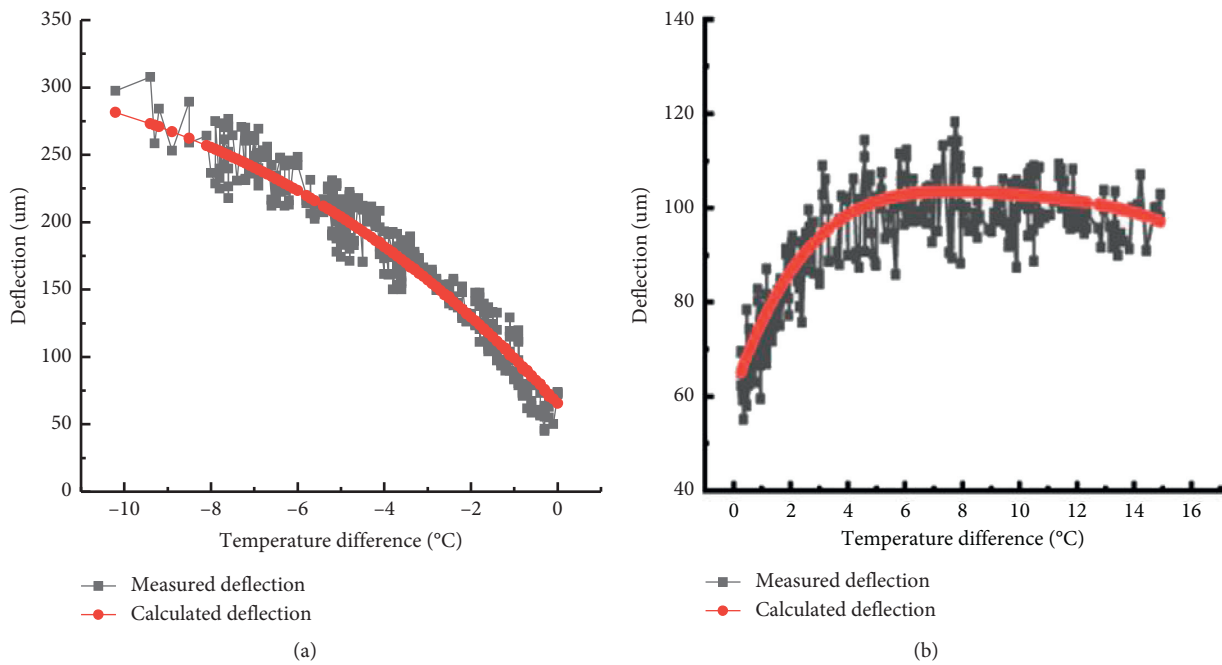


FIGURE 8: Comparison between experimental and the calculated deflection values of positive and negative temperature differences. (a) Negative temperature range. (b) Positive temperature range.

calculated value, the entire variation trend of the plate with the calculated data was fitted, and the finite element model was validated using equations (4) and (5). The accuracy of the simulated results was consistent with the test results.

The average temperature correction coefficients under different plate edge void conditions were analyzed (Figure 9).

The fitting analytical equations are expressed as follows.

Negative temperature range:

$$\varphi = -0.0003 \cdot \nabla T^3 - 0.0218 \cdot \nabla T^2 - 0.4928 \cdot \nabla T + 1.0010, \quad R^2 = 0.9997. \quad (6)$$

Positive temperature range:

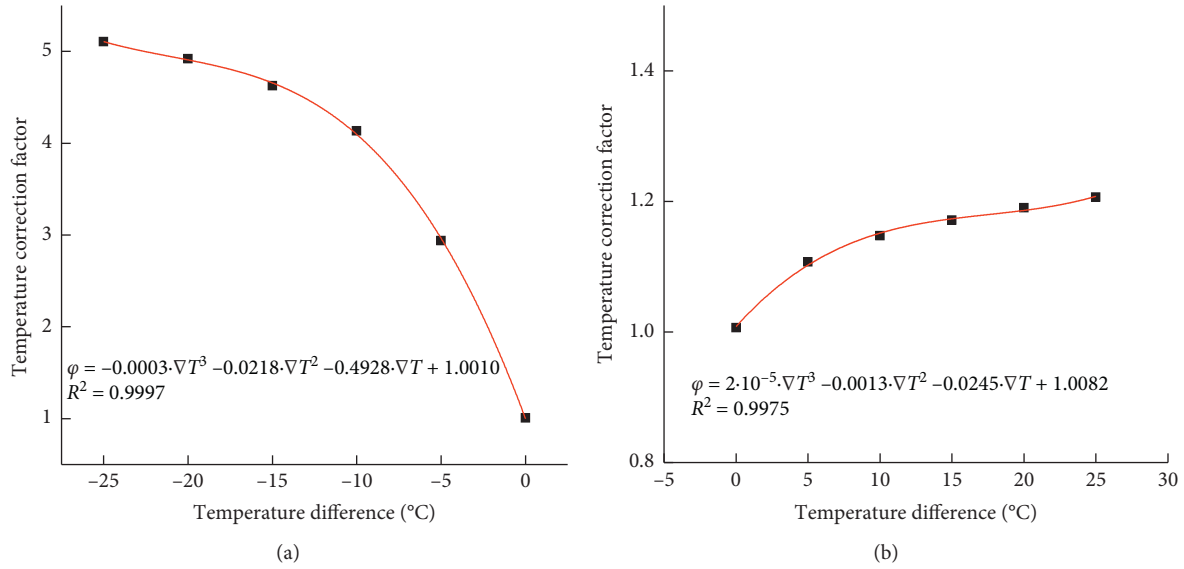


FIGURE 9: Correlation between positive and negative temperature differentials and correction coefficient. (a) Negative temperature range. (b) Positive temperature range.

$$\varphi = 2 \cdot 10^{-5} \cdot \nabla T^3 - 0.0013 \cdot \nabla T^2 + 0.0245 \cdot \nabla T + 1.0082,$$

$$R^2 = 0.9975. \quad (7)$$

Furthermore, the average temperature correction coefficients under different plate edge void conditions were evaluated (Figure 10).

The fitting analytical equations are expressed as follows.
Negative temperature range:

$$\varphi = -0.0003 \cdot \nabla T^3 - 0.0214 \cdot \nabla T^2 - 0.4854 \cdot \nabla T + 1.0006,$$

$$R^2 = 0.9997. \quad (8)$$

Positive temperature range:

$$\varphi = 2 \cdot 10^{-5} \cdot \nabla T^3 - 0.0011 \cdot \nabla T^2 + 0.0218 \cdot \nabla T + 1.0078,$$

$$R^2 = 0.9984. \quad (9)$$

3.3. Temperature Correction Factor. The temperature difference-mean temperature correction coefficient relationship for the plate angle void (Figure 9) and plate edge void (Figure 10) conditions were compared and analyzed, as depicted in Figure 11.

The variation trends of the temperature difference-average temperature correction coefficients obtained analytically and through the calculation of the two types of cement concrete pavement void conditions were consistent (Figure 11), and the relative error was lower than 1%. Therefore, considering the temperature difference-temperature correction factor obtained using equations (6) and (8), the mean value was adopted as the temperature correction

factor under the void conditions at negative temperatures. Similarly, by considering the temperature difference-temperature correction factor obtained using equations (7) and (9), the mean value was selected as the temperature correction factor under the void condition at positive temperatures.

Negative temperature range:

$$\varphi = -0.0003 \cdot \nabla T^3 - 0.0216 \cdot \nabla T^2 - 0.4888 \cdot \nabla T + 1.0002,$$

$$R^2 = 0.9997. \quad (10)$$

Positive temperature range:

$$\varphi = 2 \cdot 10^{-5} \cdot \nabla T^3 - 0.0011 \cdot \nabla T^2 + 0.0229 \cdot \nabla T + 1.0092,$$

$$R^2 = 0.9981. \quad (11)$$

4. Field Test Verification

4.1. Experimental Verification. Outdoor full-scale experimental tests can reflect the actual pavement conditions in a complex environment better. Hence, the test section of the comprehensive test site of the Water Conservancy and Traffic Infrastructure Safety Protection of Zhengzhou University was investigated to improve the consistency of test results. Design data for standard cement concrete pavements were adopted: the plane size was 4 m × 5 m, 24 cm thick concrete pavement was placed on 18 cm thick cement stabilized macadam base, the subbase consisted of 16 cm thick graded broken stone, and six pavement plates were cast. A schematic of the pavement structure is depicted in Figures 12 and 13.

Related instruments used for the validation test include a temperature sensor, hand-held infrared temperature

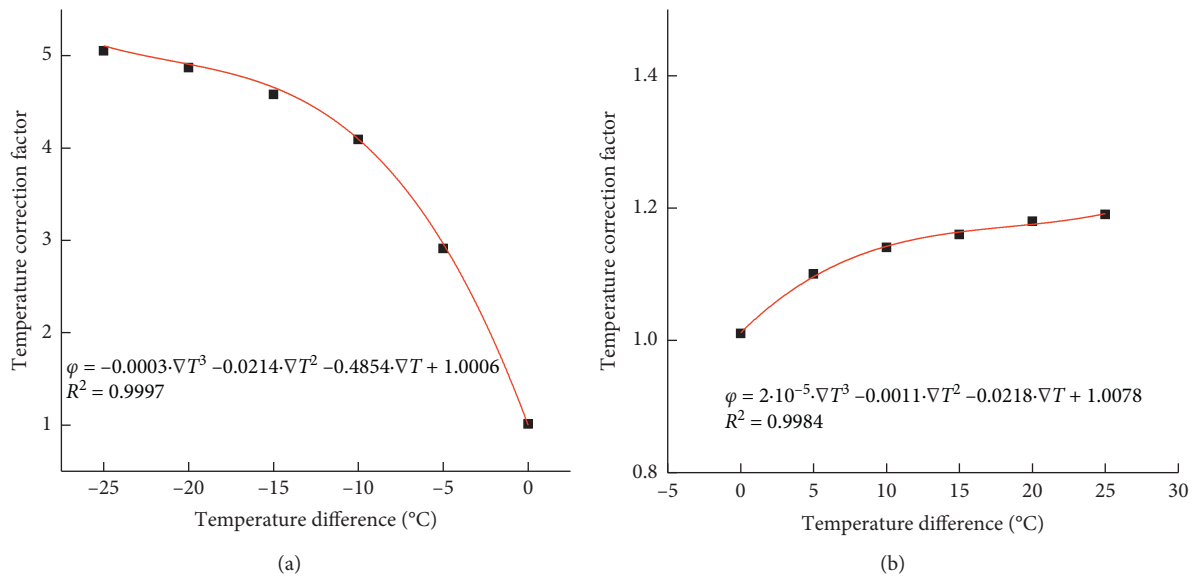


FIGURE 10: Correlation between positive and negative temperature differentials and correction coefficient. (a) Negative temperature range. (b) Positive temperature range.

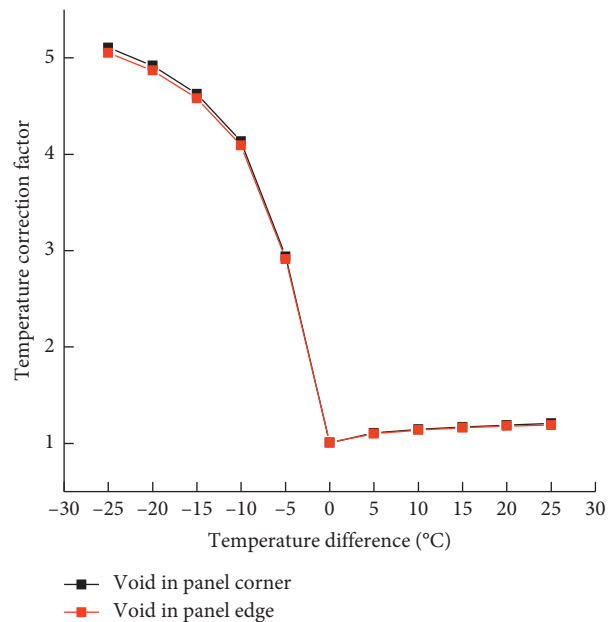


FIGURE 11: Temperature difference-mean temperature correction coefficient under plate angle void and plate edge void conditions.

detector, crane, FWD, hand-held grinding machine, and two cement concrete pavement plates with stable foundations. One plate was used to simulate the conditions of the plate corner voids, and the other plate was used to simulate the conditions of the plate edge voids. The field test process is shown in Figure 13, and the specific experimental steps were as follows:

- (1) The temperature sensor was embedded in the specific location of the predrilled cement concrete pavement slab, and the buried depth was the thickness of the pavement slab. After the sensor was embedded, it

was sealed with premixed cement concrete and compacted with force.

- (2) The intact cement concrete pavement slab without voids was lifted using a crane, and the panel corner void was set at the corner of the top panel of the base course with the plate angle fixed as the circle center; the void radius and void depth were 1 m and 2 cm, respectively. The panel edge void was set at the edge of the top slab of the base course with 0.5 m as the void width and 2 cm as the void depth.

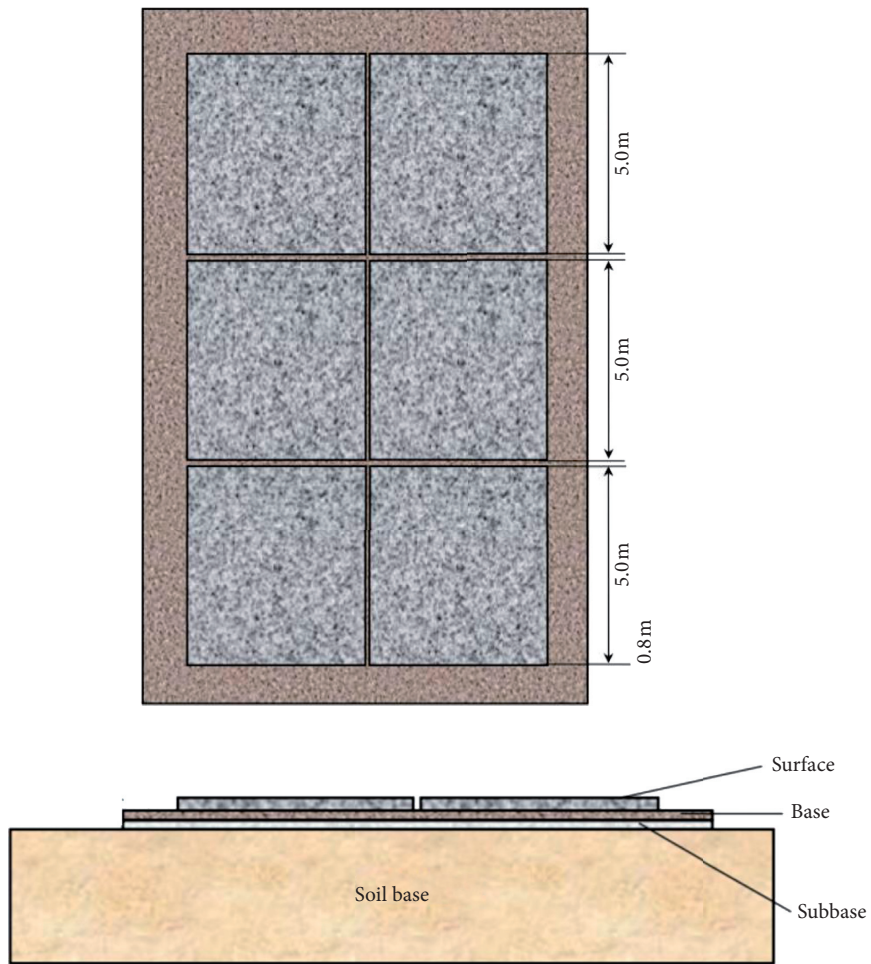


FIGURE 12: Schematic of full-scale cement concrete pavement structure.

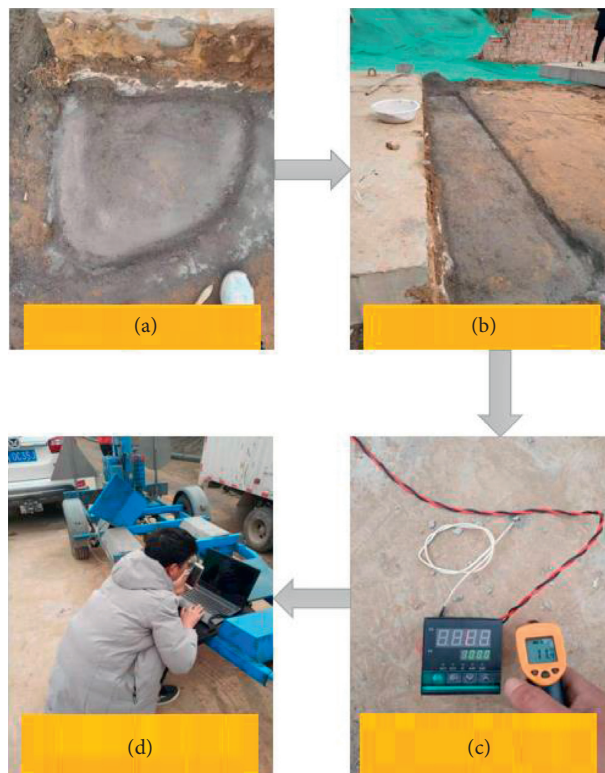


FIGURE 13: Flow chart of the field test. (a) Void in panel corner. (b) Void in panel edge. (c) Road surface temperature detection. (d) Detection of road surface deflection.

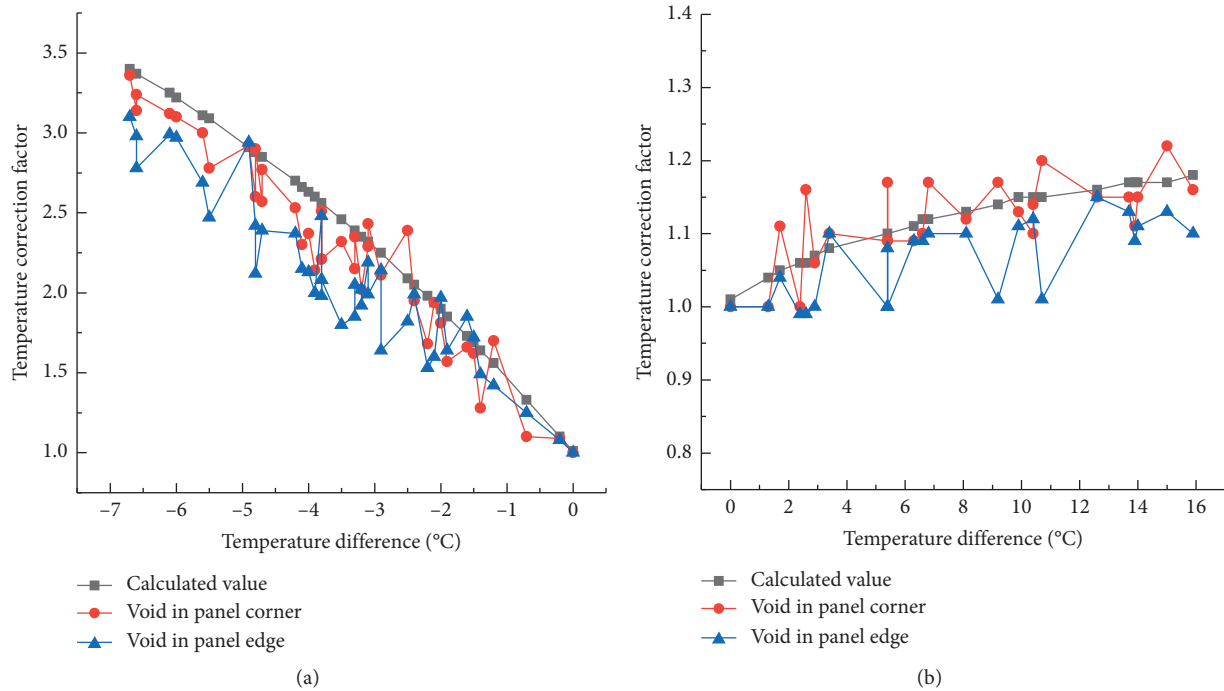


FIGURE 14: Comparative analysis of model calculated values and field test results. (a) Negative temperature range. (b) Positive temperature range.

- (3) In addition, an infrared temperature detector was used to collect temperature data for the top and bottom of the slab, and an FWD was used to collect deflection data for the center point of the plate corner load. The interval for the above data collection was once every 1 h.

4.2. Analysis of Test Results. After the above test data were sorted, the deflection value corresponding to a zero temperature difference during daily tests was selected as the standard value of all the deflection tests for that day, and the ratios of all deflection values (including zero temperature difference) to the above standard value was counted, in other words, the temperature correction coefficient (Figure 14).

A comparison between the model results and test results showed that when the pavement slab had a negative temperature difference, the actual temperature correction coefficient of the panel corner and edge voids fluctuated up and down within a narrow fluctuation range, and the average fluctuation was not higher than 7%. When the pavement slab had a positive temperature difference, the actual temperature correction coefficients of the panel corner and edge void fluctuated within a narrow fluctuation range of less than 5% on the average. These results show that, in practice, the temperature correction coefficient can be used for correcting the measured deflection precisely.

5. Conclusion

In this study, through the establishment of coupled temperature and load finite element model of cement pavement, the effect of temperature difference at the bottom and top of

the slab and deflection of the center point of the plate corner load under different void, climatic, and load conditions was investigated. In addition, the temperature difference between the top and bottom and the correlation of deflection temperature correction coefficient was analyzed. Furthermore, the temperature correction coefficient was developed considering the temperature difference between the top and bottom, and the accuracy of the temperature correction coefficient was verified experimentally.

- (1) Based on the monitoring and analysis of the temperature field of a cement concrete pavement through full-size outdoor tests for up to one year, the relationship between the plate top temperature of the cement concrete pavement and the temperature difference at plate top and bottom of the cement concrete pavement in each season was established.
- (2) The deflection of the plate angle load center point under the coupled action of temperature and load in each season was calculated, and its variation was evaluated. It was found that, considering the effect of the temperature difference, the deflection decreased with increasing negative temperature difference but decreased with increasing positive temperature difference under each void condition.
- (3) At the same temperature difference, the deflection difference of the center point of the plate angle load under different void conditions was small.
- (4) The temperature correction coefficient was introduced to derive the deflection correction equation for the cement pavement, considering the temperature difference in different seasons and under

different void conditions. In the case of a negative temperature difference, the correction coefficient decreased with an increase in temperature difference; at a positive temperature difference, the correction coefficient increased with an increase in temperature difference.

- (5) Two specific conditions of plate corner and plate edge voids were selected for the tests. It was found that the error between the measured and calculated values of the temperature correction coefficients for these two conditions was not higher than 7%, which demonstrated the accuracy of the temperature correction coefficient.

Data Availability

The data used to support the findings of this study are included within the article.

Conflicts of Interest

The authors declare that they have no conflicts of interest.

Acknowledgments

The authors acknowledge the support received from the National Key Research and Development Plan (Grant no. 2018YFB1600200), the National Natural Science Foundation of China (Grant nos. 51878624 and 51878622), Major Scientific and Technological Special Project in Henan (Grant no. 181100310400), Henan Science Fund for Distinguished Young Scholars (Grant no. 202300410354), Natural Science Foundation of Henan Province (Grant no. 202300410746), the Program for Science and Technology Innovation Talents in Universities of Henan Province (Grant no. 19HAS-TIT041), and Key Research Projects of Higher Education in Henan Province (Grant no. 18A580001).

References

- [1] Q. Chen, G. Wang, and W. Pan, "Research on relationships among different disease types of cement concrete pavement based on structural equation model," *Mathematical Problems in Engineering*, vol. 2020, no. 123X, 13 pages, Article ID 9580616, 2020.
- [2] Z. Liu, F. Xu, and G. Cao, "Study on cement concrete pavement treatment methods of common damage diseases," *Applied Mechanics and Materials*, vol. 716–717, pp. 307–309, 2015.
- [3] C. Zhang and Y. Cai, "Study on technologies of detecting voids in cement concrete pavement based on dynamic deflection," Master thesis, Zhengzhou University, Zhengzhou, China, 2016.
- [4] L. I. Xiang and Y. Peng, "Dynamic response analysis of void under slab to cement concrete pavement," *Journal of Beijing University of Technology*, vol. 43, no. 12, pp. 1922–1928, 2017.
- [5] Q. Wang, X. Wang, and C. Wang, "Differentiation of the cavity beneath cement pavement slab based on deflection difference and pumping height," *Journal of Highway and Transportation Research and Development*, vol. 25, no. 12, pp. 84–87, 2008.
- [6] S. Chun Li, "Correlation of non-destructive pavement test devices," *Advanced Materials Research*, vol. 912–914, pp. 613–616, 2014.
- [7] D. J. White, P. K. R. Vennapusa, and Y. Zhang, "Assessment of support conditions of concrete pavement using FWD deflection basin data," *Journal of Testing and Evaluation*, vol. 47, no. 4, pp. 21–29, 2018.
- [8] Y. Huang, J. Yuan, Y. Tan et al., "Identification of void beneath airport cement concrete pavement and its influence," *Journal of Tongji University: Natural Science*, vol. 40, no. 6, pp. 861–866, 2012.
- [9] Y. H. Zhong, B. Zhang, C. C. Guo, and J. Qi, "Research on the identification method for void location of semi-rigid base pavement," *Advances in Structural Engineering*, vol. 94–96, pp. 1257–1260, 2011.
- [10] C. Zhang, H. He, Y. Xue, and Z. Luo, "Comparative test and analysis of falling-ball instrument and FWD deflection detection method," in *Proceedings of the IOP Conference Series: Earth and Environmental Science*, vol. 514, p. 22065, Vienna, Austria, May 2020.
- [11] R. Wu, Q. Peng, and J. Xiaobo, "Identification of the void between the cement concrete pavement slab and foundation based on finite element analysis using orthogonal experiment method," *Gongcheng Lixue/Engineering Mechanics*, vol. 25, no. Suppl P189, pp. 197–192, 2008.
- [12] Y. Wu, T. Liu, Z. Huang, B. Chen, and Z. Zheng, "Experimental study on detection of void in concrete pavement slab by FWD," in *Proceedings of the IOP Conference Series: Earth and Environmental Science*, pp. 1755–1315, Vienna, Austria, May 2020.
- [13] Z. H. A. O. Hongduo and M. A. Lukuan, "Investigation into effects of temperature variations on airport cement pavements based on measured data," *Journal of Tongji University: Natural Science*, vol. 47, no. 12, pp. 1764–1771, 2019.
- [14] L. Wang and C. Hu, "Built-in temperature's regional characteristics of cement concrete pavement and its effect on slab curling," *Journal of Traffic and Transportation Engineering*, vol. 18, no. 3, pp. 19–33, 2018.
- [15] L. Zhang, Y. Luo, X. Chen et al., "Temperature field characters and numerical simulation of asphalt overlay structure upon previous cement pavement surface," *Journal of Highway and Transportation Research and Development*, vol. 36, no. 5, pp. 11–19, 2019.
- [16] L. Wen and X. Guo, Baozhu, "Cause analysis on the void under slabs of cement concrete pavement," in *Proceedings of the IOP Conference Series: Materials Science and Engineering*, vol. 205, Shenyang, China, 2017.
- [17] S. Zeng, X. Zeng, and Xu Jia, "Criterion for void identification beneath cement concrete pavement slab corner," *Journal of Central South University (Science and Technology)*, vol. 40, no. 1, pp. P248–P255, 2009.
- [18] S. Chen, Z. Wang, C. Zhang et al., "Dynamic finite element simulation analysis of void in cement concrete pavement," *Journal of China & Foreign Highway*, vol. 37, no. 4, pp. 53–57, 2017.
- [19] C. Toth, C. Toth, Szentpeteri, and I. Szentpeteri, "Effects of climatic factors on the shape of deflection bowl," in *Proceedings of the 3rd International Conference on Road and Rail Infrastructure—CETRA 2014: Road and Rail Infrastructure III*, University of Zagreb, Split, Croatia, April 2014.
- [20] T. Jing and Z. Yan, "Research on the temperature status of cement concrete pavement," *Journal of Tongji University*, vol. 5, no. 3, pp. 88–98, 1980.

- [21] X. Duan, *The Thermal Stress Study of Void beneath Slab on Cement Concrete Pavement*, Chongqing Jiaotong University, Chongqing, China, 2016.
- [22] J. Zhao, Z. Tan, and B. Liu, "Effect and correction on slab interior deflection of cement concrete pavement due to temperature gradient," *Journal of Tongji University (Natural Science)*, vol. 35, no. 5, pp. 617–620, 2007.
- [23] L. I. Sheng, S. Chen, Z. Liu, and H. Zhan, "Some problems on deflection test of old cement concrete pavement," *Journal of Central South University (Science and Technology)*, vol. 46, no. 12, pp. 4713–4718, 2015.
- [24] Y. Dou, M. Song, J. Sun, F. Xiong, and S. Zheng, "Numerical analysis of cement concrete pavement crack under the coupling of temperature and load," *Concrete*, vol. 40, no. 6, pp. 56–60, 2018.
- [25] S. Li, B. Zhang, F. Wang et al., "Experimental study on correction of deflection temperature of cement concrete pavement," Master Thesis, Zhengzhou University, Zhengzhou, China, 2019.
- [26] Y. Ding and Y. Zhong, "Identification of void in cement concrete pavement and evaluation of polymer grouting effect by considering temperature's effect," Master thesis, Zhengzhou University, Zhengzhou, China, 2019.

Research Article

Influence of the Activator Concentration and Solid/Liquid Ratio on the Strength and Shrinkage Characteristics of Alkali-Activated Slag Geopolymer Pastes

Zikai Xu,¹ Jinchao Yue,¹ Guanhong Pang ,¹ Ruixia Li,¹ Peng Zhang,¹ and Shengtang Xu ²

¹School of Water Conservancy Engineering, Zhengzhou University, Zhengzhou 450001, China

²Xinyang Highway Development Center, Xinyang 464000, China

Correspondence should be addressed to Shengtang Xu; xust0326@zzu.edu.cn

Received 5 January 2021; Revised 25 January 2021; Accepted 1 February 2021; Published 10 February 2021

Academic Editor: Jiaolong Ren

Copyright © 2021 Zikai Xu et al. This is an open access article distributed under the Creative Commons Attribution License, which permits unrestricted use, distribution, and reproduction in any medium, provided the original work is properly cited.

Geopolymers have distinct advantages such as having energy-saving properties, being an environmentally protective material, and having high mechanical strength and durability. However, the shrinkage of the geopolymer materials is one of the major problems to affect its practical application. In this study, blast furnace slag-based geopolymer pastes were prepared using sodium silicate and sodium hydroxide as activators to investigate the effect of the activator concentration and solid/liquid ratio on strength and shrinkage properties. For a better understanding of the reaction mechanism and microstructure of the geopolymer pastes, a multitechnique approach including scanning electron microscopy, X-ray diffraction, and Fourier transform infrared spectra was carried out. The results showed that the geopolymers compressive strength increased significantly as the activator concentration increased. The increase in activator concentration first increased the flexural strength and then decreased and reached the maximum when the activator concentration was 40%. A higher activator concentration, as well as a lower solid/liquid ratio, generally led to serious geopolymers drying shrinkage. These findings are expected to be ascribed from the changes in the content of the alkali-activated product (i.e., hydrate calcium aluminosilicate), which depends on the activator concentration. The increase in C-A-S-H gel (hydrate calcium aluminosilicate) compacts paste densifiers but causes shrinkage fracture concerns. These results provide an appropriate proportion for alkali-activated slag geopolymer pastes with better mechanical strength and antidry-shrinkage cracking properties, which are beneficial for the further applications of geopolymer materials.

1. Introduction

Geopolymers are formed by the reaction of alkali hydroxide or silicate solution with solid aluminosilicate to form a three-dimensional network structure consisting of silica tetrahedrons and aluminum oxide tetrahedrons [1–3]. Geopolymers exhibits excellent characteristics including high strength, low CO₂ emissions, excellent corrosion resistance, and durability, compared to traditional cementitious binders [3–5]. The geopolymerization process is more environmentally friendly and may be carried out under ambient conditions or at low temperatures. The raw materials used for geopolymerization do not require extra energy consumption and are industrial byproducts such as fly ash and blast furnace slags [6].

Therefore, geopolymers have the potential to partially replace cement when preparing concrete.

Geopolymer strength has been examined in many previous studies. Atiş et al. [7] found that the mechanical strength of alkali-activated slag materials decreased according to the activators used: Na₂O•nSiO₂ > NaOH > Na₂CO₃. Aydın Baradan [8] also found that alkali-activated slag pastes using Na₂O•nSiO₂ as an activator had higher compressive strength, higher fluidity, lower adsorption water, lower porosity, and a larger setting time range than those using NaOH. Liu et al. [9] reported that when the water/cement ratio increased from 0.30 to 0.38, the compressive strength of the geopolymer decreased from 82.9 MPa to 63.4 MPa, and the initial and final setting times increased from 10 to 13 min to 22 and

26 min, respectively. Cheng et al. [10] thought that the solid reactants increased and the porosity decreased with increasing solid/liquid ratio, which led to an increase in strength. While Heah et al. [11] drew the opposite conclusion using an orthogonal test, and the different results may have been caused by the different solid/liquid ratio adjustment ranges. Moreover, the results showed that the activator concentration, sodium silicate modulus, alkali metal ions, and solid/liquid ratio influenced the geopolymers mineral composition, microstructure, and mechanical properties [12–17]. The activator concentration is the key factor that determines the properties of geopolymers. Tuyan et al. [18] suggested that geopolymers compressive strength increased with increasing activator concentration and decreased with increasing sodium silicate modulus when Na_2O concentration was lower than 10%. The optimum activator concentration corresponded to an M (molar ratio of silica to sodium oxide) ratio of 1.6 and Na_2O content of 10% by binder weight. However, Alonso and Palomo [13] argued that increasing the activator concentration would delay the polymerization time and limit the ion mobility and the formation of hard structures, decreasing the mechanical properties.

In addition, geopolymers shrinkage during the setting and hardening processes is relatively obvious, which limits the geopolymers application [19, 20]. Excessive shrinkage may lead to cracking, thereby reducing not only the strength and stiffness but also the service life of the structure [21–23]. Many studies regarding the shrinkage behavior of geopolymers have been conducted in the last decade. Deb et al. [24] found that the drying shrinkage of geopolymers strain increased as the content of fly ash increased. Ridditirud et al. [25] found that the curing temperature and solid/liquid ratio played key roles in determining the drying shrinkage of fly ash-based geopolymers. Mermerdaş et al. [26] suggested that geopolymers with a higher content of binders and NaOH molarities showed a lower drying shrinkage, resulting in an increase in autogenous shrinkage. Ling et al. [27] thought the drying shrinkage of fly ash-based geopolymer pastes increased with decreasing module and activator concentration, but the total porosity is slightly lower. Kamhangrittrirong et al. [28] reported that the drying shrinkage significantly decreased with increasing fly ash content and decreasing sodium hydroxide concentration. When the ratio of sodium silicate to sodium hydroxide was 1.0, the shrinkage resistance of the geopolymer was the best.

In this study, we investigated the effects of the activator concentration and solid/liquid ratio on the mechanical strength development and shrinkage behavior of slag-based geopolymer pastes to provide an experimental basis and references for the performance optimization of geopolymers.

2. Materials and Methods

2.1. Materials. Blast furnace slag powder is the main material to prepare the geopolymer pastes. The specific surface area of the slag powder is $436 \text{ m}^2/\text{kg}$. The chemical composition is analysed by X-ray fluorescence spectrometer, and

the test results are shown in Table 1 which consist of 43.41% CaO , 22.99% SiO_2 , and 11.60% Al_2O_3 . Alkali activator is prepared by blending sodium silicate solution ($\text{Na}_2\text{O} = 8.5 \text{ wt\%}$, $\text{SiO}_2 = 26.8 \text{ wt\%}$, and sodium silicate modulus $\text{SiO}_2/\text{Na}_2\text{O}$ (molar mass ratio) = 3.25) with sodium hydroxide pellets (99 wt% purity).

2.2. Geopolymer Pastes Preparation. The preparation of geopolymer pastes is similar to the process of cement pastes preparation. First, sodium silicate solution and solid sodium hydroxide are prepared into alkali activators with a modulus of 1.5 and 2. The concentration of alkali activators is adjusted to 30, 40, 50, 60, and 70% (wt%) by adding deionized water. This activator is cooled to room temperature (24 h) and mixes with slags with solid/liquid ratios of 1.5 : 1, 1.25 : 1 and 1 : 1. After 5 min of stirring (2 min at a low speed and 3 min at high speed), the mixtures are cast into a mould with a size of $\text{Ø}50 \times 50 \text{ mm}$ for compressive strength tests and a mould with a size of $40 \times 40 \times 160 \text{ mm}$ for testing the flexural strength and drying shrinkage. The specimens are cured in a standard curing box (20°C and 95% RH) for 24 h and demoulded. Then, the specimens are stored under ambient conditions until testing (3, 7, and 28 d).

2.3. Test Methods

2.3.1. Mechanical Properties. The compressive strength and flexural strength of the specimens are determined after 3, 7, and 28 d of curing via microcomputer controlled pressure testing systems, according to the standard of Cement-Test Methods-Determination of strength (ISO 679:2009). The values of the compressive strength and flexural strength are the averages of six separate tests. Data deviating more than 10% from the mean are eliminated.

2.3.2. Setting Time. The setting time is tested according to a standard method for Portland cement normal consistency, setting time, and soundness water requirements (GB/T 1346-2011). The setting time is measured by a Vicat apparatus, and the test interval is 5 min. The values of the setting time are the averages of three separate tests.

2.3.3. Shrinkage Properties. The shrinkage property test is based on the modified ring constraint method [29]. The evenly stirred geopolymer pastes are poured into a mould composed of a resin board with a size of $200 \times 200 \times 3 \text{ mm}$ with an inscribed circle diameter of 150 mm and a glass bottom plate. After setting for 24 h at room temperature, the morphology and the number of cracked blocks are observed and counted.

According to the JC/T 603-2004 standard test method for mortar drying shrinkage, the drying shrinkage is reported by measuring three specimens to obtain an average value. The specimens continue to be cured in a constant temperature water bath at 20°C for 2 d after demoulding. Then, the test pieces are removed, the water on their surfaces is wiped, and their initial length is measured with an

TABLE 1: Chemical composition of the blast furnace slag (wt%).

Oxide	CaO	SiO ₂	Al ₂ O ₃	MgO	SO ₃	Fe ₂ O ₃
Content (%)	43.41	22.99	11.60	6.47	2.31	1.19

accuracy of 0.001 mm. The samples are then put into drying and shrinking box for curing at a temperature of $20 \pm 2^\circ\text{C}$ and relative humidity of $60 \pm 5\%$. The length of the samples after drying is tested with an accuracy of 0.001 mm. Drying shrinkage is determined from equation (1), where L_0 (mm) is the demoulded length, L_d (mm) is the measured length, and 160 (mm) is the effective length of the specimens without two head nails. The values of the drying shrinkage are the averages of three separate tests.

$$\text{drying shrinkage} = \frac{L_0 - L_d}{160} \times 100. \quad (1)$$

2.3.4. Microscopic Test. A KYKY-EM6200 scanning electron microscope is used to analyse the microstructure and morphology of the geopolymer pastes. MiniFlex 600 X-ray diffraction (XRD) is used to analyse the diffraction pattern of the geopolymer pastes. Fourier transform infrared spectroscopy (FTIR) is recorded on a Bruker VERTEX 70v in transmittance mode with a frequency between 4000 and 500 cm^{-1} to analyse the geopolymer functional group composition via the KBr compressed pellet methodology.

3. Results and Discussion

3.1. Compressive Strength of the Geopolymers. Figure 1 shows the effect of the activator concentration on the compressive strength of geopolymers at 3, 7, and 28 d with a solid/liquid ratio of 1.25:1. The compressive strength increases with increasing the activator concentration under the same modulus. The compressive strength at 3 d (6.70 MPa), 7 d (7.77 MPa), and 28 d (11.65 MPa) is the lowest when the sodium silicate modulus is 1.5 and the activator concentration is 30%. The compressive strength is the highest when the activator concentration is 70%, reaching 30.45 MPa (3 d) and 32.23 MPa (7 d), and 32.27 MPa (28 d). The phenomenon of “flash coagulation” appeared when the activator concentration exceeds 70%, which makes geopolymers difficult to apply. There is a similar result when the sodium silicate modulus is 2. A low modulus is beneficial to the slag hydration reaction, and polymerization proceeds more easily, but a modulus that is too large is not conducive to the formation of early strength under the same activator concentration.

Figure 2 shows the 7 d and 28 d compressive strengths of geopolymers at various solid/liquid ratios. The compressive strength increases with increasing solid-liquid ratio. At the same solid/liquid ratio (28 d), when the activator concentration is 30%, the increase is the largest, from 7.23 MPa to 17.92 MPa, but the smallest increase is at 70%, from 27.43 MPa to 32.62 MPa. This is probably due to the increase in the solid/liquid ratio, increasing the mass fraction of slag powder in the geopolymer. The contact between the

activator concentration and the reacting materials improved [11]. More slag participates in the reaction, resulting in a denser structure and higher compressive strength.

3.2. Flexural Strength of the Geopolymers. Figure 3 shows the influence of the activator concentration on the geopolymers flexural strength at a solid/liquid ratio of 1.25:1. The sodium silicate modulus has little effect on the flexural strength. The flexural strength first increases subsequently and decreases with increasing activator concentrations. The flexural strength (28 d) is the highest when the activator concentration is 40%, reaching 5.45 MPa (modulus of 1.5) and 5.33 MPa (modulus of 2), respectively. However, the flexural strength shows a sharp decrease when the activator concentration exceeds 40%. There is a certain relationship between the degree of shrinkage cracking and flexural strength. The increase in activator concentration promotes the ion reaction in solution to produce more calcium aluminosilicate and silicic acid (H_2SiO_3), which leads to a sharp decrease in geopolymers flexural strength [30].

Figure 3 indicates that when the activator concentration is 40%, the flexural strength is optimum. The effect of the solid/liquid ratio on the flexural strength is shown in Figure 4 (the sodium silicate modulus is 1.5 with an alkali concentration of 40%). The results show that the flexural strength increases with increasing solid/liquid ratio. When the solid/liquid ratio is 1:1, the flexural strength is the lowest, reaching 4.12 MPa at 28 d. When the solid/liquid ratio is 1.75:1, the flexural strength is the highest, reaching 7.75 MPa at 28 d. Geopolymers may collapse from the excessive water used for preparation. The excess water is expected to evaporate in the process of condensation and hardening, leaving a large number of pores in the specimen and decreasing flexural strength.

3.3. Setting Time of the Geopolymers. Figure 5 shows the effect of the activator concentration and solid/liquid ratio on the geopolymer setting time. Both the initial and final setting times gradually decrease with increasing activator concentration. Under the same activator concentration, the difference between the initial and final setting times gradually decreases with increasing activator concentration. When the activator concentration is $\leq 40\%$, the smaller the solid/liquid ratio is, the longer the initial setting time is. However, when the activator concentration is greater than 40%, the higher the solid/liquid ratio is, the shorter the initial setting time is. The setting time is related to the degree of polymerization [31]. In an aqueous solution, Na^+ exists as a hydrated ion. As the activator concentration is enhanced, a large amount of water and Na^+ are required to form a hydrated state, resulting in the rapid reduction of free water and a shorter setting time. The solid/liquid ratio also influences the setting time. Weng and Sagoe-Crentsil [32] found that an increased amount of water accelerated dissolution and hydrolysis through the reaction heat curve but inhibited polymerization. That is, the increased water prolonged the setting time. Therefore, it is important to select an appropriate solid/liquid ratio to control the geopolymer setting time. The required setting time depends on the application. For example, a higher solid/liquid ratio can be chosen to shorten the

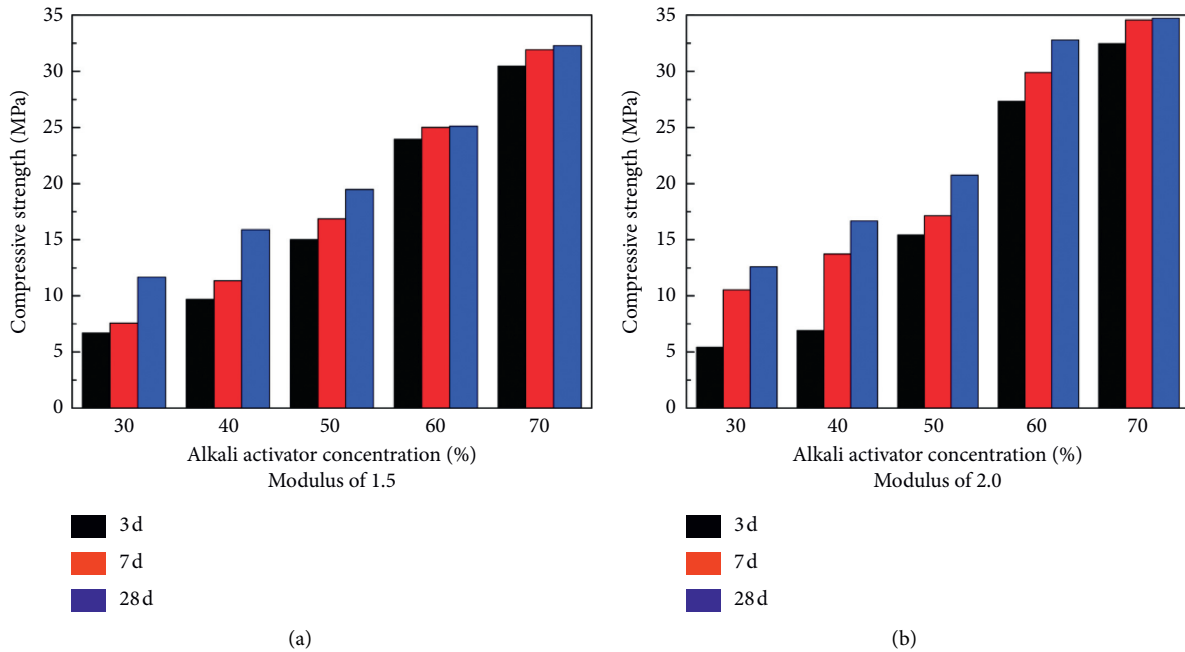


FIGURE 1: Influence of the activator concentration on the compressive strength of geopolymers.

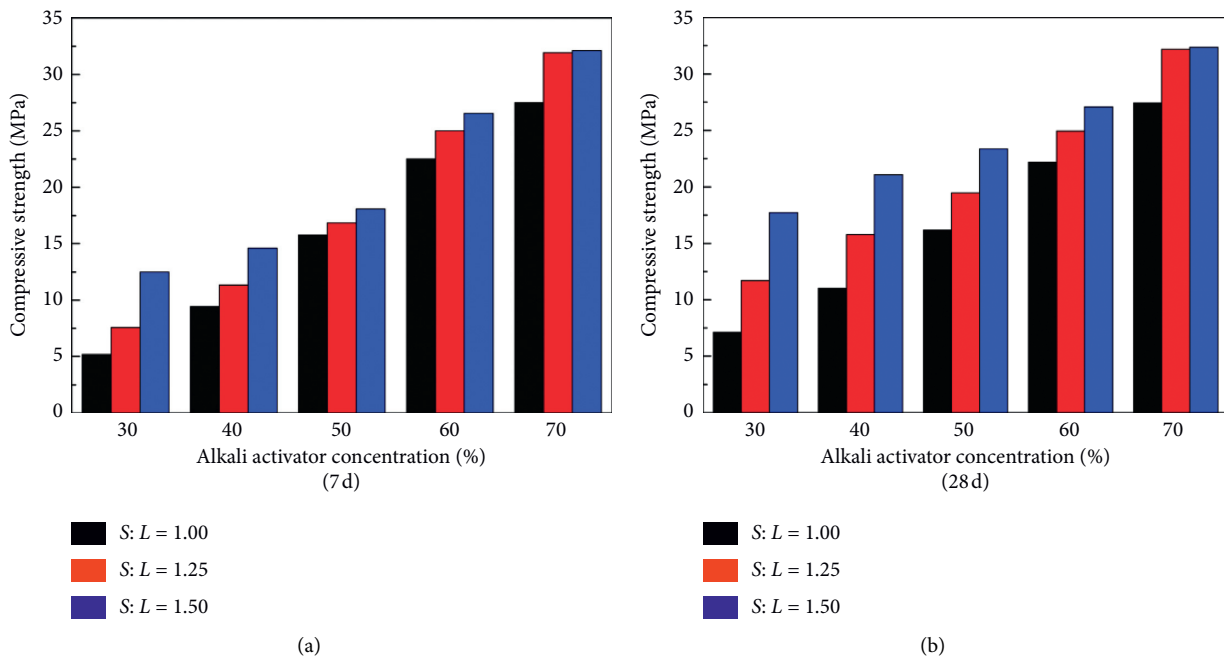


FIGURE 2: Influence of the solid/liquid ratio on the compressive strength.

setting time when geopolymers are used for the rapid repair of pavement and airport runways. A lower solid/liquid ratio can be chosen for geopolymer cement to avoid premature setting during transportation and pouring.

3.4. Shrinkage Properties of the Geopolymers. Figures 6 and 7 show the geopolymer plastic shrinkage cracking morphologies and statistics. The number of cracked blocks in the geopolymer increases with increasing activator concentration

and decreases with increasing solid/liquid ratio. When the activator concentration is small, no shrinkage cracks are found on the geopolymer surfaces. However, the geopolymers tend to exhibit more obvious shrinkage cracks with increasing activator concentration. The shrinkage block area is large, and warping appears at the sample outer edges.

Geopolymer cracking is related to the sodium silicate modulus, activator concentration, and solid/liquid ratio, as shown in Figure 7. A larger sodium silicate modulus leads to a smaller geopolymer plastic shrinkage. A smaller activator

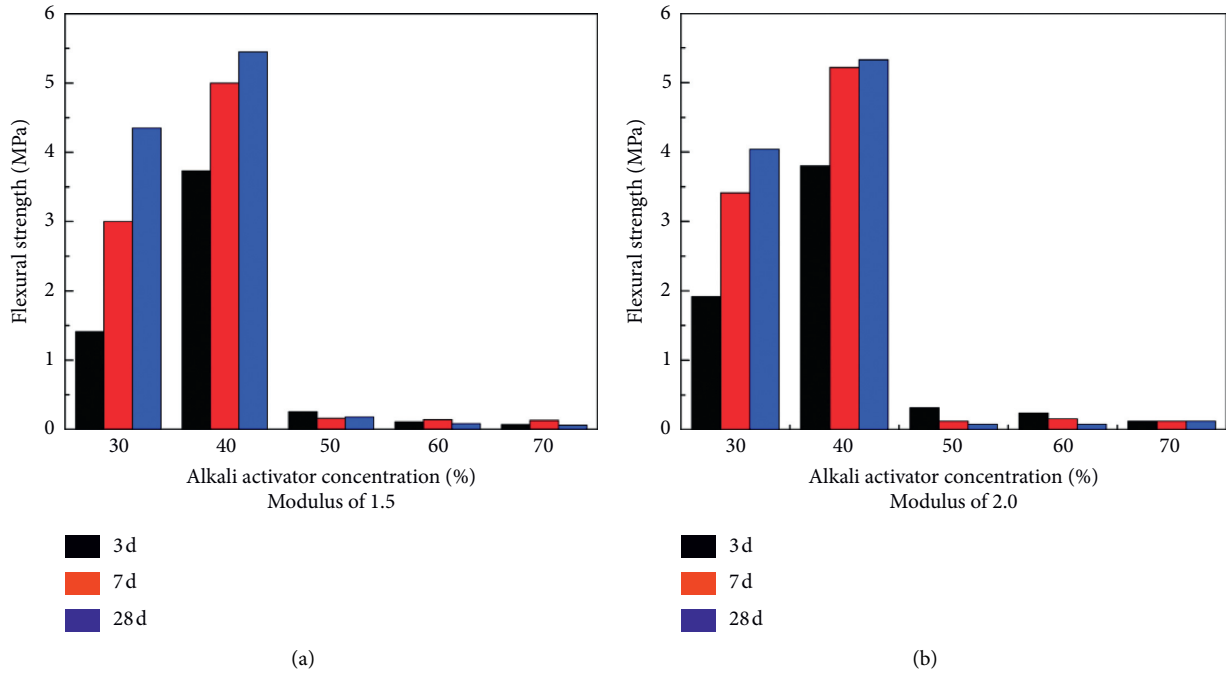


FIGURE 3: Influence of activator concentration on geopolymer flexural strength.

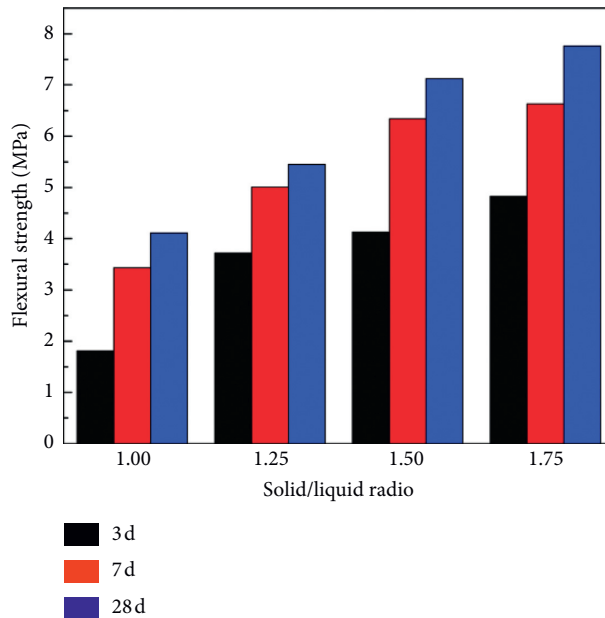


FIGURE 4: Influence of the solid/liquid ratio on geopolymer flexural strength.

concentration leads to smaller plastic shrinkage. The increase in activator concentration promotes aluminosilicate dissolution and depolymerization in slag, resulting in strong alkali metal cations binding in the structure and reduces excess alkali metal cations and other free ions [8, 33], thereby compacting the geopolymer microstructure. Moreover, the reaction of silicic acid produces by sodium silicate hydrolysis with calcium hydroxide produces by slag hydration the formed traces of C-S-H gel (calcium silicate hydrate). The formation of low content of C-S-H gel can destroy the

equilibrium of multiphase ions and further promote the dissolution of calcium oxide in the slag until the dissolution of calcium oxide makes the slurry more compact. Therefore, a higher activator concentration promotes the hydration reaction and the degree of geopolymer polymerization. However, if the activator concentration is too high, the degree of polymerization would be too large, and the gel content would be too high (>50%), resulting in more severe shrinkage cracking, which is unfavourable to the shrinkage resistance of hardened pastes.

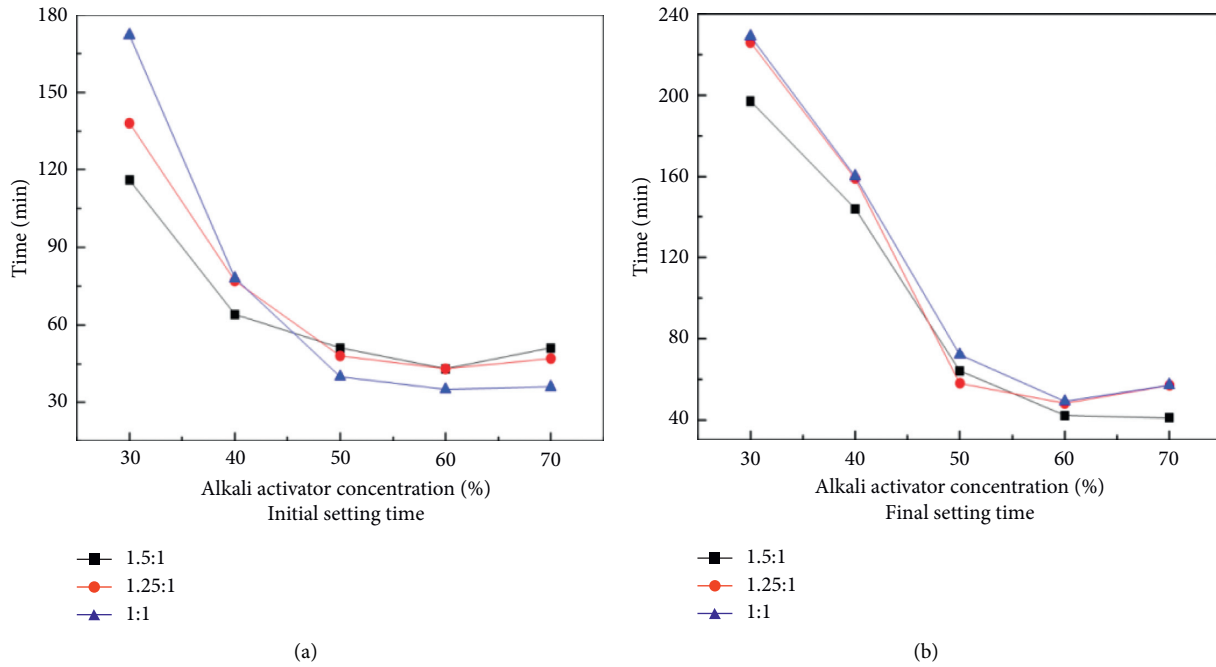


FIGURE 5: Influence of the solid/liquid ratio on the setting time.

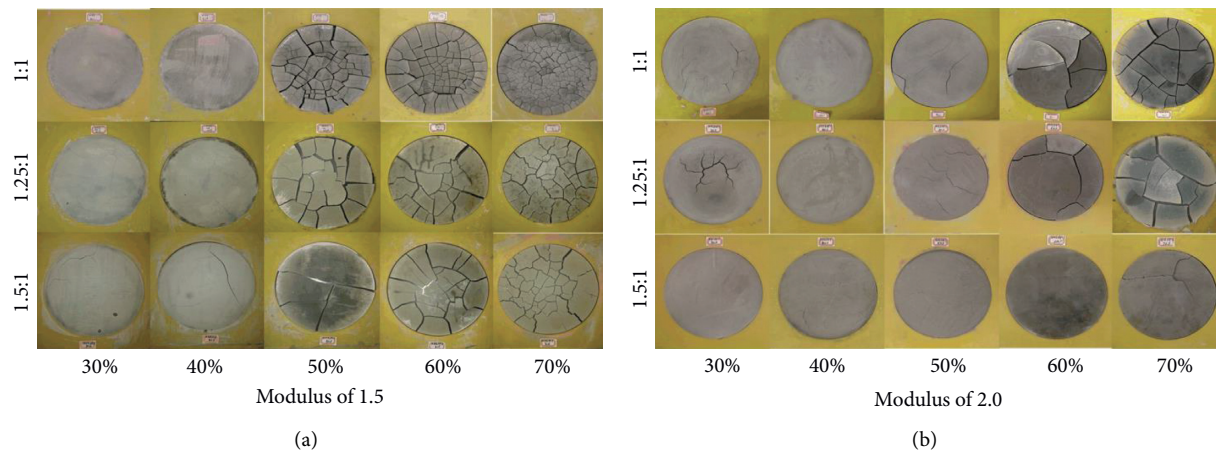


FIGURE 6: Shrinkage morphologies of geopolimer blocks with different sodium silicates.

The activator concentration is the key factor affecting the slag-based geopolimer properties. Samples with an activator concentration mixture ratio of approximately 40% are chosen for further drying shrinkage tests. Figure 8 shows the drying shrinkage of geopolymers with different activator concentrations. The drying shrinkage increases with increasing activator concentration and curing age. In the initial curing stage, the drying shrinkage changes significantly, but the difference between different activator concentrations is less obvious. The drying shrinkage (at 14 d of curing) with 36% and 42% activator concentrations are 108×10^{-5} and 119×10^{-5} , respectively, and the difference is only 11×10^{-5} . After 14 d, the increased shrinkage gradually plateaued, but the drying shrinkage of the samples prepared with different activator concentrations become larger. The drying shrinkage of samples prepared with 42% activator

concentration is the largest (188×10^{-5}) and that with 36% is the smallest (148×10^{-5}) at 56 d.

Figure 9 shows geopolimer drying shrinkage with an activator concentration of 40%. The solid/liquid ratio has little effect on the drying shrinkage in the early stage. After 14 d, the difference between the different solid/liquid ratios gradually increases with increasing solid/liquid ratio. The drying shrinkage rate first increases and subsequently decreases. When the sodium silicate modulus is 1.5, the drying shrinkage increased with increasing solid/liquid ratio. The minimum drying shrinkage of geopolymers with a solid/liquid ratio of 1:1 is 151×10^{-5} at 56 d, and the maximum drying shrinkage with a solid/liquid ratio of 1.5:1 is 171×10^{-5} . The increased solid/liquid ratio causes the activator to fully react with the slag to reduce the free water, water loss rate, and drying shrinkage. Rapid free water evaporation in the early curing

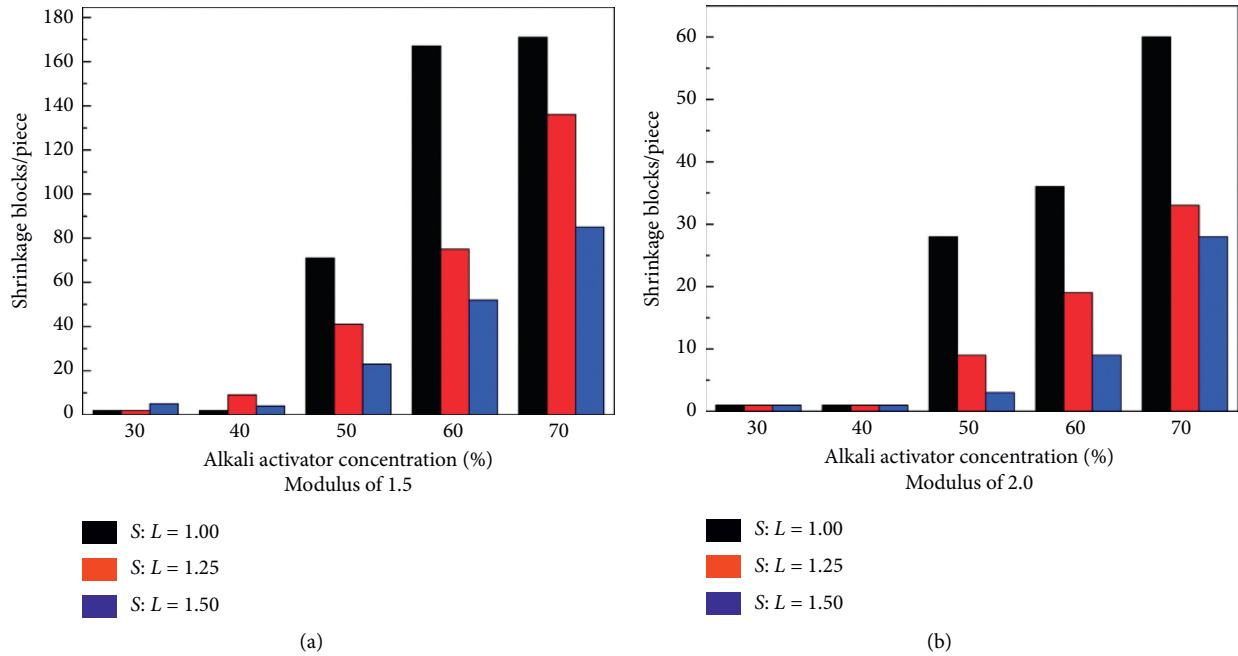


FIGURE 7: Influence of the sodium silicate modulus on the number of shrinking geopolymer blocks.

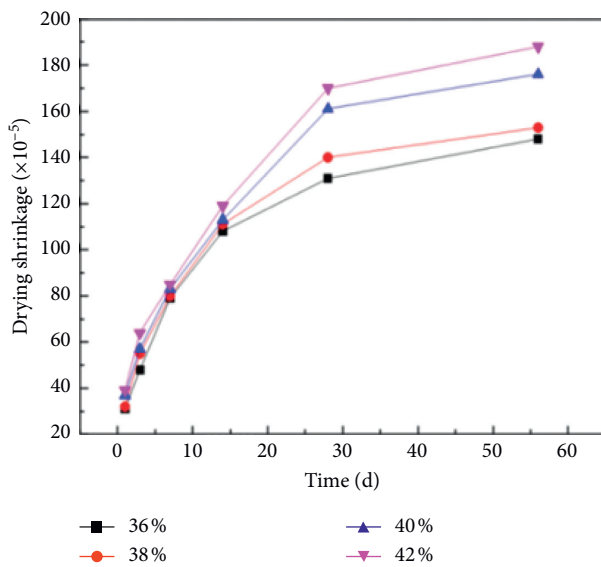


FIGURE 8: Influence of the activator concentration on the drying shrinkage rate of geopolymers.

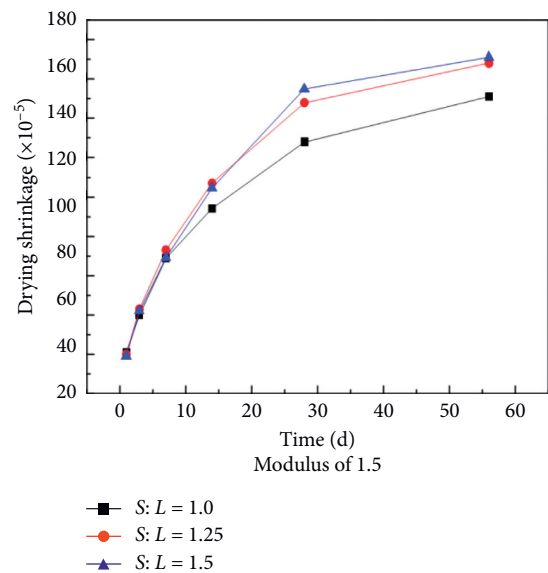


FIGURE 9: Influence of the solid/liquid ratio on the drying shrinkage of geopolymers.

stage increases the porosity of the geopolymers. The geopolymer becomes more stable in the later stage, thereby reducing the rate of drying shrinkage [23].

3.5. *Microstructure Analysis of the Geopolymers.* Figure 10 shows SEM photos of geopolymers after 28 days of curing with different activator concentrations and a solid/liquid ratio of 1.25:1. The slag surface is rough, and there are obvious differences in the microstructure of geopolymers prepared with different activator concentrations. When the activator concentration is 30% and 40%, the geopolymer surface is uneven

and relatively rough. When the activator concentration continues to increase, there are a larger number of cracks distributed inside the sample, which results in stress concentrations and reduces its mechanical properties. It should be noted that with increasing activator concentration, Ca/Si and Si/Al gradually increases. The amount of $[\text{SiO}_4]^{4-}$ and $[\text{AlO}_4]^{5-}$ monomers increases so that the Si-O-Si or Si-O-Al increases and forms more aluminosilicate skeletons, which are conducive to C-A-S-H gel formation [34, 35]. However, the degree of shrinkage cracking increases with increasing activator concentration. Excessive shrinkage leads to specimen damage

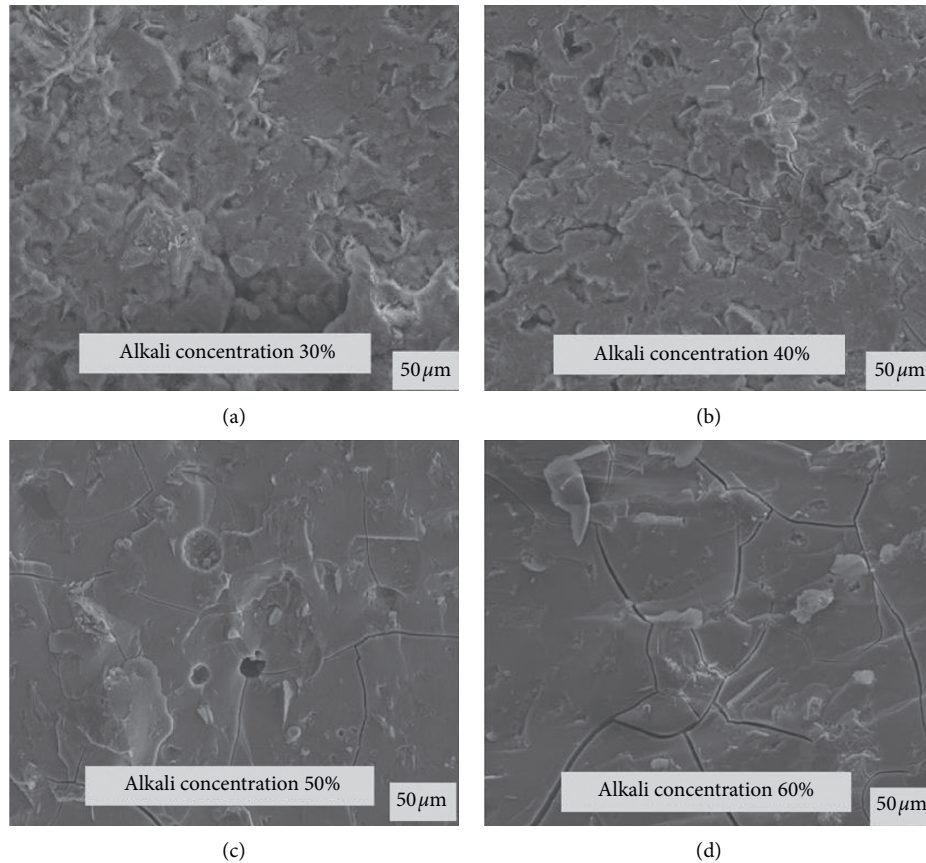


FIGURE 10: SEM images of sections of geopolymer blocks.

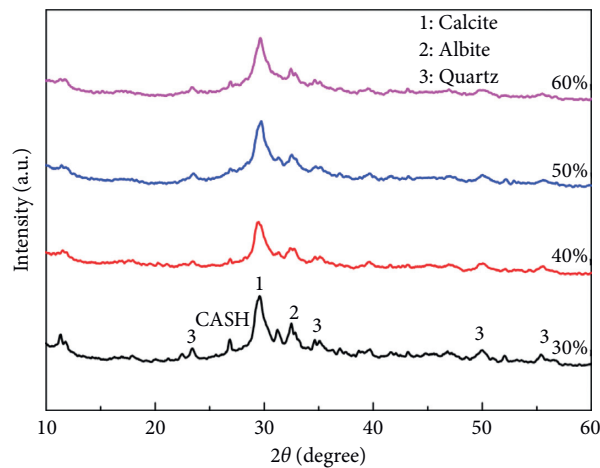


FIGURE 11: XRD pattern of geopolymers.

cracks, so the flexural strength of the geopolymer increases first and then decreases with increasing activator concentration [36].

3.6. Composition Analysis of the Geopolymers

3.6.1. XRD Analysis. Geopolymer X-ray diffraction patterns with a solid/liquid ratio of 1.25:1 after 28 d of curing are presented in Figure 11. The X-ray diffraction patterns of different activator concentrations are almost the same, and

the main crystalline phase is quartz [37]. In addition to quartz, the presence of some other phases such as calcite, albite, and C-A-S-H is observed. The “bulge peak” at approximately 29.6° (2θ) is the result of the short range of the CaO-SiO₂-Al₂O₃-MgO glassy structure of the slag [38]. The peak intensity decreases with increasing activator concentration. The C-A-S-H gel content increases as the reaction proceeded, resulting in a denser geopolymer structure. Therefore, the early compressive strength is higher.

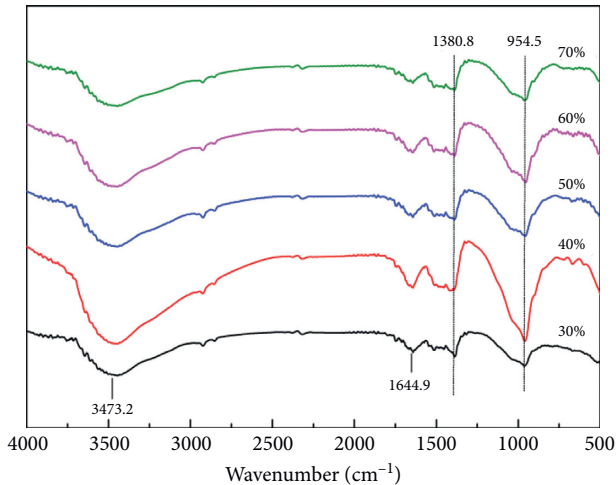


FIGURE 12: FTIR spectra of the geopolymers.

3.6.2. FTIR Analysis. Figure 12 shows the geopolymer FTIR spectra at 28 d under different activator concentrations and a solid/liquid ratio of 1.25:1. The geopolymers exhibit four distinct vibration peaks at 954.5, 1380.8, 1644.9, and 3473.2 cm^{-1} . The -OH stretching and H-O-H bending vibration bands at 3473.2 and 1650.0 cm^{-1} correspond to the chemically bound water molecules in the products. The O-C-O vibration peak at 1380.8 cm^{-1} corresponds to the carbonation products. The vibration peak at 954.3 cm^{-1} is assigned to the vibration of the asymmetric functional group T-O-Si (T refers to Si or Al), corresponding to the silicon tetrahedron of the N-A-S-H gel phase in the product and the silicon tetrahedron structural unit [39, 40]. The peak intensity of T-O-Si first increases when the activator concentration is less than 40% and then decreases. Therefore, 40% activator concentration is expected to promote the polymerization reaction most for the slag.

4. Conclusions

This study reported the effect of different factors on the strength and shrinkage of slag-based geopolymers. The main conclusions are as follows:

- (1) The activator concentration is a key factor affecting slag-based geopolymer performance. The increasing activator concentration promotes the excitation reaction for slags to form products with a higher polymerization.
- (2) The compressive strength of the geopolymers increases with increasing activator concentration. The increase in activator concentration first increases the flexural strength and then decreases, and the maximum is reached when the activator concentration is 40%. The best mechanical properties occurred at 15.90 MPa for the compressive strength and 5.45 MPa for the flexural strength at 28 d when the solid/liquid ratio is 1.25:1.
- (3) The activator concentration has an important influence on the setting time of geopolymers. The

initial and final setting time decreases with increasing activator concentration.

- (4) Geopolymer drying shrinkage increases with increasing activator concentration and decreases with increasing solid/liquid ratio. The alkali solution with a high modulus reduces the early hardening plastic shrinkage of geopolymer pastes but increases later drying shrinkage.

Using other raw materials, such as metakaolin and fly ash, for preparing geopolymers should be further investigated to optimize geopolymer properties. Furthermore, more attention should be paid to geopolymer maintenance to make them more suitable for practical projects.

Data Availability

The data used to support the findings of this study are included within the article.

Conflicts of Interest

The authors declare that they have no conflicts of interest.

Acknowledgments

This work was financially supported by the Natural Science Foundation of China (grant no. 51678534) and the Project of Science and Technology of Henan Transportation Department (grant no. 2018J4). Special thanks are due to Dr. Dan Wang of the Dalian University of Technology for her help with this article.

References

- [1] J. Davidovits, "Geopolymers: inorganic polymeric new materials," *Journal of Thermal Analysis and Calorimetry*, vol. 37, pp. 1633–1656, 2005.
- [2] L. Pelletier, F. Winnefeld, and B. Lothenbach, "The ternary system Portland cement-calcium sulphoaluminate clinker-anhydrite: hydration mechanism and mortar properties," *Cement and Concrete Composites*, vol. 32, no. 7, pp. 497–507, 2010.
- [3] Y. S. Zhang, W. Su, Q. L. Chen, and L. Chen, "Synthesis and heavy metal immobilization behaviors of slag based geopolymer," *Journal of Hazardous Materials*, vol. 143, pp. 206–213, 2007.
- [4] D. V. Reddy, J. B. Edouard, and K. Sobhan, "Durability of fly ash based geopolymer structural concrete in the marine environment," *Journal of Materials in Civil Engineering*, vol. 25, pp. 781–787, 2012.
- [5] C. Suksiripattanapong, S. Horpibulsuk, P. Chanprasert, P. Sukmak, and A. Arulrajah, "Compressive strength development in fly ash geopolymer masonry units manufactured from water treatment sludge," *Construction and Building Materials*, vol. 82, pp. 20–30, 2015.
- [6] X. Guo and X. Pan, "Mechanical properties and mechanisms of fiber reinforced fly ash-steel slag based geopolymer mortar," *Construction and Building Materials*, vol. 179, pp. 633–641, 2018.
- [7] C. D. Atiş, C. Bilim, Ö. Çelik, and O. Karahan, "Influence of activator on the strength and drying shrinkage of alkali-

- activated slag mortar," *Construction and Building Materials*, vol. 23, pp. 548–555, 2007.
- [8] S. Aydın and B. Baradan, "Effect of activator type and content on properties of alkali-activated slag mortars," *Composites Part B: Engineering*, vol. 57, pp. 166–172, 2014.
- [9] L. P. Liu, H. Tan, J. X. Deng, P. Z. Kuang, and Y. He, "Properties and reaction mechanism of blast furnace slag based geopolymer dry power materials," *The Journal of Wuhan University of Technology-Materials Science Edition*, vol. 36, pp. 36–40, 2014, in Chinese.
- [10] H. Cheng, K.-L. Lin, R. Cui, C.-L. Hwang, T.-W. Cheng, and Y.-M. Chang, "Effect of solid-to-liquid ratios on the properties of waste catalyst-metakaolin based geopolymers," *Construction and Building Materials*, vol. 88, pp. 74–83, 2015.
- [11] C. Y. Heah, H. Kamarudin, A. M. Mustafa Al Bakri et al., "Study on solids-to-liquid and alkaline activator ratios on kaolin-based geopolymers," *Construction and Building Materials*, vol. 35, pp. 912–922, 2012.
- [12] H. Bohlooli, A. Nazari, G. Khalaj, M. M. Kaykha, and S. Riahi, "Retracted: experimental investigations and fuzzy logic modeling of compressive strength of geopolymers with seeded fly ash and rice husk bark ash," *Composites Part B: Engineering*, vol. 43, no. 3, pp. 1293–1301, 2012.
- [13] S. Alonso and A. Palomo, "Alkaline activation of metakaolin and calcium hydroxide mixtures: influence of temperature, activator concentration and solids ratio," *Materials Letters*, vol. 47, no. 1–2, pp. 55–62, 2001.
- [14] X.-M. Cui, G.-J. Zheng, Y.-C. Han, F. Su, and J. Zhou, "A study on electrical conductivity of chemosynthetic Al_2O_3 - 2SiO_2 geopolymer materials," *Journal of Power Sources*, vol. 184, no. 2, pp. 652–656, 2008.
- [15] T. W. Cheng and J. P. Chiu, "Fire-resistant geopolymer produced by granulated blast furnace slag," *Minerals Engineering*, vol. 16, no. 3, pp. 205–210, 2003.
- [16] D. Bondar, C. J. Lynsdale, and N. B. Milestone, "Simplified model for prediction of compressive strength of alkali-activated natural pozzolans," *Journal of Materials in Civil Engineering*, vol. 24, 2016.
- [17] S. Samantasingha and S. Prasad Singh, "Fresh and hardened properties of fly ash-slag blended geopolymer paste and mortar," *The International Journal of Concrete Structures and Materials*, vol. 13, pp. 1–12, 2019.
- [18] M. Tuyan, Ö. Andiç-Çakir, and K. Ramyar, "Effect of alkali activator concentration and curing condition on strength and microstructure of waste clay brick powder-based geopolymer," *Composites Part B: Engineering*, vol. 135, pp. 242–252, 2018.
- [19] R. Z. Si, Q. L. Dai, S. C. Guo, and J. Q. Wang, "Mechanical property, nanopore structure and drying shrinkage of metakaolin-based geopolymer with waste glass powder," *Journal of Cleaner Production*, vol. 242, Article ID 118502, 2019.
- [20] I. Khan, T. Xu, A. Castel, R. I. Gilbert, and M. Babae, "Risk of early age cracking in geopolymer concrete due to restrained shrinkage," *Construction and Building Materials*, vol. 229, Article ID 116840, 2019.
- [21] D. S. Perera, O. Uchida, E. R. Vance, and K. S. Finnie, "Influence of curing schedule on the integrity of geopolymers," *Journal of Materials Science*, vol. 42, no. 9, pp. 3099–3106, 2007.
- [22] R. J. Thomas, D. Lezama, and S. Peethamparan, "On drying shrinkage in alkali-activated concrete: improving dimensional stability by aging or heat-curing," *Cement and Concrete Research*, vol. 91, 2017.
- [23] T. Yang, H. Zhu, and Z. Zhang, "Influence of fly ash on the pore structure and shrinkage characteristics of metakaolin-based geopolymer pastes and mortars," *Construction and Building Materials*, vol. 153, pp. 284–293, 2017.
- [24] P. S. Deb, P. Nath, and P. K. Sarker, "Drying shrinkage of slag blended fly ash geopolymer concrete cured at room temperature," *Procedia Engineering*, vol. 125, pp. 594–600, 2015.
- [25] C. Ridditirud, P. Chindaprasirt, and K. Pimraksa, "Factors affecting the shrinkage of fly ash geopolymers," *International Journal of Minerals, Metallurgy, and Materials*, vol. 18, no. 1, pp. 100–104, 2011.
- [26] K. Mermerdaş, Z. Algin, and Ş. Ekmen, "Experimental assessment and optimization of mix parameters of fly ash-based lightweight geopolymer mortar with respect to shrinkage and strength," *Journal of Building Engineering*, vol. 31, Article ID 101351, 2020.
- [27] Y. Ling, K. Wang, and C. Fu, "Shrinkage behavior of fly ash based geopolymer pastes with and without shrinkage reducing admixture," *Cement and Concrete Composites*, vol. 98, pp. 74–82, 2019.
- [28] P. Kamhangrittirong, P. Suwanvitaya, W. Witayakul, P. Suwanvitaya, and C. Chindaprasirt, "Factors influence on shrinkage of high calcium fly ash geopolymer paste," *Advanced Materials Research*, vol. 610, pp. 2275–2281, 2013.
- [29] D. Shen, C. Wen, J. Kang, H. Shi, and Z. Xu, "Early-age stress relaxation and cracking potential of high-strength concrete reinforced with Barchip fiber," *Construction and Building Materials*, vol. 258, Article ID 119538, 2020.
- [30] J. I. Escalante-García, A. V. Gorokhovskiy, G. Mendoza, and A. F. Fuentes, "Effect of geothermal waste on strength and microstructure of alkali-activated slag cement mortars," *Cement and Concrete Research*, vol. 33, pp. 1567–1574, 2003.
- [31] H. Peng, S. L. Li, C. S. Cai, X. F. Zhang, and C. Cui, "Study on effect of mix and curing conditions on the mechanical properties and setting time of metakaolin-based geopolymer," *Bulletin of the Chinese Ceramic Society*, vol. 33, pp. 2809–2817, 2014, in Chinese.
- [32] L. Weng and K. Sagoe-Crentsil, "Dissolution processes, hydrolysis and condensation reactions during geopolymer synthesis: part I-Low Si/Al ratio systems," *Journal of Materials Science*, vol. 42, no. 9, pp. 2997–3006, 2007.
- [33] S. Kumar, R. Kumar, and S. P. Mehrotra, "Influence of granulated blast furnace slag on the reaction, structure and properties of fly ash based geopolymer," *Journal of Materials Science*, vol. 45, no. 3, pp. 607–615, 2010.
- [34] C. K. Yip, G. C. Lukey, and J. S. J. Deventer, "The coexistence of geopolymeric gel and calcium silicate hydrate at the early stage of alkaline activation," *Cement and Concrete Research*, vol. 35, pp. 1688–1697, 2004.
- [35] C. K. Yip, G. C. Lukey, J. L. Provis, and J. S. J. van Deventer, "Effect of calcium silicate sources on geopolymerisation," *Cement and Concrete Research*, vol. 38, no. 4, pp. 554–564, 2008.
- [36] B. S. Gebregziabihier, R. Thomas, and S. Peethamparan, "Very early-age reaction kinetics and microstructural development in alkali-activated slag," *Cement and Concrete Composites*, vol. 55, pp. 91–102, 2015.
- [37] K. Gkhan, "The effect of high temperature on the design of blast furnace slag and coarse fly ash-based geopolymer mortar," *Composites Part B: Engineering*, vol. 92, pp. 9–18, 2016.
- [38] S. Song and H. M. Jennings, "Pore solution chemistry of alkali-activated ground granulated blast-furnace slag," *Cement and Concrete Research*, vol. 29, no. 2, pp. 159–170, 1999.

- [39] A. Vásquez, V. Cárdenas, R. A. Robayo, and R. M. de Gutiérrez, "Geopolymer based on concrete demolition waste," *Advanced Powder Technology*, vol. 27, no. 4, pp. 1173–1179, 2016.
- [40] R. A. Gado, M. Hebda, M. Łach, and J. Mikula, "Alkali activation of waste clay bricks: influence of the silica modulus, $\text{SiO}_2/\text{Na}_2\text{O}$, $\text{H}_2\text{O}/\text{Na}_2\text{O}$ molar ratio, and liquid/solid ratio," *Materials*, vol. 13, no. 2, p. 383, 2020.

Research Article

A BP Neural Network Method for Grade Classification of Loose Damage in Semirigid Pavement Bases

Bei Zhang , Jianyang Liu, Yanhui Zhong , Xiaolong Li , Meimei Hao , Xiao Li, Xu Zhang, and Xiaoliang Wang

College of Water Conservancy and Engineering, Zhengzhou University, Zhengzhou 450001, China

Correspondence should be addressed to Yanhui Zhong; zhong_yanhui@163.com and Xiaolong Li; wenuandeshang@hotmail.com

Received 9 December 2020; Revised 7 January 2021; Accepted 28 January 2021; Published 10 February 2021

Academic Editor: Di Wang

Copyright © 2021 Bei Zhang et al. This is an open access article distributed under the Creative Commons Attribution License, which permits unrestricted use, distribution, and reproduction in any medium, provided the original work is properly cited.

This study aims to address the problem that loose damage of the pavement base course cannot currently be quantitatively identified, and thus the classification and recognition of the extent of looseness mainly rely on empirical judgments. Based on the finite-difference time-domain (FDTD) method, a backpropagation (BP) neural network identification method for loose damage of a semirigid base is presented. The FDTD method is used to simulate a semirigid base road model numerically with different degrees of looseness, and the eigenvalue parameters for recognition of the presence and extent of the looseness of the base layer are obtained. Then, a BP neural network identification method is used to classify and identify the loose damage of the base course. The results show that the classification and recognition of simulated electromagnetic waves have an accuracy of over 90%; the classification and recognition of radar data from an actual project have a recognition accuracy of over 80%. The good agreement between the classification and recognition results for the simulated data and measured data verifies the feasibility of the classification and recognition method, which can provide a new method for the use of ground-penetrating radar to detect loose damage and the extent of looseness in the base.

1. Introduction

A semirigid base has a high-capacity strength, good integrity, low cost, local materials, and excellent mechanical and road performance; therefore, these are widely used in road engineering for pavement bases and subbases [1]. Accordingly, more than 90% of the expressways under construction or completed in China are composed of semirigid base asphalt pavement [2, 3]. The popularization and application of semirigid bases has played an important role in the construction of expressways and economic development in China. According to the Chinese road construction specifications, the service life of expressways and first-class highways is fifteen years, while that of secondary roads is twelve years. However, owing to the substandard design and construction of some roads, as well as the rapid increase in heavy-load traffic and traffic volumes, many roads exhibit damage comprising different degrees of looseness before

their service life is reached. Under the influence of loads and environmental changes, structural shrinkage will occur in loose parts of the semirigid base, which will cause crack damage and eventually lead to reflection cracks in the pavement. The cracked pavement will directly affect the quality and service life of the road [4–6]. Therefore, it is necessary to detect damage in the semirigid base before the pavement is severely damaged. In the early stage of road detection, core sampling drilling is often used [7, 8]; however, core sampling drilling is destructive to the road structure. As a result, it is difficult to carry out a large number of sampling inspections, and it is difficult to reflect the overall quality of the road structure using only a small number of results. As a nondestructive testing method, ground-penetrating radar (GPR) [9–11] has the advantages of portability, high detection efficiency, high resolution, and strong anti-interference ability compared with ultrasonic testing [12, 13], core sampling drilling, and infrared imaging

[14]. Chahine et al. proposed an algorithm for ultrathin layer thickness estimation based on independent component analysis. The experimental results using simulation data showed that the relative error of the ultrathin layer thickness estimation was 0.9% when $B\Delta\tau = 0.45$ (where B is the bandwidth of the radar system, and $\Delta\tau$ is the minimum time delay that the system can identify); the signal-to-noise ratio was 0.35 Db [15]. Cardarelli used GPR to detect the loose area of a tunnel in combination with the seismic tomography method [16]. Karem et al. used GPR to detect buried objects, and the scale-invariant feature transform (SIFT) algorithm was applied to extract the features of each location. The results showed that the introduction of the SIFT algorithm improved the detection accuracy [17]. Tong et al. applied convolutional neural networks (CNNs) to recognize and locate concealed cracks automatically based on GPR images [18, 19]. Cubero-Fernandez et al. proposed an effective method for both pavement crack detection and classification [20]. Soola et al. combined GPR technology with infrared images to detect the depth characteristics and origin of asphalt pavement cracks. Although this detection method can determine the location and depth of subgrade cracks, its measurement accuracy is relatively poor [21]. Ditommaso et al. used GPR to analyze the problem of water pipe rupture in road structures and adopted a new operation method, the intensive matrix, to locate underground plastic drainage pipes while maintaining the original state and environmental characteristics of the system. The research results showed that the multiagent test could accurately locate the position of the plastic pipe [22]. Xu et al. used the GPR with 300 MHz shielded antenna to detect the cracks in the sand gravel subgrade. Through the radar image, the crack location and crack length can be accurately located, and the crack length can be calculated [23]. Zhang et al. also studied GPR technology and proposed a set of road damage identification methods based on GPR and a falling weight deflectometer. This method could accurately determine the location of road damage through nondestructive testing and evaluate various indicators of the road state [24, 25].

To date, GPR has been widely used to study road voids, thickness, cracks, etc.; however, little research has been conducted on the loose damage of the base. Loose damage can only be analyzed qualitatively, and the extent of the looseness of the base cannot be classified. Therefore, in this study, starting from the detection and determination of the porosity of areas subject to loose damage, the finite difference time-domain (FDTD) method was used to simulate a semirigid base road model with different degrees of looseness. Then, the GPR signal obtained from the forward simulation was numerically counted to extract the attributes related to the extent of looseness of the base course in the simulation signal, which was used to obtain the characteristics for identification of Eigenvalue parameters related to the extent of looseness of the base course. Then, the back-propagation (BP) neural network identification method was used to classify and identify the loose damage of the base course, and the degree of loose damage in the base course was evaluated. This method can reduce the dependence of interpretation of GPR detection images on empirical

judgment and provide a new method for the use of GPR to detect the presence and degree of loose damage.

2. FDTD-Based Forward Simulation of Loose Damage of the Base

2.1. Road Structure Model. Based on the design scheme of asphalt concrete pavement, the forward model is composed of four layers: the asphalt pavement, semirigid base, subbase, and earth subgrade layer. The length of the model is 2 m and the depth is 1 m. The dimensions of each road structural layer are shown in Figure 1; ϵ_r is the dielectric constant, and σ is the conductivity. The surface layer is 0.18 m deep, the base is 0.38 m deep, the subbase is 0.2 m deep, and the soil foundation is below.

Cement-stabilized macadam is one of the most commonly used materials for semirigid base courses. It is a composite material whose dielectric properties are closely related to its composition. According to the volume mixing dielectric model of cement mixtures, the dielectric constant and mention rate of each component of the cement mixture are the main factors affecting the dielectric properties of the material. In the composition of the cement mixture, the higher the dielectric constant of each component material, the larger the volume occupancy rate and the greater the dielectric property of the composite material. The following equation is the root mean square model expression for the dielectric constant of the cement concrete three-phase composite material:

$$\epsilon_r = \left(V_a (\epsilon_a)^{1/3} + V_b (\epsilon_b)^{1/3} + V_c (\epsilon_c)^{1/3} \right)^3, \quad (1)$$

where ϵ_r is the dielectric constant of the composites; ϵ_a , ϵ_b , and ϵ_c are the dielectric constants of each material; and V_a , V_b , V_c are the volume ratios of each material.

When the proportion of air in the cement-stabilized macadam exceeds the design index, looseness damage will occur in the base course. At this time, the dielectric properties of the damaged parts are different from those of the surrounding materials, which allows the semirigid base to be detected and identified by GPR. In this study, the proportion of air in the base is varied to simulate the change in the degree of looseness of the base and investigate the influence of different degrees of loose damage on the electromagnetic wave numerical simulation.

2.2. FDTD Forward Modeling Theory. The FDTD method is an important numerical method for calculating electromagnetic properties [26, 27]. Compared with the moment method and finite element method, the FDTD method has obvious advantages in terms of accuracy and efficiency. In this study, an FDTD code is written in a MATLAB environment using the FDTD method. A two-dimensional forward simulation of the electromagnetic wave propagation of a semirigid base pavement structure with or without damage is realized, and the influence of loose damage on radar electromagnetic wave propagation is studied.

Assuming that the simulated medium is homogeneous and isotropic, the propagation of high-frequency

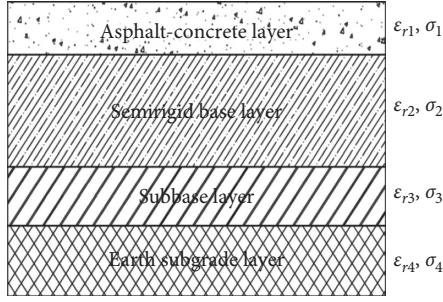


FIGURE 1: Schematic diagram of the pavement structure.

electromagnetic waves in a three-dimensional medium satisfies the following Maxwell equations [28, 29]:

$$\nabla \times H = \varepsilon \frac{\partial E}{\partial t} + \sigma E, \quad (2)$$

$$\nabla \times E = -\mu \frac{\partial H}{\partial t} - \sigma_m H, \quad (3)$$

where E is the electric field intensity (V/m), H is the magnetic field strength (A/m), ε is the dielectric constant (F/m), μ is the permeability (H/m), σ is the conductivity (S/m), and σ_m is the permeability ($1/m$).

In the two-dimensional FDTD scheme, assuming that all of the physical quantities are independent of the z -direction, i.e., the two-dimensional expansion becomes an independent transverse magnetic (TM) and transverse wave (TE), the following equations can be obtained from equations (2) and (3):

$$\text{TM} : \begin{cases} \frac{\partial E_z}{\partial y} = -\mu \frac{\partial H_x}{\partial t}, \\ \frac{\partial E_z}{\partial x} = \mu \frac{\partial H_y}{\partial t}, \\ \frac{\partial H_y}{\partial x} - \frac{\partial H_x}{\partial y} = \varepsilon \frac{\partial E_z}{\partial t} + \sigma E_x, \end{cases} \quad (4)$$

$$\text{TE} : \begin{cases} \frac{\partial H_z}{\partial x} = \varepsilon \frac{\partial E_y}{\partial t} + \sigma E_y, \\ \frac{\partial H_z}{\partial y} = \varepsilon \frac{\partial E_x}{\partial t} + \sigma E_x, \\ \frac{\partial E_y}{\partial x} - \frac{\partial E_x}{\partial y} = -\mu \frac{\partial H_z}{\partial t}. \end{cases}$$

Obviously, TM wave only has E component. Since GPR only records E component of horizontal electric field, then we deduce TM wave. Table 1 shows the values of each component of E and H the time step of spatial nodes in the two-dimensional FDTD difference equation.

For equation (3), when $E_x = E_y = H_z = 0$, the two-dimensional TM wave FDTD equation can be obtained as follows:

$$H_x^{n+1/2}\left(i, j + \frac{1}{2}\right) = H_x^{n-1/2}\left(i, j + \frac{1}{2}\right) - CP(m) \frac{E_z^n(i, j+1) - E_z^n(i, j)}{\Delta y},$$

$$H_y^{n+1/2}\left(i + \frac{1}{2}, j\right) = H_y^{n-1/2}\left(i + \frac{1}{2}, j\right) - CP(m) \frac{E_z^n(i+1, j) - E_z^n(i, j)}{\Delta x},$$

$$E_z^n(i, j) = CA(m)E_z^n(i, j) + CB(m) \times \left[\frac{H_y^{n+1/2}(i+1/2, j)}{\Delta x} - \frac{H_y^{n+1/2}(i-1/2, j)}{\Delta x} - \frac{H_x^{n+1/2}(i, j+1/2)}{\Delta y} + \frac{H_x^{n+1/2}(i, j-1/2)}{\Delta y} \right], \quad (5)$$

where $CA(m) = 1 - \sigma(m)\Delta t/2\varepsilon(m)/1 + \sigma(m)\Delta t/2\varepsilon(m)$
 $CB(m) = \Delta t/\varepsilon(m)/1 + \sigma(m)\Delta t/2\varepsilon(m)$, and $CP(m) = \Delta t/\mu(m)$.

2.3. Forward Modeling. GPR echo signals often have many different characteristics, such as varying frequency, amplitude, and phase. These characteristics reflect the characteristics of echo signals from different aspects and thus reflect the characteristics of underground targets. For loose damage of a semirigid base, because the electromagnetic properties of the damage and its surrounding media are quite different, the echo signal of the damage must differ from that in other places, and its frequency, amplitude, and

phase must also have unique properties. The different performance and characteristics of these features reflect the nature of the underground target from different angles, which provides the necessary conditions for echo signal recognition. To study the influence of damage with different extents of looseness on the electromagnetic wave numerical values, the extent of looseness in the base course was varied by adjusting the proportion of air in the base course. The porosity in the loose part was increased by 1% to a maximum of 30%. A total of 30 loose models were established. A selection of these models and their corresponding forward simulation maps are shown in Figures 2 and 3.

In this paper, different porosity is used to represent different loose degree of base. In the simulation of models

TABLE 1: Node positions of the TM wave components.

Electromagnetic field component		Spatial component sampling		Time axis t
		x	y	
TM	E_z	i	j	n
	H_x	i	$j + 1/2$	$n + 1/2$
	H_y	$i + 1/2$	j	$n + 1/2$

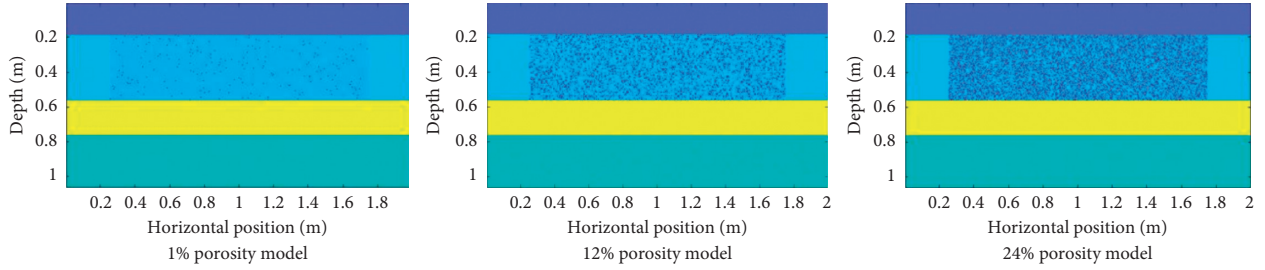


FIGURE 2: Model diagram of different porosity.

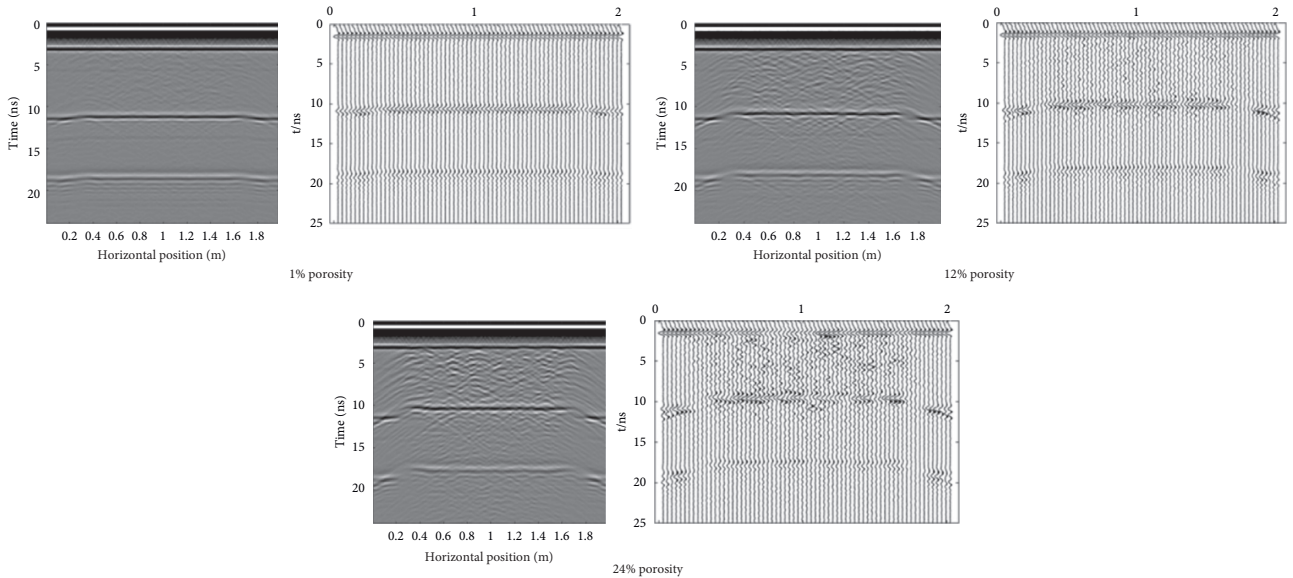


FIGURE 3: Simulation and reflection spectra for different porosity.

with different looseness degrees of the base course, owing to the air dielectric constant being 1, the dielectric constant of base material is between 9 and 12. With an increasing degree of looseness, the proportion of air in base increases gradually, so the composite dielectric constant of base material decreases with the increase of loose degree of base. As a result, the overall dielectric properties of the base material change, and the complexity of the simulation spectra corresponding to different looseness extents is different. When the base is slightly loose, the simulation map exhibits a slight change, but it is roughly consistent with that for the intact road structure. When the extent of the base looseness is severe, the loose damage appears as a discontinuity of the same phase axis, diffraction, and a disordered waveform. According to the relationship between the dielectric properties and electromagnetic wave propagation, different extents of looseness correspond to different electromagnetic

wave propagation processes, which provides samples for further classification and recognition.

2.4. Radar Signal Eigenvalue Extraction. Extraction of attributes of the GPR for the base with varying degrees of looseness is a precondition for signal classification and recognition. By preprocessing the identified GPR data, the radar signal features reflecting the extent of looseness of the base course can be extracted. By establishing the relationship between the extent of looseness of the base course and the time-domain attributes of the GPR signals, radar attributes that have a strong correlation with the extent of looseness of the base course can be selected as characteristic values for classification and recognition, and the extent of looseness of the base course can be classified and recognized. Figure 4 shows the radar signal waveforms of different looseness

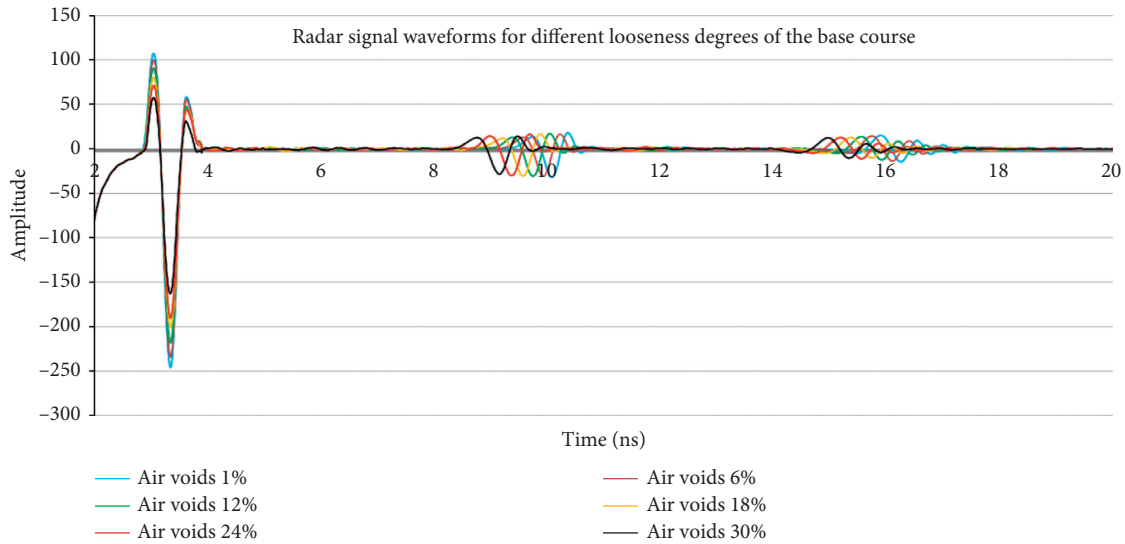


FIGURE 4: Radar signal waveforms for different looseness degrees of the base course.

degrees in the base course. A time-domain statistical analysis is used to process the GPR signal data, and waveform, amplitude, and other related information of the GPR signal in the time domain are obtained, such as the peak amplitude, trough amplitude, overall average peak amplitude, root mean square amplitude, and other time-domain characteristics.

It can be seen that the corresponding radar data also change with the increase in porosity, i.e., the looseness extent. For the models with different looseness extents, the ground coupling wave remains basically the same. With an increasing extent of looseness of the base, the proportion of air in the base area increases, and the composite dielectric constant of the material in the loose area of the base decreases. Because the dielectric constant of the base material is greater than that of the surface material, the dielectric constant gap between the base and the surface decreases with an increasing extent of looseness of the base course. As a result, the reflected wave amplitude decreases with the increase in looseness. The time delay, Δt , decreases with an increasing extent of looseness when the medium thickness is constant.

Through the time-domain attribute analysis of the radar signal after mean processing, nine time-domain eigenvalues of the signal amplitude, such as the average absolute value, variance, root mean square, standard deviation, waveform factor, peak factor, and pulse factor, are shown to have good correlations with the extent of looseness of the base course. As shown in Figure 5, the correlation between the nine eigenvalues and the extent of looseness is good, and thus these can be used for radar signal classification and recognition.

3. Identification Method for the Looseness Degree of a Semirigid Base Using a BP Neural Network

Neural networks have good learning, self-adaptive, associative memory, fault-tolerant, classification, and recognition abilities as well as good robustness [30]. BP neural

networks have significant advantages in numerical classification and recognition. Therefore, the BP neural network method is selected to realize the classification and recognition of the extent of looseness of the base course. The extracted radar signal numerical characteristics related to the extent of looseness of the base course are used as the input to the BP neural network, and the classification of the extent of looseness of the base course is ultimately output.

3.1. Sample Training. Among the 18,000 samples obtained (These 18,000 samples are obtained from the electromagnetic wave numerical simulation results in Section 2.3. The simulated radar signals are processed by time-domain analysis and the characteristic values related to the looseness of the base are extracted.), 80% are used as the training sample set and the remaining 20% are used as test data. For the training samples of the neural network, each input corresponds to an output. Suppose there is a known training set that contains h training samples, and there are h groups of inputs and outputs. Then one group of samples is $X = (x_1, x_2, \dots, x_h), Y = (y_1, y_2, \dots, y_h)$; the number of neural units in the hidden layer is p , and the number of neural units in the output layer is q . The steps of the BP neural network algorithm are as follows:

- (1) *Network Initialization.* The weights of each link are assigned to random numbers with intervals $(-1, 1)$, and the calculation precision and training times are given.
- (2) *Determination of the Training Dataset.* Some training samples are listed in Table 2. A set of samples, $X = (x_1, x_2, \dots, x_h)$, are entered, and the corresponding $Y = (y_1, y_2, \dots, y_h)$ is provided to the neural network.
- (3) *Forward Propagation of the Working Signal.* Suppose X_i^k is the sum of inputs of neuron i in layer k , then Y_i^k is the output, and the weights from the layer $k - 1$

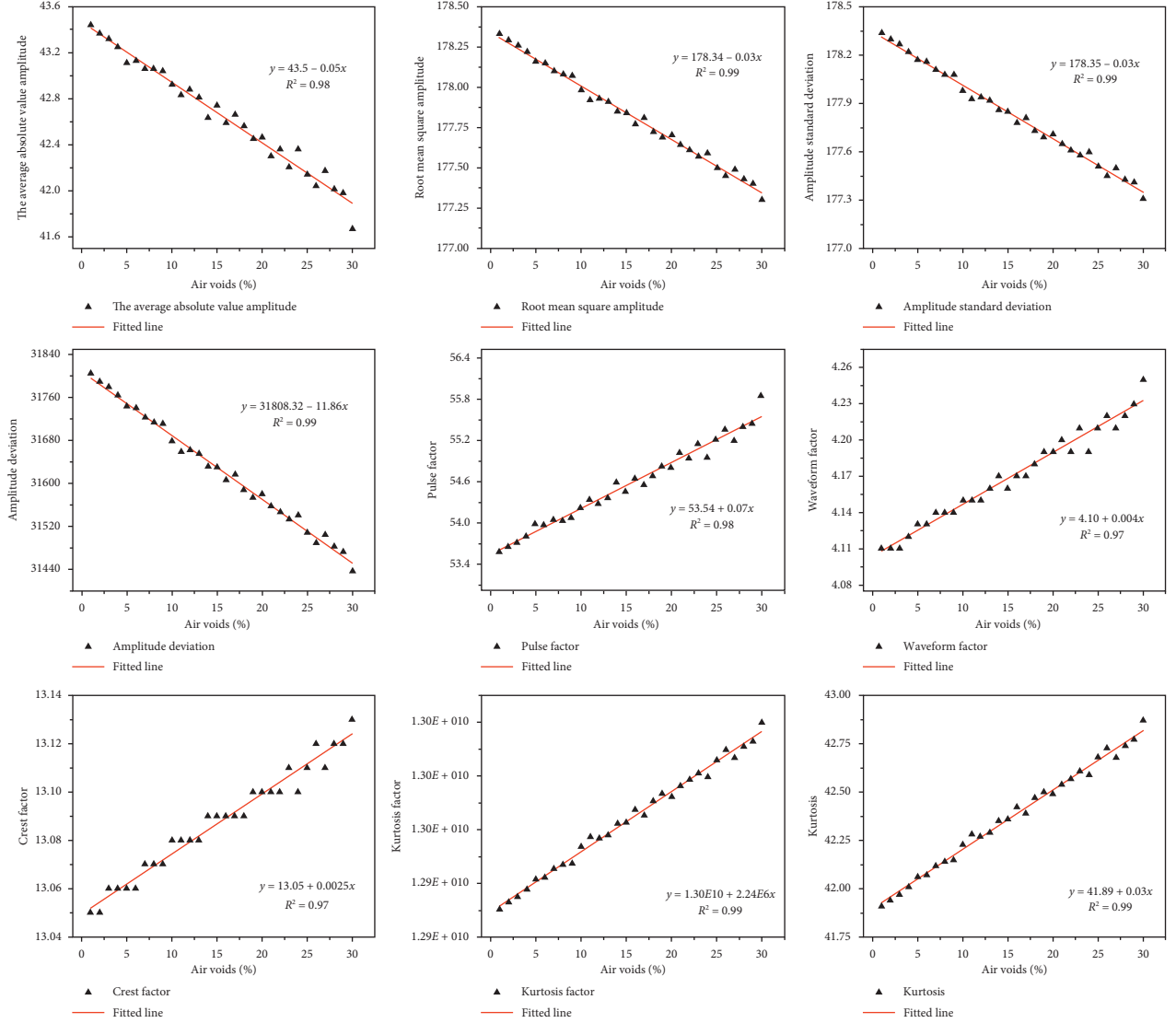


FIGURE 5: Broken line diagrams of the radar signal time-domain eigenvalues versus the looseness degree.

neurons, j , to layer k neurons, i , are w_{ij} and have the following functional relationship:

$$\begin{cases} Y_i^k = f(X_i^k), \\ X_i^k = \sum_{j=1}^{n+1} w_{ij} Y_j^{k-1}, \end{cases} \quad (6)$$

where f is the activation function. Generally, f is taken as an asymmetric sigmoid function as follows:

$$f(X_i^k) = \frac{1}{1 + \exp(-X_i^k)}. \quad (7)$$

(4) *Backpropagation of the Error Signal.* If the output layer is layer m , the actual output of the i th neuron in the output layer is Y_i^m , and the corresponding learning signal is Y_i . The error function, e , is defined as follows:

$$e = \frac{1}{2} \sum_i (Y_i^m - Y_i)^2. \quad (8)$$

The definition of d_i^k describes the error function, e , with respect to the partial derivative of Y_i^m . Thus, the following can be inferred:

when $k = m$,

$$d_i^m = Y_i^m (1 - Y_i^m) (Y_i^m - Y_i), \quad (9)$$

$k < m$,

$$d_i^k = Y_i^k (1 - Y_i^k) \sum_1 w_{1i} d_1^{k+1}.$$

(5) *Correction of the Weights.* Let the weight of a certain learning be modified as Δw_{ij} . Then, considering the correlation between the two learning tasks, the weight modification can be defined as follows:

TABLE 2: Part of the training sample set.

Sample	Attributes								
	Average absolute value amplitude	Root mean square amplitude	Amplitude standard deviation	Amplitude deviation	Pulse factor	Waveform factor	Crest factor	Kurtosis factor	Kurtosis
1	45.83	178.68	177.65	31656.78	4.33	12.84	1.30 E + 10	55.73	43.04
2	41.38	174.03	177.19	31568.74	4.23	12.92	1.29 E + 10	56.04	44.90
3	38.21	176.94	175.61	31650.92	4.15	12.93	1.30 E + 10	57.22	42.39
4	41.29	176.45	176.54	31425.52	4.28	12.54	1.29 E + 10	54.66	41.58
5	39.49	177.28	179.34	31338.37	3.86	13.13	1.30 E + 10	54.01	40.45
6	42.46	178.08	178.72	31815.35	4.31	12.77	1.30 E + 10	51.66	40.96
7	43.04	174.59	177.12	31508.84	4.13	13.35	1.30 E + 10	54.16	41.12
8	42.05	178.87	175.06	31373.60	3.86	12.56	1.29 E + 10	51.19	43.30
9	39.89	176.52	175.89	31836.04	4.38	12.90	1.29 E + 10	56.91	40.16
10	45.72	177.35	175.16	31386.90	3.97	13.18	1.30 E + 10	54.73	41.29

$$\nabla w_{ij}(t+1) = \nabla w_{ij}(t) - \nu \cdot U_{ij}, \quad (10)$$

where $\nabla w_{ij}(t+1)$ and $\nabla w_{ij}(t)$ are the weights in neuron i of layer j after $(t+1)$ th and (t) th epoch; ν is learning rate; U_{ij} is the derivative of error e w.r.t. w_{ij} in $(t+1)$ th epoch, which is the same as d_i^k of Eqs.

- (6) The iteration, E , is calculated to determine whether the training target is achieved. If the target has been reached or the iteration times have reached the upper limit, the calculation is stopped. If the target is not reached, the process returns to Step 2 for cycle execution. After training, the neural network can be tested using the test sample set, and the grid parameters can be modified continuously according to the test results.

3.2. Test Results. The 30 looseness extents considered are divided into five looseness types, which is convenient for classification and recognition using the neural network. Table 3 lists the classifications of the extent of looseness.

A total of 25 data points were selected as a group of test samples, and 720 tests were carried out; the accuracy was greater than 90%. The feasibility of the classification and recognition method for the extent of looseness of the base course was thus verified. Table 4 summarizes the results of one of the tests. The results include the number of samples, actual category of samples, and type of judgment. At the same time, correct and incorrect judgments are also given. It can be seen from the test results that there were three identification errors, but the judgment categories were similar to the actual categories, and there were no identification errors with significant differences.

4. Engineering Case Verification

4.1. Project Overview. To further verify the feasibility of the BP neural network based on GPR technology for the classification and recognition of loose damage in the base course, detection of a road in Zhengzhou city is analyzed using radar detection software in this study. The road

TABLE 3: Classification of the extent of looseness.

Air voids	≤6%	6%–12%	12%–18%	18%–24%	≥24%
Category	I	II	III	IV	V

structure is shown in Table 5. The ground-penetrating radar equipment and road site photos are shown in Figure 6.

The two-dimensional GPR used in this inspection is the GER series from the Qingdao Zhongdian Zhongyi Company. To ensure the accuracy of the detection results, it is necessary to set the antenna center frequency, measuring point spacing, sampling time window, and other measurement parameters before operating the GPR. The frequency of the GPR center antenna is determined based on the measured target depth. In general, the resolution increases with an increase in the radar antenna frequency, while the detection depth decreases. To ensure that the GPR can satisfy the detection requirements, the antenna center frequency should be reduced as much as possible while still meeting the resolution requirements to obtain the radar reflection signal at a deeper position. The maximum detection range of the GPR is 3.0 m, and thus the center antenna frequency is 400 MHz, and a time window of 80 ns is used for detection with a 3–5-point gain.

For the detection of standard sections, the survey lines are arranged along the direction of the carriageway parallel to the centerline of the lane; the influence of terrain and other interference sources is avoided as much as possible. For the detection of abnormal parts, the survey lines can be appropriately encrypted or arranged in a network. When hidden damage is detected under the road surface, two types of antennas with different frequencies should be employed simultaneously for testing to ensure accurate identification of the damaged parts. The layout of the survey lines is shown in Figure 7.

4.2. Analysis and Verification of the Ground-Penetrating Radar Test Data. Through static correction, background filtering, gain adjustment, interference wave elimination, time–depth conversion, and data visualization processing of the GPR data files, a detection Atlas of the GPR is obtained. For the areas with loose damage in the road base, core drilling sampling is carried out to determine the degree of looseness, and radar data are obtained in combination with

TABLE 4: Test results.

Sample number	Actual category	Judgment category	True/false	Air voids
1	I	I	True	<6%
2	I	I	True	<6%
3	I	I	True	<6%
4	I	I	True	<6%
5	I	I	True	<6%
6	II	II	True	6%–12%
7	II	II	True	6%–12%
8	II	II	True	6%–12%
9	II	II	True	6%–12%
10	II	III	False	12%–18%
11	III	III	True	12%–18%
12	III	III	True	12%–18%
13	III	III	True	12%–18%
14	III	III	True	12%–18%
15	III	III	True	12%–18%
16	IV	IV	True	18%–24%
17	IV	IV	True	18%–24%
18	IV	III	False	12%–18%
19	IV	IV	True	18%–24%
20	IV	IV	True	18%–24%
21	V	V	True	>24%
22	V	V	True	>24%
23	V	V	True	>24%
24	V	V	True	>24%
25	V	IV	False	18%–24%

TABLE 5: Road structure drawing.

Name of structural layer	Depth (cm)	Dielectric constant	Conductivity (mS/m)
AC-13C	4		
AC-20C	6	4–9	0.005
ATB-25	12		
Cement-stabilized macadam	34	9–14	0.05
Low-dose cement-stabilized macadam	16	9–14	0.05



FIGURE 6: Road site photos.

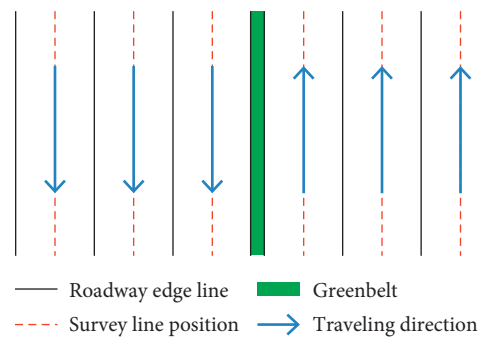


FIGURE 7: Layout of the survey lines.

data extraction software. The loose damage types are divided into categories of no loose damage, moderate loose damage, and severe loose damage. Representative GPR detection maps are shown in Figures 8 and 9 .

It can be seen from the actual radar maps in Figures 8 and 9 that the propagation of electromagnetic waves is affected by the loose road structure. Owing to the different degrees of looseness, the radar data will change to varying extents. Comparing the actual maps of severe loose damage and moderate loose damage, the radar-measured map of

severe loose damage exhibits a more complex electromagnetic wave pattern. In the actual road, the reflection of the loose area is disorderly, with multiple reflected waves superimposed. In addition, there is water in the base layer of the loose area, which significantly alters the wave amplitude. Based on the response of radar waves to different loose damage degrees, a BP neural network is used to classify and identify the radar data.

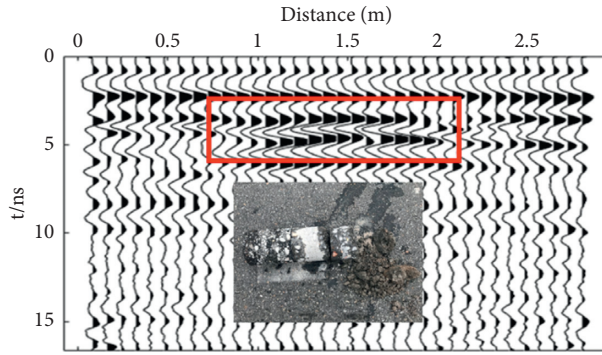


FIGURE 8: Radar reflection spectrum of moderate loose damage.

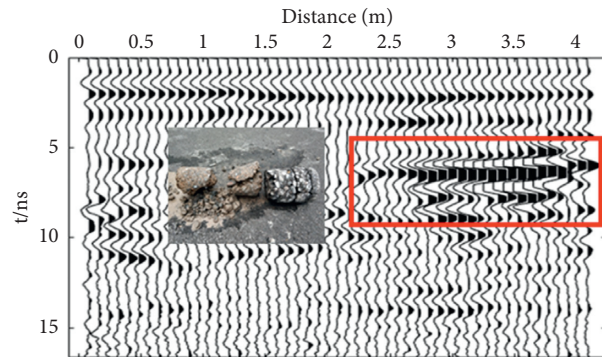


FIGURE 9: Radar reflection spectrum of severe loose damage.

TABLE 6: Classification of the extent of looseness.

Extent of looseness	Normal	Moderate	Severe
Category	I	II	III

TABLE 7: Part of the training sample set.

Sample	Attributes								
	Average absolute value amplitude	Root mean square amplitude	Amplitude standard deviation	Amplitude deviation	Waveform factor	Crest factor	Kurtosis factor	Pulse factor	Kurtosis
1	453.18	540.09	540.62	292271.33	1.40	8.33	$3.17 E + 10$	11.67	8.91
2	409.97	533.14	533.66	284795.67	1.40	8.29	$3.08 E + 10$	11.58	8.99
3	439.65	513.54	514.05	264244.13	1.40	8.49	$2.97 E + 10$	11.89	9.72
4	448.10	514.72	515.23	265457.96	1.39	8.27	$2.77 E + 10$	11.45	9.00
5	376.87	503.89	504.38	254402.69	1.38	8.28	$2.58 E + 10$	11.45	8.93
6	394.37	479.01	479.48	229899.25	1.40	8.49	$2.41 E + 10$	11.87	9.71
7	391.61	471.10	471.56	222370.98	1.40	8.53	$2.27 E + 10$	11.96	9.59
8	355.54	462.48	462.94	214309.79	1.41	8.65	$2.2 E + 10$	12.17	9.86
9	340.09	459.21	459.66	211290.84	1.41	8.76	$2.18 E + 10$	12.34	9.96
10	373.81	464.46	464.91	216141.95	1.42	8.82	$2.23 E + 10$	12.52	9.86

According to the characteristic values of the radar data, a reasonable BP neural network structure is designed to identify the types of loose damage. The characteristic values of the radar data and corresponding degree of looseness are obtained as BP neural network training samples. Of the sample data, 80% are used as training samples, and the remaining 20% are used as test samples to train and test the

BP neural network. Table 6 presents the looseness degree classification table, and Table 7 lists some sample data.

The trained neural network was tested using the measured radar data. The 150 channel-measured radar data were divided into 10 groups with 15 channels in each group, and 10 tests were conducted. Compared with the results of core drilling and sampling, the accuracy of the neural network

TABLE 8: Statistical analysis of test results.

Test group	1	2	3	4	5	6	7	8	9	10
Accuracy (%)	86	93	80	93	80	93	80	87	80	87

TABLE 9: Results of the fourth test.

Sample number	Actual category	Judgment category	True/false	Extent of looseness
1	I	I	True	Normal
2	I	I	True	Normal
3	I	I	True	Normal
4	I	I	True	Normal
5	I	I	True	Normal
6	II	II	True	Moderate
7	II	II	True	Moderate
8	II	II	True	Moderate
9	II	II	True	Moderate
10	II	III	False	Severe
11	III	III	True	Severe
12	III	III	True	Severe
13	III	III	True	Severe
14	III	III	True	Severe
15	III	III	True	Severe

was greater than 80%. Tables 8 and 9 summarize the statistical analysis of the 10 test results and present the results of the fourth test, respectively.

After testing the trained neural network numerous times, the comprehensive accuracy of the test was greater than 80%, which further verifies the feasibility of the BP neural network for the classification and recognition of the looseness degree in a semirigid base. However, the accuracy of the test results using the actual detection data was slightly lower than the recognition accuracy of the simulation data. The reason is that the numerical simulation situation is relatively ideal, whereas in the actual project, the situation is more complex and the material distribution is uneven. GPR data are affected by the surrounding environment and the acquisition system, and thus it is difficult to reflect the real situation of the underground target accurately, resulting in relatively large error in the identification process.

5. Conclusions

To solve the problem that loose damage of a road base cannot be identified quantitatively, and thus the classification and identification of the extent of looseness mainly depends on experienced judgment, this study establishes a structural model of a semirigid base asphalt pavement with different extents of looseness. The FDTD method is then used to simulate the road model with different extents of looseness, and the extent of looseness in the base is extracted using a time-domain analysis method. Then, a BP neural network is used to classify and identify loose damage in the base. The conclusions of this study are as follows:

- (1) In the simulated radar echo signal, the average absolute value, root mean square, standard deviation, waveform factor, peak factor, pulse factor, and other time-domain eigenvalues are shown to have a good correlation with the extent of looseness of the base,

allowing these values to be used as the basis for radar signal classification and recognition.

- (2) With increasing looseness of the base, the corresponding simulation map becomes more complex, and the reflected amplitude decreases with increasing looseness degree. The time delay, Δt , decreases with an increasing extent of looseness when the medium thickness is constant.
- (3) The recognition accuracy of the simulated electromagnetic wave is greater than 90%. The radar data of the actual project are classified and identified, and the recognition accuracy is greater than 80%. The results of the classification and recognition of the simulated data and measured data verify the feasibility of the classification and recognition method, which can provide a new method for the use of GPR to detect the presence and degree of loose damage.

Data Availability

The data used to support the findings of this study are included within the article.

Conflicts of Interest

The authors declare that they have no conflicts of interest regarding the publication of this paper.

Acknowledgments

The authors acknowledge the support received from the National Key Research and Development Plan (Grant no. 2018YFB1600200), the National Natural Science Foundation of China (Grant nos. 51878624 and 51878622), Major Scientific and Technological Special Project in Henan (Grant no. 181100310400), Henan Science Fund for Distinguished

Young Scholars (Grant no. 202300410354), Natural Science Foundation of Henan Province (Grant no. 202300410746), the Program for Science and Technology Innovation Talents in Universities of Henan Province (Grant no. 19HAS-TIT041), and Key Research Projects of Higher Education in Henan Province (Grant no. 18A580001).

References

- [1] S. H. A. Ai-min, "Material characteristics of semi-rigid base," *China Journal of Highway and Transport*, vol. 21, no. 001, pp. 1–5, 2008.
- [2] C. Jing, J. Zhang, and B. Song, "An innovative evaluation method for performance of in-service asphalt pavement with semi-rigid base," *Construction and Building Materials*, vol. 235, p. 117376, 2020.
- [3] X. Wang and X. Ma, "Responses of semi-rigid base asphalt pavement with interlayer contact bonding model," *Advances in Civil Engineering*, vol. 2020, no. 3, pp. 1–13, 2020.
- [4] H. Ahn and J. Lee, "Subsurface condition evaluation of asphalt pavement for pavement preservation treatments," *Journal of Testing and Evaluation*, vol. 44, no. 3, pp. 1183–1193, 2016.
- [5] Y. A. N. G. Yong, "The influence of factors on the durability of asphalt pavement," *International Journal of Civil Engineering and Machinery Manufacture*, vol. 2, no. 2, 2017.
- [6] Y. Wen, G. Hong, "Research on crack-resistance property of asphalt mixture as road stress-absorbing interlayer," *Advanced Materials Research*, p. 1333, 2011.
- [7] V. . Marecos, S. Fontul, M. D. L. Antunes et al., "Evaluation of a highway pavement using non-destructive tests: falling weight deflectometer and ground penetrating radar," *Construction and Building Materials*, p. 154, 2017.
- [8] D. Zehua, Y. Shengbo, G. Yunze et al., "Rapid detection methods for asphalt pavement thicknesses and defects by a vehicle-mounted ground penetrating radar (GPR) system," *Sensors (Basel, Switzerland)*, vol. 16, no. 12, 2016.
- [9] S. Wang, S. Zhao, I. L. Al-Qadi, and Al-Qadi, "Continuous real-time monitoring of flexible pavement layer density and thickness using ground penetrating radar," *NDT & E International*, vol. 100, pp. 48–54, 2018.
- [10] V. Sunjay and V. K. Singh, "Ground penetrating radar (GPR) applications in hydrogeological study of aquifers," *Earth Science Frontiers*, vol. 16, no. S1, p. 28, 2009.
- [11] J. Gao, D. Yuan, Z. Tong, J. Yang, and D. Yu, "Autonomous pavement distress detection using ground penetrating radar and region-based deep learning," *Measurement*, vol. 164, p. 108077, 2020.
- [12] S. Zhang, W. Shen, D. Li et al., "Nondestructive ultrasonic testing in rod structure with a novel numerical Laplace based wavelet finite element method," *Lat. Am. J. Solids Struct*, vol. 15, no. 7, 2018.
- [13] M. V. Felice and Z. Fan, "Sizing of flaws using ultrasonic bulk wave testing: a review," *Ultrasonics*, Ultrasonics, vol. 88, pp. 26–42, 2018.
- [14] V. Vyas, V. J. Patil, A. P. Singh et al., "Application of infrared thermography for debonding detection in asphalt pavements," *Journal of Civil Structural Health Monitoring*, no. 29, 2019.
- [15] K. Chahine, V. Baltazart, X. Dérobert et al., "Blind deconvolution via independent component analysis for thin-pavement thickness estimation using GPR[C]//2009 International Radar Conference Surveillance for a Safer World," IEEE, (RADAR 2009), 2010.
- [16] E. Cardarelli, C. Marrone, and L. Orlando, "Evaluation of tunnel stability using integrated geophysical methods," *Journal of Applied Geophysics*, vol. 52, no. 2-3, pp. 93–102, 2003.
- [17] A. Karem, A. B. Khalifa, and H. Frigui, "A Fisher vector representation of GPR data for detecting buried objects SPIE Defense + Security," *Detection and Sensing of Mines Explosive Objects, and Obscured Targets*, vol. XXI, 2016.
- [18] Gao, Jie, Zhang et al., "Recognition, location, measurement, and 3D reconstruction of concealed cracks using convolutional neural networks," *Construction and Building Materials*, 2017.
- [19] TongG. Zheng et al., "Innovative method for recognizing subgrade defects based on a convolutional neural network," *CONSTRUCTION AND BUILDING MATERIALS*, 2018.
- [20] A. Cubero-Fernandez, F. J. Rodriguez-Lozano, R. Villatoro, J. Olivares, and J. M. Palomares, "Efficient pavement crack detection and classification," *Eurasip Journal on Image & Video Processing*, vol. 2017, no. 1, 2017.
- [21] S. Solla, *Approach to Identify Cracking in Asphalt Pavement Using GPR and Infrared Thermographic Methods: Preliminary findings*, Ndt & E International, 2014.
- [22] R. DITOMMASO, M. MUCCIARELLI, and F. C. PONZO, "S-transform based filter applied to the analysis of non-linear dynamic behavior of soil and buildings," *Pro-ceedings of European Conference on Earthquake Engi-Neering*, vol. 30, pp. 1–13, 2010.
- [23] X. Xu, Q. Zeng, D. Li et al., "GPR detection of several common subsurface voids inside dikes and dams," *Engineering Geology*, vol. 111, no. 1-4, pp. 31–42, 2010.
- [24] B. Zhang, H. Fang, Y. Zhong et al., "Application of GPR and FWD in comprehensive evaluation of old road performance," *Journal of China & Foreign Highway*, vol. 28, no. 005, pp. 89–93, 2008.
- [25] B. Zhang and Q. Liu, "Yanhui zhong analysis of dynamic response of rigid pavement deflection under FWD load," *Journal of Highway and Transportation Research and Development*, vol. 26, no. 7, pp. 33–37, 2009.
- [26] T. Meagher, B. Jiang, and P. Jiang, "An enhanced finite difference time domain method for two dimensional Maxwell's equations," *Numerical Methods for Partial Differential Equations*, vol. 36, no. 5, 2020.
- [27] J. Lei, Z. Wang, H. Fang et al., "Analysis of GPR wave propagation in complex underground structures using CUDA-implemented conformal FDTD method," *International Journal of Antennas and Propagation*, 2019.
- [28] K. S. Yee, "Numerical solution of initial boundary value problems involving Maxwell's equations in isotropic media," *IEEE Trans. Antennas and Propagation*, p. 14, 1966.
- [29] Y. Li, Z. Zhao, W. Xu, Z. Liu, and X. Wang, "An effective FDTD model for GPR to detect the material of hard objects buried in tillage soil layer," *Soil and Tillage Research*, vol. 195, p. 104353, 2019.
- [30] X. Li, C. Yuan, and B. Shan, "System identification of neural signal transmission based on backpropagation neural network," *Mathematical Problems in Engineering*, vol. 2020, no. 1, pp. 1–8, 2020.

Research Article

Finite Element (FE) Modeling of Indirect Tension to Cylindrical (IT-CY) Specimen Test for Damping Asphalt Mixtures (DAMs)

Jiandong Huang,^{1,2} Tianhong Duan ,^{1,2} Yuantian Sun ,^{1,2} Lin Wang,² and Yawei Lei³

¹State Key Laboratory of Coal Resources and Safe Mining, China University of Mining and Technology, Xuzhou 221116, China

²School of Mines, China University of Mining and Technology, Xuzhou 221116, China

³China Construction Second Engineering Bureau Ltd., Beijing 100160, China

Correspondence should be addressed to Tianhong Duan; passionduan@cumt.edu.cn and Yuantian Sun; yuantiansun@cumt.edu.cn

Received 3 November 2020; Revised 24 November 2020; Accepted 27 November 2020; Published 21 December 2020

Academic Editor: Jiaolong Ren

Copyright © 2020 Jiandong Huang et al. This is an open access article distributed under the Creative Commons Attribution License, which permits unrestricted use, distribution, and reproduction in any medium, provided the original work is properly cited.

DAMs have recently been developed to be used as the damping layer in the so-called antivibration pavement to mitigate the effects of traffic-induced vibration while rare finite element (FE) modeling has been conducted to simulate the indirect tension to cylindrical (IT-CY) specimen test for DAMs. In the present study, the methods for the viscoelastic characterization of DAMs and the techniques to characterize the viscoelastic behavior of DAMs in FE modeling were proposed. The FE model to simulate the IT-CY test was constructed, and it was verified through the corresponding laboratory test. Good agreements were noted between the simulation results and testing results demonstrating that the FE model can provide the accurate prediction of the mechanical behavior of DAMs.

1. Introduction

In recent years, various indirect tensile tests of asphalt mixture have been widely used in the evaluation and design in pavement engineering [1–5]. Among these, the indirect tension to cylindrical (IT-CY) specimen test is a method for measuring the dynamic stiffness of asphalt mixtures. It can be applied to cylindrical specimens of various diameters and thickness, manufactured in the laboratory or cored from a road layer (Institution 2004) to reflect the mechanical properties of the asphaltic materials, provide the input mechanical parameters for the asphalt pavement design, and evaluate the crack resistance [6–12].

Based on these indirect tensile tests, various studies about the asphalt mixtures have been carried out in the past years [13, 14]. Christensen et al. applied the indirect tensile strength as the parameter to evaluate the antirutting performance of asphalt mixture and pointed out that the indirect tensile test can be used to determine the adhesive force and internal friction angle of the asphalt mixture [15]. Birgisson et al. employed the results of the superior performing asphalt pavement (Superpave) indirect tensile creep test to understand the impact of water

damage on the fracture characteristics of the asphalt mixture [16]. The boundary element method (BEM) was also carried out for the numerical simulation to understand the microstructure and fracture characteristic of asphalt mixture, using the indirect tensile test [17]. Kim et al. used the indirect tensile method to determine the dynamic modulus of the asphalt concrete, showing that the dynamic modulus master curves obtained by the uniaxial compression and indirect tensile tests have a good fit [18]. Abbas et al. used the discrete element method (DEM) to study the micromechanics of asphalt mixtures under different load conditions and numerically simulated the indirect tensile test under low-temperature conditions [19]. Zhang et al. studied the design parameters of the high-temperature characteristics of the asphalt mixture and carried out the indirect tensile test under different conditions, showing that the indirect tensile strength can replace Marshall stability as the parameter for pavement design [20]. Liang et al. conducted the indirect tensile test to evaluate the dynamic stiffness modulus of hard asphalt mixtures and understood the effects of gradation, binder/aggregate ratio, binder types, and testing temperature. Indirect tensile tests have also been conducted to evaluate the mechanical properties of lignin fiber

and glass fiber, rubberized asphalt mixture, warm asphalt mixture-reclaimed asphalt pavement as well as rutting resistance [4, 21–23]. It is evident that the indirect tensile test has been conducted and simulated from different perspectives in earlier studies [24–26]. However, to the authors' knowledge, rare numerical simulations for the IT-CY tests were conducted currently. On the other hand, as novel functional infrastructure materials, the damping asphalt mixtures (DAMs) have recently been developed to absorb vibration and noise caused by traffic loads [7, 27, 28]. DAMs can be used as the damping layer in the so-called antivibration pavement to mitigate the effects of traffic-induced vibration. The increase in damping of pavement materials can reduce ground vibrations into the loading area and within the corresponding surrounding region. This improvement is critical for reducing vibrations to improve the quality of life and to preserve the stability of buildings [29]. It has been confirmed that DAMs showed the strength to meet the requirements of the specification and had sufficient resistance to rutting and water damage [28]. However, in the case of DAMs, the IT-CY test has not been carried out in the laboratory, and the corresponding FE simulation has never been carried out in the past studies.

2. Research Objectives

The main aim of this research is to use the finite element (FE) modeling techniques to understand the mechanical behavior of DAMs in IT-CY tests. The detailed research objectives are as follows:

- (i) To propose the methods for viscoelastic characterization of DAMs and the techniques to characterize the viscoelastic behavior of DAMs in FE modeling
- (ii) To establish a reliable finite element (FE) model to simulate the IT-CY test and verify it through the corresponding laboratory test
- (iii) To design DAMs in the laboratory, conduct IT-CY tests to characterize the viscoelastic mechanical behavior, and determine the reliable input material parameters for FE modeling

3. Methodologies

3.1. Viscoelastic Characterization of Asphalt Mixtures. As far as the constitutive model of typical viscoelastic material, like the asphalt mixtures, experimental studies have demonstrated that the viscoelastic properties can be described by the so-called generalized Maxwell model (GMM), as given in Figure 1.

The GMM consists of the restoring and viscous force components, which can be simulated by the nonlinear elastic element and the nonlinear viscous element, respectively, with these two elements connected in series [30–34]. Under the effect of constant stress, the viscous flow and deformation provided by the viscous damper can increase linearly with time, so the deformation of the whole model can increase indefinitely. Degradation of the element in the model can change this kind of mechanical characteristic, that is to say, removing a damper in one basic Maxwell model (MM).

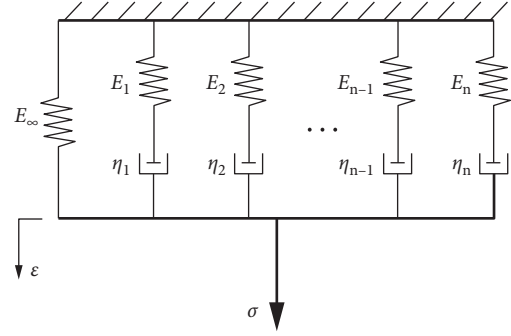


FIGURE 1: Generalized Maxwell model (GMM).

The constitutive model of the M -th Maxwell Model (MM) can be described as differential form:

$$\frac{d\epsilon}{dt} = \frac{1}{E_m} \frac{d\sigma_m}{dt} + \frac{\sigma_m}{\eta_m}. \quad (1)$$

Concerning the GMM, total stress can be calculated as the sum of all MM stress:

$$\sigma = \sigma_0 + \sum_{m=1}^M \sigma_m. \quad (2)$$

Apply integral transformation theory and Fourier transform equations (1) and (2), respectively, under the zero initial conditions to the following equations:

$$\bar{\sigma}_0 = E_0 \bar{\epsilon}, \quad (3)$$

$$\bar{\sigma}_i \left(1 + \frac{i\eta_i \omega_n}{E_i} \right) = i\omega_n \eta_i \bar{\epsilon}, \quad n = 1, 2, \dots, N. \quad (4)$$

Substitute equations (3) and (4) into (2), and Fourier transform it as follows:

$$\bar{\sigma} = E_0 \bar{\epsilon} + \sum_{m=1}^M \frac{i\omega_n \eta_i}{E_i + i\eta_i \omega_n / E_i} \bar{\epsilon}, \quad n = 1, 2, 3, \dots, N, \quad (5)$$

$$\bar{\sigma} = \bar{\epsilon} \left(E_0 + \sum_{m=1}^M \frac{i\omega_n \eta_i}{1 + i\rho_i \omega_n} \right), \quad (6)$$

where $\bar{\sigma}$ and $\bar{\epsilon}$ are complex stress and strain, respectively.

The relaxation time of the I -th MM is

$$\rho_i = \frac{\eta_i}{E_i}. \quad (7)$$

By substituting equation (7) into (6), equation (6) will be described as follows:

$$E^* = E_\infty + \sum_{m=1}^M \frac{i\omega_n E_i \rho_i}{1 + i\rho_i \omega_n}, \quad (8)$$

$$E^* = E_\infty + \sum_{m=1}^M \frac{\omega_n^2 E_i \rho_i^2}{1 + \rho_i^2 \omega_n^2} + \sum_{m=1}^M \frac{\omega_n E_i \rho_i}{1 + \rho_i^2 \omega_n^2} i. \quad (9)$$

The value of complex modulus is as follows:

$$|E^*| = \sqrt{\left(E_\infty + \sum_{m=1}^M \frac{\omega_n^2 E_i \rho_i^2}{1 + \rho_i^2 \omega_n^2}\right)^2 + \left(\sum_{m=1}^M \frac{\omega_n E_i \rho_i}{1 + \rho_i^2 \omega_n^2}\right)^2}. \quad (10)$$

3.2. Finite Element (FE) Modeling of Viscoelastic Behavior. The stress response of the viscoelastic material includes an elastic portion and a viscous portion. The elastic portion can respond immediately under the effect of load; however, the viscous portion would respond after a while. In general, the stress function of viscoelastic material is given as an integral form, and its constitutive equation may be described as follows:

$$\sigma = \int_0^t 2G(t-\tau) \frac{d\epsilon}{d\tau} d\tau + I \int_0^t K(t-\tau) \frac{d\Delta}{d\tau} d\tau, \quad (11)$$

where σ is the Cauchy stress, $G(t)$ is the shear modulus function, $K(t)$ is the bulk modulus function, τ is the past time, Δ is the bulk deformation, t is the current time, and ϵ is the shear deformation. In typical FE modeling software (e.g., ABAQUS, ANSYS, and MARC), there are two methods to describe viscoelastic integral kernel function. The first one is using GMM units by the form of Maxwell, and the second one is using the form of the Prony series. In fact, the two expression methods are consistent, and the only difference is the mathematical expression. The basic expression to describe viscoelastic properties by the Prony series is as follows:

$$G(t) = G_0 \left[\alpha_\infty + \sum_{i=1}^n \alpha_i^G \exp\left(-\frac{t}{\tau_i^G}\right) \right], \quad (12)$$

$$K(t) = K_0 \left[\alpha_\infty + \sum_{i=1}^n \alpha_i^K \exp\left(-\frac{t}{\tau_i^K}\right) \right], \quad (13)$$

where G_0 is the shear modulus, K_0 is the bulk modulus, and τ_i^K is the relaxation time of each Prony series. Another two parameters are defined as follows:

$$\alpha_i^G = \frac{G_i}{G_0}, \quad (14)$$

$$\alpha_i^K = \frac{K_i}{K_0}. \quad (15)$$

Besides, G_0 and K_0 could be calculated by the following functions:

$$G_0 = G(t=0) = G_\infty + \sum_{i=1}^n G_i, \quad (16)$$

$$K_0 = K(t=0) = K_\infty + \sum_{i=1}^n K_i. \quad (17)$$

Based on the viscoelastic mechanical theory, there is a relationship between these three parameters:

$$G(t) = \frac{E(t)}{2(1+\mu)}, \quad (18)$$

$$K(t) = \frac{E(t)}{3(1-2\mu)}. \quad (19)$$

Shear modulus $G(t)$ and bulk modulus $K(t)$ are unified in the same form as $E(t)$, and $E(t)$ would be expressed as a form of Prony series:

$$E(t) = E_\infty + \sum_{i=1}^n E_i \exp\left(-\frac{t}{\tau_i}\right). \quad (20)$$

Through the results of the experimental tests, the values of parameters in equation (10) could be fitting. By equations (18) and (19), initial and steady-state values, K_0 , G_0 , K_∞ , and G_∞ , as well as the relaxation time coefficients τ_i^G and τ_i^K can be determined.

4. Materials and Experimental Testing

4.1. Raw Materials

4.1.1. Aggregates. Basalt coarse aggregates, natural sand, and mineral filler were used for the aggregates. The physical properties were evaluated according to the EN 1097-6/7 standard, and the results are given in Table 1.

4.1.2. Binders. A plant-produced stable asphalt rubber supplied by a local manufacturer was used in the present study (ASTM D6114-97). It was produced according to the so-called wet process by mixing a Pen 50–70 base bitumen with 20% of crumb rubber, which was produced by mechanical grinding of waster scrape tires at room temperature. These scrap tires are comprised of 50% weight of truck tires and 50% weight of car tires. The gradation of the crumb rubber particles is given in Figure 2.

4.2. Mix Design. Three different rubberized open-graded asphalt mixtures are designed, which are regarded as Mix ref (mixture reference), Mix 1, and Mix 2, respectively, with the same voids in the mineral aggregate (VMA) but containing asphalt rubber content at concentrations of 5%, 15%, and 20% in order to improve the damping properties. The grain size distribution of the studied mixture respects the aggregate gradation required by the specifications for open-graded (OG) asphalt mixtures. The OG mix has been optimized and evaluated in a previous study, showing the desired mechanical properties. The nominal maximum size (NMS) of the aggregate was 8 mm, in line with the optimized design thickness of the damping layer of 3 cm [27]. The amount of binder in the mix has been increased as long as the amount of filler. Table 2 gives the passing ratio of aggregate gradation that was used in this research.

Cylindrical specimens with a diameter of 100 mm were compacted by the Superpave gyratory compactor (SGC). For mix design and all performed tests in the present study, an average of three identical samples was used as the result for

TABLE 1: Physical properties of aggregates (EN 1097-6/7).

Properties	Basalt	Sand	Mineral filler
Bulk specific gravity (G_{sb}) (kg/m^3)	2.753	2.629	2.710
Apparent specific gravity (G_{sa}) (kg/m^3)	2.863	2.690	2.650
Water absorption (%)	1.39	0.86	—

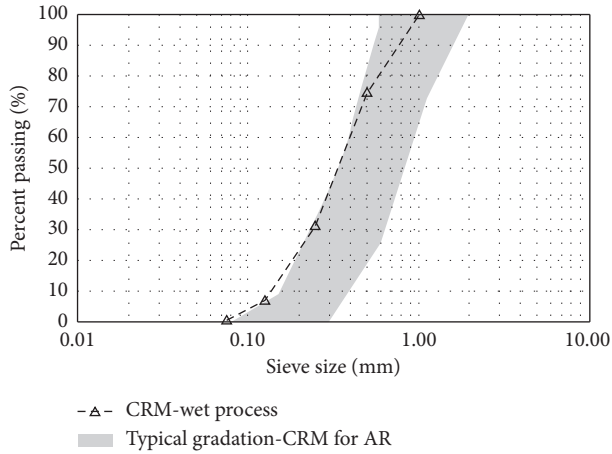


FIGURE 2: Gradation of crumb rubber particles.

TABLE 2: Passing ratio of aggregates.

Aggregate size (mm)	Passing ratio
8	100
6.3	99.5
4	71
2	28.2
1	16
0.500	12
0.250	9.2
0.125	7.1
0.063	4.4

each mixture type. As far as each kind of asphalt mixtures, volumetric properties including air voids (AVs), voids in the mineral aggregate (VMA), and voids filled with asphalt (VFA) are evaluated when numbers of gyration are 50 and 130, respectively, as shown in Table 3.

It is evident that the three asphalt mixtures were designed with similar open-graded aggregates structures due to similar VMA values for all of these three. It should be noted that the VMA value of Mix 2 was higher than the others since the additional 5% binder content is added after air voids are saturated with the binder.

4.3. Experimental Programs. Tests were carried out as per EN12697-26 using IT-CY tests by the universal testing system (UTS) to characterize the dynamic modulus of asphalt mixtures, by which the viscoelastic properties of asphalt mixtures can be defined. In this test, three cylindrical specimens were manufactured for each of the mixtures.

Figure 3 gives the load applied in the test. Notes: 1: peak load; 2: pulse repetition load; 3: rise time

TABLE 3: Volumetric properties of Mix ref, Mix 1, and Mix 2.

Material	Number of gyrations	AV (%)	VMA (%)	VFA (%)
Mix ref	130	21.7	31.4	30.8
Mix ref	50	24.2	33.5	27.9
Mix 1	130	1.3	34.9	96.3
Mix 1	50	2.4	35.6	93.1
Mix 2	130	3.5	44.9	92.3
Mix 2	50	4.3	45.4	90.6

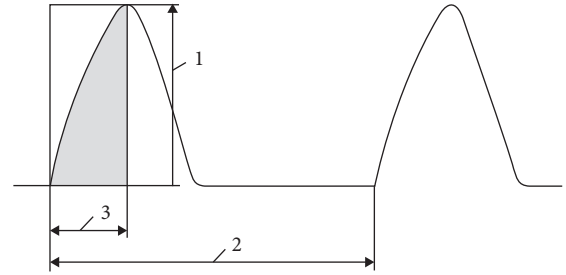


FIGURE 3: Load applied in the IT-CY test. (1) peak load; (2) pulse repetition load; (3) rise time.

The stiffness modulus value was obtained with the following equation:

$$E = \frac{F \times (\nu + 0.27)}{z \times h}, \quad (21)$$

in which E represents the stiffness modulus of the asphalt mixture, F represents the load applied in the IT-CY test, z represents the horizontal deformation during the test, h means the average thickness of the asphalt mixture specimen, and ν presents Poisson's ratio.

The dynamic stiffness modulus test was conducted under the indirect loading condition at 2 different temperatures (2 and 10°C) and 4 different loading frequencies (5, 3.3, 1.8, and 1.1 Hz). The test temperatures were selected according to the standard EN12697-26 and the selection of loading frequencies recommended in the control system software of the laboratory equipment. It should be noted that the tests must be conducted from the lowest temperature to the highest temperature and from the highest frequency to the lowest frequency. Stress and strain values were recorded continuously to calculate the stiffness modulus of the asphalt mixture.

4.4. Testing Results. Table 4 gives the results of the stiffness modulus as well as the

The stiffness modulus master curves were constructed by using the time-temperature superposition principle (TTSP) [35, 36]. The horizontal shift factors were calculated by the so-called Williams-Landel-Ferry (WLF) equation [37]:

$$\log \alpha_T = \frac{C_1 \cdot (T - T_{\text{ref}})}{C_2 + (T - T_{\text{ref}})}, \quad (22)$$

where α_T represents the shift factor; C_1 and C_2 are the equation parameters, respectively; T_{ref} represents the reference temperature; and T is the testing temperature. The stiffness modulus was modeled by using the modified

TABLE 4: Stiffness modulus of Mix ref, Mix 1, and Mix 2.

Asphalt mixture	T_{test} (°C)	Modulus (MPa)	f (Hz)
Mix ref	2	9101	5.0
	2	8525	3.3
	2	7963	1.8
	2	6625	1.1
	10	7915	5.0
	10	7245	3.3
	10	6402	1.8
	10	5523	1.1
Mix 1	2	1995	5.0
	2	1917	3.3
	2	1765	1.8
	2	1656	1.1
	10	1705	5.0
	10	1580	3.3
	10	1332	1.8
	10	1200	1.1
Mix 2	2	1376	5.0
	2	1300	3.3
	2	1175	1.8
	2	1128	1.1
	10	1127	5.0
	10	944	3.3
	10	756	1.8
	10	671	1.1

Christensen–Anderson–Marasteanu (CAM) model [38]. Figure 4 gives the master curves of the stiffness modulus.

The master curves were developed on two replicates. Results showed an acceptable variability, with the coefficient of variation of the average between two samples below 10% for all the cases. The shift factors were optimized on the dynamic modulus master curve and were then applied to the phase angle master curve. The results provided an adequate accuracy in modeling the raw data with the R^2 coefficient being above 97% for all mixes. It can be seen that as the frequency was low (or temperature was high), Mix ref and Mix 1 showed similar stiffness modulus. However, as far as to Mix 2, it showed a lower stiffness modulus. This can be due to too much free asphalt in Mix 2 playing the role of lubricant and reducing the stiffness modulus. As the frequency was high (or temperature was low), Mix 1 and Mix 2 showed similar modulus stiffness, but both of them were lower than that of Mix ref.

5. Finite Element (FE) Modeling of the IT-CY Test

5.1. Construction of the Geometrical Model. The geometrical model is given in Figure 5.

The IT-CY test was simulated using standard SGC specimen size, with a diameter of 100 mm and a thickness of about 45 mm, measured from the results of the experimental tests. It was established for three parts, including one asphalt mixture specimen and two metal bearing blocks. The width of the bearing block is 15 mm, and the inner surface has the same arc as the specimen. The time-domain analysis was selected to perform the simulation. The time step length was

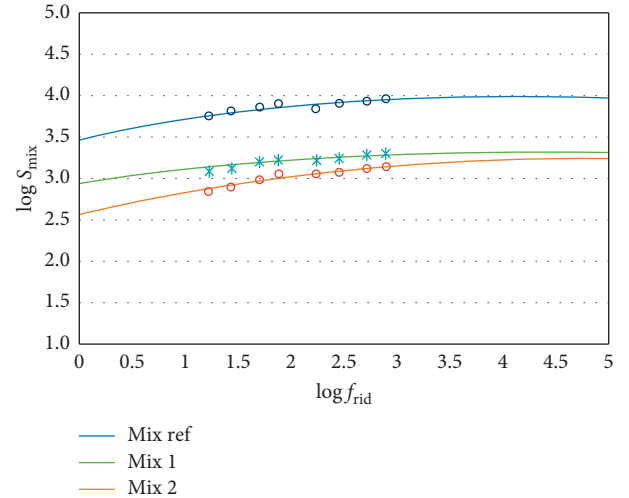


FIGURE 4: Stiffness modulus master curves.

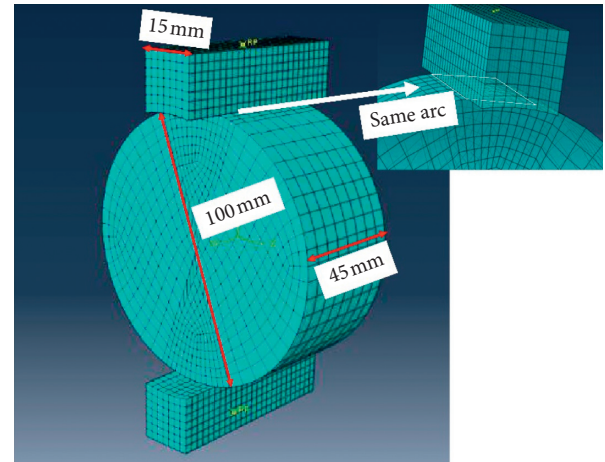


FIGURE 5: Schematic diagram of the geometrical model.

determined as 0.01 s to reduce the calculation time and total simulation time equaled 3 s.

5.2. Materials Properties. The more elements and parameters in a model, the more close to the real mechanical properties of viscoelastic material itself and reflecting the characteristics of viscoelastic materials at various stages. However, too many selected parameters will slow down the fitting process and its effect to improve accuracy not obvious. Based on some references, 7 parameters (E_0 , E_1 , E_2 , E_3 , η_1 , η_2 , and η_3) for the GMM were determined. That is to say, the GMM was consisting of 3 MM units and 1 spring in parallel connection. So, the value of m is 3, and ω_n means the reduced frequency in equation (10).

In this way, by fitting equation (10) with the least-squares method, 7 parameters characterized viscoelasticity property of asphalt mixtures will be determined. The detailed parameters of three different asphalt mixtures under 2 temperatures and 4 frequencies are shown in Table 5.

TABLE 5: Parameters for characterizing the GMM.

Mixes	E_0 (MPa)	E_1 (MPa)	E_2 (MPa)	E_3 (MPa)	η_1 (MPa•s)	η_2 (MPa•s)	η_3 (MPa•s)
Mix ref (2°C)	80	41	11748	8330	5283.7	58.0	1400.4
Mix 1 (2°C)	88	7620	10200	80	6822	760	688.2
Mix 2 (2°C)	84	5403	9200	183	8623	1589	236
Mix ref (10°C)	76	3705	1589	639	2566	25	10208
Mix 1 (10°C)	76	122	5689	2547	15236	1563	263
Mix 2 (10°C)	82	3563	325	1569	4896	14635	2894

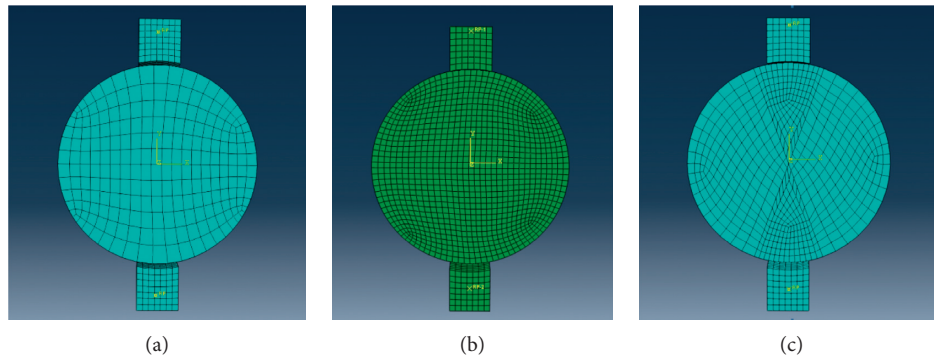


FIGURE 6: Three different meshing used in FE modeling: mesh (a), mesh (b), and mesh (c).

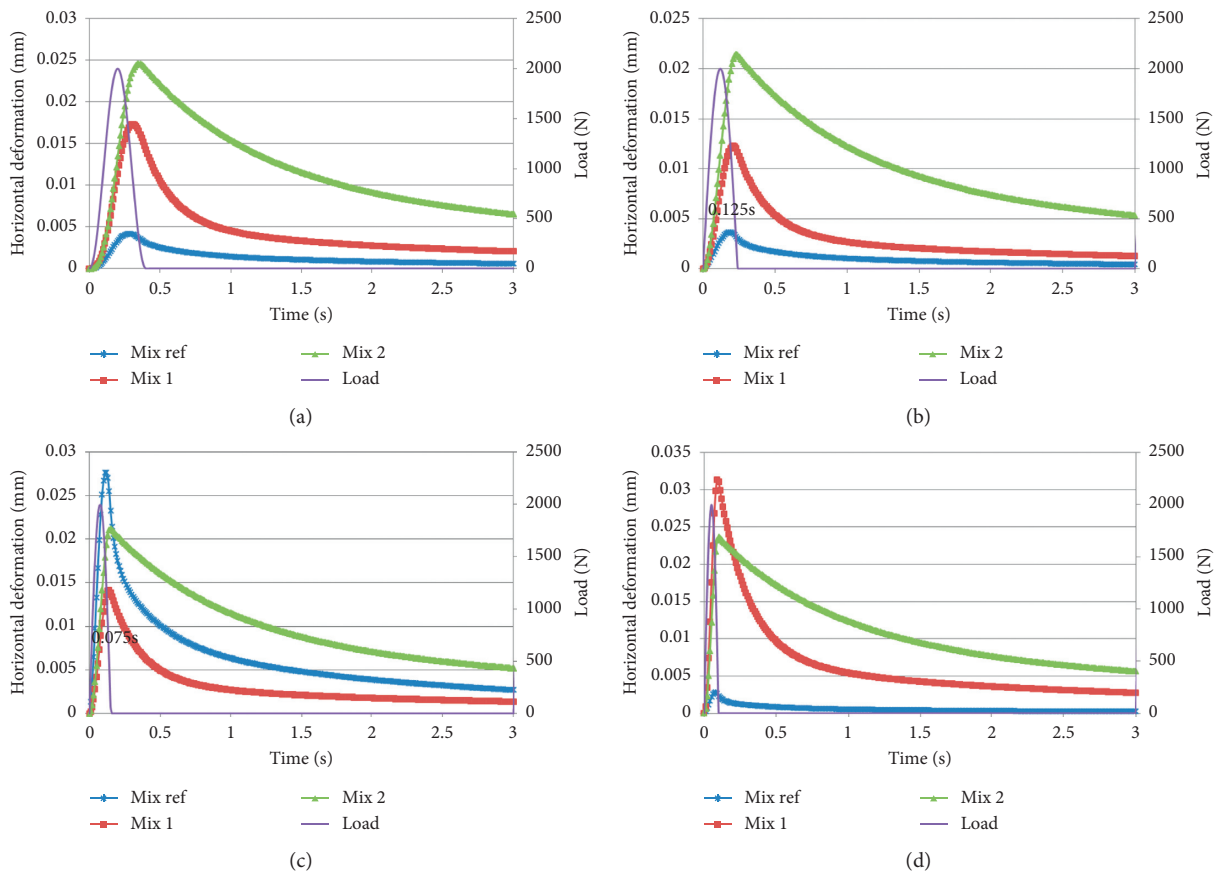


FIGURE 7: Simulation results: (a) $f=1.1$ Hz; (b) $f=1.8$ Hz; (c) $f=3.3$ Hz; (d) $f=5$ Hz in one cyclic.

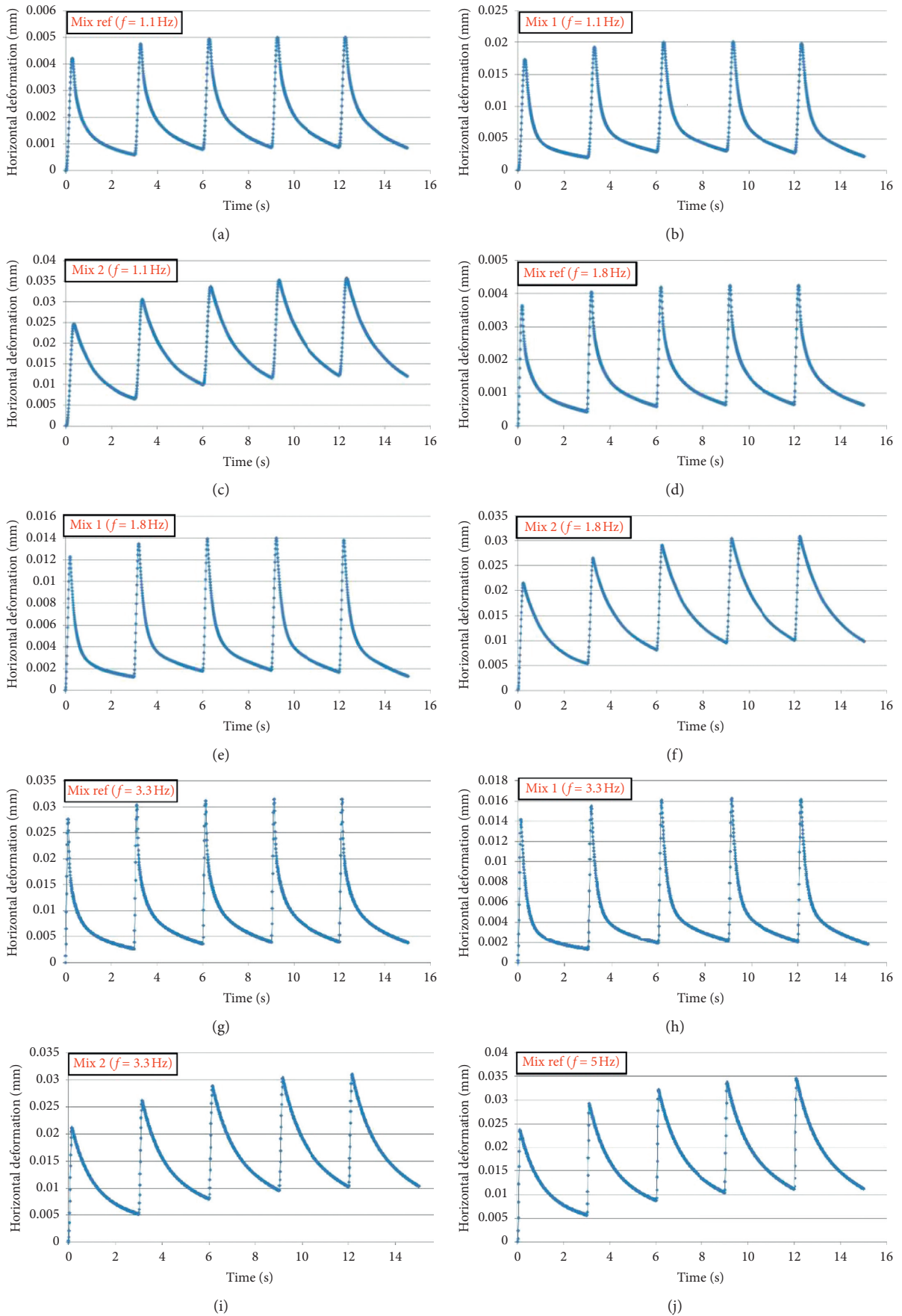


FIGURE 8: Continued.

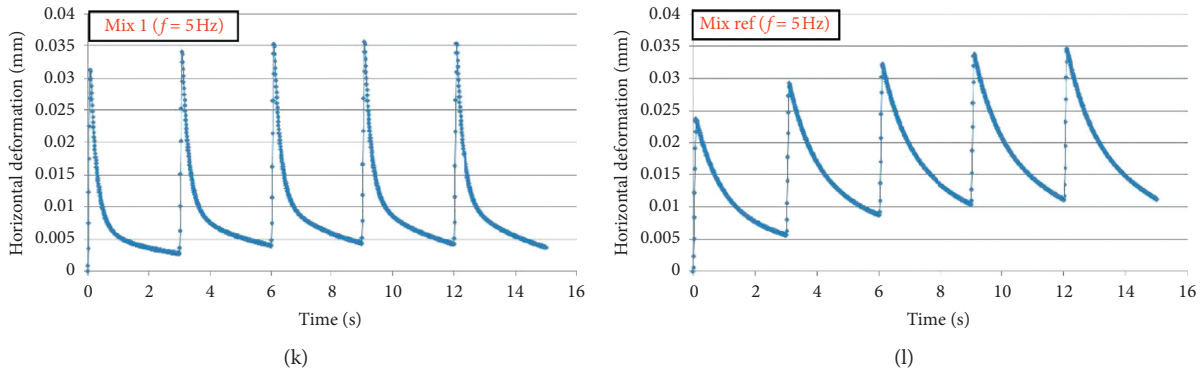


FIGURE 8: Simulation results in five cyclic at temperature 2°C.

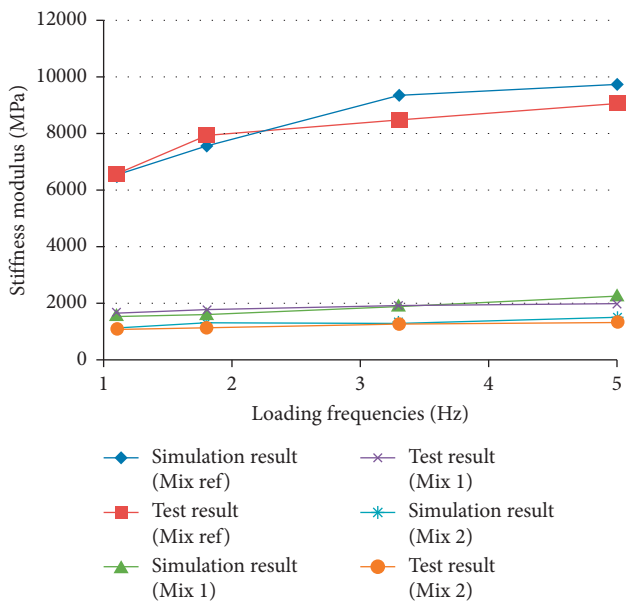


FIGURE 9: Comparisons between the simulation results and test results.

5.3. *Finite Element Meshing.* The meshes with different densities were used to compare the simulation results and to determine the convergence accuracy of the simulation, as shown in Figure 6. The grid size was determined by comparing the sizes of the sample and metal blocks. Three different grid sizes were selected by varying meshing densities.

It can be seen in Figure 6 that mesh (a) was coarse and the number of elements was minimal; thus, its computing time and storage space were relatively small, but the calculation accuracy may not be as good as the other ones. Mesh (b) was finer, and the number of elements was higher; thus, more precise calculations, more calculation time, and storage space can be foreseen. Mesh (c) was modified based on the mesh (a) and (b) with overall mesh size as same as (b), but the only partial area localized at the load was meshed more finely to prevent the local stress concentration convergence problems. However, compared with mesh (b), the computing time and storage space were much less. The

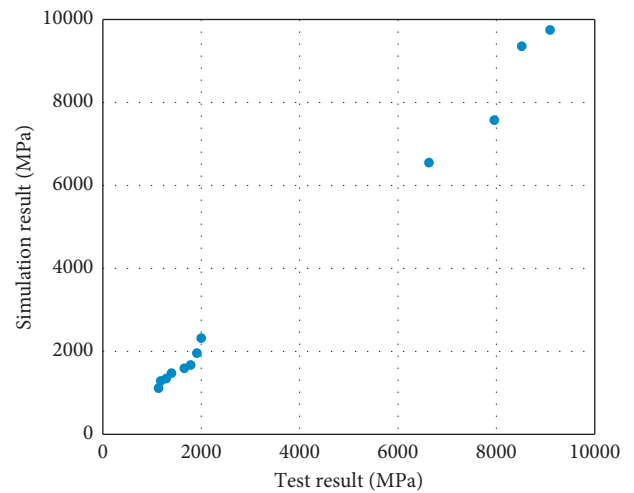


FIGURE 10: Test results vs. simulation results.

results of the preliminary simulation showed that the three methods of meshing are closed to each other, but the third kind of mesh is convergent faster, consuming less computation time and less storage space, so the third kind of the meshing method is used for detailed simulation analysis. In this simulation, the rigid body in constraint was selected for metal bearing blocks. Hexahedral reduction integral element C3D8R was selected for the asphalt mixture specimen.

6. Simulation Results and Model Validations

6.1. *Simulation Results.* Figure 7 gives the simulation results under varying loading frequencies.

It is clearly shown that the horizontal deformations increase first and then decrease as the loading time increases, and the peak value of deformations lags behind the peak loading under the same loading cycle, which demonstrates that the digital sample behaves as a viscoelastic material under dynamic load. All horizontal deformation curves show delay trends compared with the load curve. It is known that with the same input loading frequency, more delay of the deformation demonstrates the more viscosity part accounting for total parts [39]. As can be observed in Figure 7, the comparison of the delay time is Mix 2 > Mix 1 > Mix ref,

evidencing that the much more binder content in Mix 2 improved the proportion of the viscosity part. It can be indicated that the IT-CY model based on FEM in this study is capable to characterize the macroscopic viscoelastic behaviors of asphalt mixture.

To balance the computational cost and the smoothness of the horizontal deformation response curves, 300 time-increments (computation points) were assigned for each loading cycle. The responses between horizontal deformations of point A vs. time under different loading frequencies are given in Figure 8. The abscissa represents the loading time, and the ordinate represents the deformation of the specimen in the horizontal direction. The horizontal deformation at 300 time-increments was recorded under different loading frequencies (1.1 Hz, 1.8 Hz, 3.3 Hz, and 5 Hz). The stiffness modulus can be determined as per equation (21). In this way, the stiffness modulus under different loading frequencies and temperatures can be calculated for comparison with the testing results, which are presented in the following section.

6.2. Model Validation. Figure 9 gives the comparison of stiffness modulus under different loading frequencies between the test result and the simulation result.

Good agreements are observed between these results. The difference between the simulation results and test results for Mix ref, Mix 1, and Mix 2 is calculated as 5.73%, 6.45%, and 5.03%, respectively. The differences as the loading frequency equals 1.1 Hz, 1.8 Hz, 3.3 Hz, and 5 Hz are calculated as 2.06%, 6.35%, 4.99%, and 9.57%, respectively. These differences are acceptable for the proposed FE model. The above results highlight the rationality and reliability of the proposed model to simulate the IT-CY test. Also, it is evident that a big difference can be observed for higher loading frequency. That is to say, the proposed model can be more accurate for lower loading frequency. For different asphalt mixtures, the difference between the test results and simulation results was similar. Figure 10 gives a comparison of all the stiffness modulus for the three mixtures. Similar results can be observed by the comparison. These differences are considered acceptable for the developed FE model to characterize the viscoelastic properties of DAMs.

7. Conclusions

In the present study, the research process to use FE modeling techniques to understand the mechanical behavior of DAMs in IT-CY tests was conducted. Three DAMs were designed in the laboratory, and the IT-CY tests were conducted to characterize the viscoelastic mechanical behavior, by which the reliable input material parameters for FE modeling were determined. The following are the conclusions that can be drawn from the above research process:

- (i) The Prony series can be used to characterize the viscoelastic behavior of DAMs and can be determined from the IT-CY tests, by fitting the results of the GMM with the least-squares method.

- (ii) The dynamic modulus master curves were typical of asphalt mixtures. During the IT-CY test, as the frequency was low (or temperature was high), Mix ref and Mix 1 showed similar stiffness modulus higher than that of Mix 2. This can be due to too much free asphalt in Mix 2 playing the role of lubricant and reducing the stiffness modulus. As the frequency was high (or temperature was low), Mix 1 and Mix 2 showed similar modulus stiffness but both of them were lower than that of Mix ref.
- (iii) From the simulation results, the comparison of the delay time is $\text{Mix 2} > \text{Mix 1} > \text{Mix ref}$, evidencing that the much more binder content in Mix 2 improved the proportion of the viscosity part. It can be indicated that the IT-CY model based on FEM in this study is acceptable to characterize the viscoelastic behaviors of asphalt mixture. The longer delay time of DAMs supports what was the main scope of the mix design that is, increasing the damping response than the reference mixture, indicating a more viscous response under loading with a consequent higher energy dissipation and reduction of the vibratory mechanism.
- (iv) Good agreements were noted between the simulation results and test results, demonstrating that the FE model can provide an accurate prediction of the mechanical behavior of DAMs. The proposed model can be more accurate for the lower loading frequency of the IT-CY test.

Data Availability

The experimental and modeling data used to support the findings of this study are available from the corresponding author upon request.

Conflicts of Interest

The authors declare that they have no conflicts of interest.

Acknowledgments

This research was supported by the Fundamental Research Funds for the Central Universities (2017XKQY045).

References

- [1] M. Barman, M. Zaman, and S. Commuri, "Alternative analysis of indirect tensile test results for evaluating fatigue characteristics of asphalt mixes," *Construction and Building Materials*, vol. 166, pp. 204–213, 2018.
- [2] T. Singh, E. Haas, and E. Wass, "Indirect tensile test (IDT) to determine asphalt mixture performance indicators during quality control testing in New Jersey," *Transportation Research Record: Journal of the Transportation Research Board*, vol. 2672, no. 28, pp. 394–403, 2018.
- [3] Y. Zhao, "Accuracy improvement for two-dimensional finite-element modeling while considering asphalt mixture meso-structure characteristics in indirect tensile test simulation,"

- Journal of materials in civil engineering*, vol. 32, no. 10, Article ID 04020275, 2020.
- [4] P. Zieliński, "Indirect tensile test as a simple method for rut resistance evaluation of asphalt mixtures-polish experience," *Road Materials and Pavement Design*, vol. 24, pp. 1–17, 2020.
 - [5] J. uang, J. Zhang, J. Ren, and H. Chen, "Anti-rutting performance of the damping asphalt mixtures (DAMs) made with a high content of asphalt rubber (AR)," *Construction and Building Materials*, vol. 271, Article ID 121878, 2021.
 - [6] J. Fu, L. Lei, X. Ma, and Z. Liu, "Experimental procedure and finite element analysis for an indirect tensile test of asphalt concrete," *Road Materials and Pavement Design*, vol. 19, no. 8, pp. 1904–1925, 2017.
 - [7] J. Huang and Y. Sun, "Effect of modifiers on the rutting, moisture-induced damage, and workability properties of hot mix asphalt mixtures," *Applied Sciences*, vol. 10, no. 20, p. 7145, 2020.
 - [8] X. King and J. Ye, "Element analysis of indirect tensile fatigue test of asphalt mixture," *Applied Sciences*, vol. 9, no. 2, p. 327, 2017.
 - [9] W. Liu, Y. Gao, and L. Li, "Micromechanical simulation of influence factors of indirect tensile test of asphalt mixture," *Journal of Testing and Evaluation*, vol. 46, no. 2, pp. 832–841, 2017.
 - [10] S. Yue, J. Zheng, D. Chen, and L. You, "Moduli decay for the asphalt mixture under different loading conditions," *Applied Sciences*, vol. 8, no. 5, p. 840, 2018.
 - [11] Y. Sauzéat, L. Wan, and L.-J. Sun, "Three-dimensional discrete element modelling of influence factors of indirect tensile strength of asphalt mixtures," *International Journal of Pavement Engineering*, vol. 20, no. 6, pp. 724–733, 2019.
 - [12] S. He, "Investigation on indirect tensile test of asphalt mixture based on the discrete element method," *Journal of Testing and Evaluation*, vol. 48, no. 3, 2020.
 - [13] J. Huang and Y. Huang, "Effect of modifiers on the rutting, moisture-induced damage, and workability properties of hot mix asphalt mixtures," *Applied Sciences*, vol. 10, no. 20, p. 7145, 2020.
 - [14] J. Huang, M. Losa, and P. Leandri, "Determining the effect of damping layers in flexible pavements on traffic induced vibrations," in *Proceedings of the Advances in Materials and Pavement Prediction: Papers from the International Conference on Advances in Materials and Pavement Performance Prediction (AM3P 2018)*, Doha, Qatar; CRC Press, April 2018.
 - [15] D. NapierSoranakom and R. Bonaquist, "Use of strength tests for evaluating the rut resistance of asphalt concrete," *Journal of the Association of Asphalt Paving Technologists*, vol. 71, 2002.
 - [16] B. Birgisson, R. Roque, and G. C. Page, "Evaluation of water damage using hot mix asphalt fracture mechanics (with discussion)," *Journal of the Association of Asphalt Paving Technologists*, vol. 72, 2003.
 - [17] B. Birgisson and R. Roque, "And fracture in asphalt mixtures using a boundary element approach," *Journal of Materials in Civil Engineering*, vol. 16, no. 2, pp. 116–121, 2004.
 - [18] Y. R. Kim and M. Momen, "Modulus testing of asphalt concrete in indirect tension mode," *Transportation Research Record: Journal of the Transportation Research Board*, vol. 1891, no. 1, pp. 163–173, 2005.
 - [19] A. Abbas, A. Papagiannakis, and E. A. Masad, "Micro-mechanical simulation of asphaltic materials using the discrete element method," *Asphalt Concrete: Simulation, Modeling, and Experimental Characterization*, vol. 31, pp. 1–11, 2006.
 - [20] Z.-Q. Zhang, J. Tao, and B. Yang, "Research on design parameter for high temperature performance of asphalt mixture," *China Journal of Highway and Transport*, vol. 1, pp. 23–28, 2009.
 - [21] M. Guo, "Effect of WMA-RAP technology on pavement performance of asphalt mixture: a state-of-the-art review," *Journal of Cleaner Production*, vol. 71, Article ID 121704, 2020.
 - [22] D. Luo, M. Abdelsalam, and Z. Zhang, "Performance of asphalt mixtures modified with lignin fiber and glass fiber: a review," *Construction and Building Materials*, vol. 209, pp. 377–387, 2019.
 - [23] C. Xia, "Unified characterizing fatigue performance of rubberized asphalt mixtures subjected to different loading modes," *Journal of Cleaner Production*, vol. 279, Article ID 123740, 2020.
 - [24] Y. Sun, G. Li, H. Basarir et al., "Laboratory evaluation of shear strength properties for cement-based grouted coal mass," *Arabian Journal of Geosciences*, vol. 12, no. 22, p. 690, 2019.
 - [25] Y. Sun, G. Li, N. Zhang et al., "Development of ensemble learning models to evaluate the strength of coal-grout materials," *International Journal of Mining Science and Technology*, 2020.
 - [26] J. Huang, R. Alyousef, M. Suhatriel et al., "Influence of porosity and cement grade on concrete mechanical properties," *Advances in Concrete Construction*, vol. 10, no. 5, pp. 393–402, 2020.
 - [27] J. Huang, *Rubber Modified Asphalt Pavement Layer For Noise And Vibration Absorption*, University of Florence, Florence, Italy, 2019.
 - [28] J. Huang and Y. Sun, "Viscoelastic analysis of the damping asphalt mixtures (DAMs) made with a high content of asphalt rubber (AR)," *Advances in Civil Engineering*, vol. 2020, pp. 1–12, 2020.
 - [29] S. County, *Report on the Status of Rubberized Asphalt Traffic Noise Reduction in Sacramento County*, Sacramento County and Bollard & Brennan Inc, Cleveland, OH, USA., 1999.
 - [30] E. V. Dave, "Graded viscoelastic approach for modeling asphalt concrete pavements," in *Proceedings of the American Institute of Physics Conference Proceedings*, pp. 736–741, Kyoto Japan, May 2008.
 - [31] L. Zhang, H. Ma, and T. Ma, "Modeling of dynamic modulus and phase Angle master curves of rubber modified asphalt mixture," *Materials*, vol. 12, no. 10, p. 1667, 2014.
 - [32] L. Shan, "Analysis of linear viscoelastic response function model for asphalt binders," *Journal of Materials in Civil Engineering*, vol. 28, no. 6, Article ID 04016010, 2016.
 - [33] L. Shan and N. Ren, "Criterion of viscoelastic response model for asphalt binders," *Construction and Building Materials*, vol. 113, pp. 553–560, 2016.
 - [34] H. Yao, "Discrete element simulation of bending beam rheometer tests for asphalt binder," *International Journal of Pavement Research & Technology*, vol. 5, no. 3, 2012.
 - [35] M. L. Xia and N. Tapsoba, "Validation of the time-temperature superposition principle for crack propagation in bituminous mixtures," *Materials and Structures*, vol. 46, no. 7, pp. 1075–1087, 2017.
 - [36] Q. T. Di Benedetto and N. Tapsoba, "Temperature superposition principle validation for bituminous mixes in the

- linear and nonlinear domains,” *Journal of Materials in Civil Engineering*, vol. 25, no. 9, pp. 1181–1188, 2002.
- [37] J. D. Ferry, *Viscoelastic Properties of Polymers*, John Wiley & Sons, Hoboken, NJ, USA, 1980.
- [38] M. Zeng, “Rheological modeling of modified asphalt binders and mixtures (with discussion),” *Journal of the Association of Asphalt Paving Technologists*, vol. 70, 2001.
- [39] C. Zhang, *Viscoelastic Damping Material*, National Defence Industrial Press, Beijing, China, 2012.

Research Article

Prediction Model of Asphalt Content of Asphalt Mixture Based on Dielectric Properties

Yanhui Zhong ¹, Yilong Wang,¹ Bei Zhang ¹, Xiaolong Li ¹, Songtao Li ²,
Yanmei Zhong ³, Meimei Hao ¹, and Yanlong Gao¹

¹College of Water Conservancy and Environment Engineering, Zhengzhou University, No. 100 Science Rd., Zhengzhou 450001, China

²Zhengzhou Railway Vocational & Technical College, No. 56 Pengcheng Rd., Zhengzhou 451460, China

³Henan Provincial Academy of Building Research Co., Ltd., No. 4 Fengle Rd., Zhengzhou 450053, China

Correspondence should be addressed to Bei Zhang; beizhang@126.com, Xiaolong Li; wennuandeshang@hotmail.com, Songtao Li; list16@126.com, and Yanmei Zhong; zhong_yanmei@163.com

Received 25 October 2020; Revised 14 November 2020; Accepted 16 November 2020; Published 4 December 2020

Academic Editor: Jiaolong Ren

Copyright © 2020 Yanhui Zhong et al. This is an open access article distributed under the Creative Commons Attribution License, which permits unrestricted use, distribution, and reproduction in any medium, provided the original work is properly cited.

The rapid detection of asphalt content in asphalt mixture is of great significance to the quality evaluation of asphalt pavement. Based on the dielectric properties of an asphalt mixture, the prediction model of asphalt content is deduced theoretically using three types of dielectric models: Lichtenecker-Rother (L-R) model, Rayleigh model, and Bottcher equation. Under the condition of laboratory mixing at room temperature (about 20–25°C), a dielectric test of asphalt mixture is conducted to verify the applicability of the model. The test results indicate that the dielectric constant of the asphalt mixture is inversely proportional to the asphalt content and directly proportional to the aggregate size of the mixture. Among the models, the Rayleigh model has a wide range of applications and exhibits a high accuracy, with an average relative error of only 1.86%. The results provide a theoretical basis for the nondestructive testing of asphalt pavements using ground-penetrating radar.

1. Introduction

Asphalt pavement is widely used in highway construction owing to its low noise, high strength, and excellent smoothness [1, 2]. With the increasing pursuit of pavement comfort, asphalt pavements have gradually become the main structural forms of high-grade pavements [3]. The early disease of asphalt pavements is related to the construction quality, as well as the mixture oil-stone ratio. If the asphalt content is significantly low, the voidage becomes significantly high. If the asphalt content is significantly high, the thermal stability of the mixture decreases, leading to the easy onset of diseases, such as bulge and rutting. Therefore, the accurate determination of asphalt content in asphalt mixtures in the construction process plays an important role in maintaining the constructive quality of asphalt pavements [4].

At present, combustion and centrifugal extraction methods are often used to detect asphalt content [5].

However, these methods have low detective efficiency and cannot meet the requirements of rapid detection of asphalt content [6, 7]. As a novel road quality inspection method, ground-penetrating radar (GPR) has been widely used in the quality inspection of road structure layers owing to its continuous, efficient, and nondestructive testing nature [8]. Lyntton first proposed the use of a dielectric constant to calculate pavement moisture content and compactness [9]. Topp et al. used regression analysis to establish the correlation between soil dielectric constant and soil water content [10]. In the field of soil water content detection, this model provides the most widely used empirical formula. Based on the idea of soil moisture content detection, scholars worldwide began to conduct related research on the dielectric properties of the asphalt mixture. Roth used the Time Domain Reflectometry (TDR) calibration method to measure the soil volumetric water content and dielectric constant and determined the model parameters by weighted

regression, thereby improving the dielectric model proposed by Dobson et al. [11]. Chang et al. demonstrated the existence of a good correlation among the density, voidage, and dielectric constant of asphalt mixtures [12]. Hoegh et al. established the regression relationship between the permittivity and voidage of asphalt mixtures and used GPR to detect the compactness of pavement surfaces [13]. Song used GPR to monitor the change in surface dielectric constant with the number of vehicle loads, thus providing a theoretical basis for the real-time analysis of pavement compactness [14]. Hou used spectrophotometry to determine the asphalt content in emulsified asphalt mixtures [15], and Kumbargeri used asphaltene proportion as the performance index to study the aging of asphalt mixtures [16]. In the above literature, by studying the relationship between the dielectric constant and road moisture content, compactness, and other indexes, the idea has been applied to the study of the voidage correlation in asphalt mixtures, achieving a good effect. However, in view of the relationship between the dielectric properties and the compactness, density, and asphalt content of asphalt mixtures, a composite dielectric model to determine the asphalt content has yet to be reported.

To meet the current demand for the rapid detection of asphalt content, this study explores the feasibility of detecting asphalt content through the dielectric properties of asphalt mixtures. Using the Bottcher model, the Rayleigh model, and the L-R model, the asphalt content prediction model for the asphalt mixtures is developed through theoretical derivation. In addition, the applicability of the prediction model is verified through experiments. Furthermore, an asphalt content calculation method based on the dielectric properties of the asphalt mixtures is proposed, which provides a theoretical basis for the rapid and non-destructive testing of asphalt content using GPR.

2. Derivation of Prediction Model of Asphalt Content

The dielectric constant is an important parameter that reflects the dielectric properties of pavement materials. Through the analysis of the dielectric constant of pavement materials, the relevant indexes of pavement performance can be obtained [17]. Dielectric properties describe the interaction between the medium and the electric field. The dielectric properties of a medium are typically described by permittivity ϵ , conductivity σ , and permeability μ [18]. The dielectric constant is one of the most important parameters for characterizing the dielectric properties of a medium, reflecting the ability of the medium to store charge in the electric field. The dielectric constant of a composite medium considers the vacuum dielectric constant ϵ_0 (8.854×10^{-9} F/m) as the reference value, and the relative dielectric constant of the medium is used in the simulation calculation. The ratio of dielectric constant to vacuum dielectric constant is known as the relative dielectric constant of a medium [19]. The relative permittivity is calculated as follows:

$$\epsilon_r = \frac{\epsilon}{\epsilon_0} = \epsilon_r' - j\epsilon_r'' \quad (1)$$

It can be seen from the above equation that the relative permittivity of a medium is a dimensionless complex number. ϵ_r' is the real part of the relative dielectric constant and mainly reflects the storage effect of the medium on the electromagnetic wave. $\epsilon_r'' = \sigma/\omega$ is the imaginary part of the relative dielectric constant, which mainly reflects the loss characteristics of the dielectric to the electromagnetic wave [20].

The dielectric constant of multiphase composite media can be described by the dielectric constant and volume ratio of each single-phase medium, which is known as the dielectric constant model of the composite media. There exist several dielectric constant models that describe the dielectric properties of multiphase media. The classical dielectric models include the L-R model, Rayleigh model, Bottcher equation, Bruggeman-Hanai model, and Li Jianhao model [21]. Owing to the wide application ranges of the L-R model, Rayleigh model, and Bottcher equation, the prediction accuracy of the composite dielectric constant model is high. This paper deduces the proposed model based on these three models, as described as follows.

2.1. Introduction of L-R Model. The L-R model is one of the most classical dielectric models, which has been widely used in geophysical exploration and other research fields. It can be expressed as

$$(\epsilon_m)^c = \sum_{i=1}^n f_i (\epsilon_i)^c \quad (2)$$

In the above equation, the parameter c assumes a value between -1 and 1 . When c is 1 , $1/3$, or $1/2$, the L-R model is converted into classical dielectric models, namely, the linear model, cubic root model, and root mean square model, respectively, as defined in equations (3), (4), and (5):

$$(\epsilon_m) = \sum_{i=1}^n f_i (\epsilon_i), \quad (3)$$

$$(\epsilon_m)^{(1/3)} = \sum_{i=1}^n f_i (\epsilon_i)^{(1/3)}, \quad (4)$$

$$(\epsilon_m)^{(1/2)} = \sum_{i=1}^n f_i (\epsilon_i)^{(1/2)}. \quad (5)$$

In equations (2)–(5), ϵ_m denotes the dielectric constant of the medium, f_i is the volume ratio of the component i to the mixture, and ϵ_i is the dielectric constant of the component i .

2.2. Introduction of Rayleigh Model. When the medium is a two-phase composite, the Rayleigh model can be defined as

$$\frac{\epsilon_m - 1}{\epsilon_m + 2} = V_1 \frac{\epsilon_1 - 1}{\epsilon_1 + 2} + V_2 \frac{\epsilon_2 - 1}{\epsilon_2 + 2}. \quad (6)$$

The model can be extended to n -phase media as

$$\frac{\varepsilon_m - 1}{\varepsilon_m + 2} = \sum_{i=1}^n v_i \frac{\varepsilon_i - 1}{\varepsilon_i + 2}. \quad (7)$$

2.3. *Introduction of Bottcher Equation.* Equations of symmetrical two-phase composites are as follows:

$$V_1 \frac{\varepsilon_1 - \varepsilon_m}{\varepsilon_1 + 2\varepsilon_m} + V_2 \frac{\varepsilon_2 - \varepsilon_m}{\varepsilon_2 + 2\varepsilon_m} = 0. \quad (8)$$

Dielectric model applied to multiphase composites is as follows:

$$\sum_{i=1}^n v_i \frac{\varepsilon_i - \varepsilon_m}{\varepsilon_i + 2\varepsilon_m} = 0. \quad (9)$$

According to the above theoretical basis, the linear model, square root model, root mean square model, Rayleigh model, and Bottcher equation are selected to determine the asphalt content of the asphalt mixture. The derivation process and results are as follows.

2.3.1. *Lichtenecker-Rother Model.* Based on the L-R model, the relationship between the dielectric properties and asphalt content of the asphalt mixture was studied. The asphalt mixture was a multiphase composite medium composed of single-phase media, such as aggregate, asphalt, and air [22]. The L-R model of the asphalt mixture can be expressed by equation (10):

$$(\varepsilon_m)^c = f_s (\varepsilon_s)^c + f_{as} (\varepsilon_{as})^c + f_a (\varepsilon_a)^c. \quad (10)$$

Here, ε_m denotes the relative dielectric constant of the asphalt mixture. ε_s , ε_{as} , and ε_a are the relative dielectric constants of the aggregate, asphalt, and air in the asphalt mixture, respectively. f_s , f_{as} , and f_a are the volume ratios of the aggregate, asphalt, and air in the asphalt mixture. In the studied asphalt mixture, assuming $f_s + f_{as} + f_a = 1$, the volume of asphalt can be determined as follows:

$$f_{as} = 1 - f_a - f_s. \quad (11)$$

The volume composition expression of the derived aggregate is obtained by combining equations (10) and (11):

$$f_{as} = \frac{k_m - k_{as} + (k_{as} - 1)f_a}{k_s - k_{as}}. \quad (12)$$

In this equation, the expressions of the correlation coefficients k_m , k_s , k_{as} , and k_a are as follows (13). The representations of the other parameters in the equation are the same as those in equation (10).

$$k_i = (\varepsilon_i)^c \quad (i = m, s, as, a). \quad (13)$$

The dielectric constant of air is 1, that is, $\varepsilon_a = 1$, and the volume ratio of air in the asphalt mixture is f_a . Therefore, the equation for voidage e can be deduced as follows:

$$e = f_a \times 100\%. \quad (14)$$

Considering the effect of asphalt volume ratio, the asphalt content prediction models are defined as follows:

$$P_a = \frac{\gamma_{as}(1 - T - e)}{\gamma_s \times T + \gamma_{as}(1 - T - e)}. \quad (15)$$

In the above equation, $T = (k_m - k_{as} + (k_{as} - 1) \times (e \div 100\%)) / (k_s - k_{as})$.

Using the asphalt content prediction model (15), the asphalt content can be calculated based on the dielectric properties of the asphalt mixture, which are described in detail. The value of c in the L-R model of the asphalt mixture needs to be determined first [23]. In addition, the aggregate, dielectric constant, and corresponding density of the asphalt mixture must be determined. Except for the parameter c in the dielectric model, the remaining parameters can be measured in the laboratory. Therefore, the dielectric model of the asphalt mixture based on the L-R model is established first, and then the asphalt content is calculated according to the prediction model.

2.3.2. *Rayleigh Model.* The expression of the Rayleigh model of the asphalt mixture is as follows:

$$\frac{\varepsilon_m - 1}{\varepsilon_m + 2} = V_s \frac{\varepsilon_s - 1}{\varepsilon_s + 2} + V_{as} \frac{\varepsilon_{as} - 1}{\varepsilon_{as} + 2} + V_a \frac{\varepsilon_a - 1}{\varepsilon_a + 2},$$

$$k_i = \frac{\varepsilon_i - 1}{\varepsilon_i + 2}, \quad (i = m, s, as, a), \quad (16)$$

$$\varepsilon_a = 1, \quad V_a \frac{\varepsilon_a - 1}{\varepsilon_a + 2} = 0.$$

The Rayleigh model can be expressed as

$$k_m = V_s k_s + V_{as} k_{as}. \quad (17)$$

The volume of the asphalt can be deduced from equation (17):

$$V_{as} = 1 - e - V_s. \quad (18)$$

The aggregate volume can be defined as

$$V_s = \frac{k_m + (e - 1)k_{as}}{k_s - k_{as}}. \quad (19)$$

Then, the equation for asphalt content is deduced as

$$P_a = \frac{\rho_{as} V_{as}}{\rho_{as} V_{as} + \rho_s V_s} = \frac{\rho_{as}(1 - e - V_s)}{\rho_{as}(1 - e - V_s) + \rho_s V_s}. \quad (20)$$

2.3.3. *Bottcher Equation.* The expression for the Bottcher equation of the asphalt mixture is

$$V_s \frac{\varepsilon_s - \varepsilon_m}{\varepsilon_s + 2\varepsilon_m} + V_{as} \frac{\varepsilon_{as} - \varepsilon_m}{\varepsilon_{as} + 2\varepsilon_m} + V_a \frac{\varepsilon_a - \varepsilon_m}{\varepsilon_a + 2\varepsilon_m} = 0,$$

$$k_i = \frac{\varepsilon_i - \varepsilon_m}{\varepsilon_i + 2\varepsilon_m} \quad (i = a, as, a). \quad (21)$$

Then, the Bottcher equation can be expressed as

$$V_{as}k_{as} + V_s k_s + V_a k_a = 0. \quad (22)$$

The asphalt volume can be expressed as

$$V_{as} = 1 - e - V_s. \quad (23)$$

Combining equations (22) and (23), we obtain

$$(1 - e - V_s)k_{as} + V_s k_s + V_a k_a = 0. \quad (24)$$

The aggregate volume can be expressed as

$$V_s = \frac{(1 - e)k_{as} + V_a k_a}{k_s - k_{as}}. \quad (25)$$

Then, the equation for asphalt content can be deduced as

$$P_a = \frac{\rho_{as}(1 - e - V_s)}{\rho_{as}(1 - e - V_s) + \rho_s V_s}. \quad (26)$$

3. Test and Method

3.1. Test Materials. Both AC-16 asphalt concrete mixture and SMA-16 asphalt mastic macadam mixture use 90# asphalt to prepare the standard specimens, and limestone was used as the aggregate and mineral powder. The physical parameters of the two mixtures were measured according to the requirements of the code. Based on the standard sieve system (square pore sieve) of the asphalt mixture mineral aggregate gradation screening test, the mineral aggregate was divided into k grades with different particle sizes. The size of each sieve hole was recorded as $d_{m,k}$ and $r_{m,k}$ was defined as the particle size of all levels of mineral particles. The mineral material grades for the test are presented in Table 1.

3.2. Test Scheme. AC-16 and SMA-16 were selected as the experimental objects. The dielectric constants of the asphalt and aggregate single-phase medium were tested, and the dielectric properties of the AC-16 asphalt concrete and SMA-16 stone matrix asphalt with different oil-stone ratio were studied experimentally. The sample preparation process is illustrated in Figure 1, and the test process is depicted in Figure 2.

- (1) According to the specifications, the AC-16 asphalt concrete mixture and SMA-16 asphalt mastic macadam mixture were prepared [11], by making the rutting plate specimen compact using a compactor [24]. The oil-stone ratios of six specimens were as follows: 4.0%, 4.1%, and 4.2% for the first group of the AC-16 asphalt concrete mixture and 5.9%, 6.0%, and 6.1% for the second group. For the three standard specimens of the SMA-16 asphalt macadam mixture, the oil-stone ratios used were 6.9%, 7.0%, and 7.1%. Thus, there were nine standard specimens in total.
- (2) A high-temperature coaxial probe method was used to test the dielectric constant of a single-phase

medium, such as asphalt and aggregate. While testing, it is necessary to ensure that the plane of the measured object is dry and in contact with the plane of the probe. Because the dielectric constant of water at 25°C is approximately 81 and that of air is approximately 1, the existence of water and voids significantly affects the measurement accuracy.

- (3) The dielectric constants of the asphalt mixture specimens were measured using the waveguide cavity method of the network analyzer.

4. Test Results and Discussion

4.1. Main Influencing Factors of Dielectric Constant of Mixture. Figure 3 depicts the graph of the dielectric constant of asphalt and limestone versus frequency. The dielectric constants of the limestone block and asphalt are less affected by frequency in the range of 1.7–2.6 GHz. The average dielectric constants of limestone and asphalt are 7.343 and 3.002, respectively.

Based on the above test flow, the test results of the dielectric constant of the asphalt mixture are presented in Table 2. Although there is a significant difference between the oil-stone ratios of the two groups of asphalt concrete specimens (AC-16-1 to AC-16-6), their dielectric constants are similar because the asphalt concrete is composed of asphalt, coarse aggregate, fine aggregate, and mineral powder. From Figure 3, it can be observed that the average dielectric constants of the asphalt, limestone block, and mixture are approximately 3, 7, and >5, respectively, which indicates that the main factors affecting the dielectric constant of the mixture are the coarse and fine aggregates of limestone. Moreover, when the asphalt content increases, the dielectric constant of the mixture does not change significantly.

Although the oil-stone ratio of the asphalt mastic macadam mixture is large, the overall dielectric constant is slightly greater than that of the asphalt concrete macadam. This is because the mastic macadam mixture is composed of asphalt, coarse aggregate, mineral powder, and a small amount of fine aggregate. The proportion of coarse aggregates is relatively large corresponding to the larger dielectric constant of the complete mixture. Most of the calculation methods of the dielectric model of the mixture consider the dielectric constant and the proportion of different materials that compose the mixture and determine the contribution of each single medium to the overall dielectric constant based on its volume ratio; thus, the change in the dielectric constant can be explained.

4.2. Effect of Asphalt Content on Dielectric Constant. Figure 4 depicts the changing trend of the dielectric constant of the mixture with the oil-stone ratio. The dielectric constants of the three groups of specimens decrease with the increase in the oil-stone ratio. In the first and second groups, which are of the same type of asphalt concrete block, the dielectric constants decrease slightly with increasing asphalt content, and the degree of decrease follows a linear trend. In

TABLE 1: Commonly used standard sieve sizes and corresponding particle sizes of mineral aggregate.

k	1	2	3	4	5	6	7	8	9	10
$d_{m,k}$ (mm)	0.075	0.15	0.3	0.6	1.18	2.36	4.75	9.5	13.2	16
$r_{m,k}$ (mm)	0.038	0.113	0.225	0.45	0.89	1.77	3.56	7.125	11.35	14.6

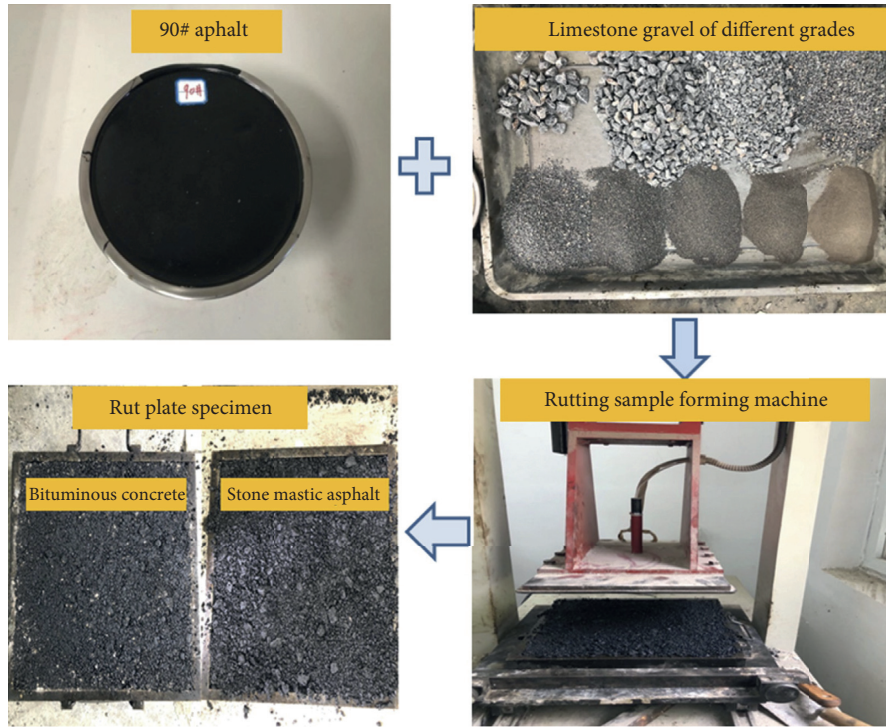


FIGURE 1: Production process of asphalt mixture.

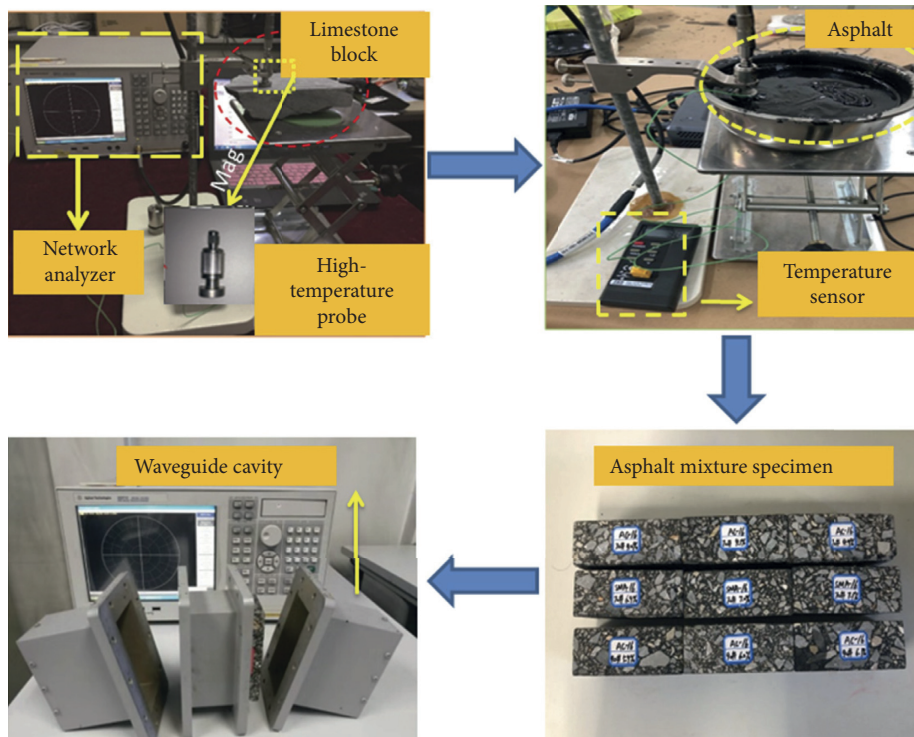


FIGURE 2: Measurement of permittivity of single medium and mixture.

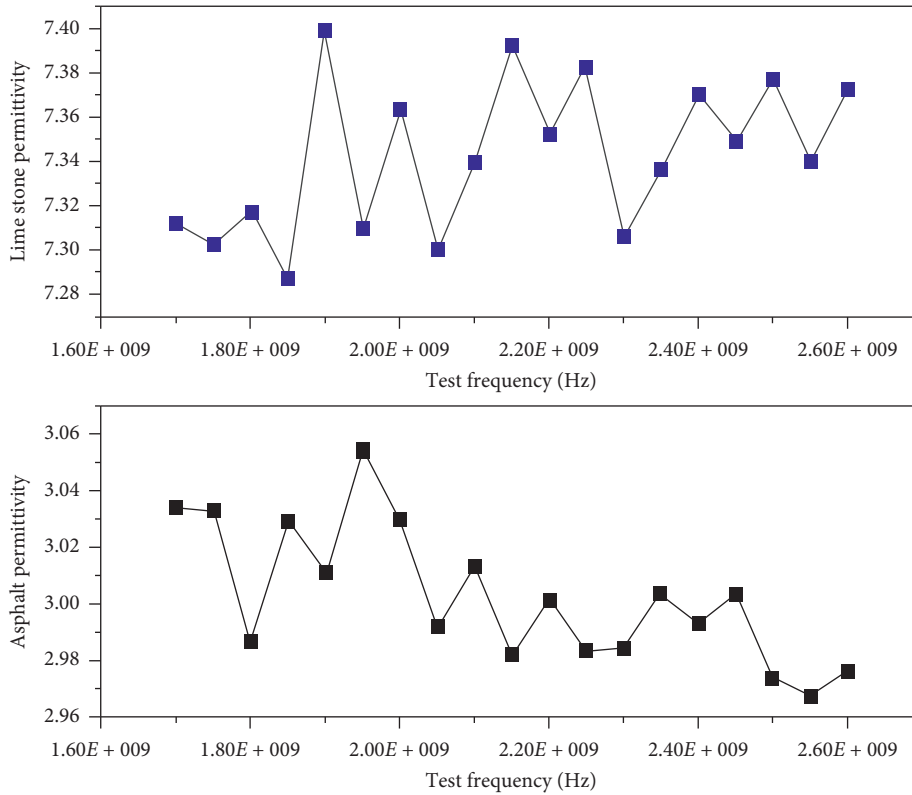


FIGURE 3: Permittivity of asphalt and limestone.

TABLE 2: Dielectric constant of asphalt mixture specimens.

Specimen number	AC-16-1	AC-16-2	AC-16-3	AC-16-4	AC-16-5	AC-16-6	SMA-16-1	SMA-16-2	SMA-16-3
Oil-stone ratio (%)	4.0	4.1	4.2	5.9	6.0	6.1	6.9	7.0	7.1
Dielectric constant	5.243	5.129	4.996	4.865	4.732	4.611	5.684	5.635	5.611

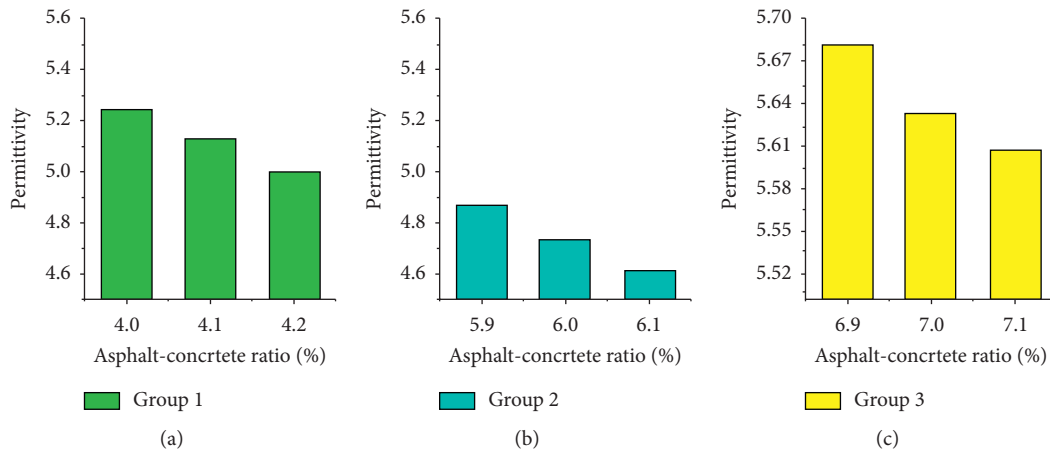


FIGURE 4: Variation of dielectric constant with the oil-stone ratio of the mixture.

the asphalt concrete, the asphalt mortar composed of asphalt and mineral powder plays the role of bonding the coarse and fine aggregates, because the mortar requires an appropriate pigment to binder ratio to achieve the optimal bonding performance. As the asphalt content increases, the volume ratio of the coarse and fine aggregates decreases, and the filling performance of the mortar is deteriorated, resulting in an increase in voidage and a downward trend in the dielectric constant of the mixture.

Owing to the lack of a certain proportion of fine aggregates, the third group of the mastic asphalt macadam mixture contains more mineral powder, coarse aggregate, and fiber stabilizer than the other two groups, resulting in an increase in the proportion of mortar. With the increase in asphalt content, the performance of the mortar gradually improves, and the ability of the coarse aggregate to bond and fill voids is enhanced. Therefore, its dielectric constant is greater than that of the asphalt concrete block. However, according to the composite model of the dielectric constant, the main factor affecting the overall dielectric constant is the proportion of a single medium with a larger dielectric constant. As the proportion of aggregate decreases, the overall dielectric constant of the specimen still exhibits a downward trend.

4.3. Accuracy Comparison of the Dielectric Model of Asphalt Content. Assuming that the voidage of the mixture is known, according to the average density of the aggregate, dielectric constant, voidage of the mixture, and volume percentage of asphalt and aggregate, the data are entered into the models, such as the derived linear, square root, root mean square, Bottcher, and Rayleigh models. The calculation results are presented in Figure 5.

Figure 6 depicts the relative errors of the prediction model: the average errors of the linear, cubic root, root mean square, Rayleigh, and Bottcher models are 175.40%, 85.58%, 108.11%, 1.86%, and 99.63%, respectively. Composite materials are composed of two or more materials, and most of them are multiphase bodies composed of solid, liquid, and gas phases. The dielectric constant of composites is closely related to the component dielectric constant, volume ratio, geometric structure, electrochemical performance, test frequency, and temperature. Most of the dielectric constant models of composite materials cannot reflect the overall asphalt content accurately by considering the dielectric constant of the composition and the volume ratio of each phase, which is a relatively simple factor.

Although nondestructive testing technology has been developed for many years, it is still a new technology, and the research on dielectric properties of road materials is still at the initial stage, so there is no corresponding standard. Influenced by material quality, manufacturing process, mixture manufacturing process, external temperature, and other factors, the average error of dielectric

property test of finished products in laboratory is generally 3%–5%. To verify the applicability of different models to asphalt mixture, the model with error less than 10% has certain applicability.

In the L-R model, the value of parameter c determines the model application range, the root mean square model is widely used in the fields of soil science and geophysics, and the cubic root model is suitable for simulating and calculating the dielectric constant of spherical and randomly distributed elliptical materials. Thus, the material type of the L-R model is different from that of the asphalt mixture. The application of the Bottcher model to two-phase symmetrical composites has a good result. The Rayleigh model considers the dielectric properties of three-phase (or higher) mixed materials, and the adjustment coefficient of the parameters is close to reality. Among the test results of the five types of models, the calculation result of the Rayleigh model is closest to the measured data, while the error is the smallest, which makes it useful as a theoretical basis to conduct the practical engineering for the detection of asphalt content in asphalt pavements using GPR.

5. Engineering Example Verification

To verify whether the accuracy and scope of application of the model established in this study meet the requirements of engineering testing, samples were taken from the asphalt pavement of the West Fourth Ring Road in Zhengzhou, as depicted in Figure 7.

We tested the asphalt content of the samples using the combustion method and obtained the real asphalt content of the pavement surface. Using the measured dielectric constant to calculate the three volume ratios of the samples, we entered the data into the asphalt content prediction model and compared the calculated results with the measured values, as illustrated in Figure 8.

It can be observed from Figure 8 that there is a significant difference between the measured value and the calculated theoretical value of asphalt content in the asphalt pavement, and the errors of the three samples are different. The relative error and average error of the calculation are depicted in Figure 9. As can be seen from Figures 8 and 9, the relative errors of samples 1, 2, and 3 are 8.80%, 14.19%, and 5.64%, respectively, and the average error of the samples is 9.47%, which is considerably higher than the accuracy of the model verified by the sample. Because the proportion of the electrical constant and volume in the asphalt mixture is minimal, using the theoretical asphalt content and dielectric constant as known conditions to calculate the three-term volume ratio of the asphalt mixture causes a large error. In addition, there is a significant difference between the asphalt mixture in the laboratory and the samples taken from the actual pavement. Thus, the main factors that must be

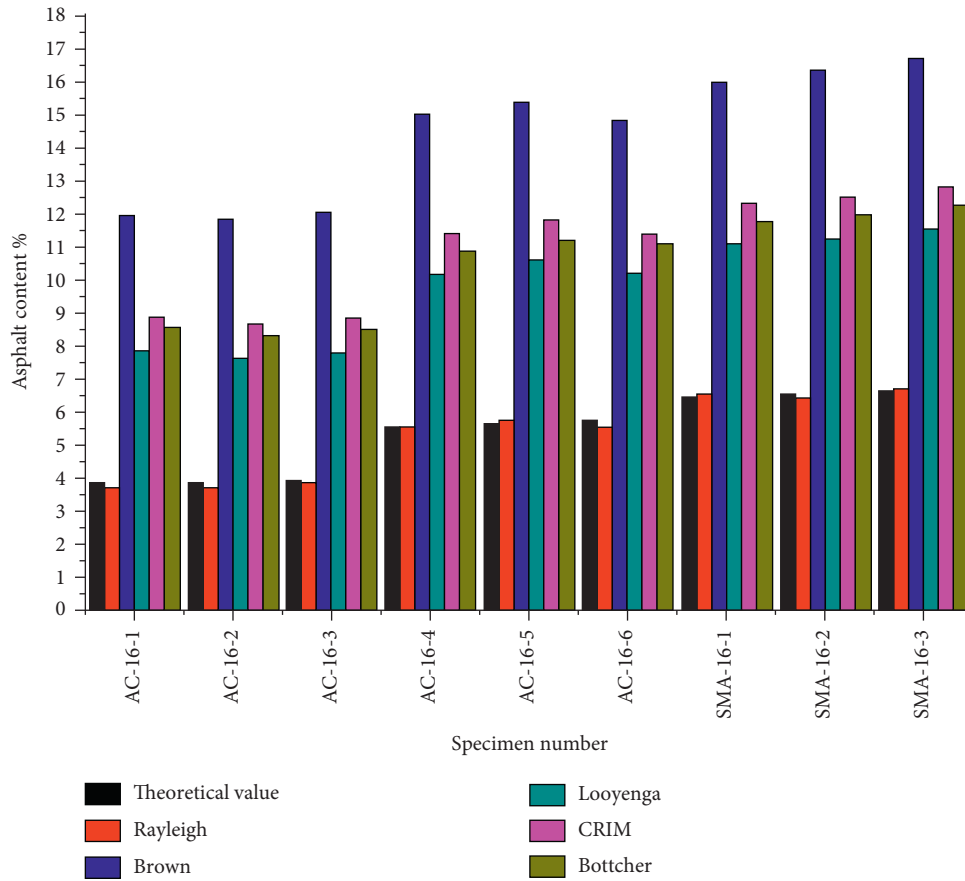


FIGURE 5: Comparison between prediction model and theoretical value.

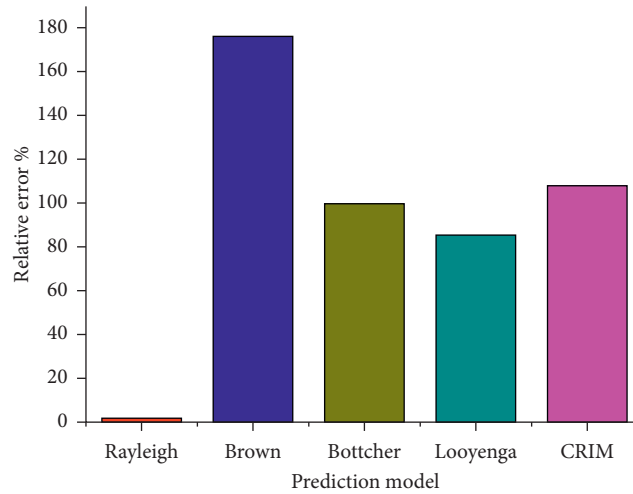


FIGURE 6: Relative error between prediction models.



FIGURE 7: On-site sampling of asphalt pavement.

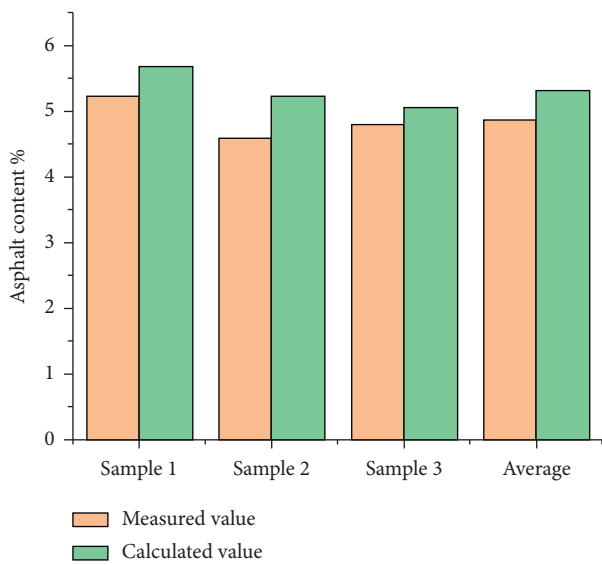


FIGURE 8: Comparison between the measured value and the calculated value of pavement sampling.

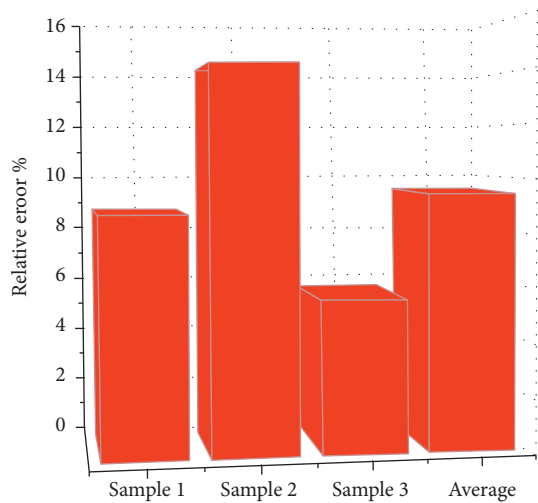


FIGURE 9: Relative error between measured and calculated values of sampling.

considered are internal factors, such as compactness, voidage, ultraviolet radiation, temperature, humidity, and other external factors. In summary, the above-mentioned factors are the reason for the large error.

6. Conclusions

In this study, three types of dielectric models suitable for asphalt mixtures were selected from various dielectric model libraries. The correlation formula between asphalt content and dielectric constant was derived, and its accuracy was verified through experiments. The results indicate the following:

- (1) In asphalt mixtures with the same gradation and mineral aggregate, as the dielectric constant of the mixture increases, the asphalt content decreases, indicating that the asphalt content is inversely proportional to the dielectric constant of the asphalt mixture.
- (2) There exists a relationship between the dielectric constant of the asphalt mixture and the particle size of the aggregate. Owing to the large dielectric constant due to the large particle size of the aggregate, the dielectric constant of the mixture increases with an increase in the aggregate size of the same type of asphalt.
- (3) According to the dielectric model of the composite, the proportion of the single medium in the mixture determines the dielectric constant of the mixture, and the single medium with a large dielectric constant is the main factor affecting the dielectric constant of the mixture. This is supported by the fact that the proportion of coarse aggregates in the asphalt mastic mixture is relatively large, and the dielectric constant of the asphalt mastic mixture is greater than that of the asphalt concrete of the same grade.
- (4) Among the established models, the calculation results of the Rayleigh model for the asphalt concrete block and asphalt mastic macadam mixture are closer to the test value, exhibiting higher accuracy.

The minimum error is 0.18%, the maximum error is 3.38%, and the average error is 1.86%. The Rayleigh model exhibits the best effect in terms of both the scope of application and accuracy rate. As an important theoretical basis for road GPR detection of the asphalt content in asphalt pavements, this study lays the foundation for follow-up work.

Data Availability

The data used to support the findings of this study are included within the article.

Conflicts of Interest

The authors declare that they have no conflicts of interest.

Acknowledgments

The authors acknowledge the support received from the National Key Research and Development Plan (Grant no. 2018YFB1600200), the National Natural Science Foundation of China (Grants nos. 51878624 and 51878622), Major Scientific and Technological Special Project in Henan (Grant no. 181100310400), the Program for Innovative Research Team (in Science and Technology) at the University of Henan Province (Grant no. 18IRTSTHN007), the Program for Science and Technology Innovation Talents in Universities of Henan Province (Grant no. 19HASTIT041), Natural Science Foundation of Henan Province (Grant no. 202300410746), and Key Research Projects of Higher Education in Henan Province (Grant no. 18A580001).

References

- [1] S. Sonny Kim, J. J. Yang, and R. Austin Etheridge, "Effects of mix design variables on flexibility index of asphalt concrete mixtures," *International Journal of Pavement Engineering*, vol. 21, p. 1275, 2020.
- [2] J. E. Edeh, U. Terry, and S. A. Okpe, "The use of cement treated reclaimed asphalt pavement-quarry waste blends as highway material," *International Journal of Pavement Engineering*, vol. 21, p. 1191, 2020.
- [3] K. Hoegh, T. Steiner, E. Zegeye Teshale, and S. Dai, "Minnesota department of transportation case studies for coreless asphalt pavement compaction assessment," *Transportation Research Record: Journal of the Transportation Research Board*, vol. 2674, no. 2, p. 291, 2020.
- [4] H. N. Yu, X. Zhu, and G. P. Qian, "Evaluation of phosphorus slag (PS) content and particle size on the performance modification effect of asphalt," *Construction and Building Materials*, vol. 256, Article ID 119334, 2020.
- [5] A. Baltrusaitis, A. Vaitkus, and J. Smirnovs, "Asphalt layer density and air voids content: GPR and laboratory testing data reliance," *Baltic Journal of Road and Bridge Engineering*, vol. 15, p. 93, 2020.
- [6] H. Liu and M. Sato, "In situ measurement of pavement thickness and dielectric permittivity by GPR using an antenna array," *NDT and E International*, vol. 64, p. 65, 2014.
- [7] L. Zhen, I. L. Al-Qadi, and S. Lahouar, "Development and validation for in situ asphalt mixture density prediction models," *NDT and E International*, vol. 44, p. 369, 2011.
- [8] T. Liu, X.-N. Zhang, Z. Li, and Z.-Q. Chen, "Research on the homogeneity of asphalt pavement quality using X-ray computed tomography (CT) and fractal theory," *Construction and Building Materials*, vol. 68, p. 587, 2014.
- [9] E. J. Jaselskis, J. Grigas, and A. Brilingas, "Dielectric properties of asphalt pavement," *Journal of Materials in Civil Engineering*, vol. 15, no. 5, p. 427, 2003.
- [10] G. C. Topp, J. L. Davis, and A. P. Annan, "Electromagnetic determination of soil water content: measurements in coaxial transmission lines," *Water Resources Research*, vol. 16, no. 3, p. 574, 1980.
- [11] K. Roth, R. Schulin, H. Fluhler, and W. Attinger, "Calibration of time domain reflectometry for water content measurement using a composite dielectricity approach," *Water Resources Research*, vol. 26, no. 10, p. 2267, 1990.
- [12] C.-M. Chang, J.-S. Chen, and T.-B. Wu, "Dielectric modeling of asphalt mixtures and relationship with density," *Journal of Transportation Engineering*, vol. 137, no. 2, p. 104, 2011.
- [13] E. Z. Teshale, K. Hoegh, and S. D. Dai, "Ground penetrating radar sensitivity to marginal changes in asphalt mixture composition," *Journal of Testing and Evaluation*, vol. 48, no. 3, Article ID 20190486, 2020.
- [14] A. L. Song and J. Gagnon, "Monitoring hot mix asphalt pavement density changes using ground penetrating radar at the FAA's national airport pavement test facility," in *Proceedings of the 15th International Conference on Ground Penetrating Radar*, p. 919, Brussels, Belgium, July 2014.
- [15] X. Hou, F. Xiao, R. Guo, Q. Xiang, T. Wang, and J. Wang, "Application of spectrophotometry on detecting asphalt content of emulsified asphalt," *Journal of Cleaner Production*, vol. 215, p. 626, 2019.
- [16] Y. S. Kumbargeri and K. P. Biligiri, "A novel approach to understanding asphalt binder aging behavior using asphaltene proportion as a performance indicator," *Journal of Testing and Evaluation*, vol. 44, p. 439, 2016.
- [17] J. Mao, L. Sun, J. Lv, and Y. Tan, "Piezoelectric and dielectric behavior of 0-3 asphalt-based composites with carbon black," *Ceramics International*, vol. 42, no. 14, p. 16132, 2016.
- [18] J. Hu, P. K. R. Vennapusa, D. J. White, and I. Beresnev, "Pavement thickness and stabilised foundation layer assessment using ground-coupled GPR," *Nondestructive Testing and Evaluation*, vol. 31, no. 3, p. 267, 2016.
- [19] K. Hoegh, S. Dai, T. Steiner, and L. Khazanovich, "Enhanced model for continuous dielectric-based asphalt compaction evaluation," *Transportation Research Record: Journal of the Transportation Research Board*, vol. 2672, no. 26, p. 144, 2018.
- [20] C. Plati and A. Loizos, "Using ground-penetrating radar for assessing the structural needs of asphalt pavements," *Nondestructive Testing and Evaluation*, vol. 27, no. 3, p. 273, 2012.
- [21] P. Shangguan, I. L. Al-Qadi, and S. Lahouar, "Pattern recognition algorithms for density estimation of asphalt pavement during compaction: a simulation study," *Journal of Applied Geophysics*, vol. 107, p. 8, 2014.
- [22] D.-H. Chen, F. Hong, W. Zhou, and P. Ying, "Estimating the hotmix asphalt air voids from ground penetrating radar," *NDT and E International*, vol. 68, p. 120, 2014.
- [23] S. Wang, S. Zhao, and I. L. Al-Qadi, "Continuous real-time monitoring of flexible pavement layer density and thickness using ground penetrating radar," *NDT and E International*, vol. 100, p. 48, 2018.
- [24] A. Ahmed, K. Emad, and M. Eyad, "Method for predicting the laboratory compaction behavior of asphalt mixtures," *Journal of Materials in Civil Engineering*, vol. 27, 2015.